Università degli Studi di Trieste
XXIX Ciclo del dottorato di ricerca in Fisica

Low-energy physics in strongly correlated materials via nonlinear spectroscopies

Settore scientifico-disciplinare: FIS/03

Dottorando **Francesco Randi**

Supervisore **Dr. Daniele Fausti**

Coordinatore **Prof. Paolo Camerini,**
Prof. Livio Lanceri

Anno Accademico 2015/2016

Contents

Introduction **ix**

Riassunto **xiii**

I Out-of-equilibrium first order phase transitions and phase separation **1**

1 The out-of-equilibrium Verwey transition and phase separation in magnetite **5**
1.1 Introduction 5
1.2 Experiments 8
1.3 Results 9
1.3.1 Equilibrium optical properties 9
1.3.2 Out-of-equilibrium optical properties 12
1.4 Discussion 16
1.4.1 Out-of-equilibrium phase transition and supply of latent heat 17
1.4.2 Nucleation of the metallic phase, out-of-equilibrium phase separation, and non-separability of the response 20
1.4.3 Equilibrium optical properties across the phase transition 27
1.4.4 Spectral response of the phase transition 28
1.5 Conclusions 29
1.6 Non-separable dynamics as a general signature of phase separation? 32

2 Modelling of the optical properties of solids **41**
2.1 The dielectric function at equilibrium 41

2.1.1 The Lorentz oscillator 42
2.1.2 Other kinds of oscillators 43
2.2 Out of equilibrium fits 44

II Exciting materials in the mid-infrared 53

1 The experimental set-up 55
1.1 Introduction to nonlinear optics 55
1.1.1 Second-order nonlinear phenomena 57
1.1.2 Phase matching 59
1.1.3 Photon downconversion 60
1.1.4 Third-order nonlinear phenomena 62
1.2 The set-up and its characterization 62
1.2.1 The set-up 63
1.2.2 Characterization of the mid-infrared pulses 69
1.2.3 Commercial solution: characterization 76
1.3 A model experiment: exciting a vibrational mode in $CuGeO_3$. 77
1.3.1 Introduction 78
1.3.2 Experiment and results 79

2 Pump-probe experiments on $Bi_2Sr_2Ca_{0.92}Y_{0.08}Cu_2O_8$ 87
2.1 Introduction 87
2.2 Experiment 89
2.3 Results and discussion 91
2.3.1 Room temperature 91
2.3.2 Pseudogap phase 102
2.3.3 Superconducting phase 103
2.4 Conclusions 112

III Fluctuations of the out-of-equilibrium optical properties 119

1 Time-dependent mean-field approach 125
1.1 Equations of motion 126
1.2 Equilibrium state 128
1.3 Displacive excitation from the symmetry-broken state 131
1.4 What mean field does and does not capture 134

2 Dynamical mean-field theory approach - theory **137**
2.1 Introduction to nonequilibrium DMFT 137
2.1.1 Kadanoff-Baym formalism for time evolution from a thermal state 138
2.1.2 Dynamical mean-field theory 143
2.1.3 Nonequilibrium dynamical mean-field theory 145
2.2 Nonequilibrium DMFT for the Holstein model 145
2.2.1 Equations for the two different sites 148
2.3 Current-current correlators 149
2.3.1 Optical susceptibility 149
2.3.2 Optical susceptibility with two sublattices 152
2.3.3 Fluctuation-dissipation relations 153
2.3.4 Fluctuations of the optical properties 154

3 Dynamical mean-field theory - Results **159**
3.1 Displacive excitation 160
3.2 Thermalization of the system 172
3.3 Fluctuations of the optical properties 180
3.4 Comparison with experiments on bismuth single crystals 182
3.5 Conclusions 186

IV Time-resolved photoemission: room for enhancements **191**

1 Time-resolved photoemission beyond the energy-time uncertainty **193**
1.1 Introduction 193
1.2 Generalized time-resolved photoemission 195
1.2.1 Theoretical formulation 195
1.2.2 Double-probe photoemission: Tomography of $G^<(t,t')$. 197
1.3 Illustration and proposals for the double probe experiment . . . 201
1.3.1 Buildup of the Kondo resonance: standard time-resolved photoemission 201
1.3.2 Buildup of the Kondo resonance: double probe photoemission 203
1.3.3 Melting of Mott gaps and amplitude mode in a superconductor 207
1.4 Conclusions 208

2 Time-resolved photoemission: the non-separable case **209**
2.1 Photoemission with non-coherent states of light 209
2.2 Theory of time-resolved photoemission spectroscopy with non-classical light pulses 212
2.3 Pulse correlation for a multimode squeezed state 217
2.4 Conclusions 219

Conclusions **227**

List of publications **233**

Acknowledgements **235**

Introduction

Many macroscopic properties of solids are determined by the behaviour of the electrons they contain. In elemental crystals or in crystals containing elements solely from the first three periods of the periodic table, the electrons in the highest energy levels can easily hop from one atom to its neighbours. They are, therefore, (potentially) highly mobile and the atomic levels give rise to very dispersive bands. Given the crystalline structure of the solid, its electrical conductance is determined by the availability of empty states for the electrons to move through the crystal. In the cases in which the bands are sequentially filled and do not overlap, whether the solid is a metal or an insulator can, therefore, be determined by simple counting of the electrons in a unit cell.

The situation changes when the character of the highest energy states make the electrons less mobile. For example, the movement of electrons is difficult through alternating d- and p-orbitals, because the hopping integral between them is low. In this context, the correlation between the position of the electrons becomes, therefore, strongly relevant in the determination of the macroscopic properties of the system. On the most "basic" level, strong correlation may determine the insulating character of a system, even though the number of electrons per unit cell would suggest a metallic character. This is the case of the Mott insulator, which cannot be captured by the mean-field models which accurately describe the properties of s- and p-metals.

More in general, strongly correlated materials display very rich phase diagrams, containing many phases in reach with small variations of the external parameters or of the chemical doping. The variety of phases encompasses superconducting states, antiferromagnets, insulators, Fermi liquid metals and strange (non-Fermi liquid) metals, charge density wave, nematic states, and others. Strong correlation is most famously realized in the oxides of the transition metals.

The rich phase diagrams of strongly correlated materials provide deep intellectual problems, such as the emergence of collective phenomena in condensed

matter, but also a wealth of possible technological application exploiting their phase transitions. For example, insulator-to-metal transitions in transition metal oxides are good candidates for new fast electronic switching.

In general, condensed matter can be studied both at and out of its equilibrium state. The first reason to perform out-of-equilibrium experiments is to gain a deeper insight on the interactions between degrees of freedom in the solid. They will, in fact, react to a strong perturbation with different relaxation timescales. If their interactions cannot be clearly identified from their equilibrium properties (e.g. their spectra), there is a higher chance to do it when they are out of equilibrium. Since the relevant timescales in condensed matter are of the order of the pico- and femtosecond, out-of-equilibrium experiments have to be perfomed using ultrashort light pulses in pump-probe experiments. An intense ultrashort light pulse, called pump, perturbs the system bringing it out of equilibrium and a second, delayed, and less intense pulse, called probe, probes its optical properties (e.g. its reflectivity) as a function of time after the excitation.

Moreover, in many cases the technological exploitation of strongly correlated materials lies in the very fact that their phase transitions can be triggered on ultrashort timescales. Out-of-equilibrium pump-probe experiments allow therefore to study, characterize, and discover new ultrafast out-of-equilibrium phase transition.

The case of magnetite (Fe_3O_4) is probably the most studied in this context, and one of the oldest. In 1939 E.J.W. Verwey identified a first-order transition at T_c =123 K between the high-temperature metallic phase of magnetite and a low-temperature insulating phase [1]. The crystalline structure of magnetite in the insulating phase has been particularly difficult to determine, and the exact nature of its refinement is still under debate [2]. In the system kept below the T_c the insulator-to-metal transition can be triggered by light pulses and is complete within picoseconds [3], i.e. it is far quicker than anything that can be called quasistatic. What happens when first-order phase transitions occur too quickly? This question is addressed in part I of this thesis in the case of the photoinduced insulator-to-metal transition in magnetite. In particular, I will discuss the occurrence of phase separation in a specific regime, and its interesting effects on the out-of-equilibrium optical properties of the system.

The experiment on magnetite has been performed with two tacit assumptions, whose justifications and limitations are addressed in part II and III of this thesis. The first and probably most evident one concerns the photon energy (or wavelength) of the light pulses used to photoexcite the system. Technical reasons constrain commercial ultrafast pulsed lasers to very narrow spectral regions. In particular, titanium-doped sapphire lasers produce light

with photon energies close to 1.5 eV. Pump-probe experiments have therefore been traditionally performed with such pulses, in the assumption that the excitations they create in the system are "right", in that they are either tuned to the relevant transitions or that the excitations they produce are sufficiently general in character.

This issue is of particular relevance for the excitation of degrees of freedom with energies of the order of 0.1 eV or below, which are far removed from the 1.5 eV photon energy of the Ti:Sapphire lasers. For example, in the high critical temperature cuprate superconductors the relevant energies of the superconducting state are of the order of tens or one hundred millielectronvolts. The mismatch between these energy scales and the available photon energies can be cured building pulsed light sources with tunable photon energy in the mid-infrared spectral range. These exploit nonlinear optical phenomena to produce light pulses at the desired photon energy using the pulses from the commercial laser source. In chapter II.1 I will describe the optical set-up we have built for this purpose.

$Bi_2Sr_2Ca_{0.92}Y_{0.08}Cu_2O_8$ is a representative member of the familiy of the cuprates and is a superconductor at temperatures below 96 K. In chapter II.2 I will discuss how we were able, thanks to the tunable mid-infrared pulses, to identify a scattering channel for electronic excitations at room temperature and to study the response of the system along different directions both at room temperature and in the low-temperature phases of the system.

The second tacit assumption done in the experiment on magnetite is that the state of the system after the photoexcitation rapidly becomes an effectively thermal state. In many cases this is a safe assumption. For example, in simple metals, photoexcited electrons will quickly relax down to states close to the Fermi energy and thermalize. Their state will then display the standard features of thermal states, such as the fact that their occupation of electronic levels is described by the Fermi function.

There are more complicated situations in which this need not be the case. For example, when coherent dynamics are present in degrees of freedom with whom electrons are coupled, electrons may not be able to thermalize at all times. In part III, this situation is discussed for the case of coherent lattice vibrations in solids, with the aid of numerical calculations. For particular phases of the vibration, the electronic subsystem is indeed "less thermal" than for other phases, and I discuss how such kind of information can be retrieved from the out-of-equilibrium optical properties of the solid, comparing our calculations with experimental results obtained on bismuth single crystals.

Besides optical spectroscopy, a very important tool to study condensed matter is photoelectron spectroscopy, which allows to measure the single par-

ticle spectrum of the system. At equilibrium it gives access to the band structure of the occupied levels in the system. The spectroscopy of electrons photoemitted from a solid can be performed also in a time-resolved manner in a pump-probe scheme. A first pulse (usually with a photon energy of 1.5 eV) brings the system out of its equilibrium, and a subsequent ultraviolet pulse photoemits the electrons. In this way, the occupation of the bands can be studied as a function of time after the excitation. Moreover, changes in the band structure itself can be detected.

Time-resolved photoemission is affected by the so-called energy-time uncertainty relation. In fact, the light pulses employed to photoemit the electrons necessarily have a spectrum of finite width, which increases upon decreasing the temporal duration of the pulses. This is reflected in a spread in the kinetic energy of the photoemitted electrons. Therefore, a tradeoff must be made between the temporal and energetic resolution in time-resolved photoemission. Such limitation becomes extremely relevant in the study of the nonequilibrium dynamics of the emergent properties of strongly correlated materials. While these become manifest in very sharp spectral features, it is known that some of them can evolve on timescales shorter than the inverse width of their spectroscopic fingerprint [8]. This kind of dynamics beyond the spectral uncertainty limit cannot be resolved in standard time-resolved photoemission.

The energy-time uncertainty relation is often erroneously associated to the uncertainty relations stemming from the Heisenberg principle. Its consequences on time-resolved photoemission have been, therefore, always considered as an unavoidable limitation. However, the energy-time uncertainty is not of fundamental nature [9]. In part IV I discuss how time-resolved photoemission can be enhanced. In chapter IV.1 we theoretically propose an experimental scheme which allows to bypass the energy-time uncertainty in time-resolved photoemission using two photoemitting pulses. Moreover, in chapter IV.2, we theoretically study the features of time-resolved photoemission if it were performed with statistical and quantum light.

Riassunto

Molte delle proprietà macroscopiche dei solidi sono determinate dal comportamento degli elettroni che essi contengono. Nei cristalli elementali e nei cristalli formati solamente da elementi dei primi tre periodi della tavola periodica, gli elettroni nei livelli energetici più alti possono saltare facilmente da un atomo ai suoi vicini. Essi sono, perciò, potenzialmente molto mobili e i livelli atomici danno origine a delle bande molto dispersive. Data la struttura cristallina del solido, la sua conducibilità elettrica è determinata dalla disponibilità di stati vuoti che gli elettroni possano sfruttare per muoversi attraverso il cristallo. Nei casi in cui le bande sono riempite in successione e non si sovrappongono, se il solido sia un metallo o un isolante può essere determinato dal semplice conteggio degli elettroni in una cella unitaria.

La situazione cambia se il carattere degli stati a più alta energia è tale da rendere meno mobili gli elettroni. Ad esempio, il moto degli elettroni attraverso un'alternanza di orbitali d e p è difficoltoso, poiché l'elemento di matrice interatomico tra di loro è piccolo. In una tale situazione, la correlazione tra le posizioni degli elettroni gioca un ruolo molto rilevante nella determinazione delle proprietà macroscopiche del solido. L'effetto più "basilare" che ciò può produrre è che la forte correlazione renda un solido isolante, a dispetto del fatto che il numero di elettroni per cella unitaria suggerisca un carattere metallico. Questo è il caso degli isolanti di Mott, che non possono venire descritti dai modelli di campo medio, i quali invece riescono a descrivere accuratamente le proprietà dei metalli s e p.

Più in generale, i materiali fortemente correlati presentano dei diagrammi di fase molto ricchi, contenenti varie fasi raggiungibili attraverso piccole variazioni dei parametri esterni o del drogaggio chimico. La moltitudine delle fasi possibili include stati superconduttivi, antiferromagnetici, isolanti, metallici del tipo liquido di Fermi e non (metalli strani), stati nematici, onde di densità di carica e altri. Le più conosciute realizzazioni della forte correlazione elettronica si trovano negli ossidi dei metalli di transizione.

I ricchi diagrammi di fase dei materiali fortemente correlati forniscono questioni intellettuali profonde, come l'emergenza di fenomeni collettivi nella materia condensata, ma anche una varietà di possibili applicazioni tecnologiche delle loro transizioni di fase. Ad esempio, le transizioni di fase da isolante a metallo negli ossidi dei metalli di transizione sono buone candidate per ottenere nuove elettroniche di *switch* ultraveloci.

In generale, la materia condensata può essere studiata sia all'equilibrio che fuori equilibrio. La prima ragione per effettuare esperimenti fuori equilibrio è che essi possono fornire nuove informazioni sulle interazioni tra i gradi di libertà nel solido. Questi ultimi, infatti, risponderanno a una forte perturbazione con diversi tempi di rilassamento. Se le loro interazioni non possono essere identificate chiaramente dalle proprietà del solido all'equilibrio (ad esempio dai suoi spettri), ci sono più possibilità di farlo quando esso è fuori equilibrio. Siccome i tempi caratteristici in questione nella materia condensata sono dell'ordine del pico- e femtosecondo, gli esperimenti fuori equilibrio devono essere effettuati con impulsi di luce ultracorti in esperimenti di pompa e sonda (di *pump-probe*). Un primo impulso di luce ultracorto e intenso (detto impulso di pompa, o pump) perturba il sistema portandolo fuori equilibrio. Un secondo impulso, meno intenso e ritardato rispetto al primo (detto impulso di probe), sonda le proprietà ottiche del sistema (ad esempio la sua riflettività) in funzione del tempo trascorso dall'eccitazione.

Inoltre, in molti casi lo sfruttamento tecnologico dei materiali fortemente correlati sta nel fatto stesso che le loro transizioni di fase possono essere indotte su tempi scala ultracorti. Gli esperimenti di pump-probe permettono quindi di studiare, caratterizzare e scoprire nuove transizioni di fase ultraveloci.

Il caso della magnetite (Fe_3O_4) è probabilmente il più studiato in questo contesto, e uno dei più antichi. Nel 1939 E.J.W. Verwey identificò, a $T_c = 123$ K, una transizione di fase del primo ordine tra la fase metallica ad alta temperatura e una fase isolante a bassa temperatura [1]. La struttura cristallina della magnetite nella fase isolante è stata particolarmente difficile da determinare e l'esatta natura dei suoi raffinamenti è tuttora dibattuta [2]. In un campione tenuto a temperatura minore di T_c, la transizione di fase da isolante a metallo può essere fotoindotta tramite un impulso di luce intenso [3] con una fluenza [1] al di sopra di una soglia, ed è completa entro qualche picosecondo, ovvero avviene molto più velocemente di qualsiasi cosa che si possa chiamare quasistatico. Cosa succede quanto una transizione di fase del primo ordine avviene troppo velocemente?

[1] La fluenza è la densità di energia depositata da un impulso nel campione per unità di superficie

La parte I di questa tesi si occupa dello studio di questa transizione di fase fuori equilibrio in esperimenti di *pump-probe* con impulsi nel vicino infrarosso e visibile. I nostri dati rivelano che, in prossimità della soglia per l'innesco della transizione di fase, esiste un regime strettamente legato alla fornitura del calore specifico nella transizione di fase all'equilibrio. In questo regime, la transizione di fase procede attraverso la nucleazione di eccitazioni locali in volumi del campione nella fase ad alta temperatura, ovvero nel campione avviene separazione di fase fuori equilibrio. Per fluenze degli impulsi di pompa ben al di sopra della soglia, il campione viene portato nella fase ad alta temperatura immediatamente ed omogeneamente.

Uno dei risultati più interessanti che ho riportato è che, in prossimità della soglia, ovvero nel regime in cui avviene la separazione di fase, la variazione relativa della riflettività del campione $\frac{\Delta \mathrm{R}}{\mathrm{R}}(h\nu, t)$ mostra una specifica proprietà matematica: non è separabile (o fattorizzabile) nello spazio degli spettri e delle evoluzioni temporali. Questo è un modo formale per dire che $\frac{\Delta \mathrm{R}}{\mathrm{R}}(h\nu, t)$ non può essere scritta come il prodotto di una singola caratteristica spettrale e una singola evoluzione temporale uguale per tutte le energie del fotone (o lunghezze d'onda) della luce, ma deve essere scritta come una somma di due o più di questi termini (o componenti spettro-temporali). Ben al di sotto e ben al di sopra della soglia, $\frac{\Delta \mathrm{R}}{\mathrm{R}}$ è invece separabile, ovvero può essere espressa come una singola componente spettro-temporale. Siccome questa è una proprietà puramente matematica dei dati, che non coinvolge nessun modello specifco, si può congetturare che essa sia una caratteristica generale della separazione di fase fuori equilibrio, al di là del caso specifico della magntite. Analizzando i dati presenti nella letteratura riguardo ad esperimenti simili [4], ho mostrato che questa caratteristica può essere trovata in almeno un altro materiale, il biossido di vanadio (VO_2).

L'esperimento sulla magnetite è stato effettuato facendo uso di due assunti sottaciuti, delle cui giustificazioni e limitazioni si occupano le parti II and III di questa tesi. Il primo di essi, e probabilmente il più evidente, riguarda l'energia del fotone (o lunghezza d'onda) degli impulsi di luce utilizzati per fotoeccitare il sistema e indurre la transizione di fase. Per ragioni tecniche, i laser impulsati commerciali sono limitati alla produzione di luce in intervalli di energie del fotone molto stretti. In particolare, i laser allo zaffiro drogato con titanio producono luce con energie del fotone di circa 1.5 eV. Pertanto, tradizionalmente gli esperimenti di *pump-probe* sono stati effettuati con questo genere di impulsi, assumendo che le eccitazioni che essi creano nel sistema siano "giuste", ovvero che essi siano risonanti con le transizioni rilevanti o che le eccitazioni prodotte abbiano un carattere sufficientemente generale.

Questa questione è di particolare rilevanza per le eccitazioni di gradi di

libertà con energie dell'ordine di 0.1 eV o minori, molto diverse dall'energia del fotone di 1.5 eV dei laser al Ti:Al_2O_3. Per esempio, nei cuprati superconduttori ad alta temperatura critica, le scale di energia più importanti per lo stato superconduttivo sono dell'ordine di 0.1 o 0.01 eV. La discrepanza tra queste energie e le energie del fotone disponibili può essere curata costruendo sorgenti di luce impulsata con energia del fotone regolabile nel medio infrarosso. Queste sorgenti sfruttano processi ottici non-lineari per la produzione, a partire dagli impulsi prodotti dai laser commerciali, di impulsi di luce all'energia del fotone desiderata. Nel capitolo II.1 descrivo l'apparato ottico che ho costruito con questo scopo.

$Bi_2Sr_2Ca_{0.92}Y_{0.08}Cu_2O_8$ è un membro rappresentativo della famiglia dei cuprati ed è un superconduttore a temperature minori di 96 K. Esso è il composto a drogaggio ottimale di ittrio della famiglia di materiali detta Bi2212, il cui composto madre è $Bi_2Sr_2CaCu_2O_8$. Nel capitolo II.2 descrivo esperimenti di pump-probe che abbiamo condotto su questo materiale con impulsi di pompa nel medio infrarosso, ovvero con energie del fotone tra 0.1 e 0.2 eV. I nostri dati rivelano che la dinamica indotta dall'eccittazione dipende fortemente dal vettore d'onda degli stati elettronici. A temperatura ambiente, riportiamo evidenze di un accoppiamento degli elettroni con un ordine di carica fluttuante ed eccitazioni di spin. In particolare, eccitazioni totalmente simmetriche e eccitazioni lungo le direzioni che nello stato superconduttivo sono le direzioni antinodali sono accoppiate a coppie di eccitazioni di spin. Lungo le direzioni che a bassa temperatura sono le direzioni nodali, le eccitazioni sono accoppiate anche ad un modo vibrazionale associato a una modulazione superstrutturale del reticolo, che oscilla coerentemente dopo l'eccitazione da parte dell'impulso di pompa. Abbassando la temperatura al di sotto di 130 K, il campione entra nella fase di pseudogap e questa oscillazione reticolare coerente scompare. Ciò può significare o che l'accoppiamento tra gli elettroni e la modulazione superstrutturale cambia, oppure che quest'ultima scompare abbassando la temperatura. Nella fase superconduttiva, siamo stati in grado di osservare separatamente la dinamica delle eccitazioni di pseudogap e un altro tipo di dinamica mediante misure selettive in vettore d'onda.

Il secondo assunto impiegato nella discussione dell'esperimento sulla magnetite è che lo stato del sistema dopo la fotoeccitazione diventi rapidamente uno stato efficacemente termico. In molti casi questa è un'ipotesi che può essere fatta in modo sicuro. Ad esempio, nei metalli semplici gli elettroni fotoeccitati rilassano velocemente verso stati vicini all'energia di Fermi e termalizzano. Il loro stato avrà quindi le caratteristiche di uno stato termico, tra cui il fatto che l'occupazione degli stati elettronici è descritta dalla funzione di Fermi. Esistono situazioni più complicate in cui questo non avviene necessariamente.

Ad esempio, gli elettroni potrebbero non riuscire a termalizzare continuamente quando sono presenti delle dinamiche coerenti in gradi di libertà a cui essi sono accoppiati.

Un sottile assunto che consegue dall'assunzione di un generico stato termico è che le informazioni che si possono ottenere in un esperimento "ottico" si esauriscano nel valor medio delle proprietà ottiche. Gli esperimenti "ottici" di pump-probe (ovvero che fanno uso di soli impulsi di luce) sono effettuati misurando l'intensità degli impulsi di probe a ritardi diversi tra pump e probe. Per rimuovere il rumore, ad ogni ritardo tra pompa e probe la misura avviene mediando le intensità di centinaia o di migliaia di impulsi. Le fluttuazioni dell'intensità sono quasi sempre transcurate.

Nella parte III discuto queste due questioni. Che informazioni aggiuntive possono essere ottenute misurando le fluttuazioni delle proprietà ottiche di un sistema fuori equilibrio? Come avviene la termalizzazione di un sistema quando la dinamica non è "banale"? Abbiamo mostrato che, in generale, le fluttuazioni delle proprietà ottiche sono legate alle fluttuazioni delle correnti nel sistema. Per contestualizzare questo risultato, abbiamo effettuato simulazioni numeriche delle vibrazioni reticolari coerenti in teoria di campo medio dinamico fuori equilibrio [5,6] (*nonequilibrium dynamical mean-field theory*), utilizzando il modello di Holstein. Abbiamo mostrato che la teoria di campo medio dinamico fuori equilibrio è in grado di descrivere le caratteristiche principali delle vibrazioni coerenti nei sistemi di Peierls dopo un'eccitazione impulsiva, ovvero l'eccitazione tramite dislocazione (*displacive excitation*), l'ammorbidimento della frequenza della vibrazione, lo smorzamento della dinamica e, infine, la fusione della fase a simmetria rotta. Queste caratteristiche forniscono una basilare dinamica non banale per esplorare teoricamente che informazioni aggiuntive possono essere ottenute misurando le fluttuazioni delle proprietà ottiche. Verificando se le relazioni di fluttuazione-dissipazione fossero rispettate fuori dall'equilibrio, abbiamo mostrato che, mentre la gap viene modulata a seguito dell'eccitazione, il sistema oscilla tra stati termici e stati non-termici. Ciò produce delle proprietà caratteristiche nello spettro delle fluttuazioni della corrente, che possono essere sondate attraverso la misura delle fluttuazioni dell'intensità degli impulsi di probe. Con le nostre simulazioni siamo stati in grado di riprodurre dati sperimentali ottenuti in esperimenti di questo tipo su cristalli elementali di bismuto, mostrando che questo genere di esperimenti può dare accesso a nuove informazioni nelle spettroscopie ottiche fuori equilibrio.

A parte le spettroscopie ottiche, uno strumento molto importante nello studio della materia condensata è la spettroscopia fotoelettronica, che permette di misurare lo spettro di singola particella del sistema. All'equilibrio, essa dà

accesso alla struttura a bande dei livelli occupati. La spettroscopia degli elettroni fotoemessi da un materiale può essere effettuata anche in modo risolto in tempo, in uno schema di pump-probe: un primo impulso (comunemente con un'energia del fotone di 1.5 eV) porta il sistema fuori equilibrio e un successivo impulso ultravioletto (o di raggi X) fotoemette gli elettroni. In questo modo si può studiare come cambia l'occupazione elettronica delle bande in funzione del tempo trascorso dall'eccitazione. Inoltre, si possono anche misurare eventuali cambiamenti nella struttura a bande stessa.

La fotoemissione risolta in tempo è influenzata dalla relazione di indeterminazione tra energia e tempo. Infatti, gli impulsi di luce impiegati per fotoemettere gli elettroni hanno necessariamente uno spettro di largezza finita, la quale aumenta al diminuire della durata dell'impulso. Ciò si riflette in un allargamento dello spettro delle energie cinetiche degli elettroni fotoemessi. Per questo motivo, negli esperimenti di fotoemissione risolta in tempo è necessario scendere a un compromesso tra le risoluzioni temporale ed energetica. Questa limitazione diventa di grande rilevanza nello studio delle dinamiche delle proprietà emergenti nei materiali fortemente correlati. Mentre queste proprietà si manifestano solo in delle caratteristiche spettrali molto strette, è noto che alcune possono evolvere su scale temporali più corte dell'inverso della larghezza energetica della loro impronta spettrale [8]. Questo tipo di dinamica, al di là del limite di indeterminazione spettrale, non può essere misurato con la tradizionale fotoemissione risolta in tempo.

La relazione di indeterminazione tra il tempo e l'energia è spesso erroneamente associata alle relazioni di indeterminazione che derivano dal principio di Heisenberg. Pertanto, le sue conseguenze sulla fotoemissione risolta in tempo sono sempre state considerate come inevitabili [7]. Tuttavia, la relazione di indeterminazione tra energia e tempo non è di natura fondamentale [9]. Nel capitolo IV.1 descrivo la nostra proposta teorica per aggirare l'indeterminazione tra energia e tempo nella fotoemissione risolta in tempo. Ciò può essere fatto utilizzando due impulsi di probe per fotoemettere gli elettroni dal sistema. Questo doppio impulso si può ottenere dividendo, ritardando e ricombinando un singolo impulso originario. In funzione del ritardo tra i due impulsi di probe, la probabilità totale che un elettrone venga fotoemesso cambia. Grazie a questa dipendenza è possibile ricostruire tomograficamente la funzione di Green $G(t, t')$, la quale contiene tutte le informazioni riguardo alla risposta di singola particella del sistema. Abbiamo illustrato questa proposta teorica attraverso simulazioni numeriche della formazione della risonanza di Kondo, un prototipo di dinamica di un fenomeno emergente che avviene al di là del limite di indeterminazione spettrale, ovvero su tempi scala più corti rispetto all'inverso della larghezza della sua caratteristica spettrale. Inoltre, abbiamo

discusso come l'apparato sperimentale proposto sia rilevante a possa trovare delle applicazioni anche in altri casi, come ad esempio nello studio della fusione di gap di Mott o delle dinamiche dei superconduttori.

Infine, nel capitolo IV.2 presento la nostra discussione dell'utilizzo di luce quantistica o statistica nella fotoemissione. Impulsi di luce quantistici o statistici con forme specifiche permetterebbero di misurare delle correlazioni specifiche nella dinamica dei sistemi fuori equilibrio con una singola misura, senza il bisogno di effettuare una sequenza tomografica di misure con impulsi classici come discusso nel capitolo IV.1.

Bibliography

[1] E. J. W. Verwey. Electronic conduction of magnetite (Fe_3O_4) and its transition point at low temperatures. *Nature (London)*, 144:327–328, 1939.

[2] M. S. Senn, J. P. Wright, and J. P. Attfield. Charge order and three-site distortions in the Verwey structure of magnetite. *Nature (London)*, 481:173–176, 2012.

[3] S. de Jong, R. Kukreja, C. Trabant, N. Pontius, C. F. CHang, T. Kachel, M. Beye, F. Sorgenfrei, B. Back, C. H. Bräuer, et al. Speed limit of the insulator-metal transition in magnetite. *Nat. Mater.*, 12:882–886, 2013.

[4] S. Wall, L. Foglia, D. Wegkamp, K. Appavoo, J. Nag, R.F. Haglund, Jr., J. Stähler, and M. Wolf Tracking the evolution of electronic and structural properties of VO_2 during the ultrafast photoinduced insulator-metal transition Phys. Rev. B **87**, 115126 (2013).

[5] A. Georges, G. Kotliar, W. Krauth, and M.J. Rozenberg "Dynamical mean-field theory of strongly correlated fermion systems and the limit of infinite dimensions" Rev. Mod. Phyis. **68**, 13 (1996).

[6] H. Aoki, N. Tsuji, M. Eckstein, M. Kollar, T. Oka, and P. Werner "Nonequilibrium dynamical mean field theory and its applications" Rev. Mod. Phys. **86**, 779 (2014).

[7] J. K. Freericks, H. R. Krishnamurthy, and Th. Pruschke. "Theoretical description of time-resolved photoemission spectroscopy: Application to pump-probe experiments", Phys. Rev. Lett., **102**, 136401 (2009).

[8] B. Lechtenberg and F. B. Anders, "Spatial and temporal propagation of Kondo correlations", Phys. Rev. B **90**, 045117 (2014).

[9] L. Landau and E. Lifschitz, “Quantum mechanics - Non-relativistic theory”, Course of theoretical physics **3**, 157 (§44: The uncertainty relation for energy), Pergamon Press (1977).

Part I

Out-of-equilibrium first order phase transitions and phase separation

In the modern classification, phase transitions fall into two main categories. First-order phase transitions involve latent heat. Phase transitions that do not involve latent heat are called second-order or continuous phase transitions. In first-order phase transitions a finite amount of heat has to be supplied (or extracted) for the transition to be complete over the whole system. While the latent heat is exchanged, phase coexistence takes place, i.e. part of the system will be in one phase and the rest in the other.

In such a process, the temperature of the system remains constant. To introduce a notation that I will use later in this part of the thesis, let us consider a system which is heated from below the critical temperature of the transition. At the critical temperature T_c, we can say that its temperature is T_c^- when no portion of the latent heat has been supplied, while it is T_c^+ when the latent heat has been fully supplied.

What happens when a first-order phase transition occurs too quickly? The most common example of such a situation comes from our everyday life. When water is heated over fire and latent heat is supplied, water boils, i.e. phase separation takes place. Here and in the following, I will generally refer to phase separation not as the simple phase coexistence with just two separate volumes (in the current example, a volume of liquid and a volume of gasueous water), but to the situation in which there are more than two different volumes with boundaries that dynamically evolve.

This does not happen only in liquid-to-gaseuous or solid-to-liquid transitions, but also in solid-to-solid phase transitions. In chapter 1 of this part I will discuss the occurrence of phase separation during the supply of latent heat in an insulator-to-metal transition which takes place in magnetite (Fe_3O_4), the so-called Verwey phase transition [1].

We studied its occurrence out of equilibrium in pump-probe experiments with ultrashort light pulses, which can be used to trigger the phase transition when the sample is at a temperature below the critical temperature [2, 3].

We have shown that, when out-of-equilibrim phase separation occurs, the variation of the reflectivity of the sample has a specific mathematical property, i.e. it is non-separable (or non-factorizable) as a function of pump-probe delay and probe photon energy.

Since the occurrence of phase separation during the delivery of latent heat is a general phenomenon, one would naturally expect that the behaviour found in magnetite would appear also in other similar out-of-equilibrium phase transitions. In particular, the non-separability of the variation of the reflectivity would be a signature of phase separation to look for. Using data from the literature [4], I will show that this may indeed the case at least for another sample (vanadium dioxide, VO2).

In chapter 2 I will briefly describe the modelling of the optical properties of solids both at and out of equilibrium, with a small reference for its implementation.

Chapter 1

The out-of-equilibrium Verwey transition and phase separation in magnetite

1.1 Introduction

The Verwey phase transition [1], occurring at $T_V = 123\,\mathrm{K}$ in magnetite (Fe_3O_4), is presumably the most studied metal-to-insulator transition in the large family of transition metal oxides [1, 5]. Detailed investigations of the structure revealed a stunning complexity [6–17]. Magnetite crystallizes with an inverse spinel structure (figure 1.1a), characterized by two different groups (A and B) of Fe ion sites. Group A is constituted by tetrahedrally coordinated Fe_A^{3+} sites with a $3d^5$ electronic configuration with spin S=5/2. Group B, instead, is made of octahedrally coordinated sites formally occupied by Fe_B^{3+} ($3d^5$, S=5/2) and Fe_B^{2+} ($3d^6$, S=2) ions. At $T_c = 858\,\mathrm{K}$, ferrimagnetic order sets in with ferromagnetic coupling within the B sublattice and antiferromagnetic coupling between A and B sites such that the A sites carry minority spins $\downarrow$. The original picture of the Verwey transition at T_V involves a metallic high-temperature phase showing an equal number of Fe_B^{3+} and Fe_B^{2+} ions randomly

[1] The content of this chapter, apart from part of section 1.6, has been published in Physical Review B [3]. Here, it has been partly reformulated and restructured, to best fit the thesis.

distributed on the B sites opposed to an insulating low-temperature phase with a charge-ordered B sublattice [1], breaking the cubic symmetry in favour of a monoclinic one. Since the B ions form a frustrated pyrochlore lattice, the charge-order superstructure is rather involved, reflecting the competition between Coulomb interactions and the coupling to both the lattice and the orbital degrees of freedom [5,15]. Recently, it has been shown that the picture may need to be refined even further [6]. On top of the charge order, x-ray studies suggest that the single minority $\downarrow$ electron of an Fe_B^{2+} ion is delocalized over the neighbouring Fe_B^{3+} sites, forming linear units of three Fe sites dubbed trimerons [6]. Such units are organized in a network where different trimerons are connected via angles of 60° or 120°. Since the Fe_B^{3+} sites are part of up to three different trimerons (sharing different t_{2g} orbitals [6]), the trimeron lattice tends to equalize the charges on the Fe_B sites and to increase the polarizability [18]. Furthermore, having the minority spin delocalized on different sites reduces the expected entropy associated to the Verwey transition to values closer to experimentally observed ones [6, 19]. In this interpretation, it has been proposed [6] that the Verwey transition should be seen as a transition between a frozen trimeron network and a fluctuating network with shorter correlation length.

Time-resolved X-ray diffraction experiments [2] investigated the destruction of the insulating phase after the excitation with ultrashort pulses at 1.55 eV. It has been found that the photo-induced structural change occurs in a two-step process: after the initial local destruction of charge order triggered by photoexcitation, phase separation occurs, yielding metallic and residual insulating regions.

Optical measurements are an efficient tool to study the changes of electronic and structural properties at the phase transition [20–23]. In magnetite, the equilibrium optical conductivity [24–26] shows a broad Drude peak in the metallic phase as well as its suppression at the metal-to-insulator transition. The optical properties at higher energies are dominated by two features peaking at about 0.6 eV and 2 eV. By comparison with LSDA+U results, [27] these features were attributed to excitations of the minority $\downarrow$ electrons from the Fe_B^{2+} t_{2g} levels to the Fe_B^{3+} t_{2g} and e_g levels, respectively (see figure 1.1b). However, alternative interpretations invoking the A sites were proposed for the feature at 2 eV. [26, 28] Thus far, the behavior of these peaks at the Verwey transition has only been addressed at a qualitative level.

In this chapter I discuss our detailed equilibrium and out-of-equilibrium measurements of the optical properties of magnetite, which cover broad spectral and temperature ranges. With the ellipsometric data we were able to quantify the variation of the equilibrium optical properties across the Ver-

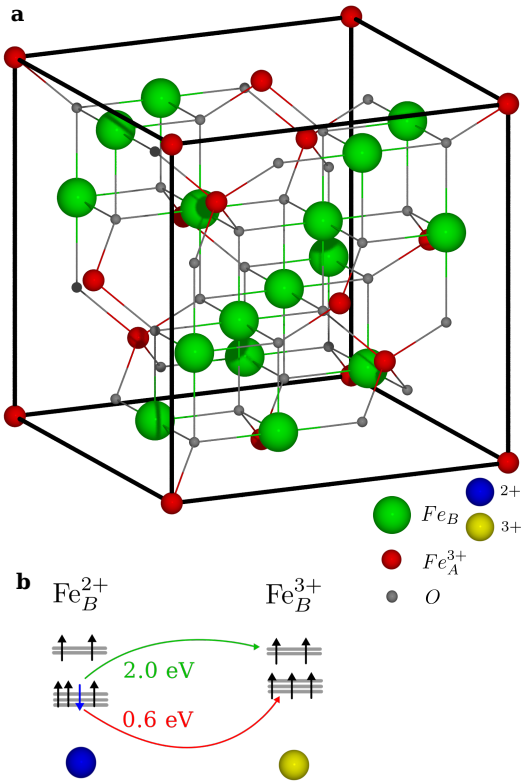

Figure 1.1: **a)** Inverse spinel high-temperature structure of magnetite. **b)** Sketch of the $Fe_B^{2+} \rightarrow Fe_B^{3+}$ transitions.

wey transition. The out-of-equilibrium measurements were performed under the same excitation conditions of the time-resolved X-ray diffraction in reference [2], to study the correspondence between the structural and optical data, and at different temperatures, to identify the analogies between the out-of-equilibrium and the equilibrium insulator-to-metal transitions. Our data confirm and extend the previous description of the dynamics of the phase transition. Moreover, we studied the consequences of out-of-equilibrium phase separation on the out-of-equilibrium reflectivity. From our observations, we propose a simple analysis to identify a mathematical property of the variation

of the reflectivity in pump-probe experiments that may be generally linked to out-of-equilibrium phase separation. Based on the modelling of the equilibrium data, we finally studied the dynamics of the spectral features of the photo-induced transient state.

1.2 Experiments

We performed pump-probe experiments on magnetite using pump pulses with a spectrum centred at 1.55 eV and a duration of 80 fs and broadband pulses with spectral components extending from 1.7 eV to 2.5 eV as probes. The laser repetition rate was 250 kHz. More details of the set-up have been described by Novelli *et al.* in reference [29]. No physical correction of the chirp of the broadband white light pulses was performed, but a post-processing correction of the chirp was applied to the data. Corrections to compensate the mismatch between the penetration depths at the pump photon energy and at the various probe photon energies (as described by Novelli et al. [30]) have been found not to be significant. The experiment was performed with the sample at 35 K, 80 K, and 140 K, i.e. at two temperatures below and one temperature above the Verwey transition. For the out-of-equilibrium measurements, two different samples were used, grown by the floating-zone technique in independent laboratories. [2, 31] One of the samples was the same as used by de Jong *et al.* [2] in the time-resolved X-ray diffraction experiment. For the measurements of the equilibrium properties, we used a sample oriented in the [100] direction and polished to obtain an optically smooth surface. In the energy range from 0.75 eV to 3.5 eV, ellipsometric data were acquired with a rotating-analyzer ellipsometer (Woollam VASE) equipped with a retarder between polarizer and sample. The angle of incidence was 70°. The sample was mounted in a liquid-He flow cryostat with optical windows under UHV conditions ($< 10^{-9}$ mbar). For the analysis of the ellipsometric data and the correction of the effects of the surface roughness, we assumed a cubic symmetry and considered a surface roughness of 4 nm. The analysis directly yields the dielectric function $\varepsilon(\omega) = \varepsilon_1(\omega) + i\varepsilon_2(\omega)$, or, equivalently, the optical conductivity $\sigma(\omega) \propto i[\varepsilon(\omega) - 1]$.

1.3 Results

1.3.1 Equilibrium optical properties

Figures 1.2a and b show the real part of the optical conductivity $\sigma(h\nu)$ and the real part of the dielectric function $\varepsilon_1(h\nu)$, for different temperatures. The solid parts of the lines represent the data measured via ellipsometry, while the dashed lines are their extrapolation based on the model of the ellipsometric data, which will discussed below.

In $\sigma(h\nu)$, the strong absorption related to $O_{2p} \rightarrow Fe_{3d}$ sets in at about 2.5 eV, while the absorption bands peaking at 0.6 and 2.0 eV have been attributed to excitations among the Fe_{3d} states [25–28]. Qualitatively speaking, the spectral weight (i.e. the integral of $\sigma_1(h\nu)$) of the band at 0.6 eV decreases with increasing temperature, in agreement with the results obtained via Kramers-Kronig transformation of reflectivity data [25, 26]. However, the literature [25,26] does not precisely address the behaviour at the Verwey transition, and there is no agreement about the temperature dependence for photon energies larger than 1.5 eV. Such spectral range is very important for the analysis of the out-of-equilibrium data presented in this chapter, which extend from 1.7 to 2.5 eV. Ellipsometry is a self-normalizing technique which directly yields the real and imaginary part of the dielectric function, without the need to perform any Kramers-Kronig transformation. It is, therefore, well suited to measure the details of the temperature dependence of the optical properties [32–34] across the Verwey transition.

The first observation can be made directly on the data. The inset of figure 1.2a shows the real part of the conductivity as a function of temperature for three selected photon energies. As can be seen, at the critical temperature the conductivity displays a discontinuity.

To perform more detailed considerations about the equilibrium optical properties of the sample, we fitted them with a model, consisting of "oscillators" representing the various transitions in the system (for a brief overview on the modelling of the optical properties of solids, see chapter I.2). We employed different lineshapes in the model. The features above 1.5 eV are best described by Gaussian oscillators, while we assumed a Tauc-Lorentz lineshape for the optical band at 0.6 eV, since the latter displays a gap-like feature when the system is an insulator. Moreover, in the metallic high-temperature phase, also a Drude oscillator $\sigma_1^{\mathrm{Drude}} = \sigma_{\mathrm{DC}}/(1+\omega^2\tau^2)$ is included in the model, to describe the free carriers and the DC conductivity of the system.

Since the Drude oscillator mainly contributes to the optical properties below the lower limit of our photon energy range, we constrained its parameters

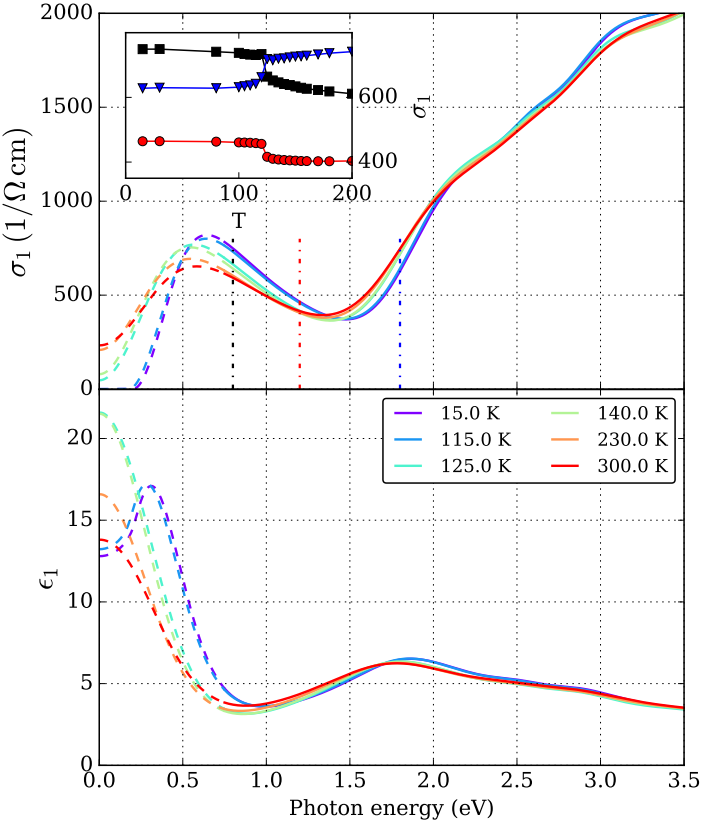

Figure 1.2: Real parts $\sigma_1(\omega)$ and $\varepsilon_1(\omega)$ of the optical conductivity (**a**) and of the dielectric function (**b**) as determined by ellipsometry (solid lines). The dashed lines show extrapolations based on fits of the ellipsometric data (see main text). The opening of a gap in σ_1 at low temperatures gives rise to the peak in ϵ_1 at about 0.3 eV. Inset: The temperature dependence of σ_1 at three photon energies (0.8, 1.2, and 1.8 eV, indicated in the main panel) highlights step-like changes at T_V.

using previous results. In particular, σ_{DC} was obtained by the measured DC conductivity, while τ was obtained from a temperature-independent scatterng rate $1/\tau$ adapted to describe the room-temperature data by Park and his collaborators in reference [26].

Such external constraints on the Drude peak allow for a reliable determination of the properties of the 0.6 eV band. The analysis of such feature has, in fact, to be performed with particular care, since our data only covers its high-energy side. Nevertheless, ellipsometry measures both the real and imaginary part of the dielectric function, and the data impose a strong constraint on the fit. The contribution of the 0.6 eV oscillator is significant and distinctive up to high energies. This can be seen in figure 1.3, where the fitted Tauc-Lorentz oscillator at 0.6 eV is plotted for two different temperatures. Once the assumption of a Tauc-Lorentz lineshape is done, such a fit gives reliable estimates of its properties. This is confirmed by the reasonable agreemen between the results of our fits and the low-energy results in the literature for ε_1 [24] and $\sigma_1(\omega)$ [25, 26]. In particular, both the photon energy of about 0.6 eV and the gap Δ in the insulating phase are matching. In fact, our fit yields $\Delta = 0.2$ eV at 15 K, while Park et al. [26] report 0.14 eV. While the quantitative results for the low-energy band have to be taken with some care, the fitted model provides a solid starting point for the analysis of the out-of-equilibrium data, which lie well within the range covered by the ellipsometric data, also given the fact that the fit fully reproduces the data.

Figure 1.4 shows the reflectivity at selected temperatures, calculated from the ellipsometric data. Also the reflectivity shows step-like changes at the critical temperature.

What happens to the oscillators identified in the model at the critical temperature? The discontinuous changes of the optical properties do not necessarily correspond to discontinuities in the spectral weight, as shown in figure 1.5. The spectral weight of the Drude feature decreases with decreasing temperature, until it vanishes at the Verwey transition. This change of the Drude spectral weight is approximately compensated by an increase of the weight of the 0.6 eV Tauc-Lorentz oscillator. In fact, figure 1.5 shows that the sum of the two spectral weights is almost constant as a function of the temperature. This is consistent with the results by Gasparov et al. [25], who reported that the spectral weight below 0.8 eV is approximately independent of the temperature. Such agreement further supports the reliability of our model.

Short-range order has been associated to the fact that the Drude and Tauc-Lorentz oscillators keep changing also above T_V [26]. Note that such an observation can be made independently of the model. In fact, $\sigma_1(T)$ also displays such fluctuations-related behaviour (see inset of figure 1.2a).

The variation as a function of temperature of the total spectral weight in the visible range (blue circles in figure 1.5) is qualitatively similar to the one of the Tauc-Lorentz 0.6 eV oscillator, but with opposite sign. The origin of this behaviour, together with the detailed assignment of the oscillators to

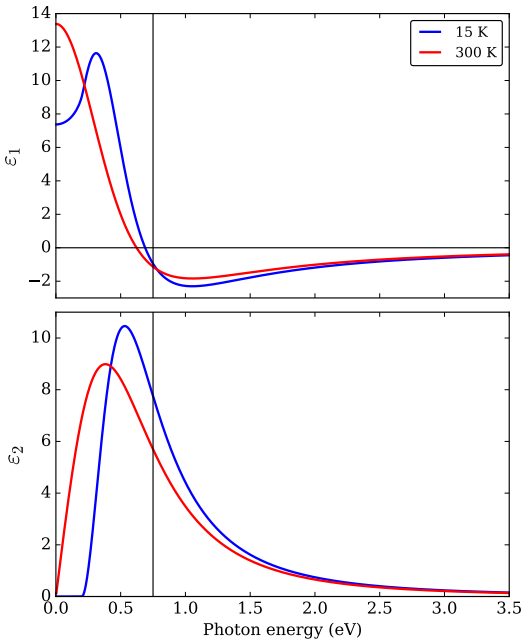

Figure 1.3: Real (**a**) and imaginary (**b**) parts of the dielectric function of the sole oscillator centred at 0.6 eV (Tauc-Lorentz lineshape). At 15 K the presence of a gap in ϵ_2 gives rise to the formation of a peak in ϵ_1 at about 0.3 eV. Vertical line: lower limit of the measured photon energy range in the equilibrium experiments.

transitions, will be discussed in section 1.4.3.

1.3.2 Out-of-equilibrium optical properties

Our out-of-equilibrium data can be split into two classes, depending on the sample temperature. The data measured with the temperature of the sample below the critical temperature T_V (35 and 80 K) show similar behaviours, which in the following I will argue to be the spectroscopic signature of the out-of-equilibrium analogue of the Verwey transition. With the sample above the transition temperature (140 K), the data do not display the distinctive features shown below T_V and linked to the photo-induced phase transition. Since the results at 35 K and 80 K are almost completely equivalent, for the

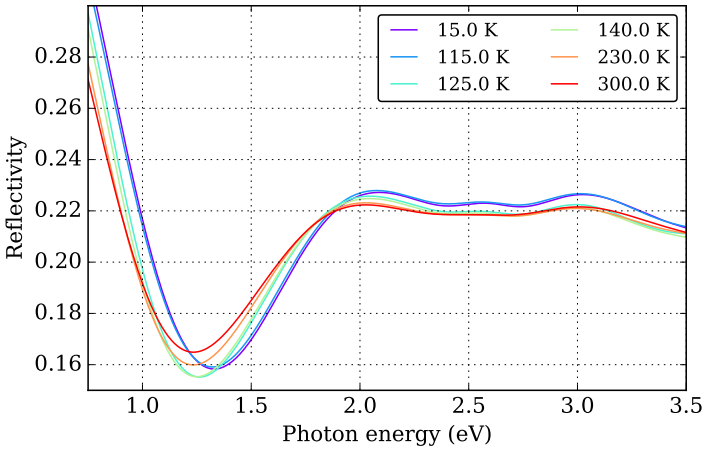

Figure 1.4: Equilibrium reflectivity derived from the ellipsometric results plotted in figure 1.2.

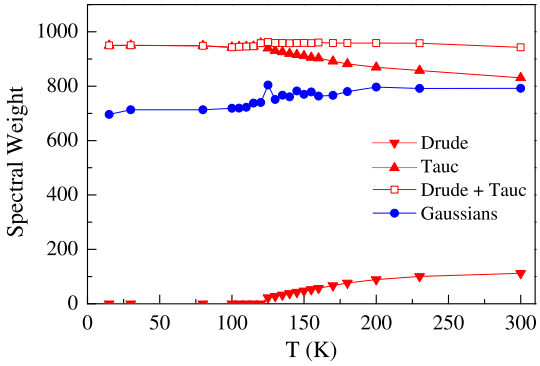

Figure 1.5: Temperature dependence of the spectral weights of different oscillators used in the model (see dashed lines in figure 1.2).

sake of clarity I will describe and discuss explicitly only the results at 35 K, underlining where the differences with the data at 80 K arise and how these differences support the picture drawn for 35 K. The results measured at 80 K are reported at the end of the chapter.

The results at 35 K allow us to identify three regimes of pump fluence

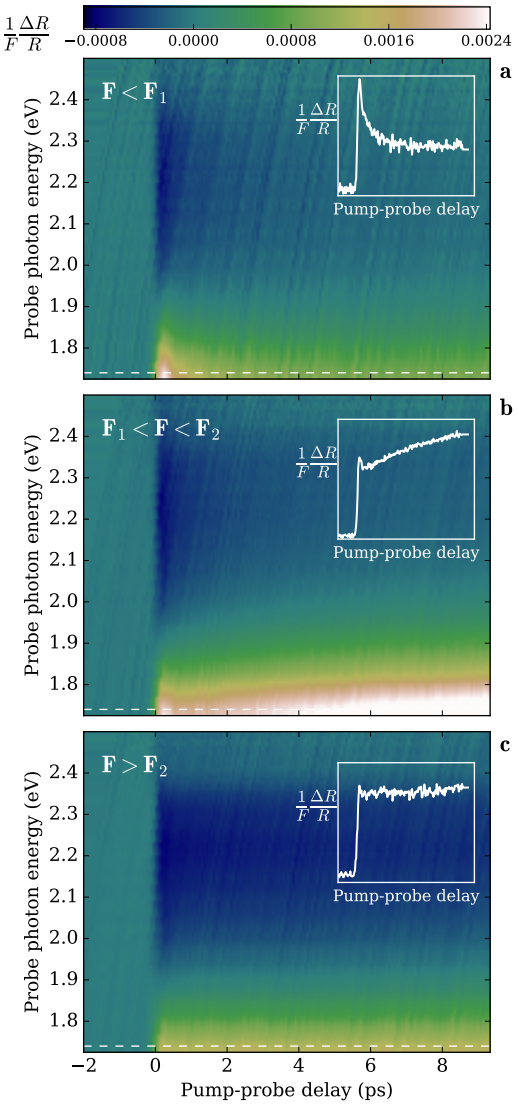

Figure 1.6: Normalized relative variation of the reflectivity $\frac{1}{F}\frac{\Delta \mathrm{R}}{\mathrm{R}}(h\nu, t)$ at 35 K for pump fluences F of (**a**) 0.5 mJ cm^{-2}, (**b**) 4.6 mJ cm^{-2}, and (**c**) 7.1 mJ cm^{-2}, characteristic of the three regimes of low, intermediate, and high fluence. Insets: $\frac{\Delta \mathrm{R}}{\mathrm{R}}(t)$ at 1.74 eV for the respective fluences. Dashed lines: photon energy corresponding to the insets.

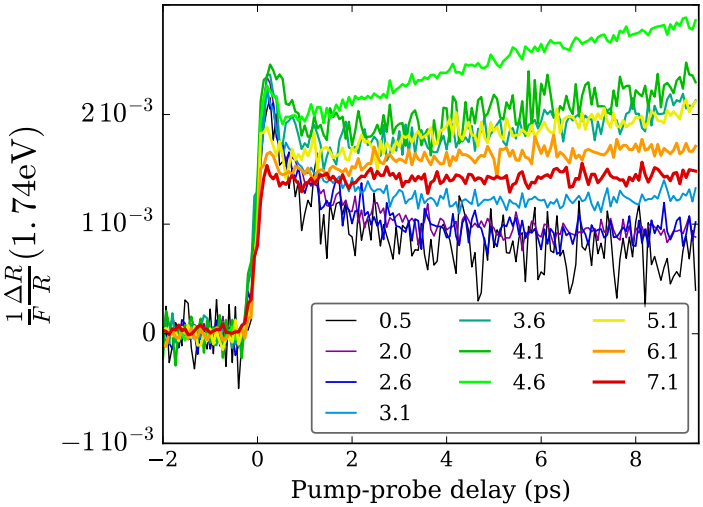

Figure 1.7: Normalized relative variation of the reflectivity $\frac{1}{F}\frac{\Delta \mathrm{R}}{\mathrm{R}}(h\nu = 1.74\,\mathrm{eV}, t)$ at 35 K for all the available pump fluences.

F in which the relative variation of the reflectivity ($\frac{\Delta \mathrm{R}}{\mathrm{R}}(t, h\nu)$) behaves in qualitatively different ways. The only difference of the results at 80 K are the pump fluences delimiting these intervals, which are shifted to lower values for higher temperature. Figure 1.6 shows three data sets for selected fluences, each of them representative of one of the three regimes. In figure 1.7 instead, $\frac{1}{F}\frac{\Delta \mathrm{R}}{\mathrm{R}}(t)$ is plotted for all the fluences F at $h\nu$=1.74 eV, a representative probe photon energy.

Below a pump fluence of $F_1 = 2.7$ mJ cm^{-2}, the relative variation of the reflectivity $\frac{\Delta \mathrm{R}}{\mathrm{R}}(t, h\nu)$ behaves as shown in figure 1.6a. In this regime, which in the following will be called *low fluence* regime, the response has two distinctive features. First of all, after a very fast increase at pump-probe delay $t = 0$ at probing energies around 1.8 eV, $\frac{\Delta \mathrm{R}}{\mathrm{R}}$ decays exponentially with a characteristic time scale of 0.9 ps to a non-zero thermal plateau (see inset of figure 1.6a and figure 1.7). The second feature is that $\frac{\Delta \mathrm{R}}{\mathrm{R}}$ scales linearly with the fluence, as can be seen in figure 1.7. This behavior is typical of the creation of excitations, whose density scales linearly with the pump fluence. The excitations then decay, bringing the system to a thermalized state with a temperature different from the initial one. The lifetime of this transient state is determined by the thermal conductivity of the system.

In the *intermediate fluence* regime, with $F_1 < F < F_2 = 5.1$ mJ cm^{-2}, a behavior like the one plotted in figure 1.6b becomes visible. Again, we can identify two characteristic features. First, the excitation is followed by two distinct dynamics. After quickly decaying for a very short time (<1 ps), the response grows again on a slower time scale τ_2 (see inset of figure 1.6b). This happens more pronouncedly on the low-energy side of the probed range. Second, while the amplitude of the initial peak ($t \simeq 0.2$ ps) still scales linearly with the fluence (as in the low fluence regime), the amplitude of the long-time dynamics does not and its characteristic timescale is not constant with the fluence (see figure 1.7). In particular, the latter becomes faster as the fluence increases. From these considerations, we can say that the creation of a sufficient number of excitations in the system triggers a new dynamical response, which evolves on a timescale which is larger than the one of the decay of the primary excitations.

In the *high fluence* regime, for $F > F_2$, $\frac{\Delta R}{R}$ progressively loses the mentioned features, as shown in figure 1.7, up to the point that, for the highest fluence used (7.1 mJ cm^{-2}), it behaves as a switch on the low-energy side of the spectrum, as shown in figure 1.6c and 1.7. In this regime, $\frac{\Delta R}{R}$ is almost independent of the fluence. Moreover, apart from a small relaxation on the high-energy side of the spectrum, $\frac{\Delta R}{R}$ displays a step-like behavior at $t = 0$ and does not evolve anymore for times at least longer than 10 ps.

1.4 Discussion

By means of time-resolved X-ray diffraction, de Jong et al. [2] have shown that holes in the charge-ordered lattice, purportedly the trimeronic lattice [6], are produced upon excitation by the pump pulse. If the pump fluence is lower than F_1, the lattice thermalizes to a higher temperature, but retains the global symmetry of the low-temperature charge-ordered phase (*low fluence* regime). If the fluence exceeds F_1, the nucleation of volumes with the symmetry of the high-temperature phase is triggered. This leads to phase separation, i.e., coexistence of uncorrelated charge-ordered regions and metallic ones (*intermediate fluence* regime). Our time-resolved spectroscopic data confirm this scenario. Moreover, we also explored higher fluences ($F > F_2$), where the dynamics is different.

The discussion will proceed as follows. First, I will discuss the intermediate fluence regime and I will show that the spectral feature of the long-time response corresponds to the nucleation of the high-temperature phase. I will afterwards discuss what we have identified as a possibly general consequence of

phase separation on a mathematical property (the separability) of the out-of-equilibrium reflectivity of a system. In the high fluence regime, we have then shown that the system is, instead, immediately (i.e., on a timescale smaller than our experimental resolution) and homogeneously brought to the high-temperature phase and the nucleation process can no longer be observed in the out-of-equilibrium optical properties. Residual localized charge order is still present in the system, but the insulating region is progressively reduced as the fluence increases. This scenario emerges from the comparison of the out-of-equilibrium with the equilibrium measurements and from the study of the separability of the variation of the reflectivity as a function of time and probe photon energy.

The results obtained at 140 K confirm that our observations can be ascribed to a photo-induced phase transition. Above the Verwey transition temperature and for the measured fluences, the response is linear and there is no evidence for a photo-induced phase transition. In the following, we will use this substantial difference to benchmark part of the proposed analysis.

1.4.1 Out-of-equilibrium phase transition and supply of latent heat

Having outlined the conclusions that can be drawn from the data, the first question that should be answered is why phase separation should be expected at all in this experiment. To do this I will first extract parameters from the data which will allow us to identify the fluences F_1 and F_2 at which the response qualitatively changes. Then I will describe how F_1 and F_2 are related to final effective temperatures of the sample and compare them with temperatures relevant at equilibrium.

Up to a certain fluence the amplitude of the initial peak in $\frac{\Delta R}{R}$ scales linearly with the fluence. To see this, we can take, as a parameter, $\frac{\Delta R}{R}$ at a probe photon energy of 1.74 eV and a pump-probe delay of 0.2 ps. This quantity is shown in figure 1.8 (blue squares). The fluence below which it scales linearly with the fluence is F_2=5.1 mJ cm^{-2}. Above F_2, where the switching-like behaviour is present, it saturates. The magnitude of $\frac{\Delta R}{R}$(0.2 ps) becomes less dependent on the fluence.

The linear behaviour ceases before for larger pump-probe delays. Plotting $\frac{\Delta R}{R}$(1.74 eV) at 8 ps (green triangles in figure 1.8), it can be seen that $\frac{\Delta R}{R}$ at large times is linear up to F_1=2.7 mJ cm^{-2}. Between F_1 and F_2, the long-time response is nonlinear and $\frac{\Delta R}{R}$(8 ps) steeply departs from the low-fluence behaviour. Above F_2, also in this case the variation of the reflectivity

saturates.

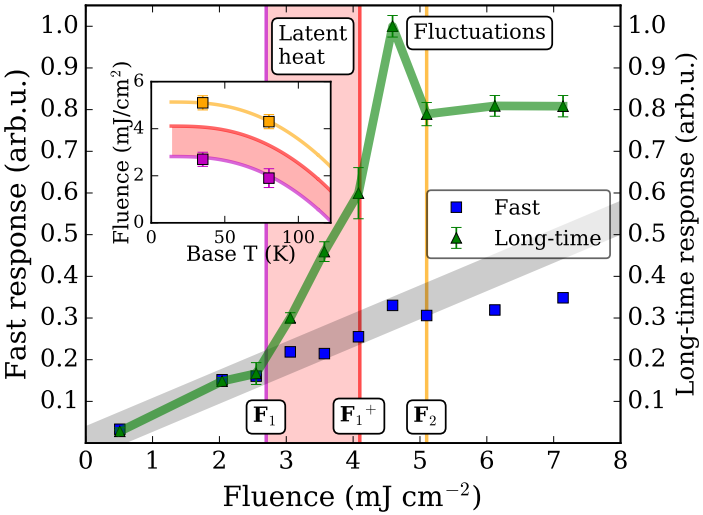

Figure 1.8: "Fast response" (blue squares): $\frac{\Delta R}{R}$ at 1.74 eV photon energy and 0.2 ps pump-probe delay. "Long-time response" (green triangles): $\frac{\Delta R}{R}$ at 1.74 eV photon energy and 8 ps pump-probe delay. Inset: The squares are the characteristic fluences extracted from the out-of-equilibrium data as a function of the sample's temperature, corresponding to: onset of the nonlinear response (magenta) and saturation of the nonlinear response (orange). The lines represent equivalent fluences calculated from thermodynamic data needed to reach T_V^- (magenta), T_V^+ (red), and 140 K (orange). The red shaded area corresponds to fluences bringing the sample to T_V^- and supplying part of the latent heat. The vertical lines and the vertical shaded area in the main figure mimic the inset.

If we assume that after the excitation the sample quickly reaches an effectively thermal state, we can estimate its final effective temperature considering the volume energy density deposited by each pump pulse. We can approximate the situation to the one in which the sample is excited uniformly. The volume of the sample is taken to be the area illuminated by the pump beam times the penetration depth α of light at the pump photon energy.

From the equilibrium thermodynamic properties we can calculate the energy Q needed to bring such a volume of magnetite from its initial temperature

T_i to a temperature T, which reads

$$Q(T) = n_{\mathrm{mol}} \int_{T_i}^{T} d\tilde{T}\; c_{\mathrm{mol}}(\tilde{T}), \tag{1.1}$$

where c_{mol} is the molar specific heat and n_{mol} is the number of moles contained in the volume of the sample. For this calculation we used the specific heat measured by Takai et al. in reference [35], reported in figure 1.9. Since the surface of the sample reflects part of the pump pulse and only a fraction (1-R) of the total energy will cross the surface, the total energy carried by the pump pulse must be larger than $Q(T)$ in order for the sample to reach T. Moreover, out of the energy entering into the sample, only a fraction $\frac{1}{\alpha}(1-e^{-1})$ is deposited within the penetration depth α. Therefore, the fluence $F_{T_i}(T)$ needed to heat the sample from T_i to T is given by

$$F_{T_i}(T) = q(T)\frac{\alpha}{1-e^{-1}}\frac{1}{1-R}, \tag{1.2}$$

where $q(T)$ is the surface density of $Q(T)$. Inverting this equation one can obtain the effective final temperature as a function of the fluence.

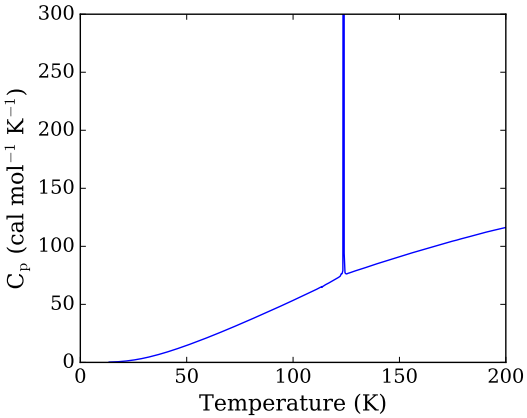

Figure 1.9: Molar specific heat of magnetite, adapted from reference [35].

The reason why in the interemediate fluence regime ($F_1 < F < F_2$) phase separation should be expected is the following. With the sample at 35 K, a pump pulse with fluence F_1 raises the temperature of the sample to T_V^-, i.e.

right to the transition temperature without supplying any portion of the latent heat. The intermediate fluence regime starts with the supply of at least part of the latent heat. As concluded via time-resolved X-ray diffraction [2], fluences above F_1 trigger the dynamic nucleation of the metallic phase and, therefore, the phase transition. The full latent heat is supplied by a fluence F_1^+ =4.1 mJ cm^{-2}, while the qualitative change of behaviour of $\frac{\Delta R}{R}$ is evident only above F_2 = 5.1 mJ cm^{-2}, which brings the sample to a temperature of 140 K. A more detailed anaysis allows to discover that the qualitative change in behaviour starts at F_1^+ and is complete at F_2, as discussed in the next section.

Between $T(F_1^+) = T_V^+$ and $T(F_2) = 140$ K the fluctuations towards charge ordering are clearly visible in the equilibrium optical properties (see the inset of the figure 1.2). While time-resolved X-ray diffraction data are not available for fluences larger than F_2, we argue that above F_2 the variation of the electronic properties progressively becomes a sudden process, and that the nucleation of the metallic phase is not present anymore. In fact, above F_2, $\frac{\Delta R}{R}$ progressively loses all the features of the response at the lower fluences, as it will be shown in more detail in the next sections.

The inset of figure 1.8 shows the values of $F(T_V^-)$, $F(T_V^+)$ and $F(140\text{ K})$ as a function of the initial temperature of the sample. The squares are the values of F_1 and F_2 for the sample at 35 K and 80 K. As shown, the characteristic fluence F_1 and F_2 correctly scale with the temperature and at 80 K are lower than the ones at 35 K. In fact, with a starting temperature of 80 K, less heat is needed to bring the sample to the critical temperature T_V.

1.4.2 Nucleation of the metallic phase, out-of-equilibrium phase separation, and non-separability of the response

In this section an analysis is presented, suggesting that the response of magnetite is homogeneous over the illuminated sample for base temperatures below T_V in the low and high fluence regimes, while the dynamics triggered in the intermediate regime involves phase separation.

The discussion will proceed as follows. At first, I will discuss the fact that in the intermediate fluence regime $\frac{\Delta R}{R}(h\nu, t)$ is non-separable, i.e. it can, and must, be written as the sum of two different spectral features evolving in time in two different ways. Subsequently, the two observed spectro-temporal features will be linked to: i) the production and relaxation of excitations in the charge-ordered phase, and ii) the nucleation of the high-temperature phase.

As a visual reference for what follows, $\frac{1}{F}\frac{\Delta R}{R}$ at 1.74 eV is plotted in fig-

ure 1.10a for representative fluences of the three regimes.

Since the fast response scales linarly up to F_2, but the long-time response does just up to F_1, we can ask ourselves what differentiates the two dynamics between F_1 and F_2. We can extract the nonlinear contribution from the intermediate-fluence $\frac{\Delta R}{R}$, which we can call $\frac{\Delta R}{R}'$, by calculating

$$\frac{1}{F}\frac{\Delta R}{R}' = \frac{1}{F}\frac{\Delta R}{R} - \frac{1}{F_0}\frac{\Delta R}{R}\bigg|_0, \tag{1.3}$$

where F_0 is the lowest fluence used in our experiment and which we take to produce a purely linear response. In the low fluence regime the above subtraction is trivially zero.

As a sample result of the subtraction (1.3) in the intermediate fluence regime, figures 1.10b and c show $\frac{\Delta R}{R}'$ for $F = 4.6$ mJ cm^{-2}. Three properties of $\frac{\Delta R}{R}'$ can be underlined. The first one is that at 0.2 ps (i.e. the temporal position of the fast peak in the total response) $\frac{\Delta R}{R}'$ is zero at all probe photon energies. This confirms that the fast peak is linear at all photon energies throughout the intermediate regime. The nonlinear contribution to $\frac{\Delta R}{R}$ is therefore a purely slow dynamics. The second property of $\frac{\Delta R}{R}'$ is that the timescale τ_2 with which it grows matches the one obtained from the time-resolved diffraction experiment for the nucleation of the metallic phase [2] in the same excitation conditions. These two aspects show that the decomposition in equation (1.3) is physically meaningful. This itself is the third important property of $\frac{\Delta R}{R}'$. In fact, it is remarkable from the spectroscopic point of view that the total reflectivity can be written as the *sum* of two physically meaningful terms. The additivity of the response is consistent with the scenario in which the total reflectivity of the sample is the sum of the reflectivities of different regions in different phases, which are sufficiently defined to have their own optical properties. In the case of out-of-equilibrium magnetite, these different regions are patches in the insulating and in the metallic phases.

Also the fluence dependence of τ_2, reported in table 1.1 supports this picture. With increasing fluence the density of local excitations in the charge-ordered lattice increases, and the nucleation time τ_2 becomes shorter, eventually leading to a percolative path in the high-temperature phase.

The analysis described above seems sufficiently justified in the intermediate fluence regime, because the linearity of the fast peak clearly indicates a common feature of the low and intermediate fluence regimes. Moreover, the result of the decomposition in equation (1.3) is consistent with the time-resolved X-ray diffraction data [2] and with the fact that latent heat is being

Fluence (mJ cm^{-2})	τ_2 (ps)
3.1	5.6
3.6	5.3
4.1	3.8
4.6	3.6

Table 1.1: τ_2 at 35 K for different pump-fluences in the intermediate regime.

supplied when $F_1 < F < F_1^+$. In the high fluence regime the latent heat is fully delivered and the X-ray data are missing. How can we know whether the decomposition (1.3) is applicable also for $F > F_2$? Furthermore, how can we check that in the intermediate fluence regime such decomposition is sound and that it does not originate from a biased physical picture of the underlying dynamics? One could, in fact, argue that any function ($\frac{\Delta R}{R}$) can be written as the sum of two other functions (linear and nonlinear contributions, in this specific case).

To answer these questions, we have to use singular value decomposition, a so-called blind decomposition. Such algorithm allows to decompose $\frac{\Delta R}{R}(h\nu, t)$, which for the present case can be written as a matrix $[\frac{\Delta R}{R}]_{h\nu,t}$ where the row and column indices are the probe photon energy and the pump-probe delay, respectively. Differently from equation (1.3), this analysis does not involve physical assumptions, nor the usage of other data sets (as is the case for the linear response at F_0 in equation (1.3)). Singular value decomposition allows to write $\frac{\Delta R}{R}$ as a sum of spectro-temporal components

$$\frac{\Delta R}{R}(h\nu, t) = \sum_i s_i \ \text{spectrum}_i(h\nu) \otimes \text{evolution}_i(t), \tag{1.4}$$

where the spectra and the evolutions are the so-called left and right singular vectors and s_i are the singular values. Singular value decomposition is obtained from the general problem of the factorization of a matrix imposing that the sets of left and right singular vectors be orthonormal bases. This may lead to singular vectors which are not suitable for a physical interpretation.

Despite this limitation, there is one result of the decomposition which is independent of the constraints. If there is more than one relevant [2] singular value, then the matrix is not separable, i.e. it cannot be factorized as a single product of a spectral feature with one single temporal evolution for all the photon energies.

[2] with respect to the noise level

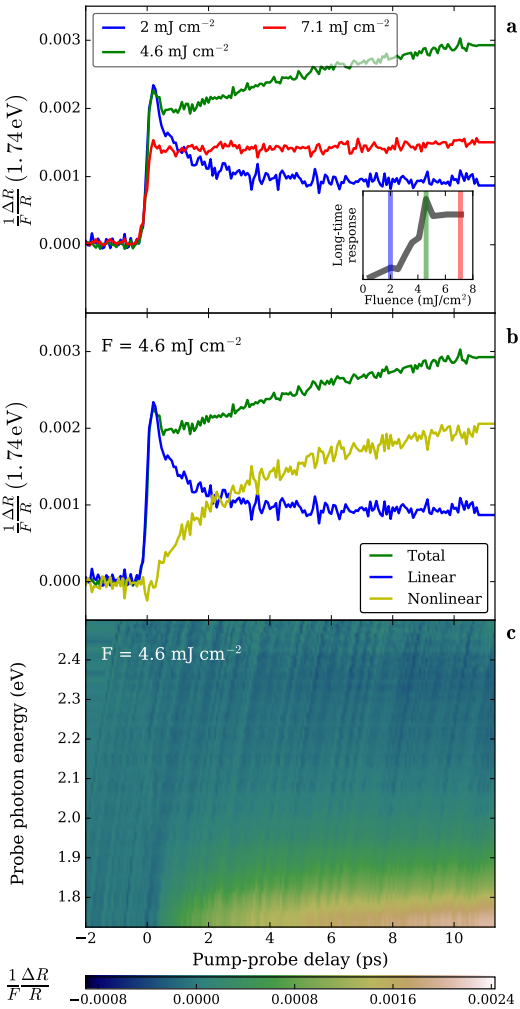

Figure 1.10: **a)** $\frac{1}{F}\frac{\Delta \mathrm{R}}{\mathrm{R}}(t)$ at 1.74 eV for 2.0 mJ cm^{-2} (blue), 4.6 mJ cm^{-2} (green), 7.1 mJ cm^{-2} (red) pump fluences. Inset: visual reference to figure 1.8. **b)** Green: as in (a). Blue (yellow): linear (nonlinear) term of $\frac{1}{F}\frac{\Delta \mathrm{R}}{\mathrm{R}}$ for F = 4.6 mJ cm^{-2} at 1.74 eV photon energy. **c)** $\frac{1}{F}\frac{\Delta \mathrm{R}}{\mathrm{R}}'(h\nu, t)$ for F = 4.6 mJ cm^{-2}.

In the measured $\frac{\Delta R}{R}(h\nu, t)$ at all fluences, the relevant singular values are at most two. Figures 1.11a and b show the singular values (ordered by magnitude) of $\frac{\Delta R}{R}(h\nu, t)$ for a fluence in the low regime and a fluence in the intermediate regime. As can be seen, the majority of the singular values forms a continuous distribution and corresponds to noise. An indicator of whether more than one component is needed to describe $\frac{\Delta R}{R}$ is the ratio of the second largest singular value to the largest one [3]. A large ratio means that two spectro-temporal components are needed to describe the data and that $\frac{\Delta R}{R}$ is not separable (i.e. not factorizable) in $(h\nu, t)$ space. We can call such ratio "non-separability" in $(h\nu, t)$ space.

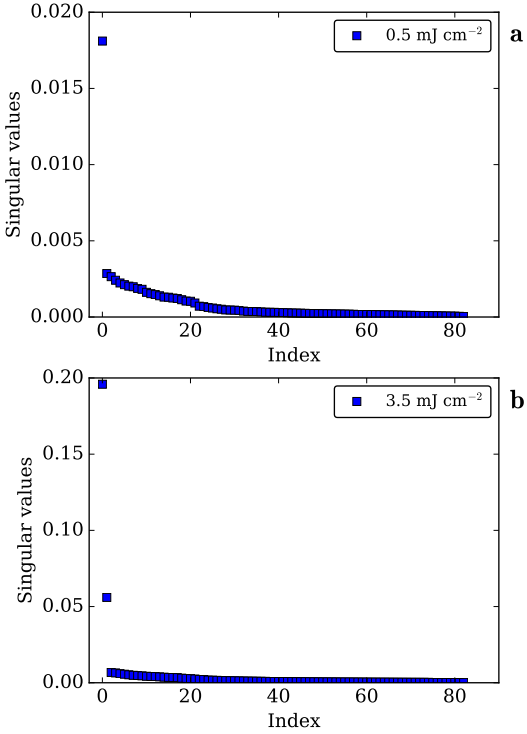

Figure 1.11: Ordered singular values obtained from the singular value decomposition of $[\frac{\Delta R}{R}]_{h\nu,t}$ at 0.5 mJ cm^{-2} (**a**) and 3.5 mJ cm^{-2} (**b**).

[3] From both, the noise level needs to be subtracted.

Figure 1.12 shows the "non-separability" of $\frac{\Delta R}{R}$ as a function of the fluence. At the lowest pump fluence the non-separability is zero, meaning that $\frac{\Delta R}{R}$ contains a single spectro-temporal component. As the flunce is increased up to F_1^+, the non-separability of $\frac{\Delta R}{R}$ increases. While only a portion of the latent heat is supplied, the relevance of the second spectro-temporal component increases, because the holes in the charge-ordered lattice have to nucleate to form islands in the high-temperature phase.

Beyond F_1^+, the non-separability decreases instead, and above F_2, $\frac{\Delta R}{R}$ approximately becomes separable again. Once the latent heat is fully delivered, the transition homogeneously occurs over the whole sample, as confirmed by the fact that $\frac{\Delta R}{R}$ can be expressed almost as a single spectro-temporal feature.

To benchmark this kind of analysis on the out-of-equilibrium reflectivity, we performed it on the data measured at 140 K. Since this temperature is larger than T_V, we expect no phase separation after the excitation, and the sample to be homogeneous. Singular value decomposition shows that $\frac{\Delta R}{R}$ at 140 K is exactly separable (i.e. factorizable in $(h\nu, t)$ space) at all fluences. This result supports the picture outlined so far.

There is a minor problem that should be addressed, i.e. the specific shape of the onset of the non-separability. In figure 1.12 there is no sharp increase of the non-separability at the threshold F_1, as one would expect from the picture of the triggering of the phase transition. The explanation for this is the following. The constraint of orthogonality for the singular vectors produce effects also on the singular values. In fact, if a small perturbation of the form

$$B = b\, f(h\nu) \otimes g(t) \tag{1.5}$$

is added to a separable matrix M

$$M = s\, u(h\nu) \otimes v(t), \tag{1.6}$$

then the singular values of the matrix

$$M + B = s'_1 u'_1(h\nu) \otimes v'_1(t) + s'_2 u'_2(h\nu) \otimes v'_2(t) \tag{1.7}$$

will not be exactly s and b, but will depend also on the scalar product of $f(h\nu)$ and $g(t)$ with the singular vectors of M+B. For this reason, the quantitative relation between the singular values and the weights of the physical components (in the present case, linear and nonlinear) must be considered with some care, and the shape of the non-separability at the threshold fluence does not resemble the edge of the physical components (figure 1.8). On the other hand, the minimal interpretation of the result, i.e. the existence of one or more

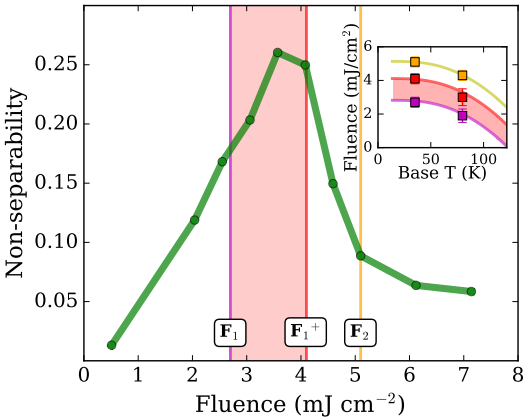

Figure 1.12: Ratio of the second largest and largest singular values (from both, the noise level was subtracted), as a function of fluence. Inset: same inset as in figure 1.8, with the addition of the fluences at which the "non-separability" starts to decrease (red squares), as measured at 35 and 80 K. These match the calculated equivalent fluences needed to deliver the full latent heat to the sample (red line).

than one non-zero singular values, is not affected by the above quantitative considerations.

The convergence of all these indications allow us to conjecture that the non-separability of $\frac{\Delta R}{R}(t, h\nu)$ may be a necessary condition for the identification of phase separation in out-of-equilibrium systems, as will be discussed further in section 1.6.

It should be noted that, alternatively, phase separation may be occurring between different depths in the sample. Since the pump intensity decreases exponentially with depth from the surface, the probe may be measuring an external and internal "layer" of the sample, respectively above and below threshold. However, the time-dependent coherence length of the low-temperature phase measured via X-ray diffraction [2] indicates the presence of islands in one phase embedded in a matrix in the other phase.

1.4.3 Equilibrium optical properties across the phase transition

In this section, the assignment of the oscillators included in our model to transitions between different states in magnetite is discussed, considering the LSDA+U calculations by Leonov et al. [27]. The $O_{2p} \rightarrow Fe_{3d}$ charge-transfer excitations have, in general, a large dipole moment and, therefore, a spectral weight which is much larger than for transitions between different 3d states of iron. The strong charge-transfer transitions are found above 2.5 eV [26, 27]. The spectral features below 2.5 eV (at 0.6 and 2 eV) can therefore be attributed to transitions between Fe_{3d} states. Magnetite presents two inequivalent classes of Fe sites (A and B) and Fe sites with valencies 2+ and 3+. This produces many possible transitions. Nevertheless, it is possible to exclude some of them with the following simple argument. The $3d^5$ configuration with $S = 5/2$, i.e. with all the spins parallel, is very stable, and the transitions of the type $3d_i^5 3d_j^5 \rightarrow 3d_i^4 3d_j^6$ are typically observed at energies above 3 eV [36,37]. Therefore, the 0.6 eV and 2.0 eV features are reasonably due to $3d_i^6 3d_j^5 \rightarrow 3d_i^5 3d_j^6$ transitions.

The results by Leonov et al. [27] indicate that the occupied state with the energy closest to the Fermi level is the one of minority spins $\downarrow$ in the t_{2g} level of the Fe_B^{2+} sites. The lowest unoccupied state has been identified as the $t_{2g} \downarrow$ on the Fe_B^{3+} sites. The optical band at 0.6 eV can be assigned to the intersite $Fe_B^{2+}\, t_{2g} \downarrow \rightarrow Fe_B^{3+}\, t_{2g} \downarrow$ transition [27]. Its spectral weight increases as the charge disproportionation between Fe_B^{2+} and Fe_B^{3+} sites increases, i.e. upon decreasing the temperature and going towards the charge-ordered phase.

In Fe_3O_4, neighbouring Fe_B sites are connected via 90° Fe-O-Fe bonds. This allows, in addition to the $t_{2g} \rightarrow t_{2g}$ intersite hopping, also the $t_{2g} \rightarrow e_g$ hopping (see, e.g., reference [5]). The LSDA+U results position such $Fe_B^{2+}\, t_{2g} \downarrow \rightarrow Fe_B^{3+}\, e_g \downarrow$ transition at about 2 eV. [4] The temperature dependence of the spectral weight of the $t_{2g} \rightarrow e_g$ excitation is more subtle than for the $t_{2g} \rightarrow t_{2g}$ one. In fact, since in both cases the transition involves a minority spin $\downarrow$ hopping from Fe_B^{2+} to Fe_B^{3+} sites, one would expect that the spectral weights shoud change in the same way. This does not agree with what we observe experimentally. The measured variation with temperature of the two spectral weights is opposite. This is, however, consistent with the considerations made by Leonov et al. [27]. In fact, they find that charge order is strongly screened by a change of covalency. This means that, below T_V, the Fe_B^{3+} sites show an

[4] Note that the assignments of the 0.6 and 2.0 eV oscillators confirm that a pump photon energy of 1.5 eV is suited to produce excitations that induce the phase transition, since they tend to destroy the charge order.

enhanced occupation of the $e_g \downarrow$ level, as a consequence of the hybridization with O_{2p} states. Therefore, the spectral weight for excitations to e_g states is *reduced* entering the charge-ordered phase.

Other possible transitions between Fe_{3d} states can be excluded. The Pauli principle prohibits a hopping of the minority electrons on a Fe_B^{2+} to Fe_A sites, since the minority spin states on the A sublattice are fully occupied. Alternatively, it hase been proposed [26, 28] that the band at 2.0 eV corresponds to the excitation of majority $\uparrow$ spin electrons from a Fe_B^{2+} site to an e_g state on an Fe_A site. The LSDA+U calculations show however that this excitation is expected at a slightly larger energy than the one descibed above [27].

1.4.4 Spectral response of the phase transition

Based on the previous section, I present the last evidence that supports the intepretations proposed so far. The spectral analysis of the features appearing in $\frac{\Delta R}{R}$ allows to show that they are indeed associated to the charge-ordered (linear component) and charge-disordered phase (nonlinear component). To do this, we fitted $\frac{\Delta R}{R}$ by varying parameters of the oscillator model of the equilibrium optical properties. From such fits two kinds of information can be obtained. The first is the minimal set of free parameters (or oscillators) needed to account for the observed $\frac{\Delta R}{R}$. The second is the temporal evolution of the free parameters. Out of the numerical results that can be obtained, the evolutions of the spectral weights of the oscillators are the most robust, and our discussion is limited to them.

In the low fluence regime, the variation of the reflectivity, which is linear with F, can be described by variations of the 0.6 and 2.0 eV oscillators. i.e. of the $Fe_B^{2+}t_{2g} \rightarrow Fe_B^{3+}t_{2g}$ and the $Fe_B^{2+}t_{2g} \rightarrow Fe_B^{3+}e_g$ transitions. The fit is shown in figure 1.13a for pump-probe delay t=0.2 ps (blue line). Modifications of the charge-transfer excitation between O_{2p} and Fe_{3d} are, instead, not needed to describe the observed dynamics. Figure 1.13b shows the temporal evolution of the spectral weights of the two oscillators involved. As excitations are created in the system at t = 0, the spectral weight of the $Fe_B^{2+}t_{2g} \rightarrow Fe_B^{3+}t_{2g}$ (0.6 eV) transition decreases, while the one of the $Fe_B^{2+}t_{2g} \rightarrow Fe_B^{3+}e_g$ transition (2 eV) increases, then relaxing to a thermal plateau. The opposite signs of these variations are consistent with the opposite temperature behavior of the two features observed in the equilibrium data, see figure 1.5. On one side the partial destruction of the charge order reduces the spectral weight of the 0.6 eV oscillator, while on the other the de-hybridization of the $Fe_B^{3+}e_g$ and O_{2p} states increases the weight of the 2 eV oscillator.

These fits have been performed imposing the conservation of the total spec-

tral weight. This constraint makes the result of the fitting procedure more stable. It is also an appropriate constraint, since, without it, the spectral weight is approximately conserved and the result of the fit are, both qualitatively and quantitatively, very similar to the constrained results. While the constraint helps to reduce the noise, it enhances the correlation between the two spectral weights in figure 1.13b. As can be seen, the noise of the two curves is evidently correlated, as a consequence of close-by minima in the space of the parameters. Nevertheless, the amplitudes and the signs of the variation of the spectral weights are independent of the details of the fitting procedures.

In the intermediate fluence regime, the nonlinear term $\frac{\Delta R}{R}'$ is linked to the nucleation of the metallic phase. As shown in figure 1.13a (cyan line), the nonlinear $\frac{\Delta R}{R}'$ can be accounted for by the sole change of the $Fe_B^{2+}t_{2g} \rightarrow Fe_B^{3+}t_{2g}$ transition at 0.6 eV. Figure 1.13c shows that its spectral weight decreases with the characteristic timescale of the slow dynamics, consistently with the picture in which the charge-disordered phase is nucleating. [5]

These results suggest that the hybridization of $Fe_B^{3+}e_g$ and O_{2p} states is not involved in the nucleation process, but is exclusively linked to the increase of the temperature of the system.

1.5 Conclusions

We reported measurements of both equilibrium and out-of-equilibrium optical properties of magnetite on a broad spectral range and at different temperatures across the Verwey insulator-to-metal phase transition. The equilibrium optical properties show a step-like behavior at the transition between the charge-ordered and charge-disordered phases. Our measurements allowed us also to determine the behavior of the spectroscopic features as a function of temperature. The most important ones in this discussion are the intersite transitions of minority spins $\downarrow$ from the $Fe_B^{2+}t_{2g}$ levels to the t_{2g} and e_g levels of Fe_B^{3+} atoms. As expected, the spectral weight of the $Fe_B^{2+}t_{2g} \rightarrow Fe_B^{3+}t_{2g}$ oscillator grows upon cooling, i.e. upon increasing the charge disproportionation. The temperature dependence of the spectral weight of the $Fe_B^{2+}t_{2g} \rightarrow Fe_B^{3+}e_g$

[5] Since the out-of-equilibrium data only conver the spectral range from 1.7 to 2.5 eV, we cannot access all the details of the low-energy response and we cannot ascertain, for instance, an actual onset of metallicity associated to a Drude feature. However, it can be excluded that the introduction of the Drude feature alone can describe the data, because such a fit poduces results which are incompatible with the measurements. Introducing a Drude feature in addition to the changes of the 0.6 eV oscillator does allow to fit the data, but changes the results in a mild way. Despite these shortcomings in our analysis, the nonlinear response can remarkably be fitted with changes of the 0.6 eV oscillator only.

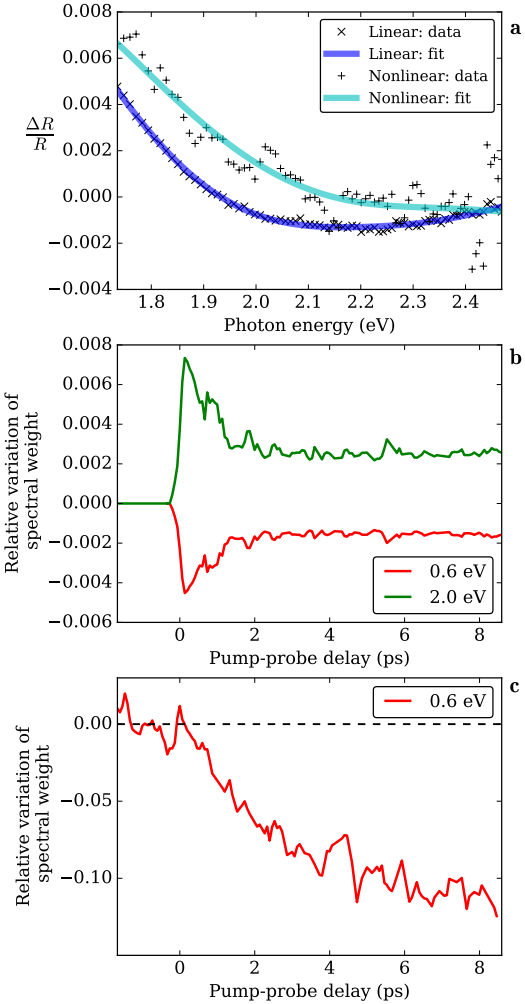

Figure 1.13: **a)** Linear and nonlinear terms in $\frac{\Delta R}{R}$ at 0.2 ps and 8.0 ps respectively, and their fits. **b)** Variation of the spectral weight as a function of pump-probe delay of the 0.6 (red) and 2.0 (green) oscillators as resulting from the fit of the linear/low-fluence $\frac{\Delta R}{R}$. Inset: sketch of the involved transitions. **c)** Variation of the spectral weight of the 0.6 eV oscillator from the fit of the nonlinear term of $\frac{\Delta R}{R}$.

oscillator is, instead, opposite. It decreases upon cooling, as charge ordering enhances the hybridization of Fe_B^{3+} e_g with O_{2p} orbitals and hence gives rise to an increased minority spin $\downarrow$ occupation of the $Fe_B^{3+}e_g$ states.

The out-of-equilibrium data allowed us to draw various conclusions on the observed dynamics. Its dependence on the excitation fluence reveals that the photoexcitation process can trigger the out-of-equilibrium transition analogous to the Verwey phase transition, as already reported by de Jong et al. [2]. Below a certain threshold fluence ($F < F_1$, *low fluence* regime), the dynamical response we observe is the one associated to a warmer charge-ordered lattice, homogeneous over the sample. With larger fluences ($F_1 < F < F_2$, *intermediate fluence* regime), regions of the high-temperature phase can nucleate, eventually leading to isolated remnants of the charge-ordered lattice. [2] This picture of the nature of the nucleating phase is supported by the spectral analysis of our out-of-equilibrium data. Moreover, the latter contain also indications about the phase separation occurring in the sample. In fact, in the intermediate fluence regime $[\frac{\Delta R}{R}]_{h\nu,t}$ is not a separable matrix, i.e. it cannot be expressed as a single spectral feature evolving in time. This supports the interpretation that the observed response is the sum of the responses of distinct regions. Finally, we have shown that above a further threshold fluence ($F > F_2$, *high fluence* regime), the transition to the high-temperature phase is homogeneous over the sample, and nucleation is not observed in the electronic properties as it is in the intermediate fluence regime. The mentioned characteristic fluences are surprisingly linked within the experimental error to the equilibrium thermodynamics of magnetite and, in particular, to the delivery of latent heat to the sample. This suggests that the photoexcitation with 1.5 eV photons acts as a sudden heating. Furthermore, the photo-induced phase can be qualitatively linked to the equilibrium high-temperature phase studying its spectral fingerprint in the visible, which maps the local charge order. We stress that our visible probe cannot measure the Drude response associatd to a metallic behavior. Further measurements addressing the low-energy optical properties are, therefore, necessary to ascertain the full correspondence between the photo-induced phase and the equilibrium high-temperature metallic one.

1.6 Non-separable dynamics as a general signature of phase separation?

Our results about the phase separation in the system may have a general relevance beyond the particular case-study of magnetite. Although the details as the lattice order and the timescales involved could be different, the behavior we discussed in this work may be valid in general for photoexcited out-of-equilibrium systems displaying a first-order phase transition. Furthermore, the picture emerging from this work suggests also that a non-separable out-of-equilibrium reflectivity may be a general fingerprint of out-of-equilibrium phase separation and may represent a straightforward way to highlight the possible occurrence of phase separation in other out-of-equilibrium experiments.

As a first test of this hypothesis, I performed the analysis of the results of analogous pump-probe experiments on vanadium dioxide (VO_2), by Wall et al. [4]. Vanadium dioxide displays a first-order insulator-to-metal transition at $T_c = 340$ K, linked to a structural transition from a low-temperature monoclininc (M_1) phase to a high-temperature rutile (R) phase. The general characteristics of the response to photoexcitation of VO_2 at $T < T_c$ may therefore be expected to be similar to the case of Fe_3O_4 discussed in this chapter. This seems indeed to be the case. Performing singular value decomposition on $\frac{\Delta R}{R}|_{VO_2}(h\nu, t)$ and calculating the non-separability (as discussed in section 1.4.2), one obtains the result shown in figure 1.14 as a function of the fluence in units of the threshold fluence (i.e. $F_{threshold} = 1$). As in Fe_3O_4 (see figure 1.12), the non-separability is peaked in the close-to-threshold regime and goes towards zero on both sides. Remarkably, this hints to a possible generality of the non-separability of $\frac{\Delta R}{R}$ as a signature of phase separation in out-of-equilibrium first-order phase transitions. Further studies on different systems would be needed to further test such conjecture. It remains also to be studied in what other conditions, besides phase separation, $\frac{\Delta R}{R}(h\nu, t)$ may be non-separable.

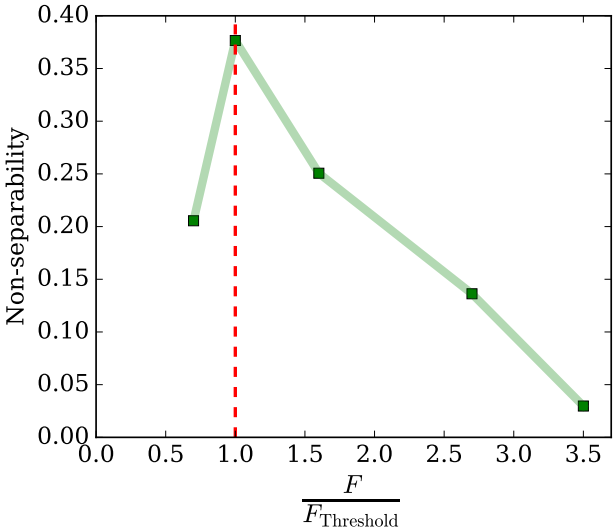

Figure 1.14: Non-separability of the relative variation of the reflectivity $\frac{\Delta R}{R}(h\nu, t)$ of VO_2, as a function of the pump-fluence. The latter is in units of the threshold fluence for the triggering of the out-of-equilibrium phase transition.

Results at 80 K

As mentioned in section 1.3.2, the data at 80 K are completely analogous to the ones at 35 K, which have been described in detail. The only difference between the two datasets are the values of the characteristic fluences F_1 and F_2. In agreement with the thermal interpretation of the energy delivered to the sample by the pump pulses, they are lower at 80 K, since the system needs less energy to reach the transition temperature. In the following figures, from 1.15 to 1.19, we plot the data measured at 80 K and their analysis, as discussed in the main text for 35 K.

Characteristic timescales The characteristic timescales τ_2 for the slow response in the intermediate fluence regime at 80 K are reported in table 1.2.

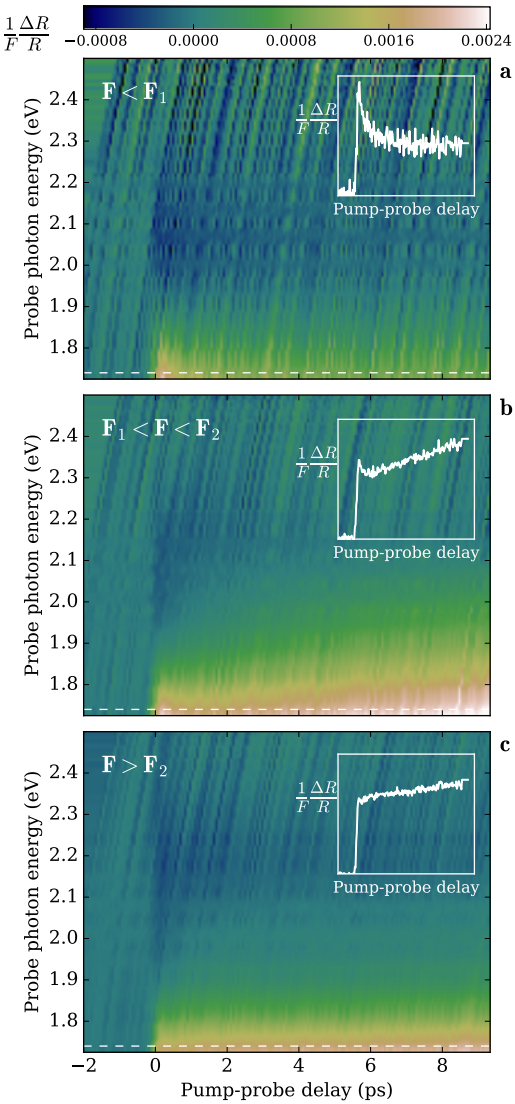

Figure 1.15: **a,b,c)**: Normalized relative variation of the reflectivity $\frac{1}{F}\frac{\Delta R}{R}$ measured at 80 K as a function of pump-probe delay and probe photon energy for fluences of 0.6, 2.9, and 5.7 mJ cm^{-2} respectively. **a,b,c)** inset: temporal profile of the colour plots at 1.74 eV. Dashed lines: photon energy corresponding to the insets.

Fluence (mJ cm^{-2})	τ_2 (ps)
2.2	6.5
2.9	4.3
4.3	1.7

Table 1.2: τ_2 at 80 K for different pump-fluences in the intermediate regime.

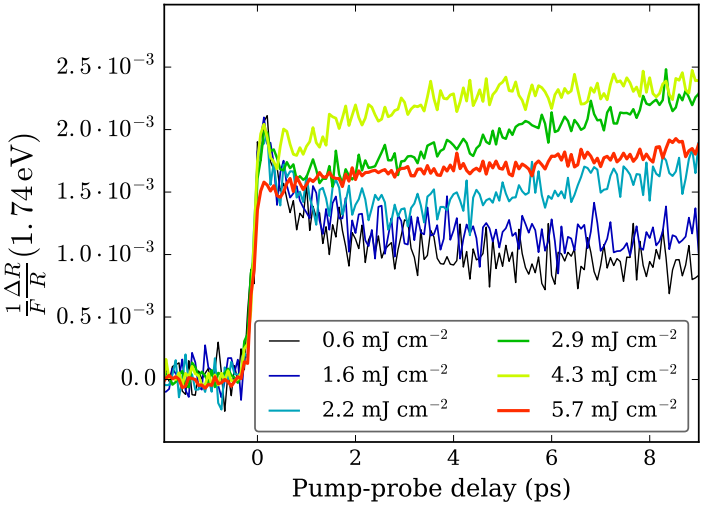

Figure 1.16: Normalized relative variation of the reflectivity $\frac{1}{F}\frac{\Delta \mathrm{R}}{\mathrm{R}}$(1.74 eV) measured at 80 K for different pump fluences.

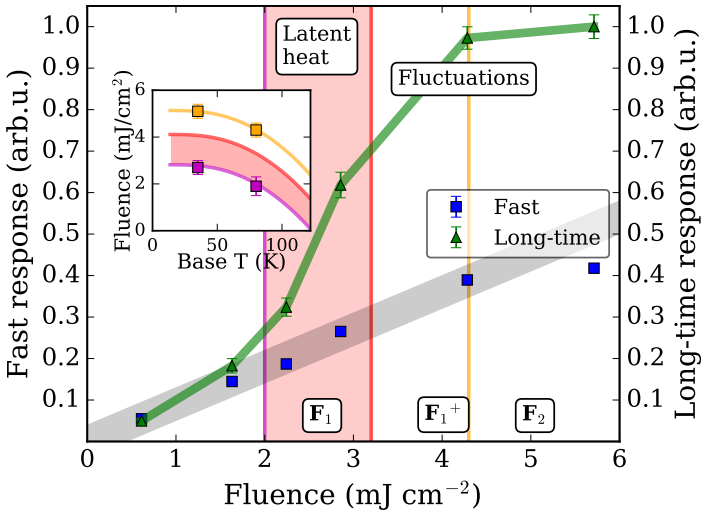

Figure 1.17: 'Fast response" (blue squares): $\frac{\Delta R}{R}$ at 1.74 eV photon energy and 0.2 ps pump-probe delay. "Long-time response" (green triangles): $\frac{\Delta R}{R}$ at 1.74 eV photon energy and 8 ps pump-probe delay. Inset: The squares are the characteristic fluences extracted from the out-of-equilibrium data as a function of the sample's temperature, corresponding to: onset of the nonlinear response (magenta) and saturation of the nonlinear response (yellow). The lines represent equivalent fluences calculated from thermodynamic data needed to: reach T_V^- (magenta), reach T_V^+ (red), reach 140 K (yellow). The red shaded area corresponds to fluences bringing the sample to T_V^- and supplying part of the latent heat. The vertical lines and the vertical shaded area in the main figure mimic the inset.

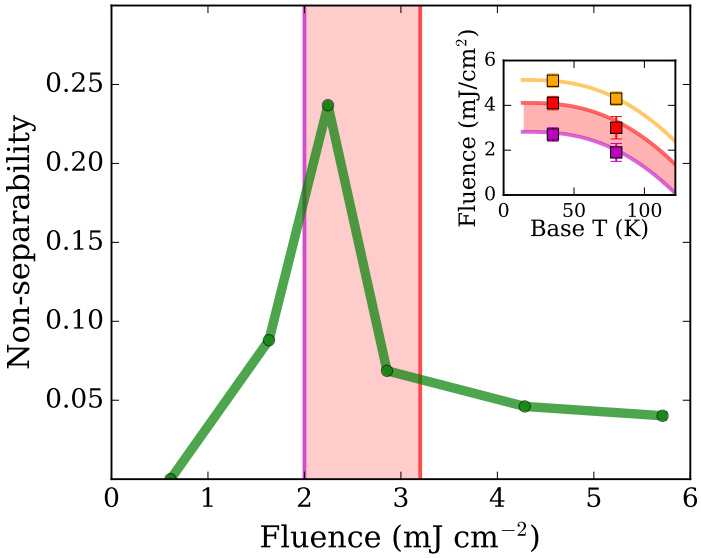

Figure 1.18: Ratio of the second largest and largest singular values (from both, the noise level was subtracted), as a function of fluence. Inset: same inset as in figure 1.17, with the addition of the fluences at which the "non-separability" starts to decrease (red squares), as measured at 35 and 80 K. These match the calculated equivalent fluences needed to deliver the full latent heat to the sample (red line).

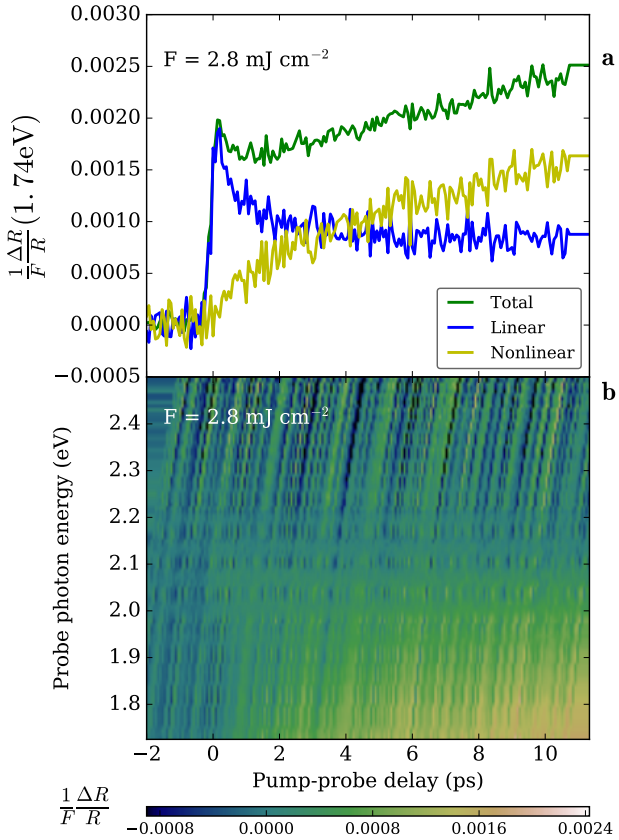

Figure 1.19: **a)** Green: $\frac{1}{F}\frac{\Delta \mathrm{R}}{\mathrm{R}}(t)$ at 1.74 eV for 2.8 mJ cm^2. Blue (yellow): linear (nonlinear) term of $\frac{1}{F}\frac{\Delta \mathrm{R}}{\mathrm{R}}$ for F = 2.8 mJ cm^{-2} at 1.74 eV photon energy. **b)** $\frac{1}{F}\frac{\Delta \mathrm{R}}{\mathrm{R}}'(h\nu, t)$ for F = 2.8 mJ cm^{-2}.

Results at 140 K

Figure 1.20 shows $\frac{\Delta R}{R}$ measured at 140 K. In agreement with the interpretation of a photo-induced phase transition for the data at 35 and 80 K, these data display a completely different behaviour. In fact, the spectrum of $\frac{\Delta R}{R}|_{140\ K}$ is different from $\frac{\Delta R}{R}|_{35,80K}$ in all fluence regimes. Moreover, $\frac{\Delta R}{R}|_{140\ K}$ does not show any nonlinearity or slow dynamics arising as a function of fluence. As already mentioned in the main text, also the singular value decomposition points towards an excitation that leaves the sample homogeneous at all the explored pump fluences, since at all fluences $\frac{\Delta R}{R}|_{140\ K}$ is exactly separable.

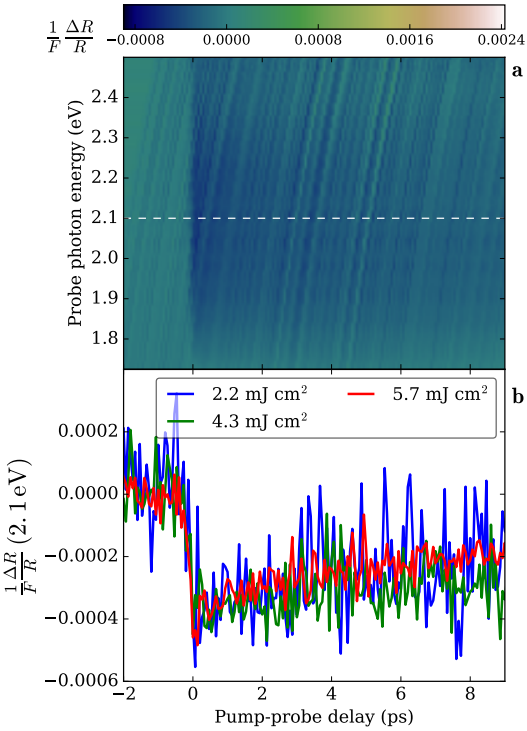

Figure 1.20: **a)**: Relative variation of the reflectivity $\frac{\Delta R}{R}$ at 140 K with 5.7 mJ cm^{-2} as a function of pump-probe delay and probe photon energy. **b)** $\frac{\Delta R}{R}$(2.1 eV) at 140 K for three different pump-fluences.

Acknowledgements

Ignacio Vergara and Markus Grüninger from the Universität zu Köln performed the ellipsometric measurements and analysed the equilibrium results. C. Schüßler-Langeheine (Helmholty Zentrum Berlin), P. Metcalf (Purdue University) and V.A.M Brabers (Eindhoven University of Technology) characterized the sample. All the authors are grateful to Daniel Khomskii for the insightful discussion and critical reading of the work.

Chapter 2

Modelling of the optical properties of solids

2.1 The dielectric function at equilibrium

The general constitutive relation of a medium relates the electric displacement in the medium with the electric field [38], and can be written as

$$D_i(t) = \epsilon_0 E_i(t) + P_i[E](t). \tag{2.1}$$

If the medium is linear, then the polarization P contains only the first power of the electric field E and is determined by a retarded response $\chi(t)$ of the medium to the electric field. The electric displacement is therefore

$$D_i(t) = \epsilon_0 E_i(t) + \epsilon_0 \int_0^\infty ds\ \chi_{ij}(t-s) E_j(s). \tag{2.2}$$

$\chi_{ij}(t)$ is, in general, a tensor relating the polarization on the direction i to the electric field on the direction j. We can remove the convolution moving to ω-space:

$$D_i(\omega) = \epsilon_0 E_i(\omega) + \epsilon_0 \chi_{ij}(\omega) E_j(\omega). \tag{2.3}$$

To simplify the notation, below I will omit the ω-argument. If the medium is isotropic, then the susceptibility becomes a scalar quantity, and

$$\mathbf{D} = \epsilon_0 (1+\chi)\mathbf{E}. \tag{2.4}$$

$\epsilon = (1 + \chi)$ is the relative dielectric function. The dielectric function of a system gives access to many of its properties. In the next section I will briefly describe how it can be modelled using various kind of functions. From the dielectric function the other (linear) optical properties can be calculated. The (complex) refractive index is $n = \sqrt{\epsilon}$, and the reflectivity at normal incidence is $R = \left|\frac{n-1}{n+1}\right|^2$.

Analogously to the dielectric function, also another quantity is used to describe the optical properties of a system: the conductivity. For an isotropic medium

$$\mathbf{J} = \sigma \mathbf{E}. \tag{2.5}$$

With no free charges

$$\mathbf{J}(\mathbf{t}) = \frac{d}{dt}\mathbf{P}(\mathbf{t}), \tag{2.6}$$

which can be rewritten in ω-space as

$$\mathbf{J} = -i\omega P = -i\omega\epsilon_0\chi\mathbf{E}. \tag{2.7}$$

Comparing equations (2.5) and (2.5) we obtain that

$$\sigma = -i\omega\epsilon_0(\epsilon - 1). \tag{2.8}$$

A common notation is to call $\mathrm{Re}\,\epsilon = \epsilon_1$, $\mathrm{Im}\,\epsilon = \epsilon_2$, $\mathrm{Re}\,\sigma = \sigma_1$, and $\mathrm{Im}\,\sigma = \sigma_2$. Such quantities can be obtained from two main kinds of measurements. The first is the measurement of the reflectivity of the system with a subsequent Kramers-Kronig analysis, to obtain the modulus and phase of the complex reflectance $r = \frac{n-1}{n+1}$. The second is ellipsometry, which directly allows to measure the real and imaginary parts of ϵ.

2.1.1 The Lorentz oscillator

The most standard lineshape of transitions between energy levels is described by the solution of the following equation for a forced and viscously damped oscillator [39],

$$m\frac{d^2}{dt^2}\mathbf{r} + m\Gamma\frac{d}{dt}\mathbf{r} + m\omega_0^2\mathbf{r} = -e\mathbf{E}(\mathbf{r}, t). \tag{2.9}$$

From such an equation one obtains a susceptibility $\chi^{(L)}$ of the form

$$\chi^{(L)}(\omega) = \frac{A}{(\omega_0^2 - \omega^2) - i\Gamma\omega}, \tag{2.10}$$

where A is an amplitude (corresponding to the plasma frequency), and ω_0 and Γ are the parameters defined in the differential equation (2.9). Since such susceptibility is obtained as a solution of an oscillator equation, the function it describes is generally called "oscillator", namely Lorentz oscillator. Note that for $\omega_0 = 0$, such lineshape becomes the Drude lineshape for free electrons in an effective medium.

The total susceptibility of a system is then described as the sum of Lorentz oscillators, possibly a Drude lineshape for metals, and a constant which accounts for oscillators at higher energies that are not considered. The dielectric function is, in general,

$$\epsilon(\omega) = \epsilon_\infty + \sum_j \chi_j^{(L)}(\omega). \tag{2.11}$$

2.1.2 Other kinds of oscillators

The Lorentzian lineshape does not account for all the lineshapes that can be found in solids.

Gaussian oscillator When disorder is present in a lattice, or when the lattice structure is very complicated, the lineshape can be a Gaussian. The imaginary and real part of the dielectric function for a Gaussian oscillator are [40, 41] [1]

$$\epsilon_2(\omega) = A\left[e^{-\frac{(\omega-\omega_0)^2}{\Gamma^2/(4\log(2))}} - e^{-\frac{(\omega+\omega_0)^2}{\Gamma^2/(4\log(2))}}\right], \tag{2.12}$$

$$\epsilon_1(\omega) = A\frac{2}{\pi}\left[D\left(\frac{\omega-\omega_0}{\Gamma/\left(2\sqrt{\log(2)}\right)}\right) - D\left(\frac{\omega+\omega_0}{\Gamma/\left(2\sqrt{\log(2)}\right)}\right)\right], \tag{2.13}$$

where $D(z)$ is the Dawson function

$$D(z) = -i\frac{\sqrt{\pi}}{2}e^{-z^2}\mathrm{erf}(iz). \tag{2.14}$$

Note that ϵ_1 and ϵ_2 are related by the Kramers-Kronig relations.

[1] The expression is rather complicated because of the adopted convention for the parameters.

Tauc-Lorentz oscillator Spectra with energy gaps may be well described by the so-called Tauc Lorentz oscillator [42–44], which gives an imaginary part of the dielectric function of the form

$$\epsilon_2(\omega) = \begin{cases} A\frac{1}{\omega}\frac{\omega_0\Gamma(\omega-\Delta)^2}{\omega(\omega^2-\omega_0^2)+\omega^2\Gamma} & \text{if } x \geq \Delta \\ 0 & \text{if } x < \Delta \end{cases} \tag{2.15}$$

The expression for ϵ_1 is very complicated and is omitted. It can be found in reference [43, 44].

2.2 Out of equilibrium fits

The various oscillators described in the previous section are primarily employed to produce models of the equilibrium optical properties measured in one or more of the ways mentioned. This is, however, not their only possible application. In a pump-probe experiment the response of the system is given by the third-order nonlinear susceptibility $\chi^{(3)}$. However, it is usually assumed that, when the system can be safely considered in an effectively thermal state, the variation of the optical properties (e.g. of the reflectivity) can be described by variations of the parameters (central frequencies, widths, ...) of their equilibrium model.

In the case of materials whose spectra are not very simple, a fit of $\frac{\Delta R}{R}(h\nu, t)$ with the entirety of the parameters held as free can easily become unjustifiable. A minimal set of parameters has therefore to be found, whose variation is able to describe the observed $\frac{\Delta R}{R}(h\nu, t)$. The remaining parameters are constrained to be fixed. On physical grounds one can then choose to impose further constraints on the parameters. Apart from constraining single parameters around certain values, other kinds of constraints with more global character exist. As an example, it may be imposed that the total spectral weight be conserved (as done for the analysis of the linear term of the $\frac{\Delta R}{R}(h\nu, t)$ of magnetite in chapter 1), or that two specific oscillators exchange spectral weight.

Such constraints to the fit can be implemented using the so-called penalty functions. Instead of using the standard fitting routines, the unconstrained fit can be performed

1. defining the target (fitting) function;

2. defining an "error" function which uses the target function to calculate the quadratic difference (error) between the model with a given set of parameters and the data;

3. minimizing the error function in the space of the parameters using a minimization algorithm.

With such a setting, constraints can be implemented adding specific quantities, called penalties, to the quadratic error. Simple constraints of fixed parameters correspond to adding to the quadratic error the square of the difference between the selected parameter at the current iteration and the desired value of that parameters (e.g. the initial one). To strictly enforce the constraint, such difference must be multiplied by a very large coefficient (say, 10^6). A "global" constraint like the conservation of the total spectral weight can be implemented similarly. Within the error function, the spectral weight should be calculated with the current parameters. The penalty is then simply the squared difference between the such calculated value and the desired spectral weight (e.g. the initial one), multiplied, also in this case, by a large coefficient.

Without the penalty, the error function is simply minimized in the parameters space according to the landscape determined by the data. When the penalty is added, such landscape changes to take into account the possibly highly nontrivial relations among the parameters. Below, I report an example of such procedure in Python.

```
def target(x, parameters):
  y = ... # E.g., sum of oscillators.
  return y

def spectralweight(parameters, ...):
  y = ...
  return y

def error(parameters, targetfunction, dataX, dataY, parameter1_0,  \
                                  spectralweigth, spectralweight_0):
  #Standard quadratic error
  e  = np.sum( np.power(targetfunction(dataX, parameters) - dataY) )

  #Simple constraint of fixed parameter, set equal to the initial value
  e += 1e6*np.power(parameters[1]-parameter1_0, 2)

  #Conservation of spectral weight, set equal to the initial value
  e += 1e6*np.power( spectralweight(parameters) - spectralweigth_0)

  return e
```

```
#Define the guess initial parameters
intial_parameters = [...]

#Desired value for parameters[1]
parameter1_0 = ...

#Desired spectral weight
spectralweight_0 = spectralweight(initial_parameters, ...)

#Minimization routine
Result = scipy.minimize.optimize(error, x0=initial_parameters, args=(target, \
                        X, Y, parameter1_0, spectraweigth, spectralweight_0))
final_parameters = Result['x']
```

Bibliography

[1] E. J. W. Verwey. Electronic conduction of magnetite (Fe_3O_4) and its transition point at low temperatures. *Nature (London)*, 144:327–328, 1939.

[2] S. de Jong, R. Kukreja, C. Trabant, N. Pontius, C. F. CHang, T. Kachel, M. Beye, F. Sorgenfrei, B. Back, C. H. Bräuer, et al. Speed limit of the insulator-metal transition in magnetite. *Nat. Mater.*, 12:882–886, 2013.

[3] F. Randi, I. Vergara, F. Novelli, M. Esposito, M. Dell'Angela, V.A.M. Brabers, P. Metcalf, R. Kukreja, H.A. Dürr, D. Fausti, M. Grüninger, and F. Parmigiani Phase separation in the nonequilibrium Verwey transition in magnetite Phys. Rev. B **93**, 054305 (2016).

[4] S. Wall, L. Foglia, D. Wegkamp, K. Appavoo, J. Nag, R.F. Haglund, Jr., J. Stähler, and M. Wolf Tracking the evolution of electronic and structural properties of VO_2 during the ultrafast photoinduced insulator-metal transition Phys. Rev. B **87**, 115126 (2013).

[5] Daniel I Khomskii. *Transition metal compounds*. Cambridge, 2014.

[6] M. S. Senn, J. P. Wright, and J. P. Attfield. Charge order and three-site distortions in the Verwey structure of magnetite. *Nature (London)*, 481:173–176, 2012.

[7] E. Nazarenko, J. E. Lorenzo, Y. Joly, J. L. Hodeau, D. Mannix, and C. Marin. Resonant x-ray diffraction studies on the charge ordering in magnetite. *Phys. Rev. Lett.*, 97:066403, 2006.

[8] J. E. Lorenzo, C. Mazzoli, N. Jaouen, C. Detlefs, D. Mannix, S. Grenier, Y. Joly, and C. Marin. Charge and orbital correlations at and above the verwey phase transition in magnetite. *Phys. Rev. Lett.*, 101:226401, Nov 2008.

[9] J. Garcia, G. Subías, J. Herrero-Martín, J. Blasco, V. Cuartero, M. Concepción Sánchez, C. Mazzoli, and F. Yakhou. Reexamination of the temperature dependences of resonant reflections in highly stoichiometric magnetite. *Phys. Rev. Lett.*, 102:176405, 2009.

[10] S. C. Weng, Y. R. Lee, C. G. Chen, C. H. Chu, Y. L. Soo, and S. L. Chang. Direct observation of charge ordering in magnetite using resonant multiwave x-ray diffraction. *Phys. Rev. Lett.*, 108:146404, 2012.

[11] J. Blasco, H. Garcia, and G. Subias. Structural transformation in magnetite below the Verwey transition. *Phys. Rev. B*, 83:104105, 2011.

[12] D. J. Huang, H. J. Lin, J. Okamoto, K. S. Chao, H. T. Jeng, G. Y. Guo, C. H. Hsu, C. M. Huang, D. C. Ling, W. B. Wu, C. S. Yang, and C. T. Chen. Charge-orbital ordering and Verwey transition in magnetite measured by resonant soft x-ray scattering. *Phys. Rev. Lett.*, 96:096401, 2006.

[13] J. Schlappa, C. Schüßler-Langeheine, C. F. Chang, H. Ott, A. Tanaka, Z. Hu, M. W. Haverkort, E. Schierle, E. Weschke, G. Kaindl, and L. H. Tjeng. Direct observation of t_{2g} orgibal ordering in magnetite. *Phys. Rev. Lett.*, 100:026406, 2008.

[14] A. Tanaka, C. F. Chang, M. Buchholz, C. Trabant, E. Schierle, J. Schlappa, D. Schmitz, H. Ott, P. Metcalf, L. H. Tjeng, and C. Schüßler-Langeheine. Symmetry of orbital order in Fe_3O_4 studied by Fe $L_{2,3}$ resonant x-ray diffraction. *Phys. Rev. Lett.*, 108:227203, 2012.

[15] J. P. Wright, J. P. Attfield, and P.G. Radaelli. Charge ordered structure of magnetite Fe_3O_4 below the verwey transition. *Phys. Rev. B*, 66:214422, 2002.

[16] Y. Fujii, G. Shirane, and Y. Yamada. Study of the 123 K phase transition of magnetite by critical neutron scattering. *Phys. Rev. B*, 11:2036–2041, 1975.

[17] S. M. Shapiro, M. Iizumi, and G. Shirane. Neutron scattering study of the diffuse critical scattering associated with the Verwey transition in magnetite. *Phys. Rev. B*, 14:200–207, 1976.

[18] Jeroen van den Brink and Daniel I Khomskii. Multiferroicity due to charge ordering. *J. Phys.: Condens. Matter*, 20(43):434217, 2008.

[19] J. P. Shepherd, J. W. Koenitzer, R. Aragón, C. J. Sandberg, and J. M. Honig. Heat capacity studies on single crystal annealed Fe_3O_4. *Phys. Rev. B*, 31:1107–1113, Jan 1985.

[20] A. Cavalleri, M. Rini, and R. W. Schoenlein. Ultra-broadband femtosecond measurements of the photo-induced phase transition in vo2: From the mid-ir to the hard x-rays. *Journal of the Physical Society of Japan*, 75(1):011004, 2006.

[21] M. Chollet, L. Guerin, N. Uchida, S. Fukaya, H. Shimoda, T. Ishikawa, K. Matsuda, T. Hasegawa, A. Ota, H. Yamochi, G. Saito, R. Tazaki, S. Adachi, and S. Koshihara. Gigantic photoresponse in -filled-band organic salt (edo-ttf)2pf6. *Science*, 307(5706):86–89, 2005.

[22] Daniele Fausti, Oleg V. Misochko, and Paul H. M. van Loosdrecht. Ultrafast photoinduced structure phase transition in antimony single crystals. *Phys. Rev. B*, 80:161207, Oct 2009.

[23] S. Borroni, E. Baldini, A. Mann, C. Arrel, Frank van Mourik, J. Teyssier, J. Lorenzana, and F. Carbone. On the Verwey transition in magnetite: the soft modes of the metal-insulator transition. 2015.

[24] A. Schlegel, S. F. Alvarado, and P. Wachter. Optical properties of magnetite (Fe_3O_4). *J. Phys. C*, 12:1157, 1979.

[25] L. V. Gasparov, D. B. Tanner, D. B. Romero, H. Berger, G. Margaritondo, and L Forrò. Infrared and raman studies of the Verwey transition in magnetite. *Phys. Rev. B*, 62(12):7939–7944, 2000.

[26] S.K. Park, T. Ishikawa, and Y. Tokura. Charge-gap formation upon the Verwey transition in Fe_3O_4. *Phys. Rev. B*, 58:3717–3720, 1998.

[27] I. Leonov, A. N. Yaresko, V. N. Antonov, and V. I. Anisimov. Electronic structure of charge-ordered Fe_3O_4 from calculated optical, magneto-optical Kerr effect, and o k-edge x-ray absorption spectra. *Phys. Rev. B*, 74:165117, Oct 2006.

[28] K. J. Kim, S. Choi, H. J. Lee, J. H. Lee, and J. Y. Park. Evolution of structural and optical-absorption properties in $V_xFe_{3-x}O_4$. *Solid State Comm.*, 143:285–288, 2007.

[29] Fabio Novelli, Daniele Fausti, Julia Reul, Federico Cilento, Paul H. M. van Loosdrecht, Agung A. Nugroho, Thomas T. M. Palstra, Markus

Grüninger, and Fulvio Parmigiani. Ultrafast optical spectroscopy of the lowest energy excitations in the mott insulator compound yvo_3: Evidence for hubbard-type excitons. *Phys. Rev. B*, 86:165135, Oct 2012.

[30] Fabio Novelli, Giulio De Filippis, Vittorio Cataudella, Martina Esposito, Ignacio Vergara, Federico Cilento, Enrico Sindici, Adriano Amaricci, Claudio Giannetti, Dharmalingam Prabhakaran, et al. Witnessing the formation and relaxation of dressed quasi-particles in a strongly correlated electron system. *Nat. Comm.*, 5:5112, October 2014.

[31] A. J. M. Kuipers and V. A. M. Brabers. Thermoelectric properties of magnetite at the verwey transition. *Phys. Rev. B*, 14:1401–1405, Aug 1976.

[32] A. Gössling, M. W. Haverkort, M. Benomar, Hua Wu, D. Senff, T. Möller, M. Braden, J. A. Mydosh, and M. Grüninger. Mott-hubbard versus charge-transfer behavior in lasrmnO_4 studied via optical conductivity. *Phys. Rev. B*, 77:035109, 2008.

[33] A. Gössling, R. Schmitz, H. Roth, M. W. Haverkort, T. Lorenz, J. A. Mydosh, E. Müller-Hartmann, and M. Grüninger. Mott-hubbard exciton in the optical conductivity of ytiO_3 and smtiO_3. *Phys. Rev. B*, 78:075122, 2008.

[34] J. Reul, A. A. Nugroho, T. T. M. Palstra, and M. Grüninger. Probing orbital fluctuations in rvO_3 (r = y, gd, or ce) by ellipsometry. *Phys. Rev. B*, 86:125128, 2012.

[35] S. Takai, Y. Akishige, H. Kawaji, T. Atake, and E. Sawaguchi Low temperature heat capacities and Verwey transition of magnetite J. Chem. Thermodyn. **26**, 1259–1266 (1994).

[36] J. Reul, L. Fels, N. Qureshi, K. Shportko, M. Braden, and M. Grüninger. Temperature-dependent optical conductivity of layered lasrfeO_4. *Phys. Rev. B*, 87:205142, 2013.

[37] R. V. Pisarev, A. S. Moskvin, A. M. Kalashnikova, and Th. Rasing. Temperature-dependent optical conductivity of layered lasrfeO_4. *Phys. Rev. B*, 79:235128, 2009.

[38] D.J. Griffiths, Introduction to electrodynamics (3rd ed.), Prentice Hall (1999).

[39] F. Wooten Optical Properties of Solids Academic Press, 1972.

[40] D. De Sousa Meneses, M. Malki, and P. Echegut Structure and lattice dynamics of binary lead silicate glasses investigated by infrared spectroscopy J. of Non-crystalline solids **352**, 769–776 (2006).

[41] S.A. MacDonald, C.R. Schardt, D.J. Masiello, J.H. Simmons Dispersion analysis of FTIR reflection measurements in silicate glasses J. of Non-crystalline solids **275**, 72–82 (2000).

[42] J. Tauc, R. Grigorovici, A. Vancu Optical Properties and Electronic Structure of Amorphous Germanium Physica status solidi (b) **15** (2), 627 (1966).

[43] G.E. Jellison and F.A. Parameterization of the optical functions of amorphous materials in the interband region Appl. Phys. Lett., 69:371, 1996.

[44] G.E. Jellison and F.A. Erratum: Parameterization of the optical functions of amorphous materials in the interband region Appl. Phys. Lett., 69:2137, 1996.

Part II

Exciting materials in the mid-infrared

Chapter 1

The experimental set-up

1.1 Introduction to nonlinear optics

When light from the Sun passes through the windows, apart from absorption and reflection, its electric field does not change its oscillation frequency. Reds remain red and greens remain green. The induced polarization in the glass of the windows is in fact linear with the impinging electric field. The same happens with the everyday reflection from a mirror. This is the situation described by linear optics. Fortunately for the world of the spectroscopic techniques, linear optics is just a first-order expansion (in the electric field) of the actual phenomena. When the field amplitude is large, nonlinear optics comes into play, and the frequency of light can be transformed when it interacts with matter.

This is of fundamental importance for spectroscopy and in particular for time-resolved spectroscopies, that use ultrashort pulses. Within ultrashort pulses, in fact, the peak electric field amplitude is easily large enough for nonlinear optical effects to be relevant. Therefore, while commercial pulsed laser sources offer very high pulse energies with a very small frequency (or wavelength) tunability of the emitted light, nonlinear optical processes can be exploited to extend the spectral range on which light pulses can be obtained.

The goal of this part of my project has been to perform pump-probe experiments on strongly correlated materials using pump pulses in the mid-infrared spectral range. From the original source, which produces light pulses with 1.5 eV photon energy, pulses in the mid-infrared range ($\sim$ 100 meV) have been generated using nonlinear optical processes in specific crystals. In the follow-

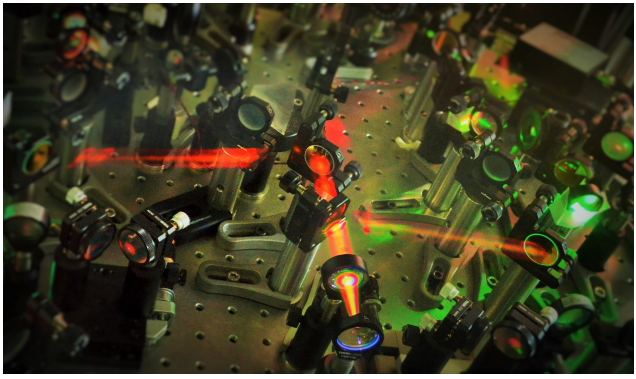

Figure 1.1: Typical nonlinear process. White visible light is generated from an infrared beam.

ing, I will briefly describe the relevant processes involved and then move to the description and the characterization of the set-up used.

To introduce how nonlinearities in optical processes arise, let us start from the Maxwell equations

$$\nabla \cdot \mathbf{D} = \rho \tag{1.1}$$
$$\nabla \cdot \mathbf{B} = 0 \tag{1.2}$$
$$\nabla \times \mathbf{E} = -\partial_t \mathbf{B} \tag{1.3}$$
$$\nabla \times \mathbf{H} = \partial_t \mathbf{D} + \mathbf{J}. \tag{1.4}$$

We consider regions of space where no free charges nor free currents are present, i.e. $\rho = 0$ and $\mathbf{J} = 0$, and we take the medium to be non-magnetic, i.e. $\mathbf{B} = \mu_0 \mathbf{H}$. Since we are interested in the cases in which the medium is nonlinear we take

$$\mathbf{D} = \epsilon_0 \mathbf{E} + \mathbf{P}, \tag{1.5}$$

where $\mathbf{P}$ nonlinearly depends on $\mathbf{E}$.

From the Maxwell equations one can proceed as usual for the derivation of the wave equation for $\mathbf{E}$ [1]. Within the approximation of "slowly varying amplitude" [2], a forced wave equation is obtained for the electric field, of the form

$$\Box \mathbf{E} = -\mu_0 \partial_t^2 \mathbf{P}. \tag{1.6}$$

In a lossless and dispersionless medium, the role of the nonlinear terms of the polarization can be made explicit, writing $\mathbf{P} = \mathbf{P}^{(1)} + \mathbf{P}^{(\mathrm{NL})}$. In this way, $\mathbf{P}^{(1)}$

can be reabsorbed in the left-hand member of the equation, defining $\Box_n$ as the d'Alembertian operator for a wave travelling with group velocity $\frac{c}{n}$ in a medium and writing

$$\Box_n \mathbf{E} = -\mu_0 \partial_t^2 \mathbf{P}^{(\mathrm{NL})}. \tag{1.7}$$

Without any significant nonlinear polarization $\mathbf{P}^{(\mathrm{NL})}$, the equation reduces to the standard wave equation of linear optics for light travelling in a medium. If $\mathbf{P}^{(\mathrm{NL})}$ is instead significant, it acts as a source which forces the electric field. Given the nonlinear functional form of $\mathbf{P}^{(\mathrm{NL})}(E)$, such forcing term produces electric fields oscillating with frequencies that were not present in the spectrum of the electric field before its interaction with the medium.

1.1.1 Second-order nonlinear phenomena

The most important nonlinear phenomenon used to generate light pulses in the mid-infrared range starting from pulses in the near-infrared is photon down-conversion, or difference frequency generation. This effect is described by the second-order term in $\mathbf{P}^{(\mathrm{NL})}(E)$, i.e. by a term of the form

$$P_i^{(2)}(t) = \epsilon_0 \chi_{ijk}^{(2)} E_j E_k. \tag{1.8}$$

Here χ_{ijk} is a third-rank tensor connecting the polarization in the direction i and the electric fields polarized along j and k, which vanishes for centrosymmetric crystals. As an illustration of the possible effects that can arise from such quadratic term, let us consider an electric field that, before the interaction with the medium, contains just two spectral components

$$\mathbf{E(t)} = \mathbf{E}_1(t) + \mathbf{E}_2(t), \tag{1.9}$$

where $\mathbf{E}_1(t) = \mathbf{E}_1 e^{i(k_1 z - \omega_1 t)}$ + cc and $\mathbf{E}_2(t) = \mathbf{E}_2 e^{i(k_2 z - \omega_2 t)}$ + cc are linearly polarized waves with unspecified polarizations j and k, travelling along $\hat{z}$. The second-order polarization will be (before it has significantly forced any new electric field)

$$P_i^{(2)}(t) = \epsilon_0 \big[\chi_{ijj}^{(2)}(|\mathbf{E}_1|^2 + E_1^2 e^{i(2k_1 z - 2\omega_1 t)} + cc) + \tag{1.10}$$

$$\chi_{ikk}^{(2)}(|\mathbf{E}_2|^2 + E_2^2 e^{i(2k_2 z - 2\omega_2 t)} + cc) + \tag{1.11}$$

$$2\chi_{ijk}^{(2)}\big(E_1 E_2 e^{i((k_1+k_2)z - (\omega_1+\omega_2)t)} + \tag{1.12}$$

$$E_1 E_2^* e^{i((k_1-k_2)-(\omega_1-\omega_2)t)} + cc\big)\big]. \tag{1.13}$$

$P_i^{(2)}(t)$, which acts as a source for the electric field, displays four classes of time dependence. There are two terms which do not oscillate at all. These

are the static fields which are generated by the process generally called *optical rectification*. There are two terms oscillating at twice the original frequencies ω_1 and ω_2, produced in the process called *second harmonic generation*. Another term oscillates at the sum of the two incoming frequencies, $\omega_1 + \omega_2$ (*sum frequency generation*). Finally there is a term oscillating at the difference between the original frequencies, $\omega_1 - \omega_2$, which originates from the so-called *difference frequency generation*.

In general, the processes of sum frequency and second harmonic generation are called of photon upconversion, because the resulting photons have higher energy than the incoming ones. The difference frequency generation instead is said of photon downconversion, since the resulting photon energies are lower than the original ones. As described in more detail in section 1.2, this kind of process allows to transform the 1.5 eV photons produced by a Ti:Sapphire pulsed laser to mid-infrared photons.

By historical convention, the photons with the highest frequency or energy are called pump photons (e.g. $\omega_1 = \omega_p$), the photons at frequency $\omega_2 = \omega_s$ are called signal photons and the ones at frequency $\omega_1 - \omega_2 = \omega_i$ are called idler photons.

The term "photon downconversion" is most easily understood in a second-quantization picture. The interaction Hamiltonian describing photon downconversion can be written as

$$H_{\text{int}} \propto \mathbf{P}^{(\text{NL})} \cdot \mathbf{E} \propto \chi^{(2)}_{ips} a_i^\dagger a_s^\dagger a_p + hc, \tag{1.14}$$

where a_p, a_s and a_i are the annihilation operators of the pump, signal and idler modes of the electromagnetic field. Such formulation allows to picture the process as a high-energy pump photon splitting into two lower-energy photons (signal and idler), whose total energy is the energy of the original pump photon. For the energy conservation to hold, in fact, pairs of a signal and idler photons have to be produced. The net result is that, while idler photons are produced, the signal beam is amplified.

The difference frequency generation process is experimentally realized in optical devices which have been historically named optical parametric amplifiers (OPA) or difference frequency generators (DFG), with different names used when the device is used for different purposes. In particular, the device is called optical parametric amplifier when its goal is to amplify the signal beam. It is called difference frequency generator if, instead, its goal is to generate the idler beam.

1.1.2 Phase matching

From the discussion done so far, it seems that the only requirement for the efficient occurrence of photon downconversion is that the relevant component of the second-order nonlinear susceptibility be large. However, there is an additional condition which has to be satisfied: the so-called phase matching condition [2, 3]. For the generation of the idler field to be efficient, the forcing term in equation (1.7) should be in phase with the idler electric field in the left-hand member of the same equation. Their phase difference is

$$\Delta\phi = \big((k_1 - k_2) - k_3\big)z - \big((\omega_1 - \omega_2) - \omega_3\big)t, \tag{1.15}$$

where k_3 and ω_3 are the wavevectors and frequency of the idler field. While $\omega_3 = \omega_1 - \omega_2$ everywhere, k_3 is not automatically equal to $k_1 - k_2$, because electric fields oscillating at different frequencies will experience different refractive indices in a medium. The request that $k_1 - (k_2 + k_3)$ is called phase matching condition and it corresponds to the conservation of momentum in the annihilation of a pump photon and creation of a pair of signal and idler photons.

In particular, it can be shown that the phase matching condition cannot be fulfilled in bulk isotropic materials in the normal dispersion region, i.e. in which $n_i < n_s < n_p$. Phase matching can be achieved in birefringent crystals, i.e. crystals in which light polarized along different directions experience different refractive indices. The most commonly used birefringent crystals have one extraordinary axis which is inequivalent to the remaining ordinary two, and the refractive index n_e for light polarized along the extraordinary axis is smaller than the refractive index n_o on the ordinary axes. Crystals with such properties are said negative uniaxial crystals. The phase matching condition can be achieved by appropriately selecting the projection of the polarizations of the various field modes on the ordinary and extraordinary axes. This is done by changing the angle θ between the optical axis of the crystal and the propagation direction of the beams [3].

If the signal and idler beams are polarized along the ordinary axis orthogonally to the pump beam, the phase matching is said to be of type I. If one of the two is polarized parallel to the pump, we talk about type II phase matching [3]. The condition $k_p = k_s + k_i$ for type II phase matching (with the idler electric field parallel to the pump one) can be written as

$$n_{ep}(\theta)\omega_p = n_{os}\omega_s + n_{ei}(\theta)\omega_i, \tag{1.16}$$

where the angle dependent refractive index n_{ex} is given by

$$\frac{1}{n_{ex}(\theta)^2} = \frac{\sin(\theta)^2}{n_{ex}^2} + \frac{\cos(\theta)^2}{n_{op}^2}. \tag{1.17}$$

Figure 1.2 pictorially shows the relation between the optical axis of the crystal and the propagation direction of the beams.

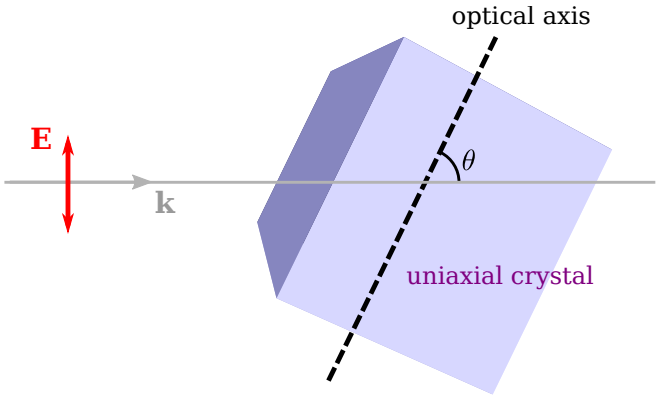

Figure 1.2: Pictorial view of the angle between the optical axis of the crystal and the beam propagation direction determining the phase matching.

1.1.3 Photon downconversion

As shown by the interaction Hamiltonian (1.14), a downconversion process involves three photons and is therefore also called a three-wave mixing. Photon downconversion can happen either spontaneously or with a stimulus. In a classical sense, it can only occur if stimulated, in the picture implicitly assumed in section 1.1.1, in which the original electric field is already oscillating also at the signal frequency ω_2. Analogously to stimulated emission, the presence of this spectral component stimulates the process.

In the full quantum picture, however, photon downconversion also occurs spontaneously, in which case it is called parametric fluorescence. Such situation corresponds to the amplification of the vacuum fluctuations. The occurrence of parametric fluorescence is easily captured if we consider the evolution of the modes of the electromagnetic field under the interaction Hamiltonian (1.14). Let us consider an initial state of the electromagnetic field in

which the pump and the signal modes are in the quasiclassical coherent states $|\alpha_p\rangle_p$ and $|\alpha_s\rangle_s$, while the idler mode is in its vacuum $|0\rangle_i$. The full state is therefore $|\Psi_0\rangle = |\alpha_p\rangle_p|\alpha_s\rangle_s|0\rangle_i$.

Up to first order, the unitary evolution operator $U(t)$ in the interaction picture is given by

$$U(t) \simeq \mathbb{I} - i\chi^{(2)}_{ips}\mathrm{T}\int ds\big(a_i^\dagger a_s^\dagger a_p + h.c.\big), \tag{1.18}$$

where T is the time-ordering operator. The above expression can be simplified in the limit in which the interaction is considered impulsive, i.e. the interaction time is sent to zero while keeping a finite interaction probability. In such case, $U(t)$ can be written as

$$U(t) \simeq \mathbb{I} - iC\big(a_i^\dagger a_s^\dagger a_p + h.c.\big), \tag{1.19}$$

where C is a constant, and the final state for the electromagnetic field is

$$|\Psi\rangle \simeq |\Psi_0\rangle - iC\big(a_i^\dagger a_s^\dagger a_p + h.c.\big)|\Psi_0\rangle. \tag{1.20}$$

If we calculate the final number of photons in the idler mode $\langle\Psi|a_i^\dagger a^i|\Psi\rangle$, we obtain

$$\langle\Psi|a_i^\dagger a^i|\Psi\rangle = |C|^2(1 + |\alpha_s|^2)|\alpha_p|^2. \tag{1.21}$$

$|\alpha_s|^2$ and $|\alpha_p|^2$ are the number of photons in the signal and pump modes, respectively. The above equation tells that, even if originally there are no photons in the signal mode, a pump photon can still split and produce an idler (and a signal) photon.

When the signal mode is populated also before the interaction with the nonlinear medium ($|\alpha_s|^2 > 0$), the incoming beam at the signal frequency is called seed. Its generation is discussed briefly in the next section.

The case of ultrashort pulses needs a further consideration. Up to now we have considered only the case of monochromatic continuous waves. Photon downconversion with pulses lasting only 10 to 100 fs is affected also by the mismatch between the group velocities of the light pulses. Since the process is efficient only when the beams interact, i.e. when the pulses overlap, there will be a length over which the pulses completely separate, which sets an approximate limit to the maximum interaction length of the pulses in the nonlinear medium [3].

1.1.4 Third-order nonlinear phenomena

At this point of the discussion one encounters the following question. To have an efficient generation of low-energy photons through downconversion, the process has to be stimulated by pre-existing seed photons at that energy. How are they produced if the only available photons before the downconversion are the ones produced by the laser? The most common way to produce a small amplitude field that can be used as seed for downconversion, for example in an optical parametric amplifier, is the process known as white light generation.

The generation of white light pulses, i.e. the broadening of the spectrum of an original light pulse, is a process produced by the third-order nonlinear polarization

$$P_i^{(3)} = \chi_{ijkl}^{(3)} E_j E_k E_l. \tag{1.22}$$

The presence of a third-order nonlinear polarization implies that the refractive index of the medium depends on the intensity of light [2]

$$n = n(I) = n_0 + n_2 I(\mathbf{r}, t), \tag{1.23}$$

where I is proportional to the squared modulus of the electric field.

Such intensity-dependent refractive index produces two effects which are relevant for the generation of white light pulses. Since the transverse section of the beam is not a constant (usually a Gaussian), the transverse dependence of $n(I)$ will produce an effective positive lense. The beam therefore collapses in a filament with very high intensity. This process is known as self-focussing [2]. Then, the temporal intensity profile of a pulse produces changes in the frequency of the electric field, shifting it to higher frequencies in the back of the pulse and to lower frequencies in the front of the pulse. This is known as self-phase modulation [2] and is the process which actually broadens the spectrum of the pulse, after self-focussing has produced the high-intensity condition.

1.2 The set-up and its characterization

To generate light pulses with photon energies in the mid-infrared range (~ 0.1 eV) from near-infrared pulses (~ 1.5 eV) a single downconversion stage is not sufficient. To have intense mid-infrared pulses one should first generate intense pulses with intermediate photon energies (~ 0.9 eV). The set-up I will describe in this section contains therefore various stages at which photon downconversion occurs.

Besides the desired photon energy, we had the further requirement for the mid-infrared pulses that their phase be stable. When talking about light

pulses, one talks about the carrier-envelope phase, i.e. the phase of the electric field relative to the envelope of the pulse. Usually, such quantity is not considered as important if the period of the oscillation of the electric field is much shorter than the pulse envelope. As shown in figures 1.3a, b, and c, the global shape of the electric field is not very much affected by its carrier-envelope phase.

The carrier-envelope phase becomes, instead, increasingly important when the oscillation period of the electric field increases with respect to the pulse envelope. As shown in figures 1.3d, e, and f, the global shape of the electric field can become significantly different for different phases. The question can arise, whether the interaction of such kind of pulses with matter depends on the phase of the electric field in addition to its power spectrum.

Pulsed lasers are not naturally phase stable. Therefore, one needs to devise phase stabilization methods. For example, the positions of the mirrors in the laser cavity can be actively controlled to obtain a stable carrier-envelope phase. As an alternative, passive stabilization methods can be implemented [4], as we did in our set-up. The key point in such passive methods is that the phase of an idler beam in difference frequency generation is stable, if the pump and the seed/signal beams have a fixed phase relation.

Our set-up therefore consists of two "twin" optical parametric amplifiers seeded by the same white light. The signal beams produced by the two parametric amplifiers inherit the same phase from the single seed pulse and their phase relation is therefore fixed, even though their absolute phase is not constant from pulse to pulse. If they are tuned to different energies, they can be used as pump and seed beams in a difference frequency generation stage to produce phase-stable mid-infrared pulses.

1.2.1 The set-up

The set-up we have built to perform pump-probe experiments with mid-infrared pump pulses is based on a Legend (Coherent) source producing light pulses at 1.54 eV photon energy at the repetition rate of 1 kHz, with a pulse energy of 2.2 mJ. The duration of the pulses is 80 fs. The system is pumped by an Evolution (Coherent) diode laser and seeded by a 78 MHz Mira oscillator. Out of the total pulse energy, 1.8 mJ are used for the generation of the mid-infrared pulses.

The optical set-up which generates the mid-infrared pulses consists of a white light generation part, two twin optical parametric amplifiers tuned at different photon energies, each with two amplification stages, and finally a difference frequency generation stage to produce mid-infrared photons starting

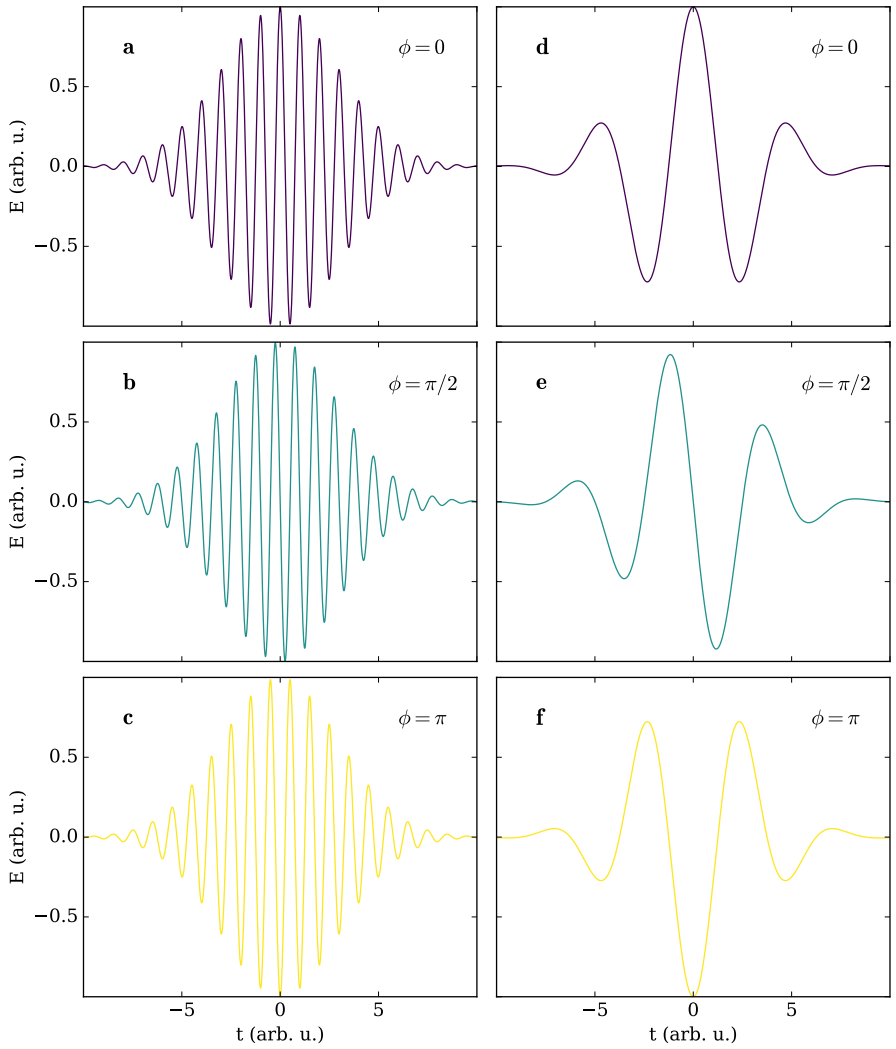

Figure 1.3: Different shapes of the electric field in a light pulse. The first column shows the case of small oscillation periods with respect to the pulse envelope, the second large periods with respect to the envelope. The three rows display the cases for carrier-envelope phase $\phi = 0$, $\pi/2$ and π.

from the products of the optical parametric amplifiers.

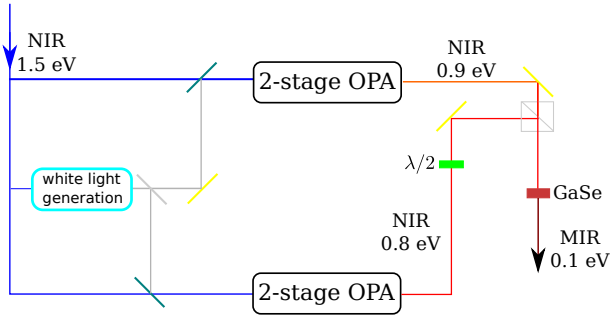

Figure 1.4: Scheme of the set-up consisting of a white light generation stage, two twin optical parametric amplifiers and a final difference frequency generation stage.

The white light pulses are generated by focussing 24 μJ pulses into an yttrium aluminum garnet (YAG). According to Bradler et al. [5], white light generation in YAG produces more energy density in the near-infrared as compared to the commonly used sapphire, as shown in figure 1.5.

The produced pulses are split and used to parallely seed the first amplification stages of the two optical parametric amplifiers, with pump pulses at 1.54 eV and 72 μJ pulse energy. The photon downconversion process takes place in two $\beta-$barium borate crystals (BBO), suitably cut to satisfy the type II phase matching conditions, with the signal field orthogonal to the pump and idler fields. The two amplifiers are tuned to produce signal beams with an energy difference corresponding to the desired mid-infrared photon energy, to be produced by difference frequency generation. The first stages of the OPAs have been built in the non-collinear geometry, which allows to achieve phase matching over a broader spectral range and to geometrically separate the signal and idler beams.

The typical photon energies at which the amplifiers were tuned are ~ 0.9 and ~ 0.8 eV, in order to generate mid-infrared pulses with photon energies of ~ 0.1 eV. Figure 1.6 shows typical spectra of the produced signal pulses.

The signal pulses produced in the first stages are used to seed the second amplification stages. There, the interaction occurs in the collinear geometry within other BBO crystals, with a total energy of ~ 800 μJ for each pump pulse.

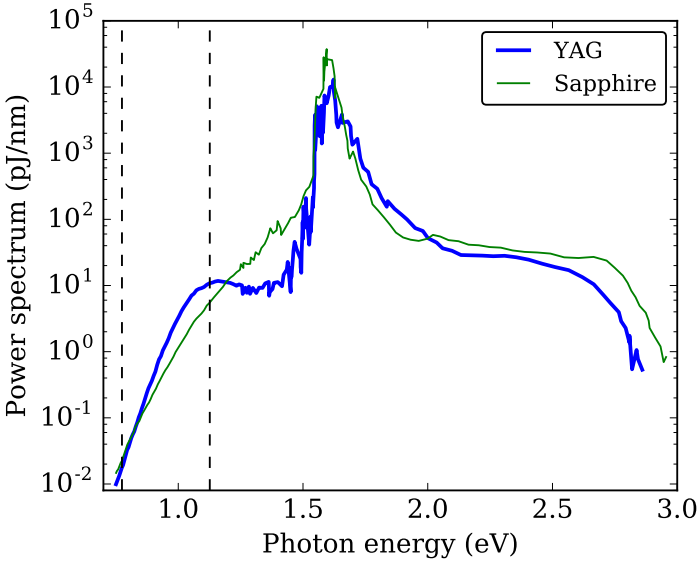

Figure 1.5: Power spectrum of the white light pulses generated in yttrium aluminum garnet (YAG) and sapphire, blue and green curves respectively (adapted from Bradler et al. [5]). The vertical dashed lines delimit the tunability range of our optical parametric amplifiers.

Finally, the two signal beams produced in the two optical parametric amplifiers are combined and collinearly interact within a gallium selenide crystal to produce mid-infrared photons via difference frequency generation. The signal beam with the highest photon energy is, in this stage, the pump beam while the one with the lowest photon energy is the seed.

After the difference frequency generation stage, the mid-infrared beam is isolated using a germanium window, which acts as a filter absorbing photons with energies above 0.3 eV.

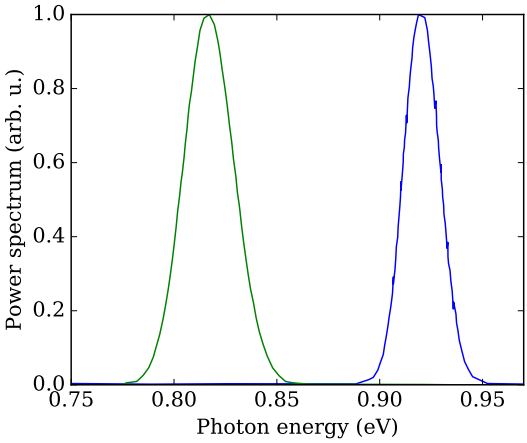

Figure 1.6: Typical spectra of the two twin optical parametric amplifiers, tuned at different photon energies. The high-energy photons will act as the pump in the difference frequency generation, while the low-energy ones as the seed.

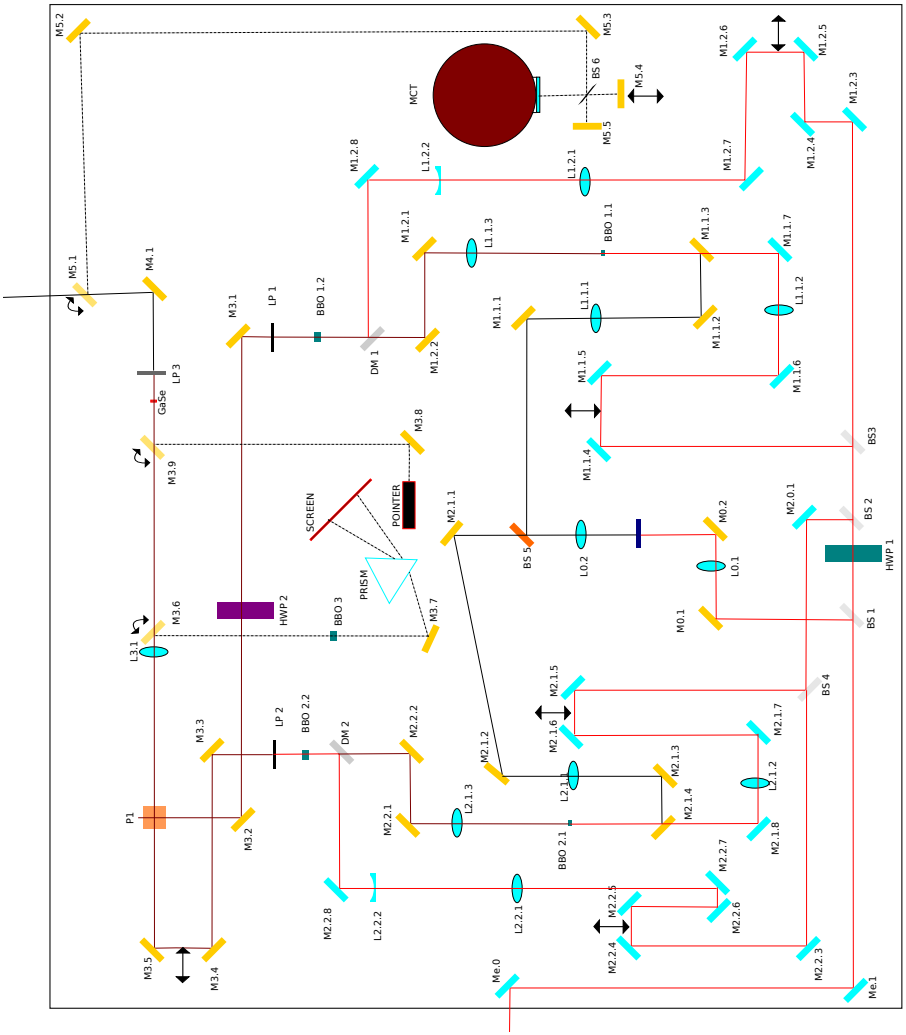

Figure 1.7: Detailed scheme of the set-up. M elements are mirrors, BS beam-splitters, L lenses, HWP half-wave plates, P polarizers, and MCT is the mercury cadmium telluride photodiode. Straight double arrows denote mechanical translators, curved double arrows flip mountings. The light pulses come from the source at the bottom of the figure and go to the pump-probe set-up on its left.

1.2.2 Characterization of the mid-infrared pulses

The characterization of the mid-infrared pulses can be performed in two ways. The first one is to measure its spectrum in an interferometer, which allows to determine in a practical and quick way the peak photon energy and the spectral width of the pulses. The second is to perform electro-optic sampling of the pulse. Electro-optic sampling is a technique which allows to directly measure the oscillating electric field in a light pulse with femtosecond resolution. It therefore allows to measure, in addition to the spectral information, the pulse duration, the carrier-envelope phase, and the possible chirp of the electric field. In comparison to interferometry, to perform electro-optic sampling is slower and involves more steps. Therefore, it is ideal to have both instruments at hand.

Spectral tunability The measurement of the interferogram of the pulses is sufficient to characterize the spectral tunability of the set-up. To this purpose, we built a Michelson-type interferometer. The photodiode used is a Hamamatsu P5274-01 mercury cadmium telluride photoconductive detector, which has to be cooled to 77 K with liquid nitrogen. The spectral response of the detector is shown in figure 1.8 [6]. As can be seen, the peak sensitivity is ~ 0.08 eV and extends over our range of interest.

A typical interferogram is displayed in figure 1.9, which shows the intensity on the detector vs the path difference in the interferometer. Figure 1.10 shows instead three sample power spectra of pulses centred at different photon energies.

The tunability of the photon energy extends from ~ 0.2 eV down to ~ 0.07 eV. However, the efficiency of the generation of the mid-infrared photons at 0.07 eV is one tenth of the efficiency at 0.11 eV, as can be seen in figure 1.11. There, the circles are the number of photons $(\frac{\text{pulse energy}}{\text{photon energy}})$ as a function of the photon energy, with roughly the same pulse energy of the near-infrared pump and seed pulses. Below 0.1 eV the number of produced photons drops. This happens because the absorption of GaSe starts growing below such photon energy.

Electro-optic sampling In addition to the interferometric characterization of the pulses, one can perform electro-optic sampling of their electric field. Electro-optic sampling is a technique that exploits the so-called Pockels' effect, which is due to the second-order nonlinear polarization. When an intense, possibly oscillating, electric field travels through a birefringent medium with a non-vanishing $\chi^{(2)}$, the refractive index of the medium changes, together with

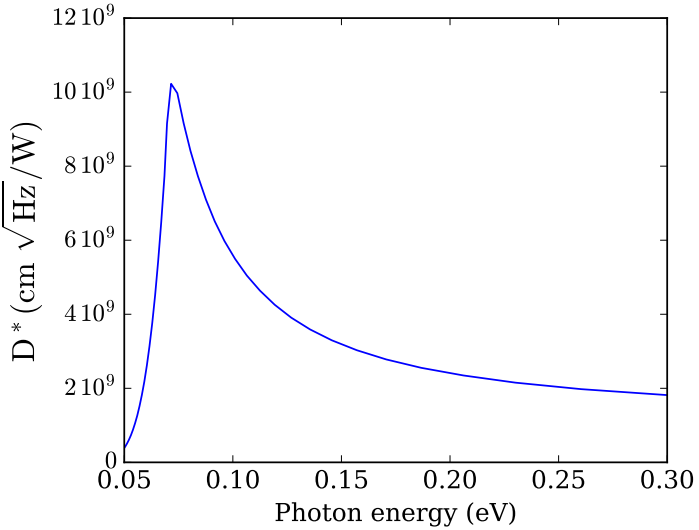

Figure 1.8: Spectral response of the Hamamatsu P5274-01 mercury cadmium telluride photoconductive detector. Adapted from reference [6].

its birefringence (i.e. the difference between the refractive indices of the two optically different axes). It can be shown [7] that the induced variation δn of the refractive index caused via a second-order nonlinear effect is proportional to the electric field. Such an effect can be detected measuring the variation of the polarization ΔP of light on timescales shorter than the variation of the electric field $E(t)$. Since for small δn the variation of the polarization is proportional to δn, and $\delta n \propto E(t)$, ΔP constitutes a measurement of the intense electric field present in the medium.

In particular, to efficiently measure an $E(t)$ oscillating at frequencies in the mid-infrared spectral range, one should employ light pulses shorter than $\sim 1/2$ of the period of the oscillation, i.e. ~ 15 fs for 0.15 eV ($\lambda_{\text{vac}} = 8$ μm).

To perform electro-optic sampling of our mid-infrared pulses, we used near-infrared pulses lasting 15 fs, produced by an argon-filled, 1 m-long, quartz hollow fiber (Kaleidoscope by Femtolaser) and compressed by a set of chirped mirrors. As nonlinear medium for the detection we used a thin ZnTe slab.

On the practical side, the measurement proceeds as a pump-probe experiment in the transmission geometry, in which the variation of the polarization of the near-infrared probe pulses is measured. By changing the delay between

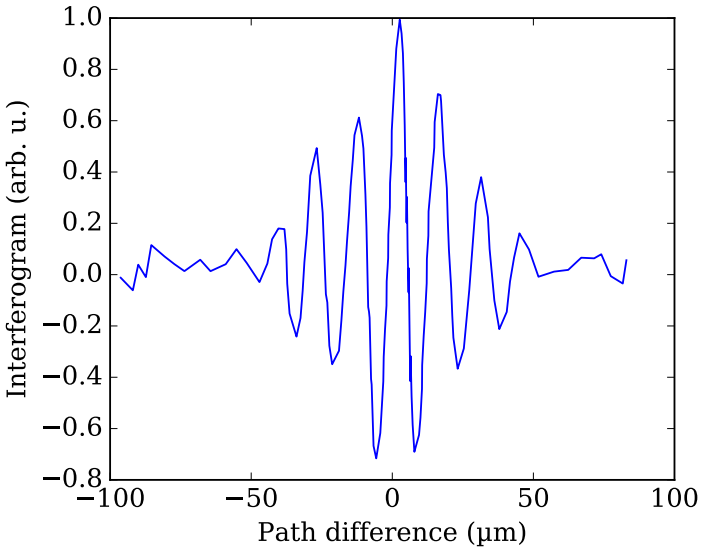

Figure 1.9: Typical interferogram of the mid-infrared pulses. The photon energy in this case is 0.09 eV (λ 14 μm).

the mid-infrared pump pulse and the near-infrared probe pulse, the latter will experience different δn produced by the mid-infrared electric field at different phases of the oscillation.

Figure 1.12a shows a typical sampling of the mid-infrared electric field. This is an actual measurement of $E(t)$ and not an interferometric measurement. The pulse duration can therefore be read off from such data. Moreover, a wavelet analysis allows to extract also information about the chirp of the pulse. Figure 1.12b shows the time-dependent spectral content of the pulse in panel a, obtained via a wavelet analysis. As shown, the back of the pulse contains slightly lower photon energies than the rest of the pulse.

When performing electro-optic sampling with mid-infrared pulses, attention should be paid to the amplitude of the electric field to be measured. As pointed out by Sell et al. [8], very large fields will produce higher-order nonlinearities which will eventually mask the measurement of the field via the Pockels' effect.

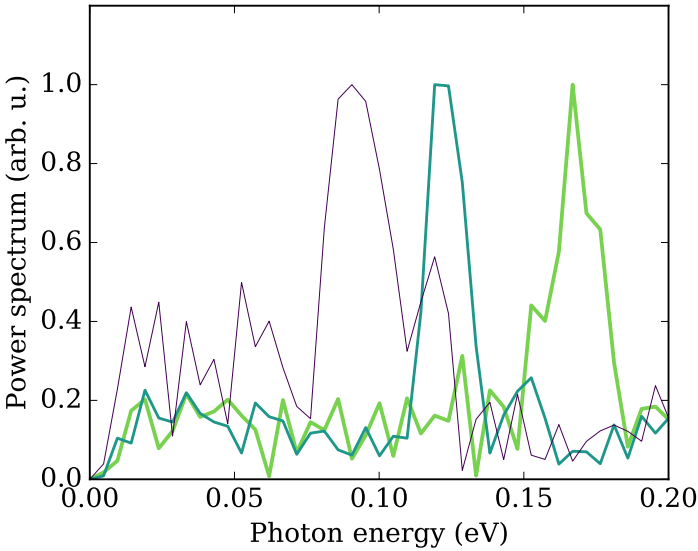

Figure 1.10: Three sample spectra of the mid-infrared pulses, centred at photon energies of 0.09, 0.13, 0.17 eV.

Carrier-envelope phase stability The very possibility to perform electro-optic sampling of the mid-infrared pulses relies on the stability of their carrier-envelope phase. Since the measurement involves more than one pulse, if the phase were random from pulse to pulse, no time-dependent variation of the polarization of the near-infrared pulse would be measured.

However, an electro-optic sampling lasts only a few minutes and is itself a proof of the carrier-envelope phase stability only over such short time span. While the phase of the mid-infrared pulse is in principle passively stabilized, the phase difference between the pump and the seed pulses used for the difference frequency generation may vary on long timescales. Since it depends on the relative path difference between the pulses, it can in fact be affected by a thermal expansion or contraction of the optical table. Previous works on similar set-ups [9] reported a shift of the phase of the mid-infrared pulses of π in 60 minutes. To achieve longer phase stability, the authors had to actively correct the path difference between the pulses used for the generation.

To test the phase stability performance of our set-up, we continuously performed electro-optic sampling for several hours. The best results have

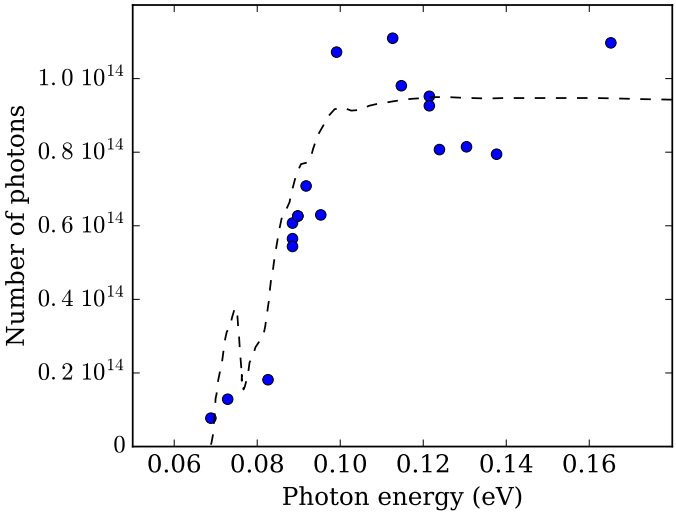

Figure 1.11: Number of photons contained in one mid-infrared pulse, as a function of the photon energy (blue circles). The dashed line is the transmittivity of GaSe (arb. u.). As can be seen, the efficiency of the generation is low for low photon energies, in corrspondence of the spectral region in which GaSe crystals absorb.

been obtained when no human was in the laboratory. Figure 1.13 shows the electro-optic sampling as a function of the "pump-probe" delay between the mid-infrared pulse and the near-infrared probe, and actual time. As can be seen, in our case a shift of π occurs in 7 hours.

The better phase stability with respect to reference [9] can probably be attributed to the geometry of the set-up. In fact, the whole set-up for the generation of the mid-infrared pulses (including the two optical parametric amplifiers) is built on a separate optical board, and the paths of the pulses that finally become the pump and seed pulses have roughly equal projections on the two axes of the board. A thermal expansion or contraction of the board therefore causes an almost equal variation of the optical paths of the two near-infrared pulses, giving a good phase stability of the mid-infrared pulses.

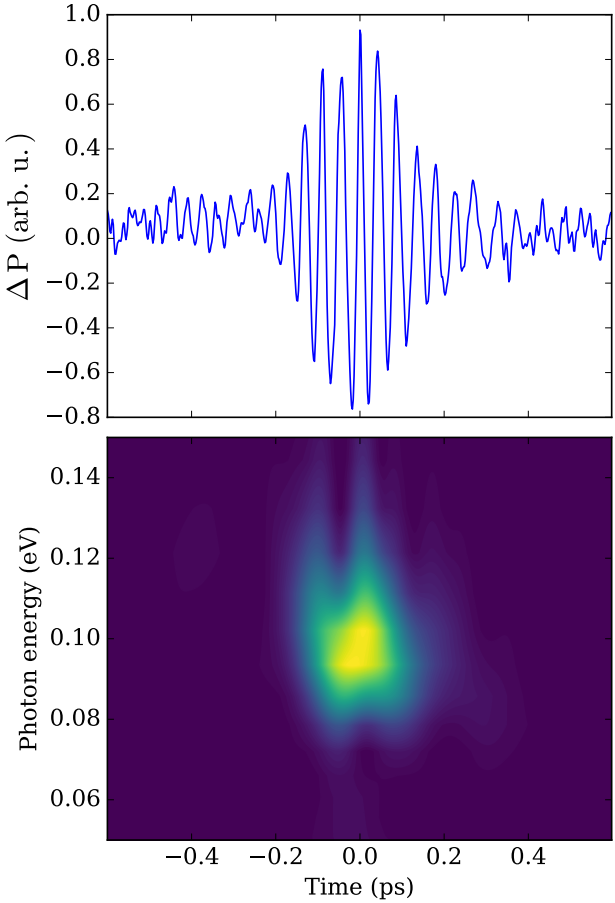

Figure 1.12: **a)** Typical electro-optic sampling obtained for a mid-infrared pulse. The photon energy is 0.095 eV ($\lambda = 13$ μm, period of the oscillation 44 fs). **b)** Time-dependent spectral content of the electric field shown in panel a, obtained via a wavelet analysis.

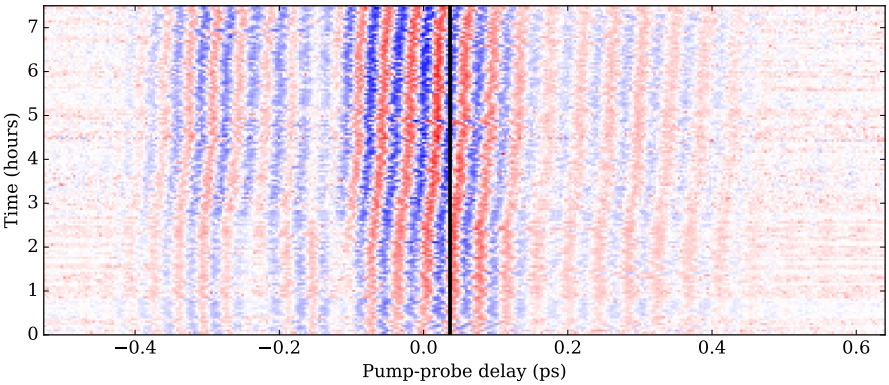

Figure 1.13: Continuous acquisition of the electro-optic sampling over 7 hours, as a function of the pump-probe delay and actual time. The vertical line serves as a reference to compare the carrier-envelope phase as a function of time.

1.2.3 Commercial solution: characterization

We have used the home-built set-up described above for the experiment on copper germanate $CuGeO_3$ discussed in section 1.3 and for the preliminary measurement for the pump-probe experiments on $Bi_2Sr_2Ca_{0.92}Y_{0.08}Cu_2O_8$, which will be discussed in chapter 2. Eventually, an equivalent commercial solution (Orpheus TWIN by Light Conversion) has become available. This source is based on the Light Conversion Pharos laser, producing 400 μJ pulses with 1.2 eV photon energy (λ_{vac} = 1028 nm) at a repetition rate of 50 kHz.

The characterization we performed of the mid-infrared pulses (produced by difference frequency generation of near-infrared pulses) is shown in figure 1.14. The number of photons produced at 0.15 eV is approximately 1/3 of the value obtained on the home-built set-up, because of the lower initial pulse energy available. Moreover, the threshold below which the efficiency becomes lower is $\sim$ 0.14 eV, a higher value with respect to our set-up. Despite these drawbacks, the commercial solution provides a higher repetition rate (50 vs 1 kHz) and a much better stability. Figure 1.15 shows the duration of the mid-infrared pulses. As shown, it rises markedly below 0.12 eV photon energy.

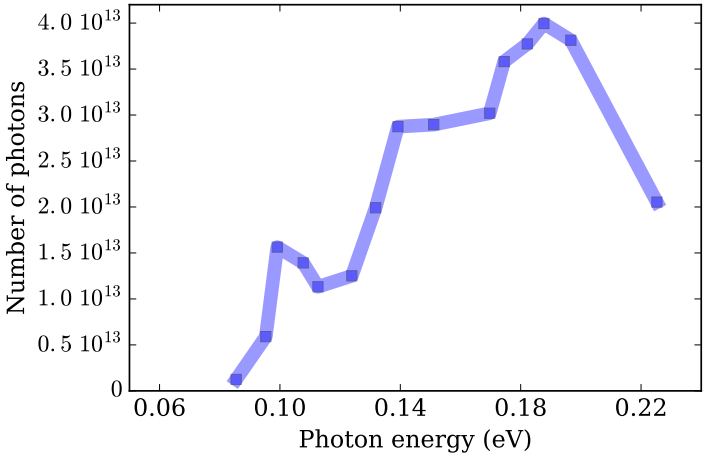

Figure 1.14: Number of photons contained in one mid-infrared pulse, as a function of the photon energy, for the Pharos-based set-up by Light Conversion.

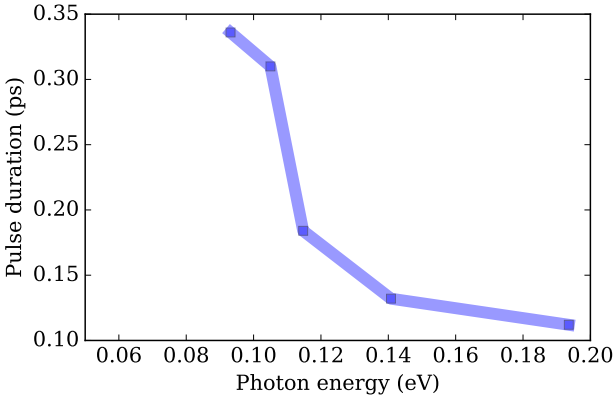

Figure 1.15: Pulse duration as a function of the photon energy, for the Pharos-based set-up by Light Conversion.

1.3 A model experiment: exciting a vibrational mode in $CuGeO_3$

Pulses with photon energies of $\sim$ 1.5 eV usually allow to produce primary excitations via interband transitions. These excitations scatter with other degrees of freedom in the solid (vibrational, magnetic, ...) and decay producing, in the most common case, an effectively thermal state, i.e. a state in which excitations are present in energy levels close to the Fermi energy.

What new kinds of primary excitations do mid-infrared pulses allow to produce? One of them is the direct creation of low-energy excitations, without the intermediate creation of excitations with energies of the order of 1 eV. This consists in more controlled excitations, closer to their thermal analogues, and will be discussed in more detail in chapter 2 in the context of pump-probe experiments on a $Bi_2Sr_2Ca_{0.92}Y_{0.08}Cu_2O_8$ sample.

Another possibility is to resonantly excite vibrational modes. Since the coherence time of a coherent vibration in a solid is "long" with respect to the one of electronic degrees of freedom ($\sim$ 10 ps), such an excitation allows for the creation of out-of-equilibrium states different from trivially thermal ones. As an example, recent works have claimed that superconducting-like states can be photo-induced exciting vibrational modes with mid-infrared pulses [10,11]. In particular, a discussion has started about the possibility of exciting Raman-active modes through their nonlinear coupling to infrared-active dipolar vibra-

tions [12].

1.3.1 Introduction

As a model experiment for our set-up, we performed pump-probe measurements on copper germanate ($CuGeO_3$), a Mott insulator [13], tuning the mid-infrared pump resonantly to a vibrational mode. Its crystal structure at room temperature is shown in figure 1.16 and it consists of chains of copper and germanium atoms, respectively octahedrally and tetrahedrally coordinated by oxygen atoms.

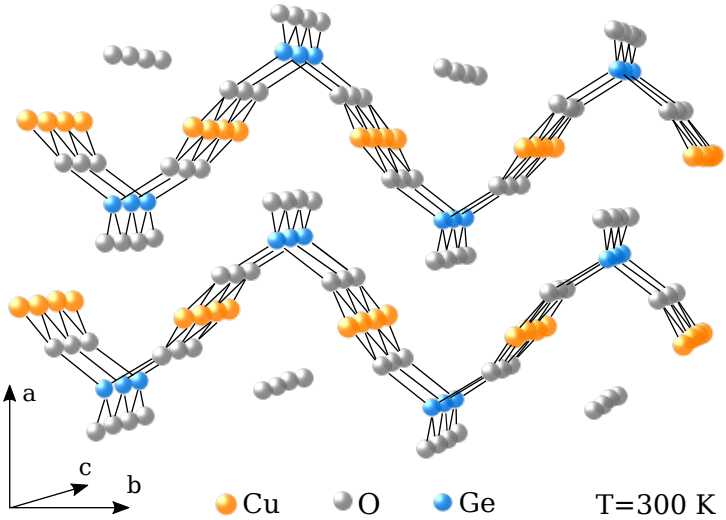

Figure 1.16: Crystal structure of $CuGeO_3$, adapted from reference [14].

$CuGeO_3$ is a good candidate to study the dynamics in systems with copper-oxygen octahedra, because the optical band arising from the d-d transitions on copper has an energy ~ 1.8 eV and is well separated from the charge-transfer edge (~ 3 eV). This can be seen in figure 1.17, which shows the real part of the optical conductivity of $CuGeO_3$ in the near-infrared and visible spectral range. Because of such a situation, the various degrees of freedom can, therefore, be directly studied without the need to separate their dynamics.

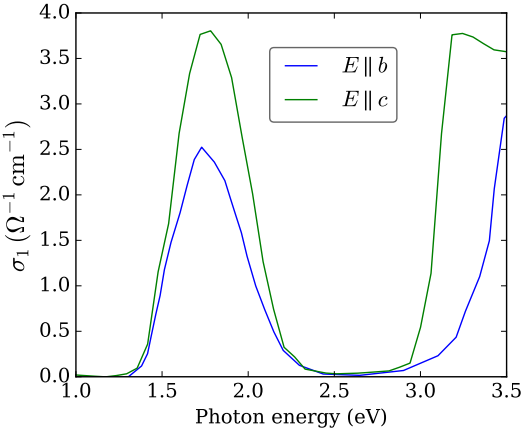

Figure 1.17: Optical conductivity of $CuGeO_3$ as a function of the photon energy, adapted from reference [14], with the light polarization parallel to the b and c axes as defined in figure 1.16 (blue and green, respectively).

The splitting between the d orbitals of the copper atoms is produced by their coordination by oxygen. It will therefore be affected by a change of the position of the oxygen atoms, which can occur if a vibrational mode is excited.

The mid- and far-infrared optical conductivity of $CuGeO_3$ is characterized by sharp vibrational resonances (see figure 1.18). Out of these, two are in the tunability range of our mid-infrared pulses. One is centred at a photon energy of 0.095 eV, while the other at the slightly lower energy of 0.087 eV. These two vibrational modes differ in polarization. The low-energy one is polarized along the direction of the copper and germanium chains (c axis of the crystal) [14] and corresponds to a vibration of the germanium and oxygen atoms alone [15], as shown in figure 1.19a. The high-energy mode is, instead, polarized on the b axis, i.e. orthogonally to the chains [14], and inolves a motion of the oxygen atoms relatively to the copper atoms (figure 1.19b). Its excitation will therefore perturb the splitting between the Cu d orbitals.

1.3.2 Experiment and results

We performed pump-probe experiments on a cleaved, 110 μm-thick $CuGeO_3$ in the transmission geometry at room temperature, with the sample exposing the *bc* plane. We measured the relative variation $\frac{\Delta T}{T}$ of the transmittivity of

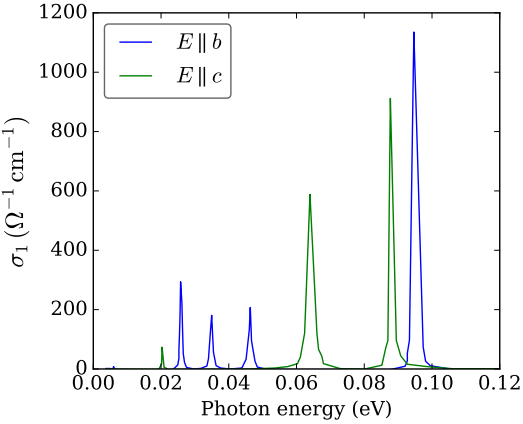

Figure 1.18: Optical conductivity of $CuGeO_3$ as a function of the photon energy, adapted from [14], with the light polarization parallel to the b and c axes (blue and green, respectively).

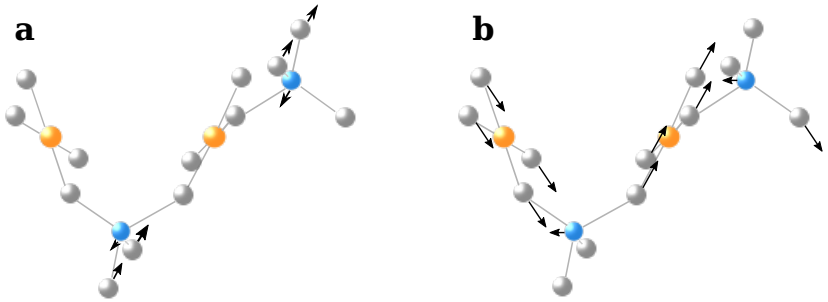

Figure 1.19: Dipolar vibrational modes with frequency in the photon energy tunability range of our setup for the generation of mid-infrared light pulses. **a** Normal mode involving only germanium and oxygen atoms. **b** Normal mode excited by the pump pulses, involving all the atomic species. Adapted from reference [15].

the sample and the variation of its birefringence. The pump pulses were tuned at different photon energies and polarized along the b axis of the crystal. The probe pulses were produced in a hollow fiber and temporally compressed to 15

fs with a set of chirped mirrors. Their spectrum extended from 1.45 to 1.75 eV. For the measurement of $\frac{\Delta T}{T}$, the probe pulses were polarized parallel to the pump pulses. The variation of the birefringence of the sample was measured, instead, as the variation of the polarization of the probe with an incoming polarization at 45° with respect to the b and c axes.

Figure 1.20 shows the results obtained with the pump pulses tuned resonantly to the copper-oxygen vibrational mode of figure 1.19b, at a photon energy of 0.099 eV. It can be easily recognized that the variation of the birefringence ($\sim \Delta P$) and of the transmittivity ($\frac{\Delta T}{T}$) display different dynamics. The relaxation of $\frac{\Delta T}{T}$ is, in fact, slower than the one of the birefringence.

The two responses can be well fitted by a single exponential decay (see section 2.3.1 for a discussion about the deconvolution of the pump pulse duration). The result of the fit gives a timescale τ for the decay of 0.15 ps and 0.22 ps for the birefringence and the transmittivity, respectively.

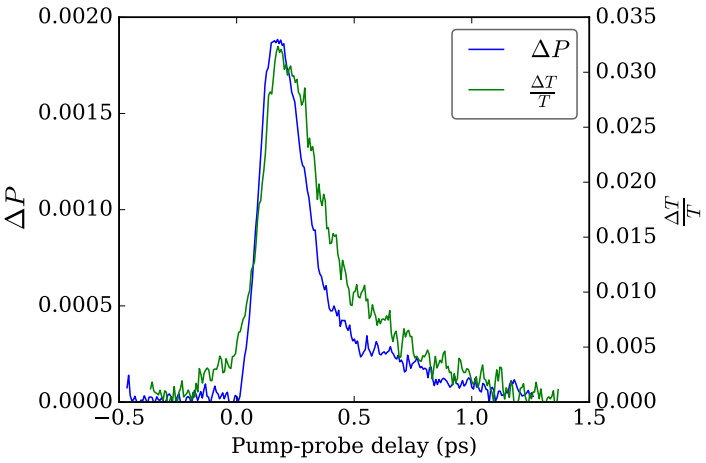

Figure 1.20: Blue (left y-axis): Variation of the polarization of the probe pulses, as a function of pump-probe delay. Green (right y-axis): Relative variation of the transmission of the $CuGeO_3$ sample.

The difference in timescales means that the observed variation of the birefringence is not of thermal origin, since it does not decay together with the out-of-equilibrium population ($\sim \frac{\Delta T}{T}$). It is instead due to an anisotropy of the excitations in the sample. It is therefore reasonable that such kind of change in the birefringence decays faster than the (isotropic) population since, if the

scattering channel is not too selective, an anisotropic excitation will persist less than an isotropic one.

A further aspect to be noticed it that neither of the two signals displays a coherent oscillation at the frequency of the resonantly excited vibrational mode. A pump-probe experiment in which the intensity of the probe pulse is measured (e.g. $\frac{\Delta T}{T}$) can be described as a third-order nonlinear process, i.e. as a four-wave mixing. At such order, because of parity, the measurement of the effects of a *dipolar* (infrared-active) vibration is not permitted. Since the system is an insulator, and no electronic excitation exists below the pump photon energy, the signal is therefore given by a population generated in a *Raman*-active vibration via a coupling between the latter and the original dipolar mode. The fact that, differently from the case of electro-optic sampling, also the variation of the polarization of the probe field does not display any oscillation, tells us that, also in this case, the signal is due to $\chi^{(3)}$ and not to $\chi^{(2)}$.

The experiment can be repeated with different pump photon energies. Figure 1.21 shows the variation of the polarization of the probe pulse, i.e. the variation of the birefringence of the sample, obtained with different pump photon energies. As can be seen, for pump photon energies which are not resonant to the vibrational mode there is no signal, or it is present but small (for a photon energy of 0.118 eV).

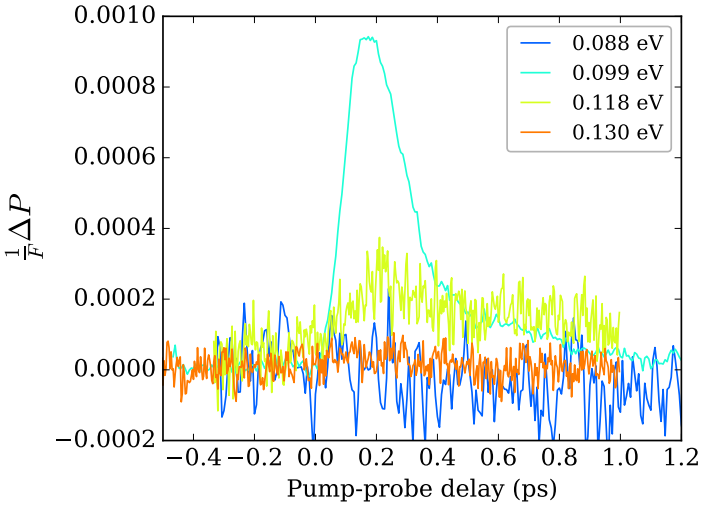

Figure 1.21: Variation of the polarization of the probe pulses as a function of pump-probe delay and for different pump photon energies.

Bibliography

[1] D.J. Griffiths, "Introduction to electrodynamics (3rd ed.)", Prentice Hall (1999).

[2] R.W. Boyd, "Nonlinear Optics (3rd ed.)", Academic Press (2008).

[3] G. Cerullo, and S. De Silvestri, "Ultrafast optical parametric amplifiers", Rev. Scientific Instruments 74, 1 (2003).

[4] A. Baltuška, T. Fuji, and T. Kobayashi, "Controlling the carrier-envelope phase of ultrashort light pulses with optical parametric amplifiers", Phys. Rev. Lett. **88** 13, 133901 (2002).

[5] M. Bradler, P. Baum, and E. Riedle, "Femtosecond continuum generation in bulk laser host materials with sub-μJ pump pulses", Appl. Phys. B 97, 561–574 (2009).

[6] Hamamatsu Photonics KK, http://www.hamamatsu.com/resources/pdf/ssd/infrared_kird9001e.pdf .

[7] X.C. Zhang and J. Xu, "Introduction to THz wave photonics", Springer (2009).

[8] A. Sell, A. Leitenstorfer, and R. Huber, "Phase-locked generation and field-resolved detection of widely tunable terahertz pulses with amplitudes exceeding 100 MV/cm", Opt. Lett. **33** 23, 2767 (2008).

[9] C. Manzoni, M.Först, H. Ehrke, and A. Cavalleri, "Single-shot detection and direct control of carrier phase drift of midinfrared pulses", Opt. Lett. **35** 5, 757 (2010).

[10] D. Fausti, R.I. Tobey, N. Dean, S. Kaiser, A. Dienst, M.C. Hoffmann, S. Pyon, T. Takayama, H. Takagi, and A. Cavalleri, "Light-induced superconductivity in a stripe-ordered cuprate", Science **331** 6014, 189–191 (2011).

[11] M. Mitrano, A. Cantaluppi, D. Nicoletti, S. Kaiser, A. Perucchi, S. Lupi, P. Di Pietro, D. Pontiroli, M. Riccò, S.R. Clark, D. Jaksch, and A. Cavalleri, "Possible light-induced superconductivity in K_3C_{60} at high temperature", Nature **530**, 461–464 (2016).

[12] R. Mankowsky, A. Subedi, M. Först, S.O. Mariager, M. Chollet, H.T. Lemke, J.S. Robinson, J.M. Glownia, M.P. Minitti, A. Frano, M. Fechner, N.A. Spaldin, T. Loew, B. Keimer, A. Georges, and A. Cavalleri, "Nonlinear lattice dynamics as a basis for enhanced superconductivity in $YBa_2Cu_3O_{6.5}$", Nature **516**, 71–73 (2014).

[13] L.F. Mattheiss, "Band picture of the spin-Peierls transition in the spin-1/2 linear-chain cuprate $GeCuO_3$", Phys. Rev. B 49, 14050 (1994).

[14] A. Damascelli, D. van der Marel, G. Dhalenne, and A. Revcolevschi, "Optical spectroscopy of pure and doped $CuGeO_3$", Phys. Rev. B **61** 18, 12063 (2000).

[15] Z.V. Popović, S.D. Dević, V.N. Popov, G. Dhalenne, and A. Revcolevschi, "Phonons in $CuGeO_3$ studied using polarized far-infrared and Raman-scattering spectroscopies", Phys. Rev. B **52** 6, 4185 (1995).

Chapter 2

Pump-probe experiments on $Bi_2Sr_2Ca_{0.92}Y_{0.08}Cu_2O_8$

In section 1.3 I discussed the pump-probe experiments we performed on $CuGeO_3$ with mid-infrared pump pulses. In that case, the pump photon energy was tuned to resonantly excite a vibrational mode. In this chapter I am going to present the results we obtained on an optimally yttrium doped $Bi_2Sr_2CaCu_2O_8$. Here, the mid-infrared excitations were not tuned to vibrational resonances and produce low-energy electronic excitations.

2.1 Introduction

The role played by phonon modes and spin excitation in cuprates is at the core of the debate regarding the nature of the superconducting phase in cuprates [1–5]. While electron-phonon coupling alone can hardly account for the high critical temperature observed, an ample set of evidences has highlighted the role played by spin fluctuations as an important ingredient to understand superconductivity in cuprates.

In the proximity to the antiferromagnetic phase, the magnetic excitation spectrum in the cuprates is well decribed by local spin excitation and superexchange interaction [6]. On the other hand, upon increasing the amount of free carries towards optimal doping, features of collective spin excitation emerging from correlated itinerant electrons are observed in the magnetic spectrum [7,8]. More specifically, the dispersion and width of magnetic excitations observed via resonant inelastic x-ray scattering and neutron scattering reveal an anoma-

lous softening in the dispersion along the nodal (π, π) direction for a q vector of 0.25 [9].

Pump-probe experiments have been widely used to study the dynamical relaxation in high-temperature superconductors. The most commonly used schemes are based on high photon energy pump pulses ($h\nu \gtrsim 1$ eV) serving mainly as a sudden photo-injection of an excess of high-energy electronic excitations. On the one hand, small-density photoexcitations have been used to study in great detail the relaxation of quasiparticles and, through that, the coupling between electronic and different degrees of freedom of both magnetic and vibrational nature [10–13]. On the other hand, the strong perturbation limit, eventually leading to photo-induced phase transitions, has been used to study the dynamical response of the superconducting order parameters [14].

In this chapter, I will present results we obtained in pump-probe experiments with mid-infrared pump pulses on the optimally doped Y-Bi2212, i.e. $Bi_2Sr_2Ca_{0.92}Y_{0.08}Cu_2O_8$, in the strange metal ($T > T^* \sim 130$ K), pseudogap ($T^* > T > T_c = 95$ K) and superconducting phases ($T < T_c$).

At room temperature, our results reveal a strongly k-dependent coupling between electrons and low-energy excitations. Electronic excitations which are either fully symmetric or in the "antinodal" directions (i.e. the directions that become the antinodal directions in the superconducting phase) are mainly coupled to magnetic excitations, while in the "nodal" directions (i.e. the ones becoming the nodal directions at low temperatures) they are coupled to both magnetic excitations and low-energy vibrational modes. The dependence on the pump photon energy of the relaxation times in the fully symmetric case and in the antinodal directions allows to identify the energy of the magnetic excitations. Moreover, while the fully symmetric and antinodal responses are linear with the pump fluence over the whole measured range, the nodal response displays a nonlinear behaviour above a threshold fluence. This happens in correspondence to the melting of a superstructural lattice modulation and the onset of the vibration of a bending mode. The emerging scenario suggests that electrons in the nodal direction are coupuled to magnetic excitations arising from itinerant electrons which are strongly influenced by the local distortion of the Cu-O-Cu angle.

Also in the low-temperature phases the response of the system to the excitation is strongly k-dependent. Our data show that in the pseudogap phase, despite the fact that the variation of the reflectivity displays a nonlinear behaviour as a function of fluence, the response along the nodal direction is linear throughout the measured fluence range. Moreover, in the superconducting phase we have been able to separately measure the reponse associated to the pseudogap excitations and to another kind of excitations along different

directions.

2.2 Experiment

The pump pulses used in our experiments had photon energies ranging from 100 to 260 meV. The pump pulses were produced with a scheme of the type discussed in chapter II.1, and their carrier envelope phase was, therefore, stable. The probe pulses instead were in the near-infrared spectral range, with photon energies between 1.35 and 1.85 eV, and had a duration of approximately 20 fs. They were produced using a non-collinear optical parametric amplifier and were temporally compressed correcting their linear chirp. The SQUID characterization of the sample yielded a critical temperature $T_c = 95$ K for the transition to the superconducting state.

The measurements were performed on the probe pulses reflected from the surface exposing the ab-plane. The sample was kept at different temperatures spanning the interval from 77 to 296 K. The measurements at room temperature were performed with the sample in air. At lower temperatures, for the experiment with the pump pulse at 140 meV photon energy, a 60 μm-thick polypropilene cryostat window was used, while for the experiment with higher pump photon energies, a 4 mm CaF_2 window was used. The latter, in contrast with the former, preserves the polarization of the probe pulse.

In a pump-probe experiment the signal is produced by the dynamics of the out-of-equilibrium state, which will be the sum of contributions having the different symmetries allowed by the point group of the system. In the case of Bi2212, the point group can be approximated as the D_{4h} group. In the (a, b)-plane the tensors for the Raman modes are

$$\overset{A_{1g}}{\begin{pmatrix} a & 0 \\ 0 & a \end{pmatrix}}, \quad \overset{B_{1g}}{\begin{pmatrix} c & 0 \\ 0 & -c \end{pmatrix}}, \quad \overset{B_{2g}}{\begin{pmatrix} 0 & d \\ d & 0 \end{pmatrix}}. \tag{2.1}$$

The upper panels in figure 2.1 show how states of the A_g, B_{1g} and B_{2g} symmetries are distributed in the Brillouin zone.

The third-order susceptibility χ^3_{ijkl} can be written as

$$\chi^3_{ijkl} = A^{ij}_{1g} A^{kl}_{1g} + B^{ij}_{1g} B^{kl}_{1g} + B^{ij}_{2g} B^{kl}_{2g}. \tag{2.2}$$

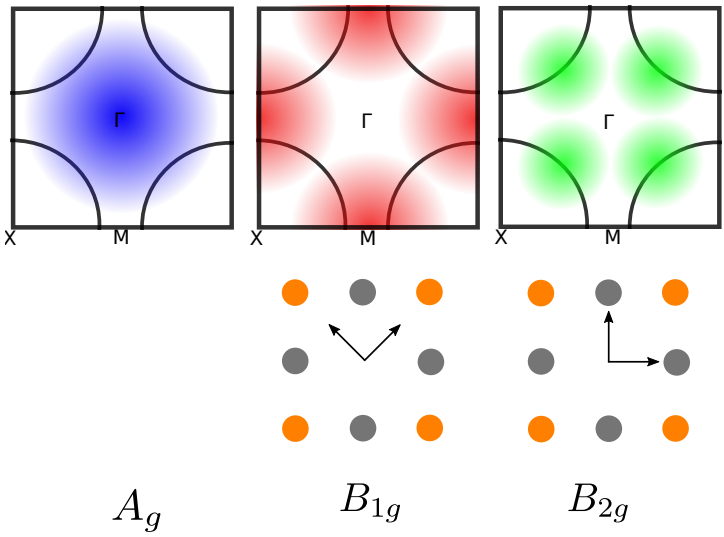

Figure 2.1: The upper panels show a sketched weighting of the Raman scattering transitions for polarization geometries transforming as A_g, B_{1g} and B_{2g} in a D_{4h} structure. The underlying black lines show a typical Fermi surface for optimally doped cuprates. The lower panels show the polarizations of the incoming light and of the emitted field with respect to the crystalline structure. Adapted from reference [15].

With i, j, k, l in the (x, y) plane (i.e. i, j, k, l =1,2), the tensor becomes

$$\chi^3_{ijkl} = \begin{pmatrix} \begin{pmatrix} a^2+c^2 & 0 \\ 0 & a^2-c^2 \end{pmatrix} & \begin{pmatrix} 0 & d^2 \\ d^2 & 0 \end{pmatrix} \\ \begin{pmatrix} 0 & d^2 \\ d^2 & 0 \end{pmatrix} & \begin{pmatrix} a^2-c^2 & 0 \\ 0 & a^2+c^2 \end{pmatrix} \end{pmatrix}. \tag{2.3}$$

From this, one can derive that the variation of the reflectivity will be the sum of an A_g term, independent of the probe pulse polarization, and B_{1g} and B_{2g} terms, which are instead dependent on the polarization of the probe [16]

$$\Delta R(\theta) \propto \Delta R_{A_g} + \Delta R_{\mathrm{B}_{1g}} \cos(2\theta) + \Delta R_{B_{2g}} \sin(2\theta), \tag{2.4}$$

where θ is the probe pulse polarization angle with respect to the crystalline axes. The above equation suggests to measure the B_{1g} and B_{2g} signals by

measuring $\frac{\Delta R}{R}$ at different probe pulse polarization angles θ. However, if the B_{1g} and B_{2g} signals are very small compared to the A_g signal, they can be masked by the global noise. One can measure such signals considering the way Raman measurements are performed at equilibrium, i.e. with different combinations of the polarization of the incoming light and the one along which the scattered intensity is measured. We use, here, the convention that the x and y directions point along the Cu-O bonds, while x' and y' are rotated by 45° with respect to the x and y vectors. In the D_{4h} point group [15] the correspondence between the geometry of the measurement (in the Porto notation) and the signals in the various symmetries is described in table 2.1. In such notation, $z(xy)\bar{z}$ means that the incoming light is travelling along z

Geometry	Signal
$z(xx)\bar{z}, z(yy)\bar{z}$	$R_{A_g} + R_{B_{1g}}$
$z(x'x')\bar{z}$	$R_{A_g} + R_{B_{2g}}$
$z(x'y'))\bar{z}$	$R_{B_{1g}}$
$z(x,y)\bar{z}$	$R_{B_{2g}}$

Table 2.1: Correspondence between the scattering geometries (in the Porto notation) and the accessible signals. Adapted from reference [15].

and is polarized along x, while the outgoing (measured) light is propagating along $\bar{z} \equiv -z$ and is polarized along y. In the context of nonlinear spectroscopies, the light which is measured along the polarization orthogonal to the incoming probe light is referred to as "emitted field". To perform this kind of experiments, a polarizer should be positioned in front of the photodiode to select the correct polarization. The measurement of the out-of-equilibrium B_{1g} and B_{2g} signals can, therefore, be performed in such geometries, with the addition of the perturbing pump pulses. To maximise the B_i signal strength, the polarization of the pump pulse should be at 45° from the polarizations of the incoming probe and the outgoing emitted field. For example, to efficiently measure the B_{1g} signal, i.e. with the $z(x'y')\bar{z}$ geometry, the pump should be polarized either along x or along y.

2.3 Results and discussion

2.3.1 Room temperature

I will start discussing the standard variation of the reflectivity as it is usually measured in pump-probe experiments, i.e. with no reference to the symmetry

of the system. I will move to the finer analysis later.

The relative variation of the reflectivity $\frac{\Delta R}{R}$ scales linearly with the fluence F up to the highest fluence used (3.5 mJ cm^{-2}). Figure 2.2 shows $\frac{\Delta R}{R}(t_p)$, at 1.63 eV and with pump photons at 140 meV, normalized with the fluence F, and shows that all the curves fall on top of each other. One can see that $\frac{\Delta R}{R}$ is linear with fluence also from the inset of figure 2.2, which shows the peak variation of the reflectivity as a function of the fluence. Moreover, the shape of $\frac{\Delta R}{R}$ shows a sudden increase at the arrival of the pump pulse, a decay, and finally a thermal plateau. Such a dynamics, together with the linearity with the fluence, is the typical behaviour associated to the creation of excitations, whose number scales linearly with the number of photons in the pump pulse, and their subsequent relaxation to a new effectively (warmer) thermal state.

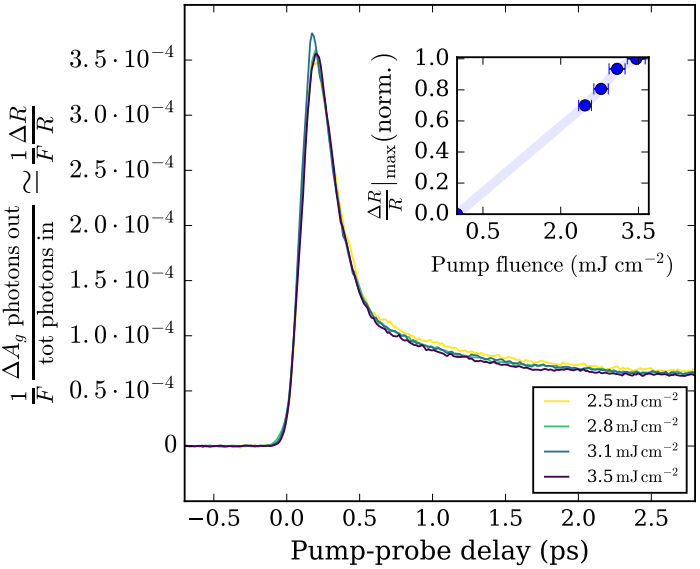

Figure 2.2: Room temperature relative variation of the reflectivity $\frac{\Delta R}{R}(t)$ (A_g signals normalized with the total intensity of the probe pulses) divided by the pump fluences, for 200 meV pump pulses and 1.6 eV probe pulses. **inset)** Peak value of $\frac{\Delta R}{R}(t)$ as a function of the pump fluence.

If the polarization of the probe pulses is rotated the signal appears as isotropic. From equation (2.4) we can therefore conclude that the measured

signal is of A_g symmetry. However, such procedure can only set the upper limit for the magnitude of a hypothetical anisotropy to the total noise level and does not exclude the existence of B_{1g} and B_{2g} signals. Small B signals can be detected using the polarization-selective measurements described in the previous section. Figures 2.3a, b, and c show the measurements performed in the A_g, B_{1g}, and B_{2g} geometries, respectively, for different pump photon energies. Focussing for the moment on the differences between different symmetries, as can be seen, the B_{1g} and B_{2g} signals are qualitatively different from the A_g signal ($\simeq$ almost isotropic $\frac{\Delta R}{R}$). The reason why they have not been detected as an anisotropy of $\frac{\Delta \mathrm{R}}{\mathrm{R}}$ is that their amplitude is two orders of magnitude smaller than the one of the A_g signal (as shown in the following figures) and they were below the noise level. When the measurement is performed in the $z(xy)\bar{z}$ or $z(x'y')\bar{z}$ geometries, the polarizer in front of the photodiode extinguishes both the A_g signal and the major part of the noise, which is polarized along the probe polarization. In these configurations the B signals are easier to detect.

An additional difference between the A_g and B signals is their sign. Both B signals are of opposite sign with respect to the A_g one. I will now discuss in more details all three kind of signals. To start, I will consider the A_g and B_{1g} ones.

$\mathbf{A_g}$ and $\mathbf{B_{1g}}$ signals Apart from their amplitude and sign, the A_g and B_{1g} signals display very similar qualitative features. As can be seen in figure 2.4 and its inset for a pump photon energy of 200 meV, also the B_{1g} signal scales linearly with the fluence, and it also displays the typical dynamics of the relaxation of excitations produced by the pump pulse.

The decay of both the A_g and B_{1g} excitations cannot be represented by a single decaying exponential. This is the case when the signal is coming from the relaxation of different degrees of freedom. In this specific case, the signal can be well fitted with the sum of two exponentials, with characteristic timescales τ_1 and τ_2, convoluted with a Gaussian given by the finite duration of the pump and probe pulses. Before discussing the fit of the data to extract τ_1 and τ_2, one should qualitatively observe that, as a function of the pump photon energy there are two variations in the signals (figures 2.3a and b). The first one is a variation of the rise time at pump-probe delay zero. This is caused by different pulse durations at different photon energies. The second is a variation of the relaxation times. The change noticed upon visual inspection is due to two factors, i.e. the longer pump pulses and a slower dynamics. These two contributions can be deconvoluted appropriately with a fit.

To perform such a fit, one could use a target function in which the convo-

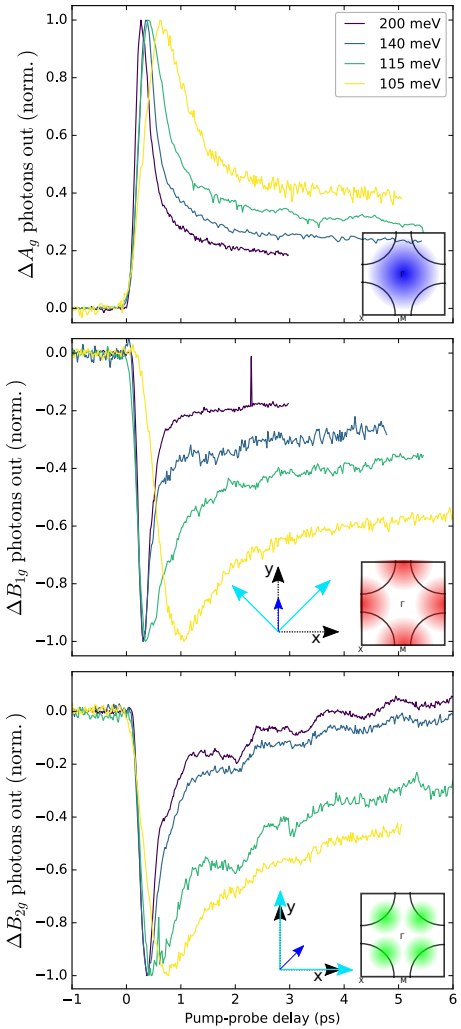

Figure 2.3: **a,b,c)** Normalized A_g, B_{1g} and B_{2g} signals (respectively) for different pump photon energies. The insets show the regions in the Brillouin zone contributing to the signal in the corresponding scattering geometry. In panels **b** and **c** the scattering geometries are depicted, with the black arrows being the Cu-O directions, the light blue arrows the probe and emitted field polarizations and the dark blue one the pump polarization.

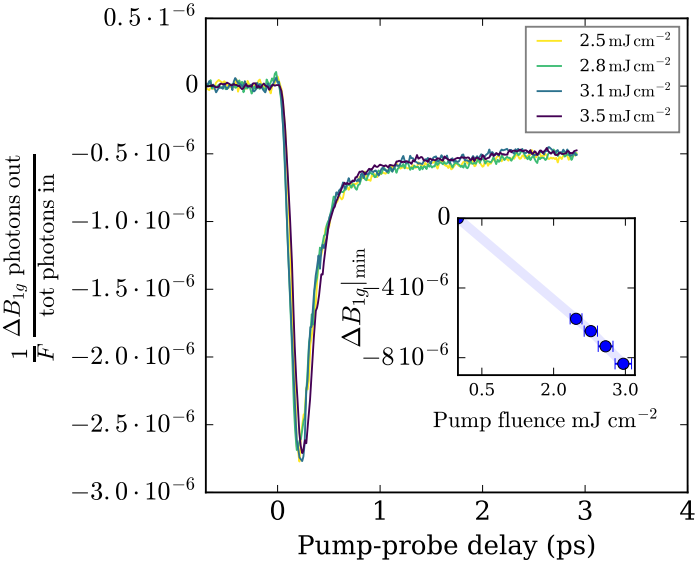

Figure 2.4: Variation of the B_{1g} intensity divided by the total probe intensity and by the fluence. **Inset**: Peak value of the signal as a function of the fluence.

lution between the intrinsic response of the system and the pulse Gaussian is calculated numerically. However, the numerical evaluation of convolutions can be subject to border effects, if the appropriate measures ar not taken. A more stable way of performing the fit is to perform the convolution analytically, and use the analytical result as the target function. To do this, let us first note that the convolution is a linear operation, and therefore we just need to calculate the result for one single exponential. Let us consider a response $f(t)$ of the system of the kind

$$f(t) = \theta(t)e^{-\frac{t}{\tau}}. \tag{2.5}$$

This response is triggered by an excitation of the form

$$g(t) = e^{-\frac{t^2}{2\sigma^2}}. \tag{2.6}$$

At pump-probe delay t_p, the convolution of the two functions is [1]

$$(f * g)(t_p) = \int_{-\infty}^{\infty} ds\, f(s) g(t_p - s) \tag{2.7}$$

$$= \int_{0}^{\infty} ds\, e^{-\frac{s}{\tau}} e^{-\frac{(t_p - s)^2}{2\sigma^2}} \tag{2.8}$$

$$= e^{-\frac{\sigma^2}{2\tau^2}} e^{-\frac{t_p}{\tau}} \int_{0}^{\infty} ds\, e^{-\left(\frac{s}{\sqrt{2}\sigma} - \frac{1}{\sqrt{2}}\left(\frac{t_p}{\sigma} - \frac{\sigma}{\tau}\right)\right)} \tag{2.9}$$

$$= \sigma\sqrt{\frac{\pi}{2}} e^{-\frac{\sigma^2}{2\tau^2}} e^{-\frac{t_p}{\tau}} \left[\mathrm{erf}\left(\frac{t_p}{\sqrt{2}\sigma} - \frac{\sigma}{\sqrt{2}\tau}\right) + 1\right]. \tag{2.10}$$

The free parameters in a fit of the sum of two of the above functions are potentially too many. To reduce their number we can take into consideration that at long pump-probe delays the data can be overlapped quite well, as shown in figure 2.5 for the A_g signal. This fact allows us to conclude that out of the two relaxation timescales, the largest (τ_2) is the same at all pump photon energies. This is a quite reasonable assumption, because a scattering channel which is active at late times will not be sensitive to the energy of the primary excitations created in the system.

The above assumption leads to the useful constraint that, for a given symmetry, all τ_2s be the same, independently of the pump photon energy. This can be imposed performing a simultaneous fit of all the data, implementing $\tau_2 \neq \tau_2(h\nu_{\mathrm{pump}})$ as a constraint via a penalty function (as explained in more detail in section 2.2 of part I).

The fit of the A_g data gives a result of 1.0 ps for $\tau_2[A_g]$. The resulting duration of the pump pulses increases monotonically with decreasing pump photon energy, as qualitativley discussed above and plotted in figure 2.6 (green triangles). The most interesting result is the behaviour of $\tau_1[A_g]$, plotted in

[1] It is usually assumed that the durations of the pump and probe pulses set the temporal resolution of a pump-probe experiment, and that, therefore, relaxations timescales τ shorter than the pulses' (combined) duration σ cannot be resolved. This general statement is not entirely correct. As shown by the analytical result of this simple convolution, the functional form of the dynamics is differnt for *any* pair of pulses' duration σ and timescale τ. What happens is that, as σ increases, the difference between dynamics with different τs becomes smaller. It is then the noise in the measurement that makes the two dynamics indistinguishable. With a sufficiently low noise and with the knowledge of the shape of the pulses, they can always be told one from the other.
I must especially thank Federico Cilento for the discussion about this topic.

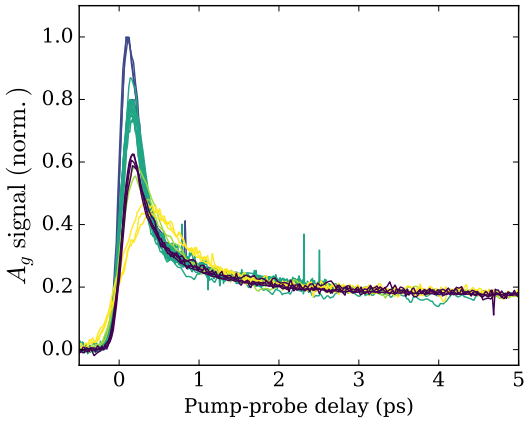

Figure 2.5: A_g signals at various pump photon energies and fluences normalized on their long-time values. The long-time dynamics for all pump photon energies and all fluence overlap.

figure 2.6 (blue circles). At a pump photon energy of 260 meV, $\tau_1 \simeq 170$ fs. Decreasing the photon energy down to 140 meV, $\tau_1[A_g]$ decreases to a value of $\simeq 110fs$, to increase again for lower photon energies.

The fit of the B_{1g} data gives a $\tau_2[B_{1g}] = 3.5$ ps. This means that the B_{1g} excitations take more time to relax back to equilibrium than the A_g excitations. Concerning the small timescale $\tau_1[B_{1g}]$, the behaviour is similar to the A_g one, as shown in figure 2.6 (red circles). Also the B_{1g} signal displays a minimum τ_1 at 140 meV. Below 140 meV, $\tau_1[B_{1g}]$ increases in an even more marked way than $\tau_1[A_g]$.

Another meaningful information that can be extracted from the fit is the ratio $\rho_{1,2}$ between the weights of the quickly and slowly decaying exponentials. As shown by the crosses and the dashed lines in figure 2.6, this ratio is peaked at 140 meV for both the A_g and B_{1g} signals. Below 140 meV, the relative amplitude of the quick relaxations drops almost to zero for the B_{1g} signal, while it reaches a finite value for the A_g signal.

The behaviours of the timescale τ_1 and of the relative amplitude $\rho_{1,2}$ of the quick relaxation hint to the fact that for pump photon energies below ~ 140 meV a scattering channel, through which the primary excitations relax, disappears. This happens because the primary excitations do not have enough energy to relax creating other excitations (or "emitting quasiparticles"). The

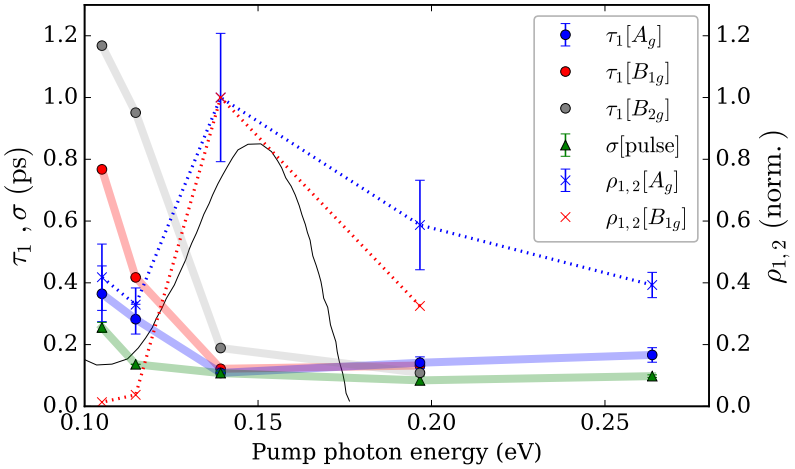

Figure 2.6: Parameters resulting from the fit of the A_g and B_{1g} with double decaying exponentials, as a function of the pump photon energy. The green triangles are the pump pulse duration. The circles are the fast relaxation timescales τ_1 of the A_g (blue) and B_{1g} (red). The $\tau_1[B_{2g}]$ (grey circles) are shown for a qualitative comparison, but their quantitative values have to be taken with some care, as discussed in the text. The crosses are the relative amplitude ρ_{12} of the quickly relaxing exponential for the A_g (blue) and B_{1g} (red) signals. The solid black line is given by equation (2.11), adapted from reference [20].

energy $E = 140$ meV is therefore the energy of the emitted excitation. What kind of excitations provide this scattering channel? The black curve in figure 2.6 is

$$W(\omega) = \frac{1}{2\pi}\frac{d^2}{d\omega^2}\left[\frac{\omega}{\tau(\omega)}\right], \tag{2.11}$$

as taken from reference [20] for Bi2212 at $T = 10$ K, plotted vs a *doubled* energy axis. In the above definition $\tau(\omega)$ is the optical scattering rate

$$\tau(\omega)^{-1} \propto \mathrm{Re}\ \sigma^{-1}(\omega). \tag{2.12}$$

The peak in the function $W(\omega)$ has been associated to magnetic excitation, comparing it with the neutron scattering spectra. Let us suppose that it corresponds to the energy of an excitation which persists also at room temperature

but, differently from low temperatures, is not visible anymore in the optical conductivity. Since the results obtained from our fit match such curve if it is plotted vs a doubled energy axis, the primary excitations produced by the pump pulses decay emitting pairs of such magnetic excitations.

The above result hints to the fact that such magnetic excitations, which are visible in the optical conductivity only at low temperatures, are present also at room temperature and determine the scattering of electronic excitations with energies down to 140 meV.

B_{2g} signal The results of the measurements of the B_{2g} signal are plotted in figure 2.7a for different pump fluences with a pump photon energy of 200 meV and a probe photon energy of 1.6 eV. Analogously to the B_{1g} case, the sign of the B_{2g} signal is opposite to the A_g one, i.e. negative. However, the response of the material in the B_{2g} symmetry is richer than in the B_{1g} one. In addition to the decaying dynamics, oscillations are present. Before discussing them, we point out that in this case, differently from the A_g and B_{1g} signals, the data are not linear with the pump fluence on the whole measured range, both concerning the oscillations and the "incoherent" relaxation, i.e. the decaying exponentials. This can be seen in figure 2.7b (blue points), where the value of the signal at pump-probe delay 200 fs is plotted as a function of the pump fluence. Up to a critical fluence $F^*_{B_{2g}} = 2.1$ mJ cm^{-2}, the response is linear to a good approximation. Above $F^*_{B_{2g}}$, the initial peak in the signal is suppressed by the emergence of a positive peak, which becomes clearly visible for the highest fluence.

A relaxation time $\tau_1[B_{2g}]$ for the dynamics in the B_{2g} symmetry can be extracted with a fit, analogously to the case of the A_g and B_{1g} signals, and is shown in figure 2.6 as the grey triangles. As can be seen, also in this case the relaxation timescale becomes larger as the pump photon energy decreases. While this result fits in the picture drawn for the A_g and B_{1g} signals, the quantitative values extracted should be considered with some care. In fact, because the curve also contain an oscillating term, the fit may be subject to border effects.

Turning to the oscillating part, depending on the pump fluence, one or more oscillations are present. At low fluences, the excitation starts an oscillation at $\nu_1 = 0.86$ THz, which lives up to more than 10 ps. Increasing the fluence the oscillation undergoes "softening", i.e. the frequency changes during the dynamics, starting from a lower value and then relaxing back to the low fluence one. This is shown by the green points in figure 2.7c, which displays the

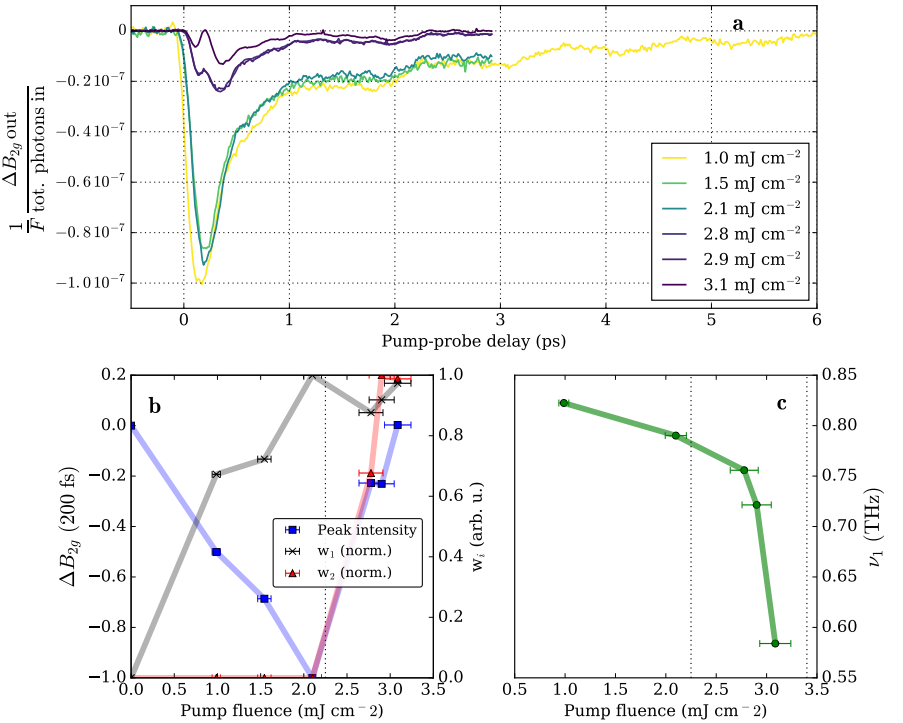

Figure 2.7: **a)** Variation of the B_{2g} intensity divided by the total probe intensity and by the fluence. **b)** As a function of the pump fluence: (blue squares, left y-axis) value of the signal at 200 fs; (black crosses, red triangles, left y-axis) normalized amplitude of the oscillation at ν_1 and ν_2. **c)** Frequency ν_1 of the low-frequency oscillation in the B_{2g} signal as a function of fluence.

initial frequency ν_1 as a function of the pump fluence [2]. Frequency softening is common to the excitation of coherent vibrations in pump-probe experiments, as the more charge is photoexcited, the more the ionic potential is initially loosened, until the relaxation of the electrons brings it back to the equilibrium shape. A classic example of this is the out-of-equilibrium behaviour of bismuth crystals [17], which is theoretically discussed in chapter III.3. The amplitude of this oscillation is plotted as the dark crosses in figure 2.7b. It grows approximately linearly with the fluence up to the critical fluence $F^*_{B_{2g}}$,

[2] The frequency ν_1 has been obtained with a fit of the data.

above which it saturates.

For fluences greater than $F^*_{B_{2g}}$, another oscillation sets in, with a frequency $\nu_2 = 3.8$ THz. Its amplitude is shown as the red triangles in figure 2.7b.

For very large fluences a third oscillation can be detected, as shown in figure 2.8 for a fluence 3.7 mJ cm^{-2}. The frequency ν_3 of such oscillation is very low ($\nu_3 = 14$ GHz, damped with a timescale of 84 ps), and it can therefore be safely attributed to the Brillouin scattering with an acoustic oscillation. It is however remarkable that such oscillation is visible only in the B_{2g} signal and not in the other symmetries.

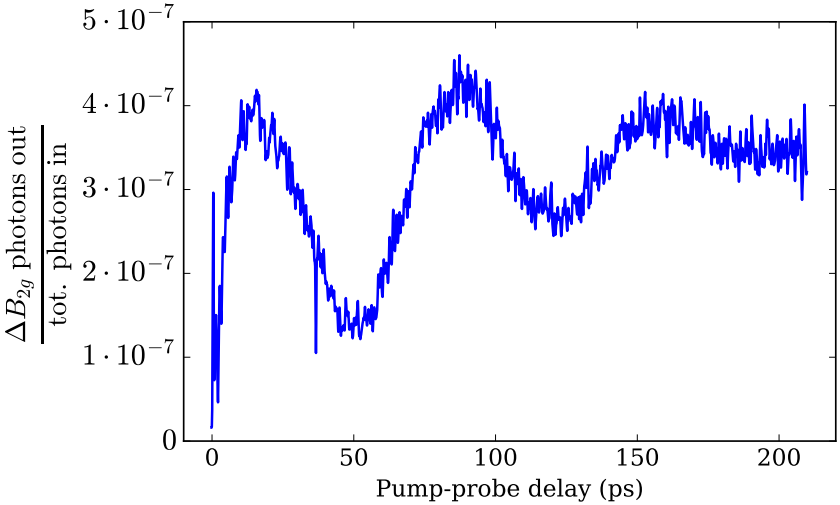

Figure 2.8: Variation of the B_{2g} intensity divided by the total probe intensity, for a fluence of 3.7 mJ cm^{-2}.

The oscillations at frequencies ν_1 and ν_2 can be identified as vibrational modes on the basis of Raman scattering measurements [18,19]. The frequency ν_1 approximately matches a peak in the Raman spectra at $\sim 27\,\mathrm{cm}^{-1} = 0.8\,\mathrm{THz}$, while the second frequency matches instead a peak at $\sim 129\,\mathrm{cm}^{-1} = 3.9\,\mathrm{THz}$. Both are vibrational modes associated to the fact that the symmetry group D_{4h} only approximately describes the lattice, and would therefore not be present if the lattice symmetry were perfectly tetragonal [3].

A remark should be done concerning the highest fluences used. While for

[3]Note that the assignments in the references refer to the undoped compound.

the same fluences there was no sign of sample damaging in the measurement of the A_g and B_{1g} signals, in this case, fluences above 3 mJ cm^{-2} produced a deterioration of the B_{2g} signal. After a prolonged exposure to high-fluence pump pulses, the characteristic features of the high-fluence response (i.e. the initial positive peak) disappear and can be obtained again only moving to another point of the sample. This could hint towards the fact that the signal in the B_{2g} symmetry is sensitive to a delicate order of the lattice, which is damaged by prolonged exposure to very intense pump pulses. This is consistent with the fact that the observed oscillations correspond to vibrational modes linked to the presence of either an orthorombic distortion of the lattice or a superstructural modulation.

Apart from the simple correspondence of the observed oscillations and the vibrational modes identified in the Raman spectra [18,19], the result presented here fit with other evidences. It has been shown that, in the superconducting phase, the distortion of the tetragonal lattice is along the nodal directions and displays a periodicity of 0.25 of the tetragonal unit cell. [9] The resulting reconstruction therefore involves four unit cells, and it has been shown to be due to a charge order modulating the density on the copper-oxygen bonds [22], as show in figure 2.9. The room-temperature vibration with frequency ν_1 could then be due to a fluctuating charge order of such kind and, in fact, it is visible only in the B_{2g} signal.

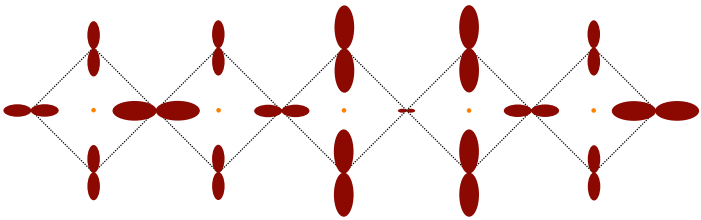

Figure 2.9: Sketch of the charge order modulating the density on the copper-oxygen bonds. Adapted from reference [22].

2.3.2 Pseudogap phase

This sample and the family of systems it belongs to have been intensively studied to a large extent because of their low-temperature phases, i.e. its pseudogap and superconducting phases. For this particular doping, $Bi_2Sr_2Ca_{1-x}Y_xCu_2O_8$ enters the pseudogap phase at approximately $T^* = 130$ K, while the transi-

tion temperature to the superconducting phase is $T_c = 95$ K. The pump-probe measurements with the pump photon energies in the mid-infrared clearly allow to distinguish the normal, the pseudogap and the superconducting phase. As shown in figure 2.10 for a pump photon energy of 140 meV and a probe photon energy of 1.63 eV, below the temperature T^*, the dynamics of the variation of the reflectivity starts to deviate from its high-temperature shape, signalling the presence of the pseudogap. At $T_c = 95\,K$ there is a sharp transition of the out-of-equilibrium behaviour of the sample, as it undergoes the transition into the superconducting phase.

In the pseudogap phase, at 100 K, the out-of-equilibrium reflectivity behaves as shown in figure 2.11a for different pump fluences and in figure 2.11b for different probe photon energies at the intermediate fluence of 0.4 mJ cm^{-2}. The pump photon energy used was 140 meV. These results match the ones obtained by exciting the same compound with a pump photon energy of 1.5 eV. The low-fluence $\frac{\Delta R}{R}$ at 1.5 eV probe photon energy displays a negative peak followed by a slightly positive thermal plateau. Increasing the fluence, a positive initial peak arises, masking the negative one.

As a function of the probe photon energy, the sign of $\frac{\Delta R}{R}$ changes at around 1.4 eV, with a negative signal on the visible side of the spectrum and a positive one on the infrared side, consistently with what previously reported for high pump photon energies [11,12]. The pump photon energies have not been tuned to any specific vibrational mode and the excitation involved only the electronic plasma.

Also in this case the measurements of the B-type signals yield different information. Figure 2.12a shows the B_{2g} signal divided by the pump fluence, for pump photon energies of 180 meV. The magnitude of the signal is two orders of magnitude smaller than the simple $\frac{\Delta R}{R}$. As can be seen also from figure 2.12b, the B_{2g} signal is linear with the fluence in this range, while $\frac{\Delta R}{R}$ is not. The dynamical response contained in the B_{2g} signal is therefore due to the creation and relaxation of excitations. Remarkably, no signatures of the charge density wave or a vibrational mode can be detected, differently from the strange metal phase at room temperature (figure 2.7). This means that, as the system enters in the pseudogap phase, either the coupling between B_{2g} electronic states and the superstructural lattice modulation changes, or the superstructural modulation disappears.

2.3.3 Superconducting phase

I now describe the results obtained with the sample in the superconducting phase at a temperature T = 78 K $< T_c$. Figure 2.13a shows the relative

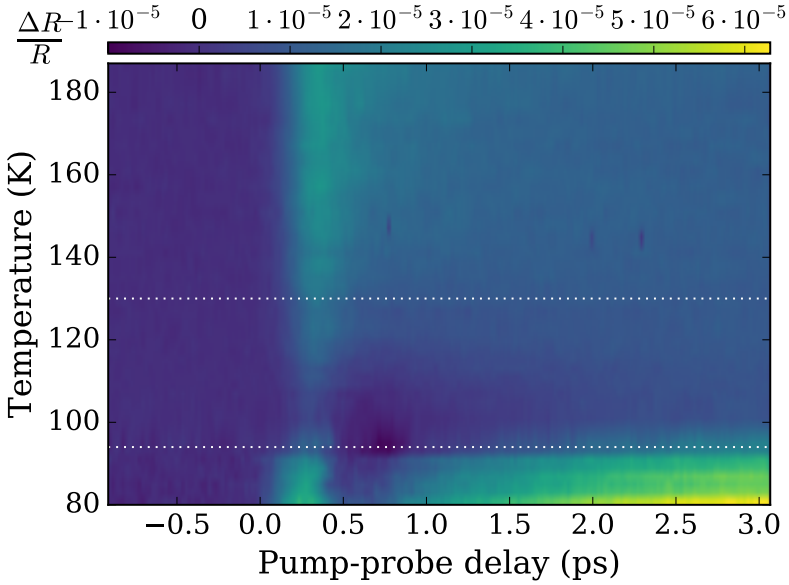

Figure 2.10: Relative variation of the reflectivity $\frac{\Delta R}{R}(t)$ as a function of pump-probe delay and sample temperature, with 140 meV pump pulses, 1.6 eV probe pulses and a pump fluence of 0.8 mJ cm^{-2}. The responses of the normal, pseudogap and superconducting phases are clearly distinguishable.

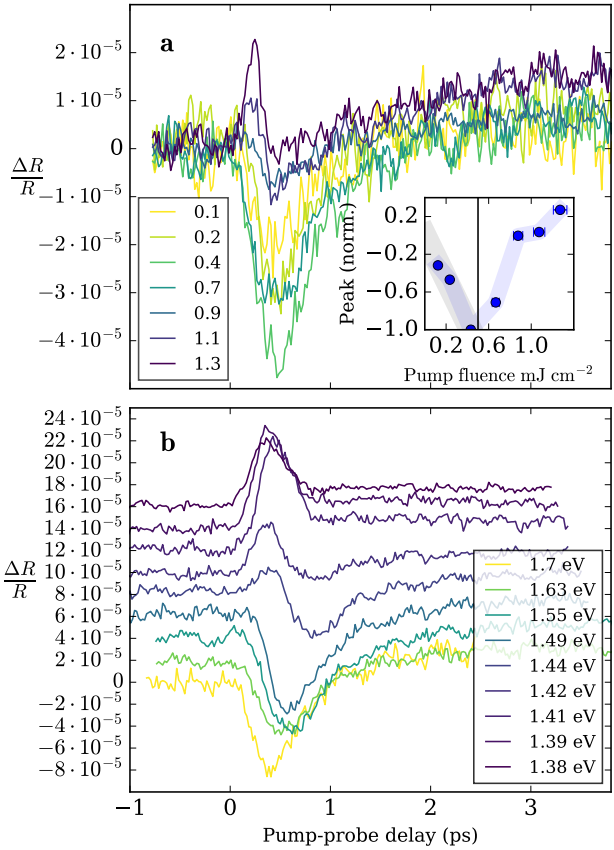

Figure 2.11: **a)** Relative variation of the reflectivity $\frac{\Delta R}{R}$ of the sample in the pseudogap phase at a temperature of 100 K, with 140 meV pump pulses and 1.6 eV probe pulses, for different pump fluences. Labels: fluence (mJ cm^{-2}). **inset)** Peak value of $\frac{\Delta R}{R}$ as a function of the pump fluence. **b)** $\frac{\Delta R}{R}$ at 100 K with 140 meV pump pulses and a pump fluence 0.4 mJ cm^{-2}, for various probe photon energy.

variation of the reflectivity $\frac{\Delta R}{R}(t)$ with pump photon energy 200 meV and probe photon energy 1.6 eV, for different pump fluences.

The results nicely resemble the ones obtained in the past exciting the sample with 1.5 eV pump photons [12–14]. At low fluences, the response displays

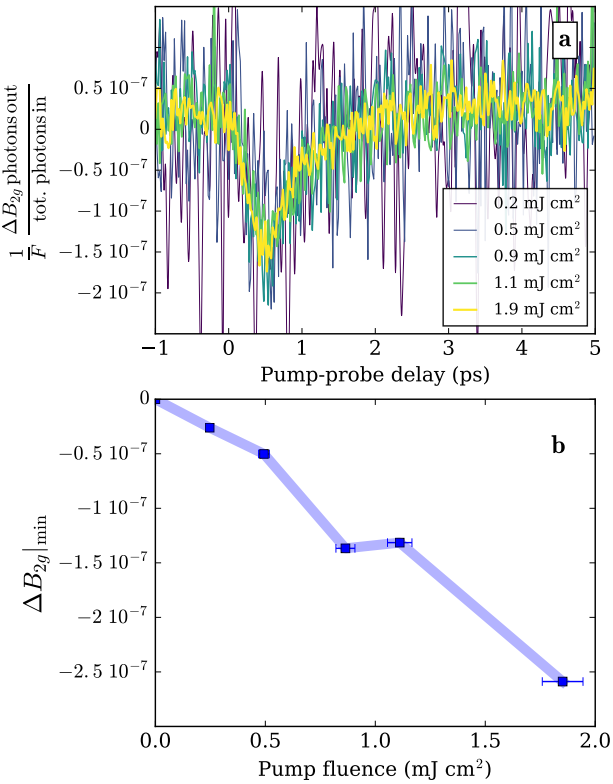

Figure 2.12: **a)** Variation of the B_{2g} intensity in the pseudogap phase, divided by the total probe intensity and by the fluence. **b)** Peak variation of the B_{2g} signal as a function of the pump fluence.

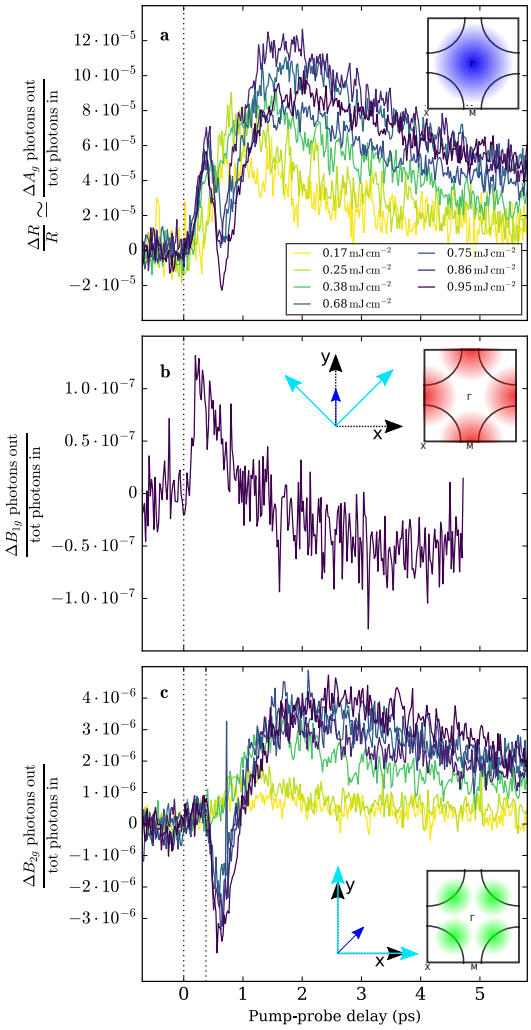

Figure 2.13: **a)** Relative variation of the reflectivity $\frac{\Delta R}{R}$ ($\simeq A_g$ signal) at 78 K, with 200 meV pump pulses and 1.6 eV probe pulses, for different pump fluences. **b)**, **c)** Variation of the B_{1g} and B_{2g} intensity divided by the total probe intensity and by the fluence. The insets show the regions in the Brillouin zone contributing to the signal and the corresponding scattering geometry.

a slow rise-time, and its relaxation timescale becomes faster with increasing fluence. This is consistent with the scenario described by the Rothwarf-Taylor equations, in which the dynamics of an out-of-equilibrium superconductor is determined by the reciprocal energy exchange between phonons and Cooper pairs. [21]. Above a critical pump fluence, the response of the system starts to change in a more marked way, signalling the destruction of the superconducting phase. First, the temporal position of the maximum of $\frac{\Delta R}{R}$ starts moving to larger pump-probe delays, as shown in figure 2.14 (blue points). Then, a fast response arises at pump-probe delays immediately after the excitation, i.e. smaller than the rise-time of the low fluence response. The value of $\frac{\Delta R}{R}(0)$ is also shown in figure 2.14 (green points), where also the value of the critical fluence can be read off ($F_c = 0.25$ mJ cm^{-2}). Apart from a scaling of the critical fluence due to the different absorption coefficient, the data obtained with 140 meV pump pulses are analogous to the ones for 200 meV pump pulses and are reported in the figure 2.15

The dependence of $\frac{\Delta R}{R}$ on the probe photon energy is shown in figures 2.16a and b for two different pump-fluences and pump photon energy 140 meV. The plotted dependence is different from the one reported, for example, by Giannetti et al. [12]. In fact, the previously reported data show a small photon energy region around 1.45 eV in which the $\frac{\Delta R}{R}$ changes sign. However, as pointed out by Cilento [11], close to optimal doping the spectral dependence of $\frac{\Delta R}{R}$ undergoes a sharp transition from a positive signal in the underdoped compound and a negative one in the overdoped compound. They reported that a nominally optimally doped $Bi_2Sr_2Ca_{1-x}Y_xCu_2O_8$ can acquire the out-of-equilibrium behaviour of the slightly underdoped case once it is exposed for some time to the atmosphere, as a consequence of a change in the oxygen content. The spectral dependence of the response to mid-infrared excitations reported here is therefore compatible with the one obtained with 1.5 eV pump photon energy.

From this discussion, it emerges that the behaviour of this sample after an excitation with mid-infrared pulses is very similar to the one after an excitation with 1.5 eV pulses. While in our experiments the pump photon energy is only slightly larger than the energy of the superconducting gap, 1.5 eV is one order of magnitude larger and an excitation at this energy can potentially induce a very different dynamics. The similarity resulting from the comparison done in this section supports the legitimacy of using effective thermal models for this kind of system in pump-probe experiments with pump pulses in the near-infrared spectral range.

Also in the superconducting phase the variation of the reflectivity appears to be isotropic within the noise level, if the polarization of the probe pulses

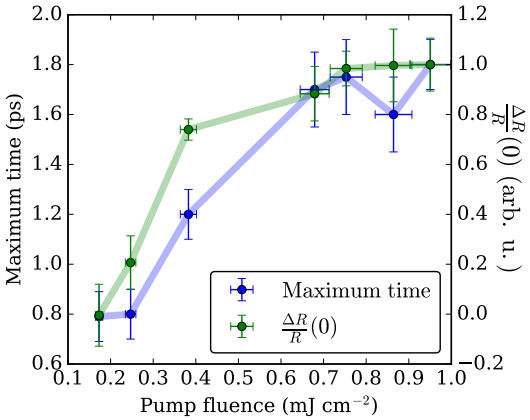

Figure 2.14: Blue (left axis): temporal position of the maximum value of $\frac{\Delta R}{R}$ as a function of the pump fluence. Green (right axis): Value of $\frac{\Delta R}{R}$ at pump-probe delay 0 (normalized), as a function of the pump fluence.

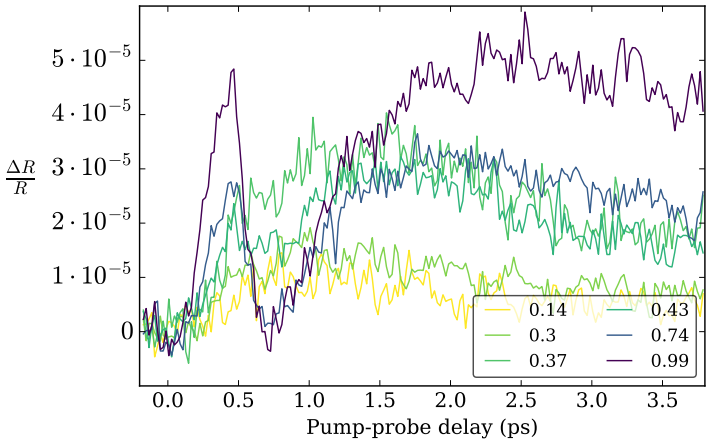

Figure 2.15: Relative variation of the reflectivity $\frac{\Delta R}{R}$ of the sample in the superconducting state at 78 K, with 140 meV pump pulses and 1.6 eV probe pulses, for different pump fluences. Labels: fluence (mJ cm^{-2}).

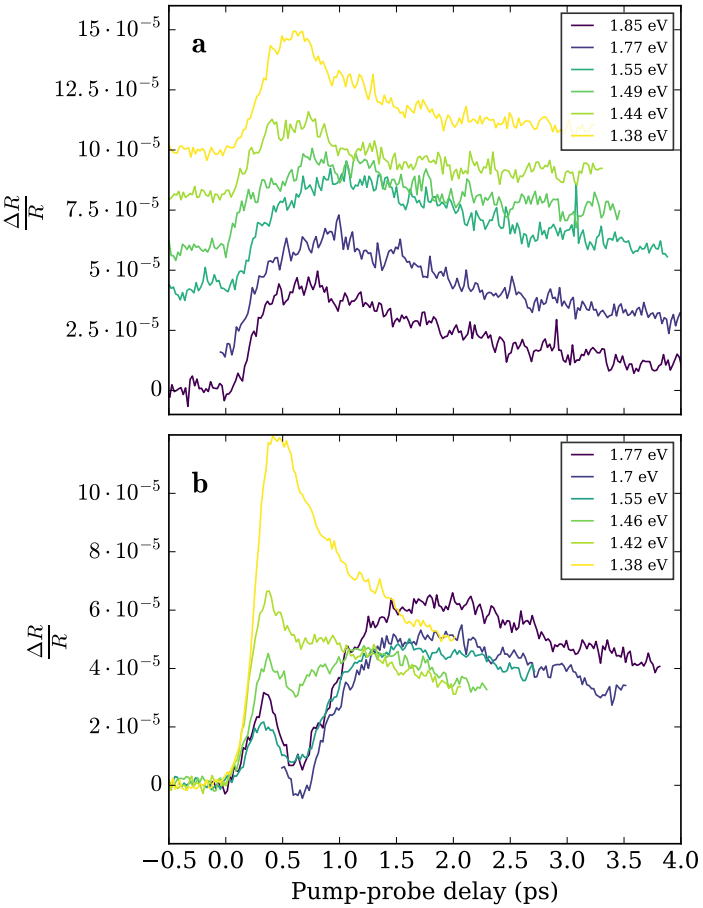

Figure 2.16: Relative variation of the reflectivity $\frac{\Delta R}{R}$ at 78 K with 140 meV pump pulses for different probe photon energies at pump fluences of 0.3 mJ cm^{-2} (**a**) and 0.8 mJ cm^{-2} (**b**).

is rotated. We can, therefore, identify it as a signal of A_g symmetry. We can, however, measure the B signals in the scattering geometries described previously. Both the B_{1g} and B_{2g} results, respectively plotted in figures 2.13b and c, are qualitatively different from the A_g ones.

The B_{1g} signal reported in figure 2.14 displays an initial positive peak, a decay and a subsequent crossing of zero. The negative feature decays then slowly to zero again. Such measurement has been acquired at a fluence $F > 1$ mJ cm^{-2}.

We can identify the nature of this dynamics comparing it with what discussed by Coslovich et al. [10, 13]. They performed pump-probe experiments with 1.5 eV pump photon energy and broadband probe pulses in the visible range. They were able to decompose $\frac{\Delta R}{R}(h\nu, t)$ in two spectro-temporal components that they associated to the response of the superconductor and the response of the pseudogap. By spectro-temporal components we mean functions $A(h\nu, t) = f_A(h\nu) \otimes g_A(t)$ and $B(h\nu, t) = f_B(h\nu) \otimes g_B(t)$ such that $\frac{\Delta R}{R}(h\nu, t) = A(h\nu, t) + B(h\nu, t)$, as discussed in more detail in chapter I.1. Their conclusion was therefore that the coexisting superconduting condensate and pseudogap produce two different responses, which are both visible even below the critical temperature for the transition to the superconducting phase. The B_{1g} signal we have measured is similar to the temporal behaviour of the pseudogap excitations in the superconducting phase, and can itself be associated to the dynamics of the pseudogap.

The B_{2g} signals reported in figure 2.13c have been acquired in the same conditions of the data in panel a of the same figure. By visual inspection, the data are clearly linked to the A_g ones, and the main difference concerns the small pump-probe delays. At low fluences, the B_{2g} signal follows the same behaviour as the A_g one, in accordance to the Rothwarf-Taylor equations. With increasing fluence the relaxation dynamics becomes faster.

Above a critical fluence $F_c = 0.25$ mJ cm^{-2}, the temporal position of the maximum positive value of the signal becomes larger, as can be seen in figure 2.17a (blue points). However, above F_c also a major difference sets in. While the A_g signal displays a fast positive peak, the B_{2g} one shows a negative initial variation, whose amplitude is plotted in figure 2.17a (green points). It is noteworthy that the B_{2g} signal is delayed by 400 fs with respect to the pump pulse.

The difference between the A_g and B_{2g} signals can be studied in more detail, noting that for large pump-probe delay the dynamics in the two symmetries is the same. If we normalize both the A_g and the B_{2g} responses with their large-time values and take the difference $A_g - B_{2g}$, we obtain the results plotted in figure 2.17c (solid lines). The result of this subtraction matches

the B_{1g} signal and the pseudogap behaviour extracted by Coslovich et al. [10], as shown by superimposing the latter on the subtraction result $A_g - B_{2g}$ in figure 2.17c (green dashed line).

From these comparisons, it can be concluded that, as shown by the subtraction in figure 2.17c, two different dynamics contribute to the A_g signal (or $\frac{\Delta R}{R}$), out of which one corresponds to the dynamics previously associated to pseudogap excitations [10, 13]. Moreover, these two dynamics are separately present in the antinodal (B_{1g}) and nodal (B_{2g}) directions in k-space.

2.4 Conclusions

In this work we have shown that, after a photoexcitation in the mid-infrared spectral range, the response of the optimally yttrium-doped Bi2212 is strongly k-dependent. Our data reveal that, in the (a, b) plane, electronic states with all symmetries are coupled to magnetic excitations also in the strange metal phase at room temperatures. In addition, the electronic states in the nodal direction are strongly coupled to the charge density wave and a bending mode of the Cu-O planes.

Also in the low-temperature phases the response of Bi2212 is k-dependent. In the pseudogap phase, we were able to detect that the response in the nodal direction is linear even with pump fluences which produce nonlinearities in the totally symetric response. Remarkably, we found that, differently from the strange metal phase, in the pseudogap phase the nodal response does not show any coupling to the charge density wave or to vibrational modes.

In the superconducting phase, the antinodal dynamics is dominated by a response associated to excitations across the pseudogap. The response at the antinode is delayed by ~ 400 fs with respect to pump pulse and displays a dynamics which can be associated to the melting of the superconducting condensate.

Acknowledgements

Andrea Damascelli and Fabio Boschini (University of British Columbia, Vancouver) provided the samples for this work.

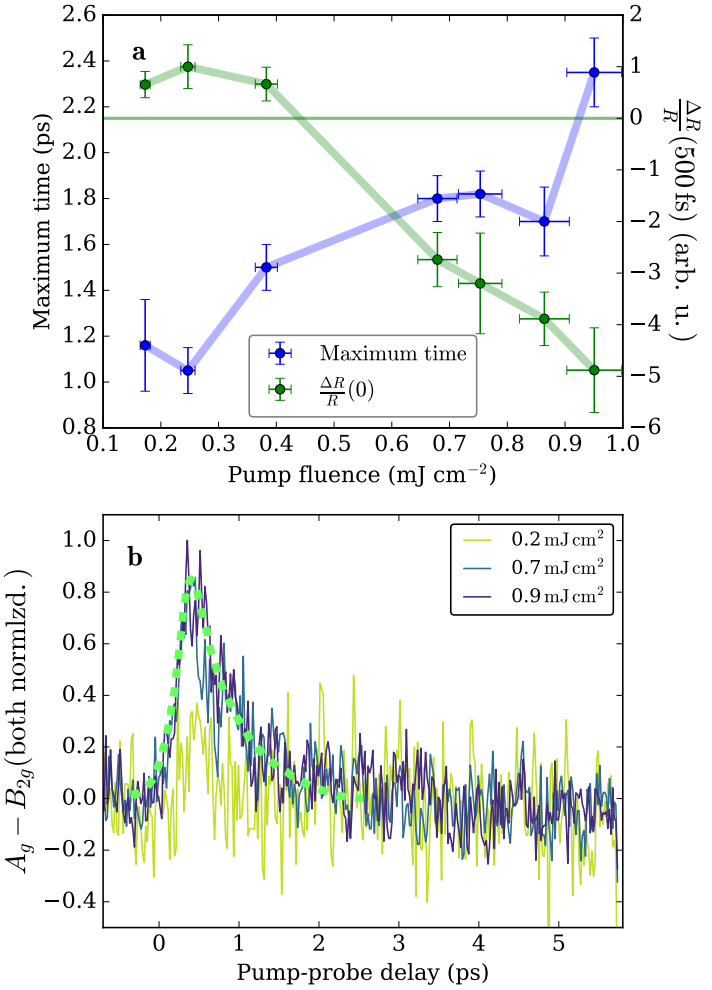

Figure 2.17: **a)** Blue (left axis): Temporal position of the maximum value of the B_{2g} signal as a function of the pump fluence, for a pump photon energy of 200 meV. Green (right axis): value of the signal at pump-probe delay 500 fs. **b)** Difference between the A_g and B_{2g} signals (both normalized so that their long-time dynamics overlap), for different pump fluences (pump photon energy 200 meV).

Bibliography

[1] A.V. Chubkov, D. Pines, and J. Schmalian, in "The Physics of Superconductors", (eds Benneman, K. H. and Ketterson, J. B.) 495, Springer (2003).

[2] T. Dahm, V. Hinkov, S.V. Borisenko, A.A. Kordyuk, V.B. Zabolotnyy, J. Fink, B. Büchner, D.J. Scalapino, W. Hanke, and B. Keimer, "Strength of the spin-flucutation-mediated pairing interaction in a high-temperature superconductor", Nat. Phys. **5**, 217–221 (2009).

[3] A.A Kordyuk, V.B. Zabolotnyy, D.V. Evtushinsky, D.S. Inosov, T.K. Kim, B. B üchner, S.V. Borisenko, "An ARPES view on the high-T_c problem: Phonons vs spin-fluctuations", Euro. Phys. J. Special Topics **188** (1), 153–162 (2010).

[4] S. Sachdev, "Colloquium: Order and quantum phase transitions in the cuprate superconductors", Rev. Mod. Phys. **75**, 913 (2003).

[5] P.A. Lee, N. Nagaosa, X.G. When, "Doping a Mott insulator: Physic of high-temperature superconductivity", Rev. Mod. Phys. **78**, 17 (2006).

[6] S.M. Hayden, G. Aeppli, R. Osborn, A.D. Taylor, T.G. Perring, S-W. Cheong, and Z. Fisk, "High-energy spin waves in La_2CuO_4", Phys. Rev. Lett. **67**, 3622–3625 (2007).

[7] H. Shimahara and S. Takada, "Fragility of the antiferromagnetic long-range-order and spin correlation in the two-dimensional t–J model" J. Phys. Soc. Jpn **61**, 989–997 (1992).

[8] I. Sega, P. Prelovsek, and J. Bonca, "Magnetic fluctuations and resonant peak in cuprates: towards a microscopic theory" Phys. Rev. B **68**, 054524 (2003).

[9] M. Guarise, B. Dalla Piazza, H. Berger, E. Giannini, T. Schmitt, H.M. Rønnow, G.A. Sawatzky, J. van den Brink, D. Altenfeld, I. Eremin, and M. Grioni, "Anisotropic softening of magnetic excitations along the nodal direction in superconducting cuprates", Nat. Comm. **5**, 5760 (2014).

[10] G. Coslovich, "Disclosing the ultrafast dynamics of competing phases in high-temperature superconductors by time-resolved optical spectroscopy", PhD Thesis, Universitá degli Studi di Trieste (2009).

[11] F. Cilento, "Non-equilibrium phase diagram of $Bi_2Sr_2Y_{0.08}Ca_{0.92}Cu_2O_{8+\delta}$ cuprate superconductors revealed by ultrafast optical spectroscopy", PhD Thesis, Universitá degli Studi di Trieste (2010).

[12] C. Giannetti, F. Cilento, S. Dal Conte, G. Coslovich, G. Ferrini, H. Molegraaf, M. Raichle, R. Liang, H. Eisaki, M. Greven, A. Damascelli, D. van der Marel, and F. Parmigiani, "Revealing the high-energy electronic excitations underlying the onset of high-temperature superconductivity in cuprates", Nat. Comm. **2**, 353 (2011).

[13] G. Coslovich, C. Giannetti, F. Cilento, S. Dal Conte, T. Abebaw, D. Bossini, G. Ferrini, H. Eisaki, M. Greven, A. Damascelli, and F. Parmigiani, "Competition between the pseudogap and superconducting states of $Bi_2Sr_2Ca_{0.92}Y_{0.08}Cu_2O_{8+\delta}$ single crystals revealed by ultrafast broadband optical reflectivity", Phys. Rev. Lett. **110**, 107003 (2013).

[14] G. Coslovich, C. Giannetti, F. Cilento, S. Dal Conte, G. Ferrini, P. Galinetti, M. Greven, H. Eisaki, M. Richle, R. Liang, A. Damascelli, and F. Parmigiani, "Evidence for a photoinduced nonthermal superconductivity-to-normal-state phase transition in overdoped $Bi_2Sr_2Ca_{0.92}Y_{0.08}Cu_2O_{8+\delta}$", Phys. Rev. B **83**, 064519 (2011).

[15] T.P. Devereaux and R. Hackl, "Inelastic light scattering from correlated electrons", Rev. Mod. Phys. **79**, 175 (2007).

[16] Y. Toda, F. Kawanokami, T. Kurosawa, M. Oda, I. Madan, T. Mertelj, V.V. Kabanov, and D. Mihailovic, "Rotational symmetry breaking in $Bi_2Sr_2CaCu_2O_{8+\delta}$ probed by polarized femotsecond spectroscopy", Phys. Rev. B **90**, 094513 (2014).

[17] O.V. Misochko "Coherent phonons and their properties", J. of Experimental and Theoretical Physics **92** (2), 246–259 (2001).

[18] R. Liu, M.V. Klein, P.D. Han, and D.A. Payne, "Raman scattering from A_g and B_{1g} phonons in $Bi_2Sr_2Ca_{n-1}Cu_nO_{2n+4}$ (n=1,2)", Phys. Rev. B **45** (13), 7392 (1992)

[19] M. Kakihana, M. Osada, M. Käll, L. Börjesson, H. Mazaki, H. Yasuoka, M. Yashima, and M. Yoshimura, "Raman-active phonons in $Bi_2Sr_2Ca_{1-x}Y_xCu_2O_{8+\delta}$: Effects of hole filling and internal pressure induced by Y doping for Ca, and implications for phonon assignments", Phys. Rev. B. **53** (17), 11796 (1996).

[20] E. Schachinger and J.P. Carbotte, "Coupling to spin fluctuations from conductivity scattering rates", Phys. Rev. B **62**, 9054 (2000).

[21] A. Rothwarf and B.N. Taylor, "Measurement of recombination lifetimes in superconductors", Phys. Rev. Lett. **19**, 27 (1967).

[22] R. Comin, R. Sutarto, F. He, E.H. da Silva Neto, L. Chauviere, A. Fraño, R. Liang, W.N. Hardy, D.A. Bonn, Y. Yoshida, H. Eisaki, A.J. Achkar, D.G. Hawthorn, B. Keimer, G.A. Sawatzky, and A. Damascelli, "Symmetry of charge order in cuprates", Nat. Mater. **14**, 796–800 (2015).

Part III

Fluctuations of the out-of-equilibrium optical properties

Introduction

Pump-probe experiments are the prime way to study condensed matter out of its equilibrium state on timescales of femto- and picoseconds. In their basic scheme, an intense ultrashort light pulse, called pump, impinges on a sample bringing it out of equilibrium, followed by a low-intensity ultrashort pulse, called probe, whose reflection is collected to measure how the reflectivity of the sample has changed after the excitation. Since the signals to be detected are typically very small with respect to the total noise, the experiment usually consists in measuring the average intensity of many (often thousands) of probe pulses reflected by the sample, for each pump-probe delay.

Little attention has been given to the accurate measurement of the fluctuation of the intensities of reflected (or transmitted) probe pulses. In the past such kind of experiments have been performed on systems in which coherent vibrational oscillations are excited by the pump pulses [1]. However, the measured statistic of the reflected intensity has turned out to be of instrumental origin [2]. Only recently, experiments have been performed with low-noise detectors with fast responses, which can significantly give access to such kind of statistics [3, 4]. In the basic implementation of such set-up, the intensity of every single probe pulse that has interacted with the sample is separately acquired with low-electronic-noise detectors. The average of these measurements gives the usual pump-probe signal (e.g. the relative variation of the reflectivity $\frac{\Delta R}{R}(t_p)$), while their variance can provide additional information about the system that is not contained in the average value.

From the theoretical point of view, additional effort is needed to identify what kind of information can be extracted, and to what extent general statements can be made about it without reference to specific models. In this work we studied such kind of statistical information in the out-of-equilibrium Holstein model, which is a good description of the general class of Peierls' systems. After an impulsive excitation, Peierls' systems display coherent lattice vibrations as, for example, in the case of bismuth single crystals [1]. The choice of this model, apart from fitting in the tradition of the first experiments of this kind, is due to the fact that it probably displays the simplest out-of-equilibrium dynamics involving a coherent excitation and not just a thermalization decay. Although the electronic system of this model is not characterized by strong correlation, the oscillating dynamics makes the information that can be extracted nontrivial.

Moreover, this model allows to discuss the common assumption that the electrons in a solid, after an intense photoexcitation, can be considered in an effectively thermal state. This may be straightforward in the case of simple

systems, but is not necessarily the case when coherent dynamics are present in degrees of freedom to whom the electrons are coupled, as it occurs in out-of-equilibrium Peierls' systems.

It is well known that a linear chain of identical and equispaced atoms is not stable at low temperatures. In fact, below a critical temperature the translational symmetry of the chain is reduced, and the atoms pair forming dimers. This process, generally referred to as Peierls' mechanism, leads to a metal-to-insulator transition. In the molecular limit (sketched in figure 1), it can be viewed as the formation of covalent bonds in homonuclear diatomic molecules. Below a certain temperature the favoured state is the one with two bound atoms. The bond forms, because the negative electronic charge is not distributed isotropically around the single atoms, but concentrates in between the two atoms, in the bonding orbital(s) σ or, eventually, π.

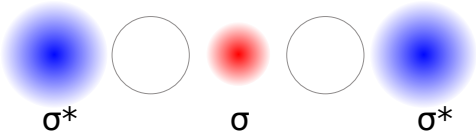

Figure 1: Bonding and antibonding orbitals in a diatomic molecule.

If a linear chain of identical atoms is involved instead, the equispaced lattice is distorted by the formation of dimers. As can be seen in figure 2, two classes of sites are defined by this distortion, which can be grouped in two sublattices, A and B. If we call A and B the sites of the bonding and of the antibonding

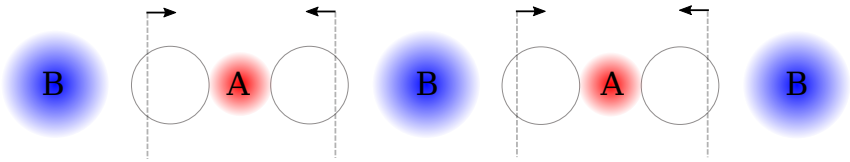

Figure 2: Formation of dimers in a linear chain of atoms. Charge concentrates in the equivalent of the bonding orbitals and two sublattices, A and B, get differentiated.

orbitals, respectively, we can see that on the A sites, besides an increase of the charge density, a reduction $X_A = +X$ of the lattice spacing takes place, while on the B sites, together with a reduction of the charge density, an increase $X_B = -X$ of the lattice spacing occurs.

The Peierls' mechanism diffusely plays a role in real condensed matter crystals. The bismuth elemental crystal is the classic example of lattice exhibiting a Peierls' distortion [5], even though the global system remains metallic also in the dimerized phase. Moreover, the mechanism is a fundamental ingredient in a variety of lattice distortions and metal-to-insulator transitions in correlated materials, sometimes acting together with Mott transitions [5].

Peierls' systems are well described by the Holstein model, which describes free electrons coupled to a vibrational mode via an electronic density-atomic displacement interaction. In real space, the one-dimensional Holstein Hamiltonian is

$$H = \sum_{rs} t_{rs} c_r^\dagger c_s + \sum_r \omega_0 b_r^\dagger b_r + g \sum_r c_r^\dagger c_r \big(b_r + b_r^\dagger\big), \tag{1}$$

where t_{rs} is the hopping between lattice sites, c_r and $c_r^\dagger$ are the annihilation and creation operators of an electron at site r, b_r and $b_r^\dagger$ are the phononic operators at site r, ω_0 is the bare frequency of the vibrational modes, and g is the coupling constant between the electrons and the vibrational modes. In the calculations I will discuss in the following chapters, we employed the alternative formulation of the Holstein Hamiltonian in momentum space

$$H = \sum_k \epsilon(k) c_k^\dagger c_k + \sum_k \omega_k b_k^\dagger b_k + g \sum_{kq} \big(b_{-q}^\dagger + b_q\big) c_{k+q}^\dagger c_k, \tag{2}$$

where $\epsilon(k)$ is the energy dispersion of the electronic band and the operators are the momentum space versions of the ones described above.

In the following, I will discuss the out-of-equilibrium dynamics of this model obtained in two main approaches. In the first of the chapters I will describe the equations and the results obtained in a time-dependent mean-field approximation. Such approximation is able to capture only some of the features of the actual dynamics of these systems. A more refined approach is therefore needed, dynamical mean-field theory. In the second chapter of this part I will, therefore, introduce the framework of nonequilibrium dynamical mean-field theory, discussing the obtained results and their comparison with the experiments in the third chapter.

Chapter 1

Time-dependent mean-field approach

The physics of systems with interacting particles easily becomes very complicated. This is clearly true for electrons interacting via the Coulomb force. The probability to find two electrons very close to each other is low because of the Coulomb repulsion, and, therefore, the motion of each electron becomes correlated with the motion of all the other electrons. This may also happen with other kind of interacting particles, e.g. electrons coupled to phonons.

Despite this, there are some cases in which the many-body problem can be simplified a lot. For example, s- and p-metals, i.e. metals in which the conduction electrons reside in delocalized s- and p-type bands, are described very well by rather crude models in which correlations between electrons are not fully included, and the effect of the electrons on the others is included only as the effect of a mean density (or mean field). This kind of approximation transforms the many-body problem into a single-particle one, which can be solved exactly.

In the case of the Holstein model, such an approach corresponds to the following two approximations of the interaction term between electrons and vibrational modes in the Hamiltonian (1). First, the electrons are coupled only to the expectation value of the atomic displacements $\langle b_q + b^\dagger_{-q} \rangle$ and not to the operators $b_q + b^\dagger - q$ themselves (and therefore not to the fluctuations of the atomic displacements). Second, the vibrational mode is coupled only to the electronic average density $\langle \sum_k c^\dagger_{k+Q} c_k \rangle$ and not to the operators $\sum_k c^\dagger_{k+Q} c_k$ themselves. This means that the Hamiltonian is rewritten as a mean-field

Hamiltonian

$$H^{\mathrm{MF}} = H^{\mathrm{MF}}_{e^-} + H^{\mathrm{MF}}_{ph} - \langle H^{\mathrm{MF}}_{e^-,ph} \rangle, \tag{1.1}$$

where $H^{\mathrm{MF}}_{e^-}$ is a Hamiltonian for free electrons which feel a potential determined by the mean atomic displacement, and H^{MF}_{ph} is a Hamiltonian for free vibrational modes which feel a force determined by the mean electronic charge density. $-\langle H^{\mathrm{MF}}_{e^-,ph} \rangle$ is the product of the mean-field terms of the Hamiltonian describing the interaction between electrons and vibrational modes, and is included to avoid double countings.

In the following I will first derive equations of motion for the relevant observables. Then I will discuss the equilibrium states of the model, and finally I will show the results of the simulation of the out-of-equilibrium evolution of the system after an excitation.

In the upcoming sections, I will try to write as many details as possible about the derivation of equations or, at least, about the steps to be done in the numerical calculations, in the hope they can be useful to other students from a non-theoretical background to trust the results more easily and get a view of the steps involved in such simulations.

1.1 Equations of motion

To study both the equilibrium state and the out-of-equilibrium dynamics of the model, the equations of motion are needed for the expectation values of the relevant observables. In the present case, the observables we will need to consider are th electronic operators $c^\dagger_p c_{p'}$ and, for the vibrational modes, the operators $b^\dagger_p$ and $b_{p'}$. In general, the temporal evolution of an operator $\mathcal{O}$ satisfies the equation

$$i \frac{d}{dt} \mathcal{O} = -[H, \mathcal{O}]. \tag{1.2}$$

To actually perform calculations, we have to write down the equations of motion for the expectation values of the above mentioned observables. In doing so with the full Hamiltonian, terms like $\langle c^\dagger_l c_m (b^\dagger_l + b_l) \rangle$ appear in the equations of motion for $\langle c^\dagger_p c_{p'} \rangle$. Their exact solution involves, therefore, the solution of equations of motion of $\langle c^\dagger_l c_m (b^\dagger_l + b_l) \rangle$ and recursively for expectation values of higher-order operators. In the mean-field approximation, this process is truncated by the factorization of $\langle c^\dagger_l c_m (b^\dagger_l + b_l) \rangle$ in $\langle c^\dagger_l c_m \rangle \langle (b^\dagger_l + b_l) \rangle$, which sets to zero higher-order correlations between the electrons and the vibrational mode. This truncation leads to the following closed set of differential equations

$$i\frac{d}{dt}\langle c_p^\dagger c_{p'}\rangle = \big(\epsilon(p')-\epsilon(p)\big)\langle c_p^\dagger c_{p'}\rangle + g\sum_q \langle b_{-q}^\dagger + b_q\rangle\big(\langle c_p^\dagger c_{p'-q}\rangle - \langle c_{p+q}^\dagger c_{p'}\rangle\big), \quad (1.3)$$

$$i\frac{d}{dt}\big(\langle b_p\rangle + \langle b_{-p}^\dagger\rangle\big) = \omega_p\big(\langle b_p\rangle - \langle b_{-p}^\dagger\rangle\big), \quad (1.4)$$

$$i\frac{d}{dt}\big(\langle b_p\rangle - \langle b_{-p}^\dagger\rangle\big) = \omega_p\big(\langle b_p\rangle + \langle b_{-p}^\dagger\rangle\big) + 2g\sum_k \langle c_{k-p}^\dagger c_k\rangle. \quad (1.5)$$

Above, the equations for $\langle b\rangle$ and $\langle b^\dagger\rangle$ have been combined into equations for $\langle b + b^\dagger\rangle$ and $\langle b - b^\dagger\rangle$, which are proportional to the position and momentum of the vibrational mode.

The number of equations above is still large, since all the momentum space indices are present. We can reduce it using the assumption that there will be a well defined wavevector Q for the distortion of the lattice. This corresponds to omitting the momentum summation for the vibrational modes and selecting only $\langle b_Q\rangle$ and $\langle b_{-Q}\rangle$. The equation of motion for $\langle c_p^\dagger c_{p'}\rangle$ becomes

$$i\frac{d}{dt}\langle c_p^\dagger c_{p'}\rangle = \big(\epsilon(p')-\epsilon(p)\big)\langle c_p^\dagger c_{p'}\rangle + g\langle b_{-Q}^\dagger + b_Q\rangle\big(\langle c_p^\dagger c_{p'-Q}\rangle - \langle c_{p+Q}^\dagger c_{p'}\rangle\big). \quad (1.6)$$

If we now restrict ourselves to $i\frac{d}{dt}\langle c_p^\dagger c_p\rangle$, we get

$$i\frac{d}{dt}\langle c_p^\dagger c_p\rangle = g\langle b_{-Q}^\dagger + b_Q\rangle\big(\langle c_p^\dagger c_{p-Q}\rangle - \langle c_{p+Q}^\dagger c_p\rangle\big). \quad (1.7)$$

As a further Ansatz, let us consider the case in which the electronic band is half filled. In such case, the Peierls' distortion will have a periodicity $Q = \pi$. Then $p - Q$ is equivalent to $p + Q$, and $p + 2Q$ to p. Therefore we get the following equation

$$i\frac{d}{dt}\langle c_p^\dagger c_p\rangle = g\langle b_{-Q}^\dagger + b_Q\rangle\big(\langle c_p^\dagger c_{p+Q}\rangle - \langle c_{p+Q}^\dagger c_p\rangle\big), \quad (1.8)$$

in which $\langle c_p^\dagger c_p\rangle$ is coupled to $\langle c_p^\dagger c_{p+Q}\rangle$ and $\langle c_{p+Q}^\dagger c_p\rangle$, which in turn are coupled also to $\langle c_{p+Q}^\dagger c_{p+Q}\rangle$. The full system of coupled equations is (reporting again equation (1.8))

$$i\frac{d}{dt}\langle c_p^\dagger c_p\rangle = g\langle b_{-Q}^\dagger + b_Q\rangle\big(\langle c_p^\dagger c_{p+Q}\rangle - \langle c_{p+Q}^\dagger c_p\rangle\big),$$

$$i\frac{d}{dt}\langle c_p^\dagger c_{p+Q}\rangle = \big(\epsilon(p+Q)-\epsilon(p)\big)\langle c_p^\dagger c_{p+Q}\rangle + g\langle b_{-Q}^\dagger + b_Q\rangle\big(\langle c_p^\dagger c_p\rangle - \langle c_{p+Q}^\dagger c_{p+Q}\rangle\big) \tag{1.9}$$

$$i\frac{d}{dt}\langle c_{p+Q}^\dagger c_p\rangle = \big(\epsilon(p)-\epsilon(p+Q)\big)\langle c_{p+Q}^\dagger c_p\rangle + g\langle b_{-Q}^\dagger + b_Q\rangle\big(\langle c_{p+Q}^\dagger c_{p+Q}\rangle - \langle c_p^\dagger c_p\rangle\big) \tag{1.10}$$

$$i\frac{d}{dt}\langle c_{p+Q}^\dagger c_{p+Q}\rangle = g\langle b_{-Q}^\dagger + b_Q\rangle\big(\langle c_{p+Q}^\dagger c_p\rangle - \langle c_p^\dagger c_{p+Q}\rangle\big) \tag{1.11}$$

This set of equations can be rewritten in the form $i\frac{d}{dt}\rho = [H,\rho]$. In fact, recasting the terms as elements of matrices we obtain

$$\begin{aligned} i\frac{d}{dt}&\begin{pmatrix}\langle c_p^\dagger c_p\rangle & \langle c_{p+Q}^\dagger c_p\rangle\\ \langle c_p^\dagger c_{p+Q}\rangle & \langle c_{p+Q}^\dagger c_{p+Q}\rangle\end{pmatrix} = \\ &\left[\begin{pmatrix}\epsilon(p) & g\langle b_{-Q}^\dagger + b_Q\rangle\\ g\langle b_{-Q}^\dagger + b_Q\rangle & \epsilon(p+Q)\end{pmatrix}, \begin{pmatrix}\langle c_p^\dagger c_p\rangle & \langle c_{p+Q}^\dagger c_p\rangle\\ \langle c_p^\dagger c_{p+Q}\rangle & \langle c_{p+Q}^\dagger c_{p+Q}\rangle\end{pmatrix}\right], \end{aligned} \tag{1.12}$$

where the position of the vibrational mode $\langle b_{-Q}^\dagger + b_Q\rangle(t)$ evolves according to

$$i\frac{d}{dt}\big(\langle b_Q\rangle + \langle b_{-Q}^\dagger\rangle\big) = \omega_Q\big(\langle b_Q\rangle - \langle b_{-Q}^\dagger\rangle\big), \tag{1.13}$$

$$i\frac{d}{dt}\big(\langle b_Q\rangle - \langle b_{-Q}^\dagger\rangle\big) = \omega_Q\big(\langle b_Q\rangle + \langle b_{-Q}^\dagger\rangle\big) + 2g\sum_k \langle c_{k+Q}^\dagger c_k\rangle. \tag{1.14}$$

1.2 Equilibrium state

Once the equations of motion are known, to start a simulation of the out-of-equilibrium dynamics we have to know the initial state of the system, i.e. the initial values of the quantities for which we solve the equations. Since the perturbation, which brings the system out of equilibrium, enters through the equations of motion (as discussed later), and we do not need to take the excited state directly as the initial one, the latter has to be the equilibrium state. To find it, we first rewrite the mean-field Hamiltonian in matrix form

$$H = \sum_{k\in RBZ} \begin{pmatrix}c_k^\dagger & c_{k+Q}^\dagger\end{pmatrix}\begin{pmatrix}\epsilon(k) & \Delta\\ \Delta & -\epsilon(k)\end{pmatrix}\begin{pmatrix}c_k\\ c_{k+Q}\end{pmatrix}, \tag{1.15}$$

where RBZ is the reduced Brillouin zone and $\Delta = g\langle b^\dagger_{-Q} + b_Q\rangle$ will become an energy gap of the system. The fermions represented by c_k and c_{k+Q} are coupled by the term Δ. Second, we rewrite H so that the central matrix becomes diagonal,

$$H = \sum_{k\in RBZ} \underbrace{\begin{pmatrix} c_k^\dagger & c_{k+Q}^\dagger \end{pmatrix} U}_{\begin{pmatrix} d_k^\dagger & e_k^\dagger \end{pmatrix}} \begin{pmatrix} E(k) & 0 \\ 0 & -E(k) \end{pmatrix} \underbrace{U^\dagger \begin{pmatrix} c_k \\ c_{k+Q} \end{pmatrix}}_{\begin{pmatrix} d_k \\ e_k \end{pmatrix}}, \tag{1.16}$$

where $E(k) = \sqrt{\epsilon^2(k) + \Delta^2}$. In this representation, the fermions d_k and e_k are free particles with energies E_k and $-E_k$. Therefore, the populations of the corresponding states at equilibrium are given by the Fermi-Dirac distribution function $f(\pm E_k)$, while the coherences, i.e. the off-diagonal terms of the density matrix, are 0. In this basis, the density matrix is

$$\rho_{d_k e_k} = \begin{pmatrix} f(E_k) & 0 \\ 0 & f(-E_k) \end{pmatrix}. \tag{1.17}$$

Since the equations of motion (1.8)-(1.11) concern the fermions c_k and c_{k+Q}, we need to know the matrix U to use the result (1.17) in the (c_k, c_{k+Q}) basis.

The two columns of U are given by the eigenvectors of the undiagonalized matrix in equation (1.15), which can be written as

$$\begin{pmatrix} u_k \\ -v_k \end{pmatrix}, \begin{pmatrix} v_k \\ u_k \end{pmatrix}. \tag{1.18}$$

Therefore

$$U = \begin{pmatrix} u_k & v_k \\ -v_k & u_k \end{pmatrix}, \quad U^\dagger = \begin{pmatrix} u_k & -v_k \\ v_k & u_k \end{pmatrix}. \tag{1.19}$$

The new fermionic operators are

$$\begin{pmatrix} d_k^\dagger & e_k^\dagger \end{pmatrix} = \begin{pmatrix} c_k^\dagger & c_{k+Q}^\dagger \end{pmatrix} U, \quad \begin{pmatrix} d_k \\ e_k \end{pmatrix} = U^\dagger \begin{pmatrix} c_k \\ c_{k+Q} \end{pmatrix} \tag{1.20}$$

and the inverse relations are

$$\begin{pmatrix} c_k \\ c_{k+Q} \end{pmatrix} = \begin{pmatrix} u_k d_k + v_k e_k \\ -v_k d_k + u_k e_k \end{pmatrix}, \quad \begin{pmatrix} c_k^\dagger \\ c_{k+Q}^\dagger \end{pmatrix} = \begin{pmatrix} u_k d_k^\dagger + v_k e_k^\dagger \\ -v_k d_k^\dagger + u_k e_k^\dagger \end{pmatrix}. \tag{1.21}$$

We can postpone the explicit calculation of u_k and v_k to equation (1.26).

We now have to calculate the equilibrium value of $\Delta = g\langle b^\dagger_{-Q} + b_Q\rangle$, which gives the initial position of the vibrational mode and allows to calculate E_k and $f(E_k)$. In order to do it, we have to obtain what is generally called a *gap equation*. The gap equation is obtained imposing the equilibrium condition on the equation of motion for the momentum of the vibrational mode. We therefore take

$$i\frac{d}{dt}\big(\langle b_Q\rangle - \langle b^\dagger_{-Q}\rangle\big) = \omega_Q\big(\langle b_Q\rangle + \langle b^\dagger_{-Q}\rangle\big) + 2g\sum_k \langle c^\dagger_{k+Q}c_k\rangle, \tag{1.22}$$

and set

$$\begin{aligned} i\frac{d}{dt}\big(\langle b_Q\rangle - \langle b^\dagger_{-Q}\rangle\big)\Big|_{\rm eq} &= 0 \\ \frac{\Delta}{g} = \big(\langle b_Q\rangle + \langle b^\dagger_{-Q}\rangle\big)_{\rm eq} &= -\frac{2g}{\omega_Q}\sum_k \langle c^\dagger_{k+Q}c_k\rangle_{\rm eq}. \end{aligned} \tag{1.23}$$

The gap Δ is given by

$$\begin{aligned} \Delta &= -\frac{2g^2}{\omega_Q}\sum_k \langle c^\dagger_{k+Q}c_k\rangle_{\rm eq} \\ &= -\frac{2g^2}{\omega_Q}\sum_k \langle \big(u_k d^\dagger_k + v_k e^\dagger_k\big)\big(-v_k d_k + u_k e_k\big)\rangle_{\rm eq} = \\ &= -\frac{2g^2}{\omega_Q}\sum_k \Big(-u_k v_k \underbrace{\langle d^\dagger_k d_k\rangle_{\rm eq}}_{f(E_k)} + u_k u_k \underbrace{\langle d^\dagger_k e_k\rangle_{\rm eq}}_{0} - v_k v_k \underbrace{\langle e^\dagger_k d_k\rangle_{\rm eq}}_{0} + v_k u_k \underbrace{\langle e^\dagger_k e_k\rangle_{\rm eq}}_{f(-E_k)}\Big) \\ &= -\frac{2g^2}{\omega_Q}\sum_k v_k u_k\big(f(-E_k) - f(E_k)\big) \\ &= -\frac{2g^2}{\omega_Q}\sum_k v_k u_k \tanh\left(\frac{\beta E_k}{2}\right). \end{aligned} \tag{1.24}$$

In particular, one of the two eigenvectors of the undiagonalized matrix in equation (1.15) is

$$\begin{pmatrix} u_k \\ -v_k \end{pmatrix} = \sqrt{\frac{1}{2}\left(1 + \frac{\epsilon_k}{E_k}\right)}\begin{pmatrix} 1 \\ \frac{E_k - \epsilon_k}{\Delta} \end{pmatrix}, \tag{1.25}$$

and, therefore,

$$v_k u_k = -\frac{\Delta}{2E_k}. \tag{1.26}$$

Inserting this result back in equation (1.24), we get the following gap equation [1]

$$\begin{aligned} \Delta &= \frac{2g^2}{\omega_Q} \sum_k \frac{\Delta}{2\sqrt{\epsilon_k^2 + \Delta^2}} \tanh\left(\beta \frac{\sqrt{\epsilon_k^2 + \Delta^2}}{2}\right) \\ 1 &= \frac{g^2}{\omega_Q} \sum_k \frac{1}{\sqrt{\epsilon_k^2 + \Delta^2}} \tanh\left(\beta \frac{\sqrt{\epsilon_k^2 + \Delta^2}}{2}\right) \end{aligned}, \tag{1.27}$$

which has to be solved iteratively.

Figure 1.1 shows the value of the gap Δ as a function of the temperature, with $g^2/\omega = 0.26$. For low temperatures, the system is gapped with $\Delta = 0.19$. The position of the vibrational mode $\left(\langle b_Q \rangle + \langle b_{-Q}^\dagger \rangle\right)_{\text{eq}} = \frac{\Delta}{g}$ is therefore different from zero, meaning that the atoms in the lattice are displaced from their original positions in an alternating way. The system is in a symmetry-broken state characterized by the formation of dimers. In this phase, two inequivalent sublattices A and B can be identified, in which A atoms are displaced from their "undistorted" positions on the one side and B atoms on the other side. The displacements X_A and X_B of the two sublattices are therefore opposite in sign: $X_A = -X_B = X$.

As the temperature $T_c \simeq 0.11$ is approached, the value of Δ decreases until it reaches zero at T_c and remains zero above T_c. For $T > T_c$ the system is in a translationally invariant phase and, since $\Delta = 0$, is a conductor.

1.3 Displacive excitation from the symmetry-broken state

We can now discuss the excitation of the system starting from the symmetry-broken phase and its subsequent out-of-equilibrium dynamics. As a perturbartion of the system we can use an ultrashort light pulse resonant with the transition between the two bands across the gap. The light pulse is inserted in the calculation via Peierls' substitution, such that

$$\epsilon(k) \to \epsilon(k - A(t)). \tag{1.28}$$

[1] The summations has to be normalized with the number of points.

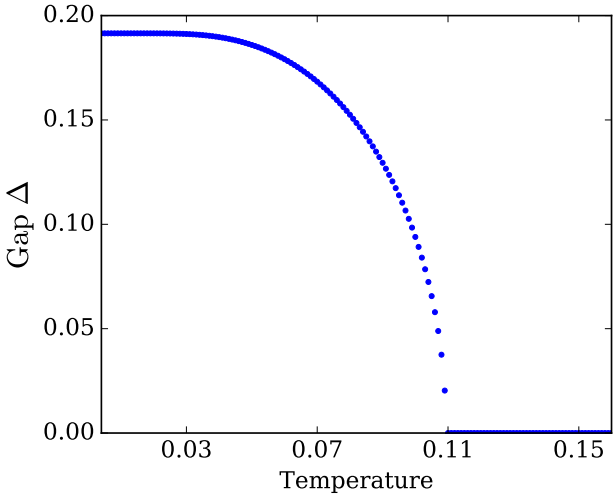

Figure 1.1: Gap calculated as a function of the temperature, with $\frac{g}{\omega_Q} = -0.7$ and $\omega_Q = 0.07$

The excitation of electrons across the gap changes the force on the atoms. If this happens quickly enough, i.e. if the light pulse is shorter than half the period of the vibrational mode, then a coherent oscillation is excited.

Figure 1.2a and b show the evolution of $X \propto \langle b_Q + b^\dagger_{-Q} \rangle$ as a function of time after the arrival of the pulse, for different excitation intensities. Two aspects of these results have to be discussed.

First, the stronger the excitation, the larger the amplitude of the oscillation. In this respect two regimes can be identified. For excitation intensities below a certain critical value (figure 1.2a), the oscillation of the atomic positions X takes place around an average value which is smaller than their equilibrium position but still different from zero. The system, even though in an excited state, remains in the symmetry-broken dimerized phase. Above the critical intensity, the symmetry-broken phase is melted (three darkest curves in figure 1.2b). An oscillation of the atomic positions is still present because the potential felt by the atoms still changes in a sudden way, but the oscillation is centred around an average value of zero, which corresponds to the atomic positions in the translationally invariant phase.

Second, the frequency of the oscillation changes as a function of the intensity of the pump pulse. Figure 1.3a shows the Fourier transform of selected

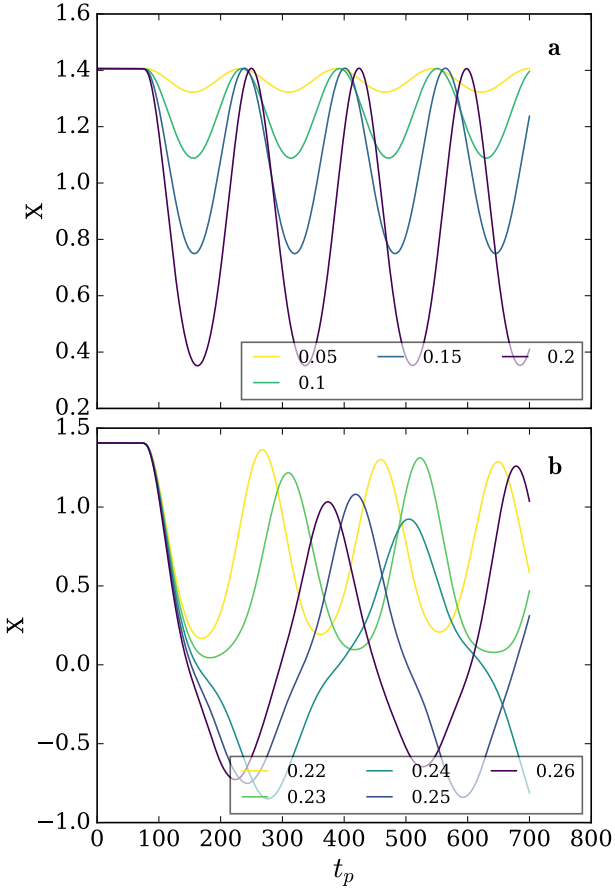

Figure 1.2: **a)** Atomic positions as a function of "pump-probe delay" for different amplitudes of the pulse vector potential that do not melt the symmetry-broken phase. **b)** Same as **a** for vector potential amplitudes close to and above the critical value for the melting of the symmetry-broken phase.

curves in figure 1.2. Up to the critical excitation intensity, the frequency ω^* of the oscillation decreases with increasing pump intensity, because the more electrons are excited, the more the atomic potential is loosened. This is what is generally called *softening* of the vibrational mode, observed for example in pump-probe experiments on bismuth and antimony single crystals, or in experiments performed on the cuprate Bi2212, reported in chapter II.2. Figure 1.3b reports the oscillation frequency ω^* as a function of the pump intensity. Approaching from below the critical intensity, ω^* keeps decreasing, eventually reaching zero at the critical intensity. This is the critical slowing down of the dynamics close to the out-of-equilibrium phase transition. Once the critical intensity is crossed the oscillation frequency ω^* starts increasing again, tending to the bare frequency of the vibrational mode. This is as expected, since, in the Hamiltonian in equation (1), the bare frequency is defined as the frequency of the vibrational mode in the translationally invariant phase.

1.4 What mean field does and does not capture

In this section I have shown that a time-dependent mean-field approach does allow to describe certain features of the displacive excitation of vibrational modes in condensed matter. In the first place, it is able to capture the excitation of coherent vibrations. It also reproduces a softening of the frequency of the oscillation with increasing excitation intensity. Above a critical intensity, the symmetry-broken phase melts, and at the threshold for the out-of-equilibrium phase transition the mean-field approach reproduces a critical slowing down of the dynamics.

However, there is one important aspect of coherent vibrations in real condensed matter that the mean-field approach is not able to capture: the decay of the electronic excitations and the damping of the oscillations. Our goal is to study how the fluctuations of the optical properties can give information about the out-of-equilibrium state of matter. The decay of the out-of-equilibrium dynamics is too important a player in determining the state of the system, not to be captured in the calculations. Therefore, I will use the results obtained in the mean-field approach just as a starting point and I will move to the discussion of calculations performed in nonequilibrium dynamical mean-field theory (DMFT) in the next sections.

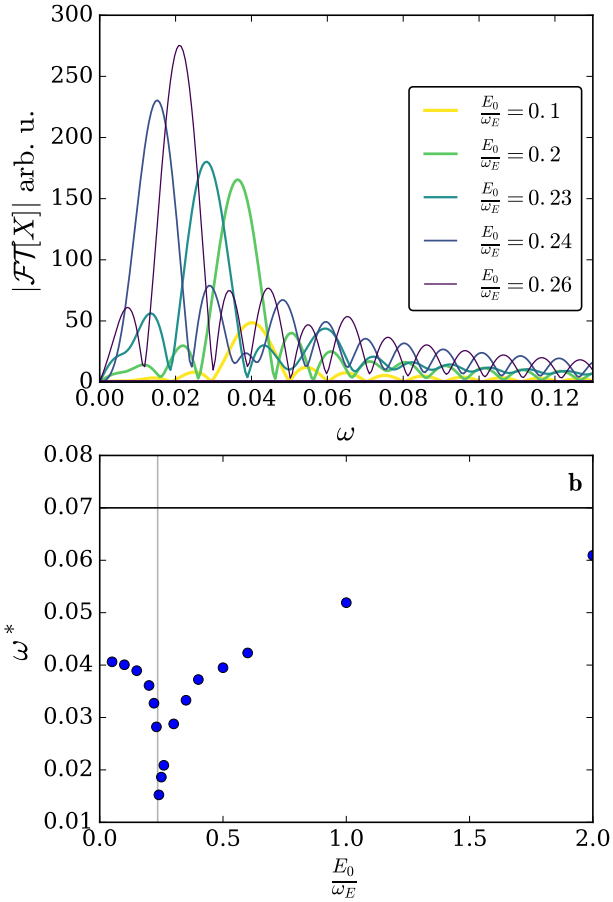

Figure 1.3: **a)** Modulus of the Fourier transform of the curves in figure 1.2a. The data have been zero padded to identify the frequency ω^* of the oscillation with a good precision. **b)** Frequency ω^* of the oscillation as a function of the peak amplitude of the pulse vector potential. The horizontal black line shows the value of the bare frequency of the vibrational mode.

Chapter 2

Dynamical mean-field theory approach - theory

2.1 Introduction to nonequilibrium DMFT

Dynamical mean-field theory (DMFT) is a mean-field approach in which, despite the suppresion of spatial fluctuations, on-site temporal fluctuations are considered [7]. This is necessary if one wants to take the quantum fluctuations into considerations. One of the main successes of dynamical mean-field theory has been to capture the Mott transition in the Hubbard model, but it can be exploited also in other situations. In this work we use it to approximate the incoherent scattering between electrons and phonons as an interaction which is local in space, i.e. k-independent.

Dynamical mean-field theory was originally formulated at equilibrium, but was later extended also to nonequilibrium situations [8]. The equations of nonequilibrium dynamical mean-field theory are formulated on an L-shaped contour in the complex-time plane. This countour straightforwardly arises when one considers the time evolution of a system from an initial thermal state [9].

In the following, I will first introduce the contour on the complex-time plane and the so-called contour-ordered Green's functions. Then I will briefly introduce dynamical mean-field theory and its nonequilibrium extension, to finally move, in section 2.2, to the description of the set-up of equations for the Holstein model and, in section 2.3, to the discussion of other observables. Among them are also the fluctuations of the optical properties, which can be

measured in pump-probe experiments and give additional information about the system with respect to the traditionally measured quantities.

The content of section 2.1 is mainly a summary of the concepts described in two reviews on the subject, the first by Georges et al. [7] about dynamical mean-field theory and the second by Aoki et al. [8] about its generalization to nonequilibrium dynamics. I have tried to restrict this summary to the concepts and formulas which are relevant for this work. Three key paragraphs are reported verbatim from the sources. There is no point of rephrasing sentences stating key concepts in reviews of a subject, other than making them more confusing for the reader. These three small paragraphs are formatted in italics.

2.1.1 Kadanoff-Baym formalism for time evolution from a thermal state

Contour-ordered formulation The formulation of the dynamics of a system on the L-shaped contour in the complex-time plane arises directly when one considers the evolution of a system which initially is in a thermal state. Let us therefore consider a system in a thermal intial state described by the density matrix $\rho(t = 0)$

$$\rho(0) = \frac{1}{Z} e^{-\beta H(0)}, \tag{2.1}$$

where Z is the partition function

$$Z = \mathrm{Tr}\, e^{-\beta H} \tag{2.2}$$

and $H(0)$ the equilibrium Hamiltonian. The density matrix $\rho(t)$ will evolve according to the von Neumann equation

$$i\frac{d}{dt}\rho = \big[H(t), \rho(t)\big] \tag{2.3}$$

and will therefore be given by

$$\rho(t) = U(t, 0)\rho(0)U(0, t), \tag{2.4}$$

where $U(0, t)$ is the unitary evolution operator from time 0 to time t. $U(t, t')$ can be written as

$$U(t, t') = \begin{cases} \mathrm{T}_t e^{-i\int_{t'}^{t} ds\ H(s)} & \text{if } t > t' \\ \bar{\mathrm{T}}_t e^{-i\int_{t'}^{t} ds\ H(s)} & \text{if } t < t' \end{cases} \tag{2.5}$$

with T_t and $\bar{\mathrm{T}}_t$ are the time-ordering and anti-time-ordering operators, respectively. Given $\rho(t)$, the expectation value $\langle \mathcal{O}(t) \rangle$ of an operator $\mathcal{O}$ at time t can be calculated as the trace

$$\begin{aligned} \langle \mathcal{O}(t) \rangle &= \mathrm{Tr}\left[\rho(t)\,\mathcal{O}\right] \\ &= \frac{1}{Z}\,\mathrm{Tr}\left[U(t,0)e^{-\beta H}U(0,t)\,\mathcal{O}\,\right]. \end{aligned} \tag{2.6}$$

Given the formal analogy of $e^{-\beta H}$ with the evolution operator U, we can write $e^{-\beta H}$ as an evolution operator in imaginary time $e^{-\beta H} = U(-i\beta, 0)$. The expectation value of the operator $\mathcal{O}$ becomes therefore

$$\langle \mathcal{O}(t) \rangle = \frac{1}{Z}\,\mathrm{Tr}\left[U(-i\beta,0)U(0,t)\,\mathcal{O}\,U(t,0)\right]. \tag{2.7}$$

Reading the evolution operators from right to left, they follow the time ordering $0 \to t \to 0 \to -i\beta$. This sequence of times is the motivation to introduce an L-shaped contour $\mathcal{C}$ in the complex-time plane (figure 2.1) with three branches $\mathcal{C}_1 : 0 \to t_{\max}$, $\mathcal{C}_2 : t_{\max} \to 0$, and $\mathcal{C}_3 : 0 \to -i\beta$. $t_{\max}$ is the time at which the expectation value of the operator is evaluated, i.e. the maximum time up to which the system is let evolve [9]. Once the contour $\mathcal{C}$ is defined, equation (2.7) can be rewritten as

$$\langle \mathcal{O}(t) \rangle = \frac{\mathrm{Tr}\left[\,\mathrm{T}_{\mathcal{C}}\, e^{-i\int_{\mathcal{C}} ds\; H(s)}\,\mathcal{O}(t)\right]}{\mathrm{Tr}\left[\,\mathrm{T}_{\mathcal{C}}\, e^{-i\int_{\mathcal{C}} ds\; H(s)}\right]}. \tag{2.8}$$

All the exponentials in equation (2.7) have been merged in a single one under the new contour-ordering operator $\mathrm{T}_{\mathcal{C}}$ which orders operators on the contour $\mathcal{C}$ in the order $0 \to t_{\max} \to 0 \to -i\beta$. $\mathcal{O}(t)$ indicates that $\mathcal{O}$ is inserted on the contour at time t. Note that, after the latest time-operator on the contour, the forward and backward branches cancel. If the operator $\mathcal{O}$ were inserted at time zero, then the real time-branches would cancel out completely, and equation (2.8) would reduce to the expectation value on the equilibrium state $\frac{1}{Z}[e^{-\beta H}\,\mathcal{O}]$.

In the contour-ordered formalism, we can also write higher-order correlation functions as expectation values of contour-ordered products of operators

$$\langle \mathrm{T}_{\mathcal{C}}\, A(t)B(t') \rangle \equiv \frac{1}{Z}[\mathrm{T}_{\mathcal{C}}\, e^{-i\int_{\mathcal{C}} ds\; H(s)} A(t)B(t')], \tag{2.9}$$

with A and B combinations of particle creation and annihilation operators. The contour-ordered product of two operators A and B is defined as

$$\mathrm{T}_{\mathcal{C}}\, A(t)B(t') = \theta_{\mathcal{C}}(t,t')A(t)B(t') \pm \theta_{\mathcal{C}}(t',t)B(t')A(t), \tag{2.10}$$

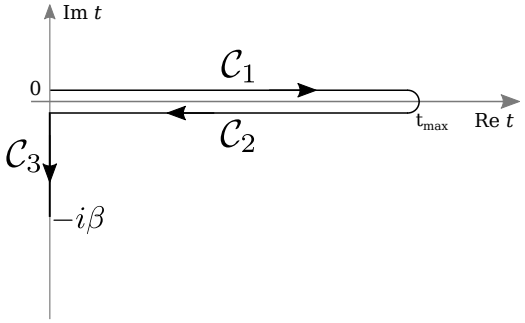

Figure 2.1: L-shaped contour in the complex-time plane.

where $\theta_{\mathcal{C}}(t,t')$ is the generalization of the Heaviside function $\theta(t-t')$ on the contour, i.e. it is 1 if t comes later than t' and 0 otherwise. The sign $\pm$ is minus if both operators are fermionic, i.e. contain an odd number of fermionic operators, and plus otherwise. Note that, since the operators have to be ordered on the contour $\mathcal{C}$, it has to be specified on which branch their time arguments lie on. If the time arguments are equal, the convention is to adopt normal ordering, in which all the creation operators are to the left of all the annihilation operators [10].

Contour-ordered Green's function *Single-particle Green's functions are the fundamental objects of many-body theories. They describe single-particle excitations as well as statistical distributions of particles* [8]. The nonequilibrium Green's function is defined as

$$G(t,t') \equiv -i\langle \mathrm{T}_{\mathcal{C}}\, c(t)c^{\dagger}(t')\rangle, \tag{2.11}$$

where t and t' lie on the contour $\mathcal{C}$, and the spin and orbital indices are omitted for notational simplicity. Since t and t' are on the contour and can belong to different branches, there can be nine different combinations of branches in the time arguments of $G(t,t')$, and therefore nine components of the Green's function ($G_{11}(t,t') : \{t \in C_1, t \in C_1\}$, $G_{12}(t,t') : \{t \in C_1, t \in C_2\}$, ...). However, there are redundancies [8] in the definition which allow to eliminate three out of nine components. Usually, combinations of the remaining six components are used in the form of six linearly-independent physical Green's functions. Using the physical Green's functions instead of all the components in the calculations, allows to exploit the redundancies and symmetries to make the

calculations more efficient. Moreover, they are important in the interpretation of the results, as discussed below. The six physical Green's functions are called G^R (retarded Green's function), G^A (advanced Green's function), G^K (Keldysh Green's function), $G^\rceil$, $G^\lceil$, and G^M (Matsubara Green's function), and are given by

$$G^R(t,t') = -i\theta(t-t')\langle[c(t), c^\dagger(t')]_\mp\rangle, \tag{2.12}$$

$$G^A(t,t') = i\theta(t'-t)\langle[c(t), c^\dagger(t')]_\mp\rangle, \tag{2.13}$$

$$G^K(t,t') = -i\langle[c(t), c^\dagger(t')]_\pm\rangle, \tag{2.14}$$

$$G^\rceil(t,\tau') = \mp i\langle c^\dagger(\tau')c(t)\rangle, \tag{2.15}$$

$$G^\lceil(\tau,t') = -i\langle c(\tau)c^\dagger(t')\rangle, \tag{2.16}$$

$$G^M(\tau,\tau') = -\langle \mathrm{T}_\tau c(\tau)c^\dagger(\tau')\rangle. \tag{2.17}$$

The upper (lower) sign has to be chosen if the c and $c^\dagger$ operators are bosonic (fermionic), $[\cdot,\cdot]_{-(+)}$ is an (anti-)commutator, $t, t' \in \mathcal{C}_1 \cup \mathcal{C}_2$, $\tau, \tau' \in \mathcal{C}_3$, and T_τ is the time-ordering operator on the imaginary-time axis. In addition to the ones listed above, two additional Green's functions can be defined, known as lesser $G^<(t,t')$ and greater $G^>(t,t')$ Green's functions:

$$G^<(t,t') = i\langle c^\dagger(t')c(t)\rangle, \tag{2.18}$$

$$G^>(t,t') = -i\langle c(t)c^\dagger(t')\rangle. \tag{2.19}$$

They are combinations of the retarded, advanced and Keldysh Green's functions:

$$G^< = \frac{1}{2}(G^K - G^R + G^A), \tag{2.20}$$

$$G^> = \frac{1}{2}(G^K + G^R - G^A). \tag{2.21}$$

As mentioned, the physical Green's functions are important because of their intuitive interpretation, which stems from their meaning at equilibrium. When the Hamiltonian H is time-independent, the real-time components of G

depend only on the difference between their arguments and can be substituted with their Fourier transforms. In this case, the imaginary part of the retarded (or advanced) Green's function is proportional to the single-particle spectral function [10]

$$A(\omega) = -\frac{1}{\pi}\mathrm{Im}G^R(\omega) = \frac{1}{\pi}\mathrm{Im}G^A(\omega). \tag{2.22}$$

Moreover, at equilibrium the imaginary part of the lesser Green's function gives the density of occupied states

$$\mp\mathrm{Im}G^<(\omega) = 2\pi A(\omega)f(\omega) \equiv 2\pi N(\omega), \tag{2.23}$$

while the imaginary part of the greater Green's function gives the density of unoccupied states.

$$-\mathrm{Im}G^>(\omega) = 2\pi A(\omega)[1 \pm f(\omega)]. \tag{2.24}$$

As a last remark, all relations concerning contour-ordered Green's functions hold also if the integral $-i\int_{\mathcal{C}} dsH(s)$ in equation (2.9) is substituted with a more general action $\mathcal{S}$ of the form

$$\mathcal{S} = -i\int_{\mathcal{C}} ds\ H(s) - i\int_{\mathcal{C}} dt\, dt'\ c^\dagger(t)\Delta(t,t')c(t'). \tag{2.25}$$

Non-interacting contour-ordered Green's function The equation of motion for the Green's function in the non-interacting case can be easily calculated. For a tight binding model $H_0 = \sum_k[\epsilon_k(t) - \mu]c_k^\dagger c_k$, one can take the derivative of $G_{0,k}(t,t') = -i\langle \mathrm{T}_{\mathcal{C}}\, c_k(t)c_k^\dagger(t')\rangle$ with respect to t and obtain that

$$[i\partial_t + \mu - \epsilon_k(t)]G_{0,k}(t,t') = \delta_{\mathcal{C}}(t,t'). \tag{2.26}$$

Taking the derivative with respect to t' yields an equivalent equation. The above equation can be rephrased into the definition of the differential operator on the contour

$$G_{0,k}^{-1}(t,t') = [i\partial_t + \mu - \epsilon_k(t)]\,\delta_{\mathcal{C}}(t,t'). \tag{2.27}$$

The solution to such equations is

$$G_{0,k}(t,t') = -i[\theta_{\mathcal{C}}(t,t') \pm f(\epsilon(0) - \mu)]e^{-i\int_{t'}^{t} ds\,[\epsilon_k(s)-\mu]}. \tag{2.28}$$

In the general case in which H_0 is not diagonal in the orbitals

$$H_0(t) = \sum_{ij}[v_{ij}(t) - \mu\delta_{ij}]c_i^\dagger c_j \tag{2.29}$$

and the system evolves according to a more general action of the form

$$S = -i \int_{\mathcal{C}} dt\, H_0(t) - i \sum_{ij} \int_{\mathcal{C}} dt\, dt'\, c_i^\dagger(t) \Delta_i j(t,t') c_j(t'), \tag{2.30}$$

both G_0 and G_0^{-1} are matrices in orbital indices, and

$$(G_0^{-1})_{ij}(t,t') = [\delta_{ij}(i\partial_t + \mu) - v_{ij}(t)]\, \delta_{\mathcal{C}}(t,t') - \Delta_{ij}(t,t'). \tag{2.31}$$

Fully-interacting Green's function: Dyson equation
To describe nonequilibrium correlated systems using Green's functions, one has to take account of self-energy corrections Σ to the non-interacting Green's function G_0. In the language of Feynman diagrams, the self-energy is the sum of all one-particle irreducible diagrams of the interacting Green's function G, i.e., diagrams that cannot be separated into two parts by cutting single G_0 lines. [8] The fully interacting Green's function is

$$G = G_0 + G_0 * \Sigma * G_0 + G_0 * \Sigma * G_0 * \Sigma * G_0 + ... \tag{2.32}$$

Equation (2.32) can be rewritten in the form of the following Dyson equation

$$G = G_0 + G_0 * \Sigma * G. \tag{2.33}$$

To see how the introduction of the self-energy corrections change the equation of motion of the fully interacting Green's function with respect to the equation (2.26) for the non-interacting one, we can convolute the operator G_0^{-1} from the left in equation (2.33), obtaining

$$[G_0^{-1} - \Sigma] * G = \delta_{\mathcal{C}}\,. \tag{2.34}$$

From the above equation we can read off the differential operator G^{-1}, which, in abstract notation, is $G^{-1} = G_0^{-1} - \Sigma$. The equation of motion for the fully interacting Green's function becomes, therefore

$$[i\partial_t - h(t)]G(t,t') - \int_{\mathcal{C}} ds\, \Sigma(t,s) G(s,t') = \delta_{\mathcal{C}}(t,t'). \tag{2.35}$$

2.1.2 Dynamical mean-field theory

In general, *the goal of a mean-field theory is to approximate a lattice problem with many degrees of freedom by a single-site effective problem with less degrees of freedom. The underlying physical idea is that the dynamics at a given site*

can be thought of as the interaction of the degrees of freedom at this site with an external bath created by all other degrees of freedom on other sites. [7]

Let us consider a model

$$H = \sum_{\langle ij\rangle,\sigma} v_{ij} c^\dagger_{i\sigma} c_{j\sigma} + \sum_i H^{(i)}_{\rm loc,} \tag{2.36}$$

where $H_{\rm loc}$ is the sum of single-particle terms and local interactions. The key assumptions of dynamical mean-field theory are i) that the electronic self-energy is local in space, i.e. k-independent

$$\Sigma_{ij}(i\omega_n) = \delta_{ij}\Sigma_{ii}(i\omega_n), \tag{2.37}$$

and ii) that $\Sigma_{ii}(i\omega_n)$ and $G_{ii}(\tau)$ can be obtained from an effective impurity model with an action S of the form

$$S_i = -\int_0^\beta d\tau\, H_{\rm loc} - \int_0^\beta d\tau\, d\tau' \sum_\sigma c^\dagger_\sigma(\tau)\Delta_i(\tau-\tau')c_\sigma(\tau'). \tag{2.38}$$

Here, Δ is the hybridization function of the system to a fictitious bath. Given such action S, the local Green's function is

$$G_{ii}(\tau) = -\frac{1}{Z}\,{\rm Tr}[{\rm T}_\tau e^{S_i} c_i(\tau) c_i^\dagger(0)] \tag{2.39}$$

and the differential operator G^{-1}_{ii}

$$G^{-1}_{ii}(i\omega_n) = i\omega_n + \mu - \Delta_i(i\omega_n) - \Sigma_{ii}(i\omega_n). \tag{2.40}$$

Since the Dyson equation of the lattice model

$$G^{-1}_{ii}(i\omega_n) = \delta_{ij}[i\omega_n + \mu - \Sigma_{ii}(i\omega_n)] - v_{ij} \tag{2.41}$$

relates G^{-1}_{ii} and Σ_{ii}, the hybridization function Δ can be eliminated and the set of equations can be closed. A closed functional relation $\Delta[G]$ can be obtained, for example, on the Bethe lattice with nearest neighbour hopping $v_*/\sqrt{z}$, when the coordination $z \to \infty$.[1] In fact, in such case

$$\Delta(i\omega_n) = v_*^2 G(i\omega_n). \tag{2.42}$$

It can be demonstrated [7] that the dynamical mean-field equations are exact when the coordination of the lattice is ∞.

[1] In the Bethe lattice the density of states is semielliptic and is of the form $D(\epsilon) = \frac{1}{2\pi v_*^2}\sqrt{4v_*^2 - \epsilon}$

2.1.3 Nonequilibrium dynamical mean-field theory

The dynamical mean-field theory equations can be extended to the nonequilibrium case by generalizing their arguments from the imaginary time axis to the L-shaped contour discussed in section 2.1.1. As discussed in section 2.1.1, the lattice Green's function $G_{ij}(t,t') = -i\langle \mathrm{T}_{\mathcal{C}}\, c_i(t) c_j^\dagger(t')\rangle$ can be obtained from (equation (2.31))

$$(G^{-1})_{ij}(t,t') = [\delta_{ij}(i\partial_t + \mu) - v_{ij}(t)]\,\delta_{\mathcal{C}}(t,t') - \delta_{ij}\Sigma_{ii}(t,t'),$$

where, again, the self-energy is considered as local[2],

$$\Sigma_{ij} = \delta_{ij}\Sigma_i(t,t'). \tag{2.43}$$

In order to evaluate the correct functional $\Sigma_{ii}[G]$ in $d \to \infty$, it is sufficient to solve a general local model with action

$$\mathcal{S}_i = -i\int_{\mathcal{C}} dt\; H_{\mathrm{loc}}(t) - i\sum_\sigma \int_{\mathcal{C}} dt\, dt'\, c_\sigma^\dagger \Delta_i(t,t') c_\sigma(t') \tag{2.44}$$

where the auxiliary field $\Delta(t,t')$ is chosen such that

$$G_{ii}(t,t') = -i\langle \mathrm{T}_{\mathcal{C}}\, c(t) c^\dagger(t')\rangle_{\mathcal{S}_i}, \tag{2.45}$$

and Σ *is implicitly defined via the Dyson equation* [8]

$$G_{ii}^{-1}(t,t') = (i\partial_t + \mu)\,\delta_{\mathcal{C}}(t,t') - \Sigma_{ii}(t,t') - \Delta_i(t,t'). \tag{2.46}$$

2.2 Nonequilibrium DMFT for the Holstein model

I now discuss how the equations presented in the previous sections have to be written to describe the Holstein model, which has already been discussed in chapter III.1 in a time-dependent mean-field approach. Such time-dependent mean-field approximation cannot capture a very important aspect of the dynamics of coherent oscillations in the out-of-equilibrium dynamics of the Holstein model: the damping of the oscillations. Since dynamical mean-field theory takes, instead, also the incoherent scattering between electrons and phonons in consideration, it is expected that it is able to capture the damping of the dynamics.

[2] Also for contour-ordered Green's functions this is exact in infinite dimensions.

Coherent oscillations of the atomic positions $\langle X \rangle$ take place when the system is in its symmetry-broken phase (as discussed in chapter III.1), in which the atomic sites are separated in two inequivalent sublattices A and B. The nonequilibrium dynamical mean-field equations discussed in the previous sections concern one single site. Such equations can therefore appropriately describe the Holstein model only when the system is in its translationally invariant phase, but not when it is in the symmetry-broken state.

This problem can be fixed writing two sets of equations for the two sublattices. However, the single-site case is simpler and it is useful to discuss it first in order to make clear which are the objects involved in the calculation. The Holstein Hamiltonian is (equation (2))

$$H = \sum_k \epsilon(k) c_k^\dagger c_k + \sum_k \omega_k b_k^\dagger b_k + g \sum_{kq} \big(b_{-q}^\dagger + b_q\big) c_{k+q}^\dagger c_k.$$

With such a Hamiltonian, the equation for the Green's function $G(t,t')$ is

$$\big(i\partial_t + \mu - \mathrm{h}_{\mathrm{loc}}\big) G(t,t') - \big(\Delta(t,t') + \Sigma(t,t')\big) * G(t,t') = \delta_{\mathcal{C}}(t,t'), \qquad (2.47)$$

where $\mathrm{h}_{\mathrm{loc}}$ is the coupling term with the vibrational mode which is local in time, and $\Sigma(t,t')$ is the self-energy describing the retarded interaction between electrons and vibrational mode. The term $\mathrm{h}_{\mathrm{loc}}(t)$ is a Hartree term and corresponds to the off-diagonal element in the mean-field Hamiltonian in equation (1.15). It is therefore

$$\mathrm{h}_{\mathrm{loc}}(t) = -\sqrt{2} g \langle X(t) \rangle. \qquad (2.48)$$

The self-energy $\Sigma(t,t')$ is calculated in the Migdal approximation and is

$$\Sigma(t,t') = i g(t) g(t') G(t,t') D(t,t'), \qquad (2.49)$$

where

$$D(t,t') = -2i \langle \mathrm{T}_{\mathcal{C}}\, X(t) X(t') \rangle \qquad (2.50)$$

is generally called phonon propagator and is the equivalent of the Green's function for the vibrational mode. "Migdal approximation" usually can have two distinct meanings [13]. One is the *unrenormalized* Migdal approximation, in which the *non-interacting* phonon propagator is used in the electronic self-energy, and therefore the dynamics of the vibrational mode is not considered. The other is the *self-consistent* Migdal approximation, in which the *dressed* phonon propagator is used. We are going to use the most complete version

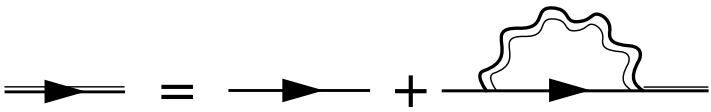

Figure 2.2: Dyson equation for the electronic Green's function in the self-consistent Migdal approximation.

of the approximation, i.e. the self-consistent one. In this case, the Dyson equation for the electrons is of the form displayed in figure 2.2.

In the self-consistent Migdal approximation, also the vibrational mode evolves as a consequence of the interaction with the electrons. Therefore, we also need an equation for the phonon propagator $D(t,t')$. The Dyson equation for $D(t,t')$ is depicted in figure 2.3, and gives an integro-differential equation

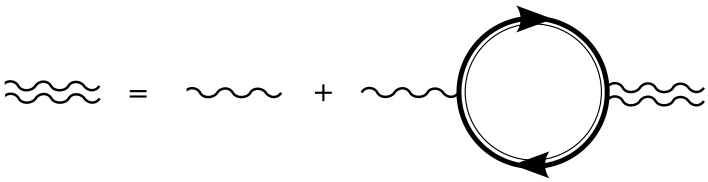

Figure 2.3: Dyson equation for the phononic Green's function in the self-consistent Migdal approximation.

similar to the one for $G(t,t')$:

$$\big(1 - P(t,t') * D_0(t,t')\big) * D(t,t') = D_0(t,t'), \tag{2.51}$$

where $P(t,t')$ is the so-called polarization bubble

$$P(t,t') = -2ig^2 G(t,t')G(t',t), \tag{2.52}$$

and $D_0(t,t')$ is the non-interacting phonon Green's function. The non-interacting $D_0(t,t')$ can be calculated as

$$\begin{aligned} D_0(t,t') = &-2i\big[\,\theta_{\mathcal{C}}(t-t')\big(e^{-i\omega_0(t-t')} + 2\cos(\omega_0(t-t'))\big)\langle b^\dagger b\rangle_\beta \\ &+ \theta_{\mathcal{C}}(t'-t)\big(e^{i\omega_0(t-t')} + 2\cos(\omega_0(t-t'))\big)\langle b^\dagger b\rangle_\beta\big], \end{aligned} \tag{2.53}$$

where $\langle b^\dagger b\rangle_\beta$ is given by the Bose function at frequency ω_0.

One last equation is needed, i.e. the equation of motion for the position $\langle X(t)\rangle$ of the vibrational mode. The vibrational mode is subject to a time-dependent force $F(t)$

$$F(t) = 2\sqrt{2}g\big(\langle c^\dagger(t)c(t)\rangle - 0.5\big). \tag{2.54}$$

This equation completes the set of equations which have to be solved self-consistently at each time t. The self-consistency cycle involves the following steps. At each time t,

1. propagate the phonon propagator $D(t,t')$ using the polarization bubble $P(t,t')$ (equation (2.51)),
2. calculate the electronic self-energy $\Sigma(t,t')$ (equation (2.49)),
3. propagate the vibrational mode position $\langle X(t)\rangle$ (equation (2.54)),
4. calculate $\mathrm{h_{loc}}(t)$ (equation (2.48)),
5. propagate the electronic Green's function $G(t,t')$ (equation (2.47)).

2.2.1 Equations for the two different sites

I now discuss the actual set of equations which have to be solved if one wants to consider both sublattices A and B and, therefore, be able to study the system in its symmetry-broken state. The two sublattices A and B are represented, in the dynamical mean-field approach, by two sites A and B. Each of the sites will have its own electronic Green's function, phononic Green's function and atomic displacement. The equations for the two Green's functions G_A and G_B, respectively of site A and B, are

$$\begin{aligned}\big(i\partial_t + \mu - h^A_{\mathrm{loc}}(t)\big)G_A(t,t') - \big(\Delta_A(t,t') + \Sigma_A(t,t')\big) * G_A(t,t') = \delta_{\mathcal{C}}(t,t'),\\ \big(i\partial_t + \mu - h^B_{\mathrm{loc}}(t)\big)G_B(t,t') - \big(\Delta_B(t,t') + \Sigma_B(t,t')\big) * G_B(t,t') = \delta_{\mathcal{C}}(t,t').\end{aligned} \tag{2.55}$$

The nearest neighbours of a given site all belong to the other sublattice, i.e. the neighbours of the A sites are only B sites and vice versa. Therefore, the hybridization functions Δ will be crossed between the A and B sites:

$$\begin{aligned}\Delta_A(t,t') = G_B(t,t'),\\ \Delta_B(t,t') = G_A(t,t').\end{aligned} \tag{2.56}$$

The time-local part of the equations involve, instead, only the on-site parts. The time-local Hamiltonians are therefore

$$\begin{aligned} h^A_{\rm loc}(t) &= g\langle X_A(t)\rangle, \\ h^B_{\rm loc}(t) &= g\langle X_B(t)\rangle. \end{aligned} \tag{2.57}$$

The atomic displacements on the two sublattices however are not independent, since $\langle X_A(t)\rangle = \langle -X_B(t)\rangle = \langle X(t)\rangle$. On the other hand, $D_A(t,t')$ and $D_B(t,t')$ are only affected by the polarization bubble at site A and site B, respectively. The equations for the phononic Green's functions D_A and D_B involve, therefore, only the on-site polarization bubbles and are

$$\begin{aligned} \big(1 - P_A(t,t') * D_{0,A}(t,t')\big) * D_A(t,t') &= D_{0,A}(t,t'), \\ \big(1 - P_B(t,t') * D_{0,B}(t,t')\big) * D_B(t,t') &= D_{0,B}(t,t'). \end{aligned} \tag{2.58}$$

The self-consistency cycle is analogous to the one described for the single-site set-up. Apart from duplicating it to include both sites A and B, the last point has to include the crossed hybridization functions Δ as described in equation (2.56).

2.3 Current-current correlators

Once the out-of-equilibrium Green's function is known, the out-of-equilibrium optical properties of the system can be computed. How a system responds to impinging light, i.e. to the application of a vector potential, and then re-emits light is determined by current-current correlators which give the optical susceptibility. At the same time, as I will show, other components or combinations of current-current correlators determine other properties of the re-emitted light. In section 2.3.4, I will focus on the calculation of the fluctuations of the intensity of light pulses reflected by the out-of-equilibrium system. In the following two sections, I will first review the derivation of the expression for the optical susceptibility $\chi(t,t')$ and then I will write down fluctuation-dissipation relations for such current-current correlators.

2.3.1 Optical susceptibility

This section reviews results discussed by Eckstein and Kollar in Ref. [14] for the case of a single site. The optical susceptibility of a system is given by

$$\chi_{\alpha\beta}(t,t'') = \frac{\delta}{\delta A_\beta(t'')}\langle j_\alpha(t)\rangle, \tag{2.59}$$

where α and β are Cartesian indices, and

$$\langle j_\alpha(t)\rangle = v_\alpha n = -\frac{ie}{V}\sum_k v_\alpha G_k^<(t,t). \tag{2.60}$$

Inserting equation (2.60) in equation (2.59) we obtain

$$\chi_{\alpha\beta}(t,t'') = -\frac{ie}{V}\sum_k\left(\frac{\delta v_\alpha(t)}{\delta A_\beta(t'')}G_k^<(t,t) + v_\alpha(t)\frac{\delta G_k^<(t,t)}{\delta A_\beta(t'')}\right), \tag{2.61}$$

where the first term is called diamagnetic susceptibility $\chi^{\rm dia}_{\alpha\beta}(t,t'')$ and the second one paramagnetic susceptibility $\chi^{\rm pm}_{\alpha\beta}(t,t'')$. The diamagnetic contribution to the optical susceptibility can be directly rewritten as

$$\chi^{\rm dia}_{\alpha\beta}(t,t'') = -\frac{ie}{V}\delta(t-t'')\sum_k \partial_{k_\beta}\partial_{k_\alpha}\epsilon_k(t)G_k^<(t,t). \tag{2.62}$$

To obtain the final expression for the paramagnetic optical susceptibility

$$\chi^{\rm pm}_{\alpha\beta}(t,t'') = -\frac{ie}{V}\sum_k v_\alpha(t)\frac{\delta G_k^<(t,t)}{\delta A_\beta(t'')}, \tag{2.63}$$

we have to calculate instead $\delta G_k^<(t,t)$. This can be done noting that $\delta G_k(t_1,t_2)$ can be obtained from

$$\delta G_k(t_1,t_2) = -\big(G_k * \delta G_k^{-1} * G_k\big)(t_1,t_2). \tag{2.64}$$

G^{-1} can be written as the difference between the non-interacting G_0^{-1} and the self-energy Σ. Therefore $\delta G_k^{-1} = \delta G_{0,k}^{-1} - \delta\Sigma$. If we neglect the vertex corrections, we can set $\delta\Sigma$ to zero, and equation (2.64) becomes

$$\begin{aligned}
\delta G_k(t_1,t_2) &= -\big(G_k * [\delta G_{0,k}^{-1}] * G_k\big)(t_1,t_2) \qquad (2.65)\\
&= \frac{e}{\hbar c}\big(G_k * [\delta_{\mathcal C}(t_1,t_2)v_\gamma(t_1)\delta A_\gamma(t1)] * G_k\big)(t_1,t_2)\\
&= \frac{e}{\hbar c}\int_{\mathcal C} ds\, G_k(t_1,s)\int_{\mathcal C} dr\,\delta_{\mathcal C}(s,r)v_\gamma(s)\delta A_\gamma(s)G_k(r,t_2)\\
&= \frac{e}{\hbar c}\int_{\mathcal C} ds\, G_k(t_1,s)v_\gamma(s)\delta A_\gamma(s)G_k(s,t_2)\\
&= \frac{e}{\hbar c}\int_{\mathcal C_1} ds_+\, G_k(t_1,s_+)v_\gamma(s)\delta A_\gamma(s)G_k(s_+,t_2)
\end{aligned}$$

$$
\begin{aligned}
&- \int_{\mathcal{C}_2} ds_- \, G_k(t_1, s_-) v_\gamma(s) \delta A_\gamma(s) G_k(s_-, t_2) \\
&+ \int_{\mathcal{C}_3} id\tau \, G_k(t_1, -i\tau) v_\gamma(-i\tau) \delta A_\gamma(-i\tau) G_k(-i\tau, t_2). \qquad (2.66)
\end{aligned}
$$

Taking the derivative of $G_k(t_1, t_2)$ with respect to $\delta A_\gamma(t')$ selects $\delta_{\beta\gamma}\, \delta_{\mathcal{C}}(s, t')$, giving

$$
\begin{aligned}
\chi^{\rm pm}_{\alpha\beta}(t, t'') &= \frac{ie^2}{\hbar c V} \sum_k v_\alpha(t) v_\beta(t'') \big(G_k^{++}(t, t'') G_k^{+-}(t'', t) - G_k^{+-}(t, t'') G_k^{--}(t'', t) \big) \\
&= -2 \frac{e^2}{\hbar c V} \sum_k v_\alpha(t) v_\beta(t'') \mathrm{Im} \big(G_k^R(t, t'') G_k^<(t, t'') \big) \\
&= -2 \frac{e^2}{\hbar c V} \sum_k v_\alpha(t) v_\beta(t'') \big(G_k(t, t'') G_k(t'', t) \big)^R(t, t'') \\
&= -2 \frac{e^2}{\hbar c V} \sum_k v_\alpha(t) v_\beta(t'') \big(G_k G_k \big)^R(t, t''). \qquad (2.67)
\end{aligned}
$$

The susceptibility $\chi^{\rm pm}(t, t'')$ is, therefore, given by the retarded component of the so-called polarization bubble $(G_k G_k)$.

The Green's function G_k at momentum k actually depends only on ϵ_k and not directly on k, because it is obtained from the equation

$$
G_{\epsilon_k} = (i\partial_t + \mu - \epsilon_k - \Sigma)^{-1}, \qquad (2.68)
$$

where $\Sigma \neq \Sigma(k)$. The momentum summation for the paramagnetic term can, therefore, be substituted with the following integral along the energy axis

$$
\int d\epsilon \, D_{\alpha\beta}(\epsilon) \mathrm{Im} \big(G_k^R(t, t'') G_k^<(t, t'') \big), \qquad (2.69)
$$

where $D_{\alpha\beta}(\epsilon) = \sum_k \delta(\epsilon - \epsilon_k) v_{k,\alpha} v_{k,\beta}$ has the form of a modified density of states. For the Bethe lattice it takes the form [14]

$$
\begin{aligned}
D_{\alpha\beta}(\epsilon) =& \delta_{\alpha\beta} \frac{Wa^2}{4\hbar^2 \sqrt{1 - (\epsilon/W)^2}} \cdot \\
& \cdot \exp\left(-2 \left[\mathrm{erf}^{-1} \left(\frac{\epsilon \sqrt{1 - (\epsilon/W)^2} + W \sin^{-1}(\epsilon/W)}{\pi W/2} \right) \right]^2 \right),
\end{aligned}
$$

where W is the bandwidth. In the numerical evaluation of the integral (2.69), the change of variable $\epsilon = -2\cos(\theta)$ (where $W = 2$) is useful to avoid singularities. With it, $D(\epsilon)d\epsilon$ becomes

$$D(\epsilon)d\epsilon = d\theta \frac{a^2}{\hbar^2} \exp\left(-2\left[\mathrm{erf}^{-1}\left(\frac{-2\big(\cos(\theta)\sin(\theta) - \theta\big)}{\pi} - 1\right)\right]^2\right). \tag{2.70}$$

With such equations, the optical properties of the system, like the optical conductivity or the reflectivity, can be computed. While their application to the single-site case is as-written, I will discuss how to use them in the set-up with the two sites A and B in the following section.

2.3.2 Optical susceptibility with two sublattices

The previous section discussed the calculation of the optical susceptibility in the case of a single-site problem. In the case of two sites $\{\mathrm{a,b}\}$[3] representing two inequivalent sublattices, we can still calculate the polarization bubble and the optical susceptibility. The Dyson equation is still

$$G_{\epsilon_k}(t,t') = (i\partial_t + \mu - h(t) - \Sigma(t,t'))^{-1}, \tag{2.71}$$

where in this case G_{ϵ_k}, h and Σ are matrices. In the $\{\mathrm{a,b}\}$ basis they are

$$G_{\epsilon_k}(t,t') = \begin{pmatrix} G^{a,a}_{\epsilon_k} & G^{a,b}_{\epsilon_k} \\ G^{b,a}_{\epsilon_k} & G^{b,b}_{\epsilon_k} \end{pmatrix}(t,t'), \tag{2.72}$$

$$h(t) = \begin{pmatrix} gX(t) & \epsilon_k(t) \\ \epsilon_k(t) & -gX(t) \end{pmatrix}, \tag{2.73}$$

and

$$\Sigma(t,t') = \begin{pmatrix} \Sigma_a(t,t') & 0 \\ 0 & \Sigma_b(t,t') \end{pmatrix}. \tag{2.74}$$

The k-summation in the expression for the paramagnetic susceptibility χ^{pm} (equation (2.67)) is

$$\begin{aligned} \sum_k v_k(t)v_k(t')\big(&G_{k,k}G_{k,k} + G_{k+Q,k+Q}G_{k+Qk+Q} \\ &- G_{k,k+Q}G_{k+Q,k} - G_{k+Q,k}G_{k,k+Q}\big)^R(t,t'), \end{aligned} \tag{2.75}$$

[3] In this section, the lowercase letters are preferred to A and B, to keep the notation more orderly.

Since

$$\hat{G}_k = \begin{pmatrix} G_k^{aa} & G_k^{ab} \\ G_k^{ba} & G_k^{bb} \end{pmatrix} = \frac{1}{2}\begin{pmatrix} 1 & 1 \\ 1 & -1 \end{pmatrix}\begin{pmatrix} G_{k,k} & G_{k,k+Q} \\ G_{k+Q,k} & G_{k+Q,k+Q} \end{pmatrix}\begin{pmatrix} 1 & 1 \\ 1 & -1 \end{pmatrix} \quad (2.76)$$

in the {a,b} basis the k-summation in equation (2.75) becomes

$$\sum_k v_k(t)v_k(t')\big(G_k^{a,a}G_k^{b,b} + G_k^{b,b}G_k^{a,a} + G_k^{a,b}G_k^{b,a} + G_k^{b,a}G_k^{a,b}\big)^R(t,t'), \quad (2.77)$$

As an example, using relations between G and G^* listed in reference [8], the first term in the above expression is

$$\begin{aligned}\big(G_k^{a,a}G_k^{b,b}\big)^R(t,t') &= \big(G_k^{a,a}G_k^{b,b}\big)^>(t,t') - \big(G_k^{a,a}G_k^{b,b}\big)^<(t,t') \\ &= \big(G_k^{a,a}G_k^{b,b}\big)^>(t,t') + \Big(\big(G_k^{b,b}G_k^{a,a}\big)^<(t',t)\Big)^*.\end{aligned} \quad (2.78)$$

These adjustments allow to compute the optical susceptibility as described in the previous section also in the two-site problem.

2.3.3 Fluctuation-dissipation relations

The previous two sections deal with the optical susceptibility, i.e. the quantity $\langle\big[j(t), j(t')\big]\rangle$, which is related to the retarded component of the polarization bubble $(GG)^R(t,t')$. Another combination of the correlator $\langle j(t)j(t')\rangle$ and $\langle j(t')j(t)\rangle$ is their anticommutator $\langle\big\{j(t), j(t')\big\}\rangle$. In analogy to χ, in the following I will call K the anticommutator

$$K(t,t') = \langle\big\{j(t), j(t')\big\}\rangle = \langle j(t)j(t') + j(t')j(t)\rangle. \quad (2.79)$$

As shown below, this quantity is related to the Keldysh component of the polarization bubble $(GG)^K(t,t')$. When the system under consideration is in a thermal state, such pairs of quantities ($(GG)^R(t,t')$ and $(GG)^K(t,t')$, or χ and K) are related by the fluctuation-dissipation relation. For χ and K, the latter is

$$\mathrm{Im}\chi^{\mathrm{pm}}(t,\omega) = \tanh\left(\frac{\beta\omega}{2}\right)\mathrm{Im}K(t,\omega), \quad (2.80)$$

where the two functions f have been partially Fourier-transformed according to

$$f(t_p,\omega) = \frac{1}{2\pi}\int ds\; e^{i\omega s} f(t_p + s/2, t_p - s/2). \quad (2.81)$$

Since this kind of relation holds only for thermal states, the comparison between χ and K will prove useful in the study of the thermalization dynamics that I will discuss in section 3.2.

Analogously to the derivation of the optical susceptibility χ of section 2.3.1, $K_{\alpha\beta}(t,t')$ is given by the sum of $K^{+}_{\alpha\beta}(t,t')$ and $K^{-}_{\alpha\beta}(t,t')$, where

$$\begin{aligned} K^{+}_{\alpha\beta}(t,t') &= \frac{ie^2}{\hbar cV}\sum_k v_\alpha(t)v_\beta(t')G^{++}_k(t,t')G^{+-}_k(t',t) \\ &= \frac{ie^2}{\hbar cV}\sum_k v_\alpha(t)v_\beta(t')G^{>}_k(t,t')G^{<}_k(t',t) \\ &= \frac{ie^2}{\hbar cV}\sum_k v_\alpha(t)v_\beta(t')\big(G_k(t,t')G_k(t',t)\big)^{>}(t,t') \\ &= \frac{ie^2}{\hbar cV}\sum_k v_\alpha(t)v_\beta(t')\big(G_kG_k\big)^{>}(t,t') \end{aligned} \tag{2.82}$$

and

$$\begin{aligned} K^{-}_{\alpha\beta}(t,t') &= -\frac{ie^2}{\hbar cV}\sum_k v_\alpha(t)v_\beta(t')G^{+-}_k(t,t')G^{--}_k(t',t) \\ &= -\frac{ie^2}{\hbar cV}\sum_k v_\alpha(t)v_\beta(t')G^{<}_k(t,t')G^{>}_k(t',t) \\ &= -\frac{ie^2}{\hbar cV}\sum_k v_\alpha(t)v_\beta(t')\big(G_kG_k\big)^{<}(t,t'). \end{aligned} \tag{2.83}$$

$K_{\alpha\beta}(t,t')$ is, therefore,

$$K_{\alpha\beta}(t,t') = -\frac{ie^2}{\hbar cV}\sum_k v_\alpha(t)v_\beta(t')\big(G_kG_k\big)^{K}(t,t'). \tag{2.84}$$

For the evaluation of the above expresison, the k-summation can be substituted with an energy integral as shown in section 2.3.1.

2.3.4 Fluctuations of the optical properties

Up to now, the discussion about the optical properties of the system has been focussed on the commutator and anticommutator of the two-times current-current correlator. The optical susceptibility $\chi(t,t')$ can be obtained from

spectroscopic measurements. The knowledge of $K(t,t')$ or of $\langle j(t)j(t')\rangle$ would then allow to perform the fluctuation-dissipation analysis discussed in the prevoius section and possibly to extract furter information. In this section I will present our discuss on how the quantity $\langle j(t)j(t')\rangle$ can be obtained in pump-probe experiments measuring the fluctuations of the intensity of the probe pulses reflected from the sample.

The intensity of light pulses is

$$I \propto \int\limits_{pulse} dt\, E(t)^2, \tag{2.85}$$

and its variance can be written as

$$\mathrm{var}[I] = \langle I^2\rangle - \langle I\rangle^2. \tag{2.86}$$

Here, we will postpone the explicit consideration of the intrinsic statistical properties of the probe light. Since the reflected light is produced by the currents in the sample, below we take the fluctuations of its intensity as solely determined by the fluctuations of the current in the sample. With $E(t) \to \langle E(t)\rangle + \delta E(t)$, the two terms in equation (2.86) are

$$\begin{aligned}\langle I^2\rangle = &\int dt_1 dt_2\, \langle E(t_1)\rangle^2 \langle E(t_2)\rangle^2 \,+ \\ &+ 4\int dt_1 dt_2\, \langle E(t_1)\rangle \langle E(t_2)\rangle \langle \delta E(t_1)\delta E(t_2)\rangle \,+ \\ &+ \int dt_1 dt_2 \Big(\langle E(t_1)\rangle^2 \langle \delta E(t_2)^2\rangle + \langle E(t_2)\rangle^2 \langle \delta E(t_1)^2\rangle \,+ \langle \delta E(t_1)^2 \delta E(t_2)^2\rangle \Big)\end{aligned} \tag{2.87}$$

and

$$\begin{aligned}\langle I\rangle^2 = \int dt_1 dt_2 \Big(&\langle E(t_1)\rangle^2 \langle E(t_2)\rangle^2 + \langle E(t_1)\rangle^2 \langle \delta E(t_2)\rangle^2 + \\ &+ \langle \delta E(t_1)\rangle^2 \langle E(t_2)\rangle^2 + \langle \delta E(t_1)^2\rangle \langle \delta E(t_2)^2\rangle \Big).\end{aligned} \tag{2.88}$$

The variance of the intensities therefore is

$$\begin{aligned}\mathrm{var}[I] = \int dt_1 dt_2 \Big(&4\langle E(t_1)\rangle \langle E(t_2)\rangle \langle \delta E(t_1)\delta E(t_2)\rangle \,+ \\ &+ \langle \delta E(t_1)^2 \delta E(t_2)^2\rangle - \langle \delta E(t_1)^2\rangle \langle \delta E(t_2)^2\rangle \Big).\end{aligned} \tag{2.89}$$

In some cases, each of the last two terms in equation (2.89) factorizes, e.g. if the light is in a coherent state, and they cancel out. Even when this does not happen, to second order in δE we have that

$$\mathrm{var}[I] = 4 \int dt_1 dt_2 \langle E(t_1)\rangle \langle E(t_2)\rangle \langle \delta E(t_1)\delta E(t_2)\rangle. \tag{2.90}$$

In the above expression, $\langle \delta E(t_1)\delta E(t_2)\rangle$ can be replaced by $\langle \delta j(t_1)\delta j(t_2)\rangle$. In fact,

$$\langle \delta E(t_1)\delta E(t_2)\rangle \sim \langle \delta A(t_1)\delta A(t_2)\rangle, \tag{2.91}$$

and the expression for the vector potential radiated from a general current density is [15]

$$A(\vec{r},t) = \frac{\mu_0}{4\pi} \int \frac{j(\vec{r}\,', t - r/c)}{r} d\vec{r}\,'. \tag{2.92}$$

Hence, we can write

$$\langle \delta A(t_1)\delta A(t_2)\rangle \sim \langle \delta j(t_1)\delta j(t_2)\rangle. \tag{2.93}$$

The correlator $\langle \delta j(t_1)\delta j(t_2)\rangle$ will be affected by the field of the impinging light pulses. In fact, from the Kubo formula we obtain that

$$\langle \delta j(t_1)\delta j(t_2)\rangle = \langle \delta j(t_1)\delta j(t_2)\rangle_0 - i \int_{t_0}^{t} dt' \left\langle [\delta j(t_1)\delta j(t_2), A(t')j(t')]\right\rangle. \tag{2.94}$$

Since the current density is zero at equilibrium, $j(t) = \langle j(t)\rangle_0 + \delta j(t) = \delta j(t)$ and the above expression becomes

$$\langle \delta j(t_1)\delta j(t_2)\rangle = \langle j(t_1) j(t_2)\rangle_0 - i \int_{t_0}^{t} dt' \left\langle [\delta j(t_1)\delta j(t_2), A(t')j(t')]\right\rangle. \tag{2.95}$$

However, limiting the total expression of $\mathrm{var}[I]$ to the lowest order in the electric field we can neglect the perturbation of $\langle \delta j(t_1)\delta j(t_2)\rangle$ by the probe pulse and write

$$\mathrm{var}[I] \sim \int dt_1 dt_2 \langle E(t_1)\rangle \langle E(t_2)\rangle \langle j(t_1) j(t_2)\rangle_0. \tag{2.96}$$

With the same arguments as above, we can substitute also $\langle E(t)\rangle$ with the current generating it, obtaining

$$\mathrm{var}[I] \sim \int dt_1 dt_2 \langle j(t_1)\rangle \langle j(t_2)\rangle \langle j(t_1) j(t_2)\rangle_0. \tag{2.97}$$

The currents in the sample are generated by the incoming electric field, via $j(t) = \int_{-\infty}^{t} ds\ \sigma(t-s)E_{\text{in}}(s)$:

$$\begin{aligned}\text{var}[I] \sim \int dt_1 dt_2 \Bigg(\int_{-\infty}^{t_1} ds_1\ \sigma(t_1 - s_1) E_{\text{in},t_p}(s_1) \Bigg) \cdot \\ \Bigg(\int_{-\infty}^{t_2} ds_2\ \sigma(t_2 - s_2) E_{\text{in},t_p}(s_2) \Bigg) \cdot \\ \langle j(t_1) j(t_2) \rangle_0 . \end{aligned} \tag{2.98}$$

In the above equation, E_{in,t_p} denotes the electric field of the probe pulse with the envelope centred at pump-probe delay t_p.

Besides the fluctuations of the current in the sample, an additional source of fluctuation of the intensity of the reflected probe pulses is the statistics of the incoming probes, due to their (quantum) state. Since in equation (2.95) we consider only the first term, i.e. only the fluctuations of the current in the sample when it is not perturbed by the probe pulses, here we can consider the two sources of fluctuations of I as independent. In the standard case of a coherent state of the incoming probe, var$[I]$ will display (in addition to equation (2.96)) a shot-noise-like term proportional to the intensity of the probe pulse at the detector.

At equilibrium and at standard temperatures, the variance of I due to the fluctuations of the current is negligible at probe photon energies in the visible and infrared spectral range, since the fluctuations of the current are very small at such frequencies. In such condition, only the intrinsic fluctuations are relevant, as it is usually assumed in quantum optics for the reflection of light by a mirror. When the sample which reflects the probe pulse is out of equilibrium, instead, $\langle j(t_1) j(t_2) \rangle$ can significantly contribute to the total fluctuation of the intensity.

Chapter 3

Dynamical mean-field theory - Results

I now discuss the results of the nonequilibrium dynamical mean-field theory calculations. In the first section of this chapter I will discuss the similarities of the results with the ones obtained in the time-dependent mean-field approach and the features added by dynamical mean-field theory. Then, I will discuss the thermalization dynamics of the system after the excitation and, finally, what kind of information can be extracted from the fluctuations of the optical properties, comparing our calculations with experimental results obtained on bismuth single crystals.

To start, figure 3.1 shows the equilibrium gap $g\langle X\rangle_{\mathrm{eq}}$ of the system. As parameters for the calculations we chose a coupling constant between the electrons and the vibrational mode $g = 0.34$, and a bare frequency of the vibrational mode $\omega_0 = 0.2$. The choice of a rather high ω_0, which is at the limit of the adiabatic regime, is dictated by the relatively short times that can be reached in nonequilibrium dynamical mean-field theory because of memory issues. As can be seen in figure 3.1, at low enough temperatures (high β) the system is in its dimerized phase. As discussed in the context of the mean-field calculation, the value of the atomic positions are the distance from the undistorted situation. A value different from zero therefore means that the system is in its symmetry-broken phase. Since the lattice is dimerized, the atomic positions are alternatively displaced from the undistorted positions on the one and on the other side. This allows to distinguish between two different sublattices, A and B. As discussed in section 2.2.1, the atoms on the A

sublattice will have a positive displacement $X_A = +X$ while the atoms on the B sublattice will have an opposite displacement $X_B = -X$. In the following I will simply refer to the "atomic positions" X as the positions X_A.

When the temperature is high, i.e. β is small, the system is in its translationally invariant phase, with $\langle X \rangle_{\text{eq}} = 0$ and two equivalent A and B sublattices. The transition temperature from the symmetry-broken phase to the translationally invariant one in around $\beta_c \simeq 5$. The plot lacks data points close to β_c because the calculation does not converge there.

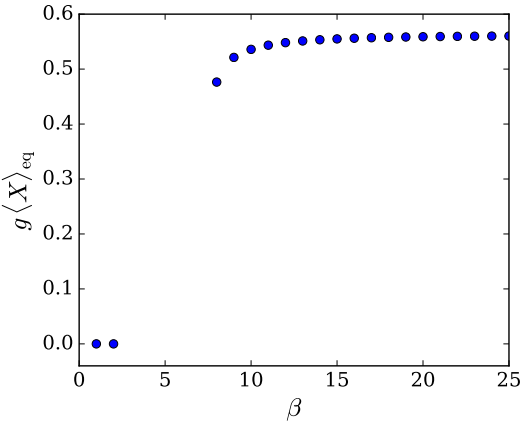

Figure 3.1: Gap of the system in its ground state for different inverse temperatures β. The lack of points close to the transition is due to difficulties in the convergence of the dynamical mean-field iterations.

3.1 Displacive excitation

Once the initial state is calculated, the out-of-equilibrium calculation has to start from the excitation. In the time-dependend mean-field calculations discussed in chapter III.1, the system was excited by a light pulse. A more convenient excitation in the case of dynamical mean-field calculations is to have an impulsive variation of the hopping h, i.e. have $h(t) = h + \delta h(t)$ with $\delta h(t)$ a sharp Gaussian, while the coupling constant g between the electronic density and the vibrational mode is kept constant. This destabilizes the symmetry-broken state, because it makes the system istantaneously more metallic. Figure 3.2 shows a sample hopping as a function of time. At "pump-probe delay"

zero, the hopping impulsively changes according to a sharp Gaussian, while it returns to unity immediately after.

Given that such an excitation scheme is more easily implementable than the one involving a light pulse, we have to check under which conditions it produces compatible effects with the ones we expect from a light pulse. With an impulsive *increase* of the hopping, the oscillation of the vibrational mode starts with an expansion of the dimers, i.e. with the atoms going towards their translationally invariant positions. If the perturbation were an impulsive *decrease* of the hopping instead, the ratio $\frac{g}{\omega}$ would impulsively increase. Even though such excitation produces, in the end, an excitation of the system towards a less dimerized phase, the oscillation of the atomic postions with $\delta h < 0$ starts towards a more dimerized condition, which does not match what happens when electrons are photoexcited out of the dimer by an ultrashort light pulse.

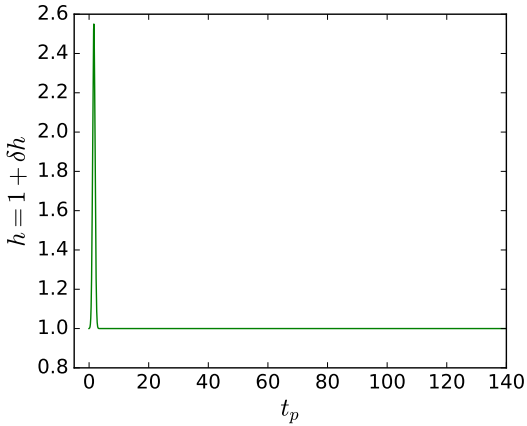

Figure 3.2: Time-dependent hopping. The impulsive change shortly after $t_p = 0$ excites the system.

Atomic displacements As initial state for the out-of-equilibrium calculation we chose the one at $\beta = 25$, i.e. in the symmetry-broken phase with an equilibrium distortion $\langle X \rangle_{\text{eq}} = 1.65$ and a gap $2\Delta = 1.1$. As expected from the results already obtained from the time-dependent mean-field calculations, the excitation of the system on sufficiently short timescales produces coherent oscillations of the atomic positions. Figure 3.3a shows the expectation value

$\langle X(t)\rangle$ of the atomic positions as a function of time for different excitation intensities. After the excitation, the atoms start oscillating around a $\overline{\langle X\rangle}$ smaller than $\langle X\rangle_{\text{eq}}$ ($\overline{\langle\cdot\rangle}$ denotes temporal average), which is however still different from zero. This means that the dimers are loosened, but the system remains in the symmetry-broken phase.

Figure 3.3b shows $\langle X(t)\rangle$ for the same initial parameters but for very intense excitations. In these cases, the symmetry-broken phase is melted. After the excitation the atoms oscillate, but the oscillation takes place around the undistorted position, i.e. $\overline{\langle X\rangle} = 0$.

As a function of the excitation intensity δh, three aspects of the dynamics can be discussed: the amplitude of the oscillation of $\langle X(t)\rangle$, its frequency, and its damping.

First, the stronger the excitation the larger the amplitude of the oscillation, as expected. In addition to this, it can be noted that there is a regime in which, during the oscillation, the system experiences even stronger distortions than at equilibrium (black horizontal line). This means that the excitation gives sufficient momentum to the vibrational mode that it can recoil beyond its starting position.

Second, the frequency ω^* of the oscillation of X changes as a function of the excitation intensity δh, as shown in figures 3.4a and b. Figure 3.4a shows the Fourier transform of $\langle X(t)\rangle$ for selected δh, while figure 3.4b shows the peak frequency as a function of δh. For very low excitation intensities, the oscillation frequency is $\omega^*|_{\delta h=0} = 0.15$. This value is different from the bare frequency $\omega_0 = 0.2$ inserted as a parameter, because of the coupling of the vibrational mode with the electrons. The frequency ω^* decreases with increasing δh until it reaches 0 at a critical value of $\delta h_c \simeq 1.7$ (grey vertical line). δh_c is the threshold value for the melting of the symmetry-broken phase, and with such an excitation the period of the oscillation tends to infinity. Just as in the mean-field case (section 1.3), this is what is generally called critical slowing down.

Above such threshold value of excitation intensity δh, as shown in figure 3.3b, the symmetry-broken phase melts, and the oscillation frequency recovers from zero and grows again. In the mean-field case (section 1.3 of chapter 1), above the critical excitation intensity the frequency tends to the bare frequency of the vibrational mode, which is larger than the oscillation frequency for very low excitation intensities. Here, instead, the limit value of the frequency for large intensities is smaller than the low-intensity value, and is not the bare frequency. In fact, the system is metallic once it has been brought to the translationally invariant phase, and the screening of the vibrational frequency through the self-energy is more effective than in the dimerized

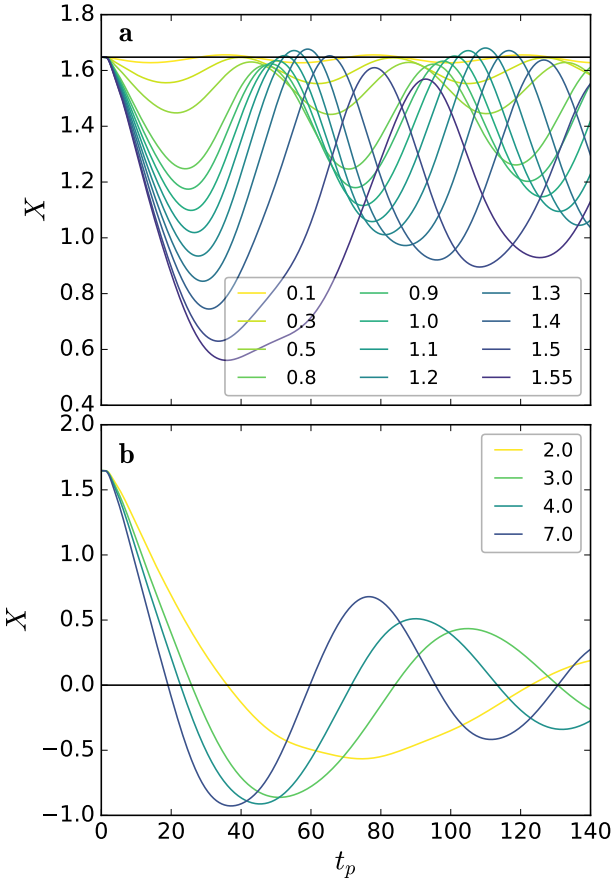

Figure 3.3: **a** (**b**) Atomic displacemens $\langle X(t)\rangle$ as a function of time t_p for different δh below (above) the critical value δh_c. The horizontal black line in panel **a** is the equilibrium value of $\langle X\rangle$. The horizontal black line in panel **b** is the value (0) of $\langle X\rangle$ in the translationally invariant phase.

phase.

Third, the oscillation of $\langle X(t)\rangle$ is damped. This is the main feature added by nonequilibrium dynamical mean-field theory to what we could obtain in a time-dependent mean-field approach and is the reason why we shifted to the DMFT framework. The damping of the dynamics and incoherent scattering

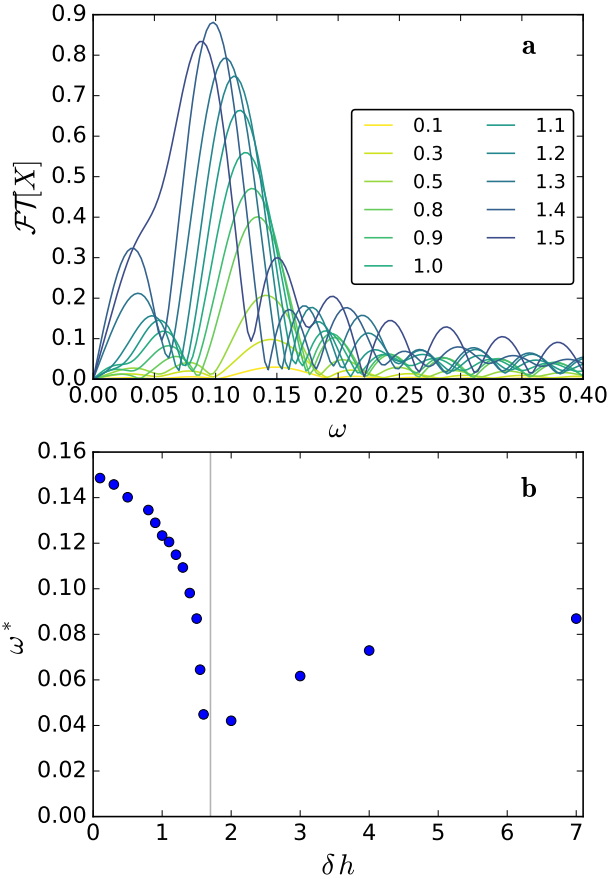

Figure 3.4: **a** Modulus of the Fourier transform of $\langle X(t) \rangle$ for different excitation intensities δh. Only the main peaks have to be considered, while the side peaks are a product of spectral leakage. **b** Peak frequency of the Fourier transforms of $\langle X(t) \rangle$ as a function of δh. Grey vertical line: threshold value δh for the melting of the symmetry-broken phase.

are very important ingrediends in the temporal evolution of out-of-equilibrium states of matter. They have to be included in the calculations, if the goal is to study the state of the system beyond the expectation values of simple observables.

The damping timescale is not the same constant for every excitation intensity, but becomes shorter as δh is increased, because more incoherent scattering is possible when the system is more excited.

Besides the three main aspects discussed, one should also note that the oscillation of $\langle X(t)\rangle$ is distorted from a perfect sinusoidal function when the system is close to melting. This consideration brings me to the brief discussion of the behaviour of the electronic occupations N_A and N_B of the sites on the two sublattices A and B. Since the system is at half filling, their sum is 1 and I will discuss therefore just one of the two occupations, namely N_A.

One should note that the numerical results obtained in the excitation regime leading to the melting of the symmetry broken phase ($\delta h > \delta h_c$) have to be taken with some care in the comparison with the experimental results on Peierls' systems. While the melting of the dimerized phase has been observed [11], the oscillations are absent in such regime, presumably because the anharmonicities overdamp the vibrational mode. For this reason, the most important parts of the following discussion are limited to $\delta h < \delta h_c$.

Occupation of the A and B sites Figures 3.5a and b show $\langle N(t)\rangle$ in the same excitation regimes described for $\langle X(t)\rangle$ in figures 3.3a and b, i.e. below and above the melting of the symmetry-broken state. The behaviour of the occupation of the sites on sublattice A (and the subsequent occupation of the B sites) is rather analogous to the one of the lattice distortion $\langle X(t)\rangle$. In fact, $\langle X(t)\rangle$ changes, via $\mathrm{h_{loc}}(t)$, the potential on the A and B sublattices, thus modulating the distribution of the charge density among them.

We can now analyze the time-dependent spectral function and the occupied density of states on the two sublattices A and B. Figures 3.6a, b, c, and d show the time-dependent spectral function $A(t_p,\omega) = -\frac{1}{\pi}G^R(t_p,\omega) = -\frac{1}{\pi}\frac{1}{2\pi}\int ds\ e^{i\omega s}G^R(t_p+s/2,t_p-s/2)$ for the A and B sites and for two excitation intensities δh, respectively. The side panels show $\langle X(t_p)\rangle$ as a reference for the oscillation. Analogously, figures 3.7a, b, c, and d show the time-dependent occupied density of states $-iG^<(t_p,\omega) = -i\frac{1}{2\pi}\int ds\ e^{i\omega s}G^<(t_p+s/2,t_p-s/2)$. There are four things to notice about these results. The first two can be seen analyzing $A(t_p,\omega)$ while the last two concern mostly $-iG^<(t_p,\omega)$.

First, after the excitation, the density of states at the Fermi energy is not zero, as it is instead at equilibrium. Second, the energies of the bands oscillate together with the atomic displacement. When $\langle X(t)\rangle$ is larger, the gap between the upper and lower bands is larger. As expected, with a more contracted dimer the "bonding" and "antibonding" levels are further apart from each other.

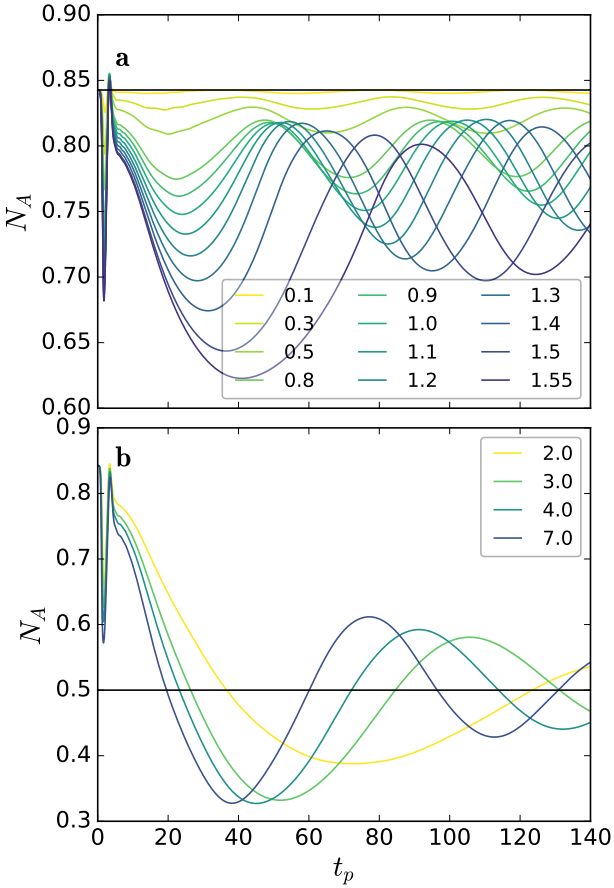

Figure 3.5: **a** (**b**) Electronic occupation of the A sites $\langle N_A(t)\rangle$ as a function of time t_p for different δh below (above) the critical value δh_c. The horizontal black line in panel **a** is the equilibrium value of $\langle N_A\rangle$. The horizontal black line in panel **b** is the value (0.5) of $\langle N_A\rangle$ in the translationally invariant phase. Note that $\langle N_B(t)\rangle = 1.0 - \langle N_A(t)\rangle$

Third, as a function of the phase of the oscillation, charge is trasferred from site A to site B and vice-versa, as already shown by the plots of $\langle N(t)\rangle$. In the colour plot in figures 3.7, this can be seen as the alternation of more intense yellow regions in the plots for the A and B sites.

Fourth, there is a distinction between the populations in the upper bands of the A and B sites. On the A sublattice only the lower band is occupied in a relevant way, even after the excitation. On the B sublattice, instead, also the upper band is partially occupied. This is because on the B sites the density of states in the upper band is larger than on the A sites.

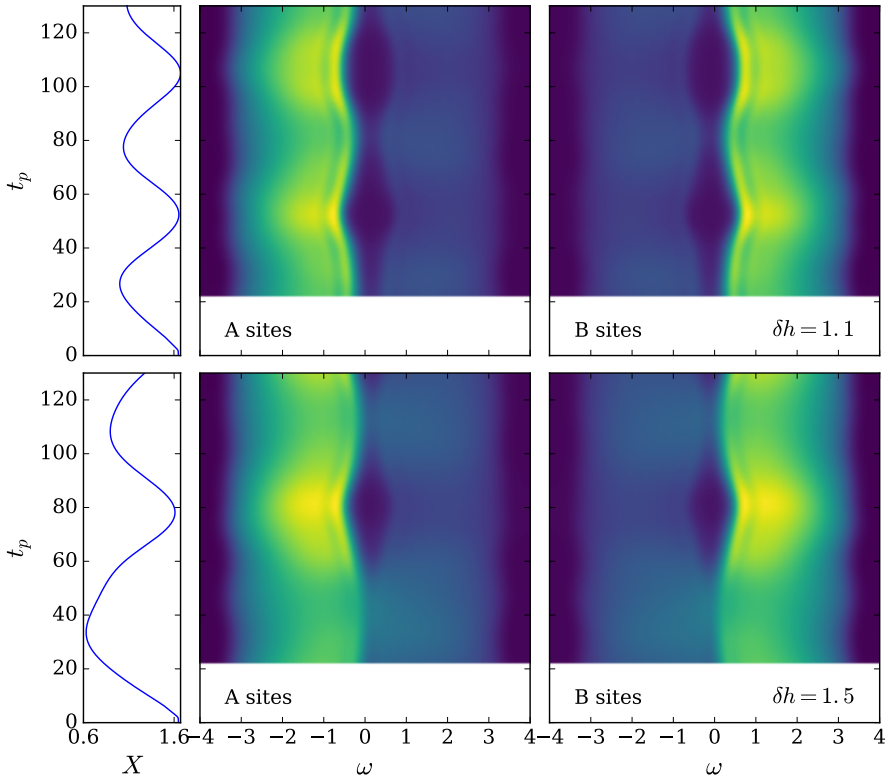

Figure 3.6: Time-dependent spectral functions $A_i(t_p, \omega) = -\frac{1}{\pi} G_i^R(t_p, \omega)$ for the $i = A, B$ sites (left and right columns, respectively) for $\delta h = 1.1$ (top row) and $\delta h = 1.5$ (bottom row). The side panels show the corresponding atomic displacements $\langle X(t) \rangle$.

Figures 3.8a, b, and c show a more direct comparison between X and n for three different δh. Figure 3.8a shows the comparison for a weak excitation. Both $\langle X(t) \rangle$ and $\langle N(t) \rangle$ are mostly regular sinusoidals. A careful inspection

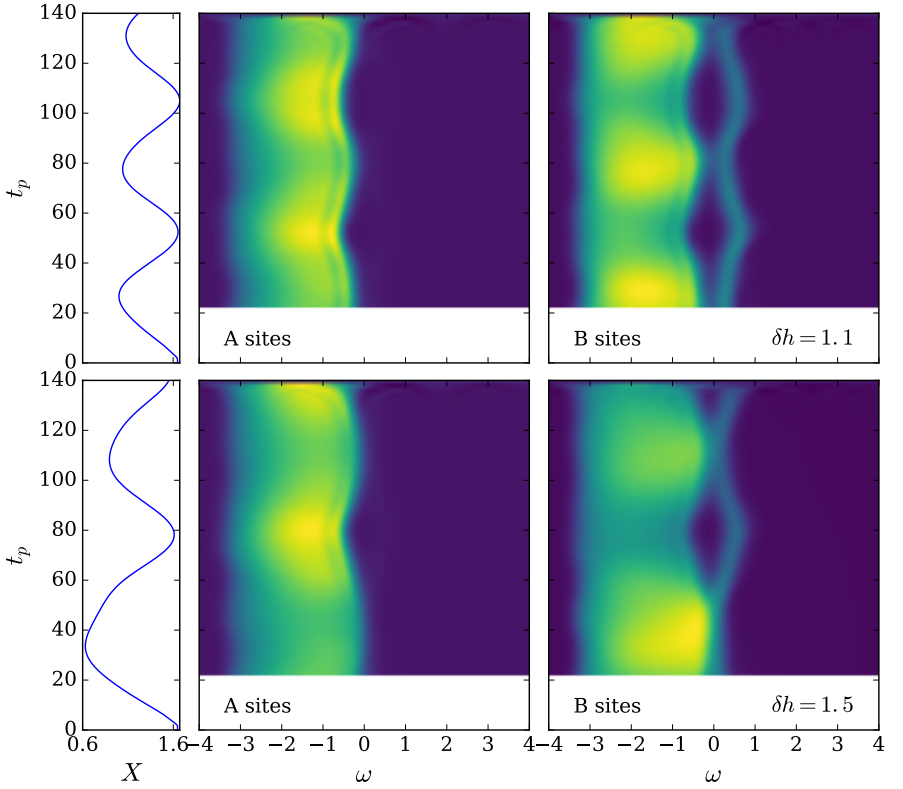

Figure 3.7: Time-dependent occupied density of states $-iG_i^<(t_p, \omega)$ for the $i = A, B$ sites (left and right columns, respectively) for $\delta h = 1.1$ (top row) and $\delta h = 1.5$ (bottom row). The side panels show the corresponding atomic displacements $\langle X(t) \rangle$.

allows to see that the minima in the oscillation of $\langle X(t) \rangle$ are slightly anticipated compared to the ones of $\langle N(t) \rangle$.

Figure 3.8b shows instead the curves obtained with $\delta h = 1.5$, i.e. close to the threshold excitation for the melting. While $\langle X(t) \rangle$ is evidently distorted from a sinusoidal function, particularly around $t = 50$, $\langle N(t) \rangle$ does not follow $\langle X(t) \rangle$ exactly. Moreover, the temporal delay between the minima of X and N is more pronounced with respect to the weak excitation regime.

Finally, figure 3.8c shows the comparison between $\langle X(t) \rangle$ and $\langle N(t) \rangle$ in the

case of melting of the symmetry-broken state. Here, the match between the two curves is rather good. This allows to conclude that, while the relationship between $\langle X(t)\rangle$ and $\langle N(t)\rangle$ is an almost straightforward linear relation in the weak and very strong excitation regimes, it becomes more complicated close to the threshold for melting.

Phononic Green's function The dynamics of the vibrational mode and of the electrons are interrelated via the mean-field $\mathrm{h}_{\mathrm{loc}}(t)$, i.e. by the force mutually exerted by the electronic density and atomic cores, and also via the respective self-energies (see section 2.2). While this is a common feature of models wih electron-phonon coupling, in this case, changes in $D(t,t') \propto \langle X(t)X(t')\rangle$ take place with a "synchronized" coherent oscillation of $\langle X(t)\rangle$. A nontrivial form of $D(t,t')$ will therefore be able to affect the oscillation in a nontrivial way, since different parts of $D(t,t')$ will be more relevant at different phases of the oscillation.

I will discuss now very briefly some features of $D(t,t')$. Having the values of $D(t,t')$ for each t,t' in the computed range, we can qualitatively analyze D along some "cuts". Figures 3.9a, b, c, and d display $\langle X^2(t)\rangle$ and $\langle P^2(t)\rangle$ for different δh, where $-2i\,\langle P(t)P(t')\rangle = \frac{\partial_t\partial_{t'}D(t,t')}{\omega_0^2} - \frac{2}{\omega_0}\,\delta_{\mathcal{C}}(t,t')$ [13]. Figures 3.9a and c show the results below the critical δh_c. The behaviour of $\langle X^2(t)\rangle$ and $\langle P^2(t)\rangle$ is highly nontrivial, but a qualitative aspect can be readily identified. For short times, a behaviour seems to exist common to all δh, while for later times the results depart from the low-intensity behaviour. The departure takes place for times which are shorter with increasing δh. The same kind of plots are reported in figure 3.9b and d for $\delta h > \delta h_c$.

This discussion about the statistical properties of the vibrational mode brings us to the question about how quickly the system thermalizes. Since to discuss this question also an analysis of the optical properties is needed, I will postpone it to section 3.2, after the discusion of the optical properties.

Optical properties The study of the optical properties of systems out of their equilibrium state provides a direct connection with the data collected in pump-probe experiments. Figure 3.10 shows the optical susceptibility $\chi_{\mathrm{eq}}^{\mathrm{pm}}(\omega)$ as a function of the frequency ω, with the system in the symmetry-broken phase at $\beta = 25$ (blue line) and in the translationally invariant phase at $\beta = 1$ (red line). As expected, the symmetry-broken phase displays a gapped susceptibility, while the translationally invariant one does not. Moreover, in the symmetry-broken phase at low temperature, the optical band is characterized by peaks due to the coupling between the electronic system and the vibrational

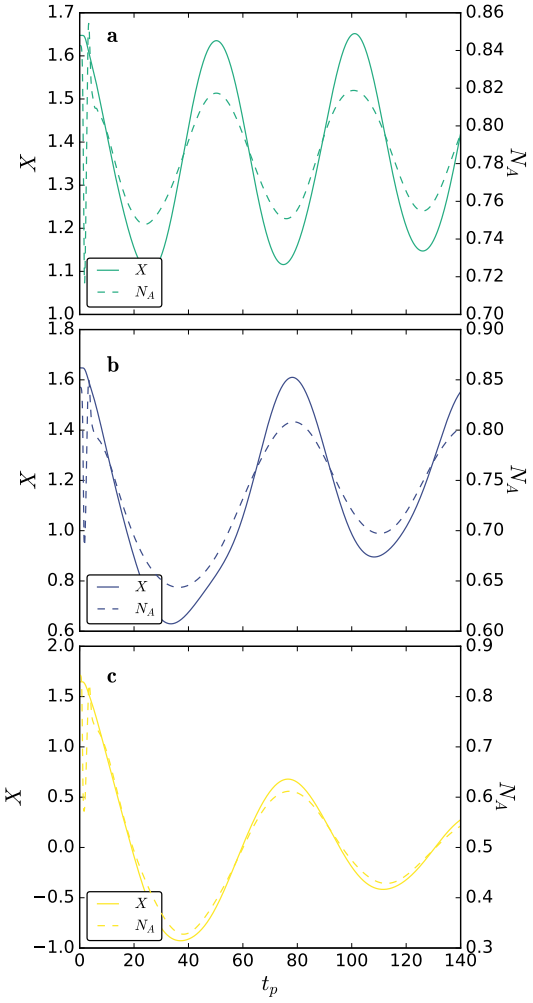

Figure 3.8: $\langle X(t) \rangle$ (solid lines, left y-axes) and $\langle N_A(t) \rangle$ (dashed lines, right y-axes) for $\delta h = 1.0, 1.5, 7.0$ (panels **a**,**b**, and **c** respectively).

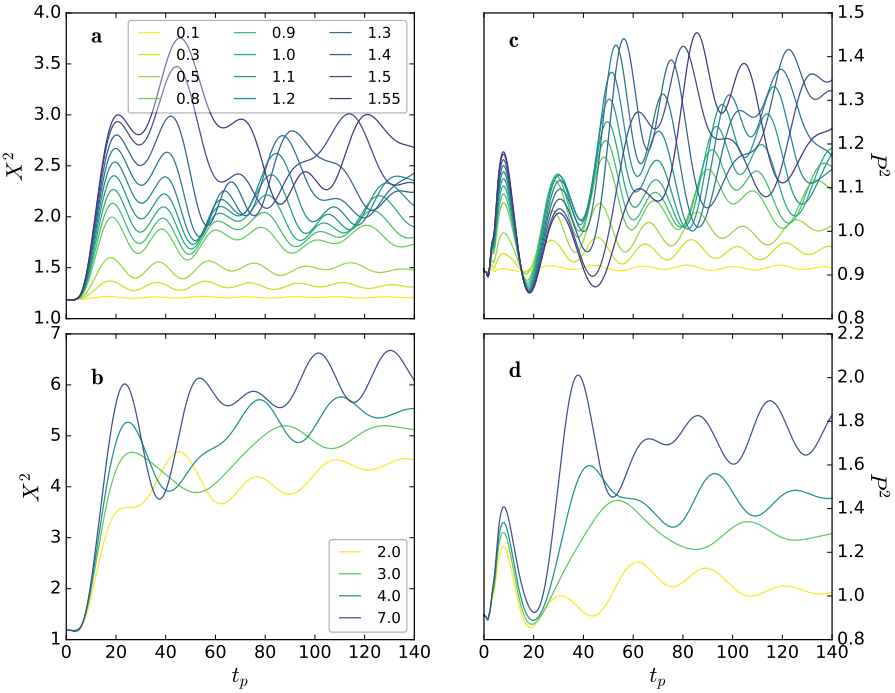

Figure 3.9: $\langle X^2(t)\rangle$ for $\delta h < \delta h_c$ (**a**) and $\delta h > \delta h_c$ (**b**), and $\langle P^2(t)\rangle$ for $\delta h < \delta h_c$ (**c**) and $\delta h > \delta h_c$ (**d**)

mode.

When the system is out of equilibrium, the optical susceptibility changes with time. Figures 3.11a and b show the evolution of $\chi^{\mathrm{pm}}(t_p, \omega)$ for $\delta h = 1.1$. Figure 3.11a shows that the optical band oscillates after the excitation, where the peak frequency is highest when the atoms are maximally dimerized, and therefore the gap is maximum, and lowest when the system is closest to the translationally invariant phase, when the gap is minimum. Figure 3.11b shows $\chi^{\mathrm{pm}}(\omega)$ at selected times t_p. As can be seen, even at the times when the gap is largest, there is a finite spectral weight for transitions at low energies. While the transitions at high energies are interband transitions, the low-energy ones are intraband transitions, which are possible because electrons have been excited from the lower to the upper band.

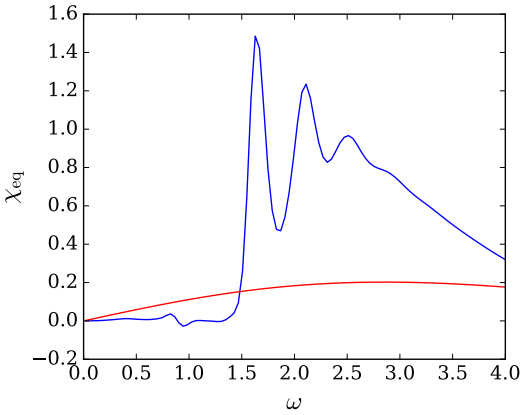

Figure 3.10: Paramagnetic part of the optical susceptibility $\chi^{\mathrm{pm}}(\omega)$ as a function of frequency ω of the system at equilibrium in its symmetry-broken (blue, $\beta = 25$) and translationally invariant (red, $\beta = 1$) phase.

3.2 Thermalization of the system

I now discuss in more depth the core issue of this part of my thesis, i.e. the study of the out-of-equilibrium state of a system subject to coherent oscillations. The most basic question that can be asked is how much the system under consideration departs from a thermal state $\rho = \frac{1}{Z} e^{-\beta H}$. This question can be answered, for example, checking how well the flucutuation-dissipation

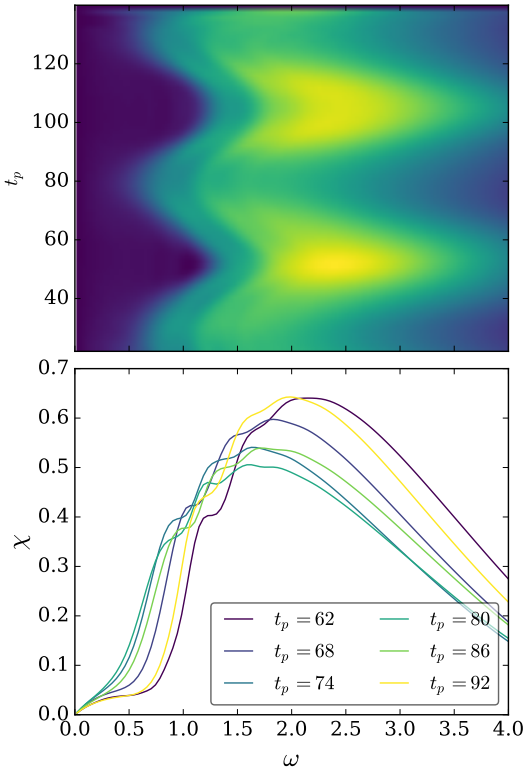

Figure 3.11: **a)** Out-of-equilibrium paramagnetic part of the optical susceptibility $\chi^{\mathrm{pm}}(t_p, \omega)$ as a function of frequency ω and of time t_p. **b)** Out-of-equilibrium paramagnetic part of the optical susceptibility $\chi^{\mathrm{pm}}(t_p, \omega)$ as a function of frequency ω for selected t_p.

relations hold out of equilibrium [12]. As discussed in section 2.3.3, at equilibrium there is a fluctuation-dissipation relation between different current-current correlators, linked to the optical properties, or equivalently between different components of the polarization bubble $P(t, t')$.

The fluctuation-dissipation relation for the commutator and anticommutator of the current-current correlators $\langle j(t)j(t')\rangle$ and $\langle j(t')j(t)\rangle$ is

$$\mathrm{Im}\chi^{\mathrm{pm}}(t, \omega) = \tanh\left(\frac{\beta\omega}{2}\right)\mathrm{Im}K(t, \omega), \tag{3.1}$$

where $K(t,t') = \langle\{j(t)j(t')\}\rangle$, as defined in section 2.3.3. This relation can be fitted with β as free parameter, and two results can be obtained: the best-fit β_f (giving the effective temperature of the electronic degrees of freedom) and the quadratic error in the fit. The latter gives information on how well the fluctuation-dissipation relation holds at time t_p. While an absolute quantitative information is not straightforward to extract, the evolution in time of the error gives an indication of how the system is thermalizing.

To benchmark this procedure, we reproduced the results by Murakami et al. [13] on the Holstein Hamiltonian. They studied how the model responds to an interaction quench from $g_i = 0$ to g_f, with the system in the translationally invariant phase. The relaxation was discussed in relation to the shape of the distribution function $n(\epsilon_k, t)$ of the electrons close to the Fermi edge. At the time of the interaction quench a jump Δn develops in n at $\epsilon = 0$, which then gradually disappears. As they discuss, even though Δn is not a full indicator of how much thermal a state is, it is a good indicator of the thermalization dynamics. They showed that the rate at which Δn decreases depends on the final coupling constant g_f after the quench, as shown by the reproduction of their data in figure 3.12 [13]. With small g_f the system thermalizes slowly, while for large g_f it thermalizes more quickly. This corresponds to a crossover between an electron-dominated thermalization at small g_f and a phonon-mediated thermalization at large g_f. [13]

We performed the fluctuation-dissipation analysis to study the thermalization of the Holstein model with the same type of interaction quench. The results are plotted in figures 3.13a and b. Figure 3.13a shows the fit error. The smaller it is, the better the system is thermalized. As can be seen, this kind of analysis produces results which are analogous to the ones obtained by Murakami et al. [13], i.e. decreasing thermalization time with increasing amplitude of the quench.

Figure 3.13b shows the best-fit inverse temperature β_f, which has to be read off from such a plot taking the fit error into account. When the error is large, the value of β extracted from the fit cannot be considered as an actual temperature. One can see that for long times, i.e. when the fit error is small and the system is thermalized, β_f decreases for increasing g_f, as expected.

The same kind of analysis can be done for the vibrational mode, testing the fluctuation-dissipation relation between different components of the phononic Green's function [8],

$$D^R(t_p,\omega) - D^A(t_p,\omega) = \tanh\left(\frac{\beta\omega}{2}\right) D^K(t_p,\omega), \tag{3.2}$$

where $D^{R,K,A}(t_p,\omega) = \frac{1}{2\pi}\int ds\; e^{i\omega s} D^{R,K,A}(t_p + s/2, t_p - s/2)$. Testing the

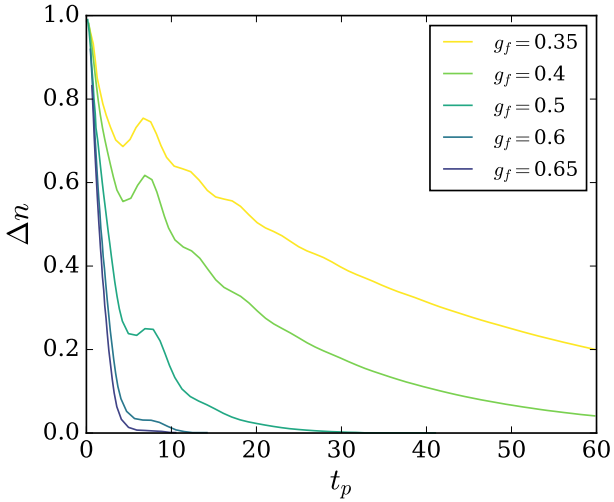

Figure 3.12: Jump Δn of the distribution function $n(\epsilon_k, t)$ at the Fermi energy after an interaction quench from $g_i = 0$ to various g_f. Adapted from Murakami et al. [13].

above relation allows to separately estimate if the phononic system is in a thermal state and what its effective temperature is.

Figure 3.14 shows the results obtained, analogously to the results for the electronic system. The temporal behaviour of the fit error in figure 3.14a shows that the timescale for the thermalization of the vibrational mode does not strongly depend on the magnitude of the quench, consistently with the result by Murakami et al. [13]. Figure 3.14b show instead that the effective temperature of the vibrational mode is the same as the one of the electrons.

Coherent oscillation We can now move back to the excitation of coherent oscillations in the dimerized phase of the Holstein model. If we perform the analysis of the fluctuation-dissipation relations discussed above in this situation, we obtain nontrivial results.

The red and green curves in figure 3.15a represent the inverse temperatures of the vibrational mode and of the electrons, respectively. For the sake of clarity, in the following we will discuss only the excitation with δh=1.5. The results obtained with the other excitation intensities are analogous. Figure 3.15b displays the fit error for the electronic system, which is minimum

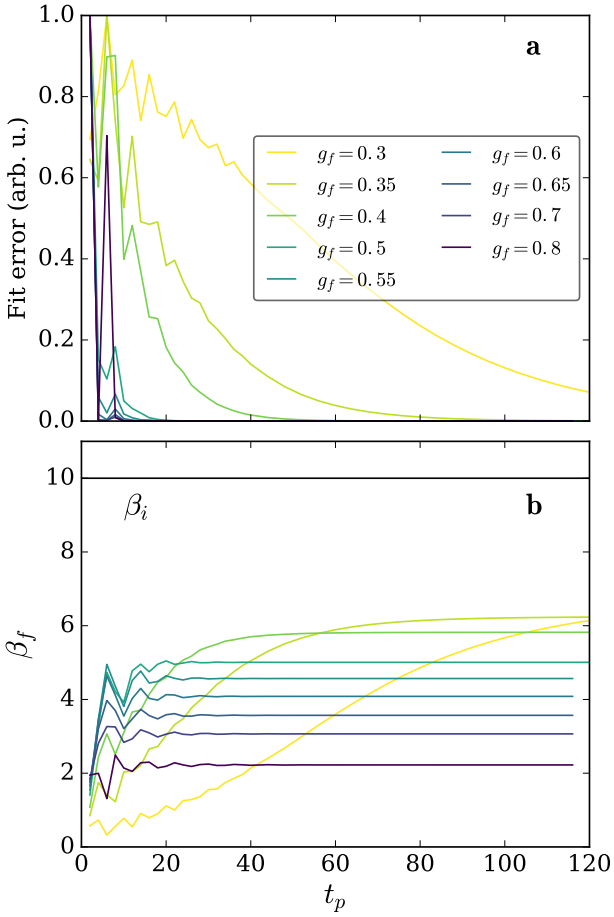

Figure 3.13: **a)** Quadratic fit error of the fluctuation-dissipation relation between $\chi(t_p, \omega)$ and $K(t_p, \omega)$ after an interaction quench from $g_i = 0$ to various g_f. **b)** Best-fit inverse temperature β_f obtained from the fit of the fluctuation-dissipation relations (with the same legend as panel **a**).

at the minima of the oscillation of N_A (dashed line in figure 3.15a), i.e. when the system is the less dimerized. This is consistent with the fact that, at the same times, the fits of the electronic and phononic temperatures give the same result.

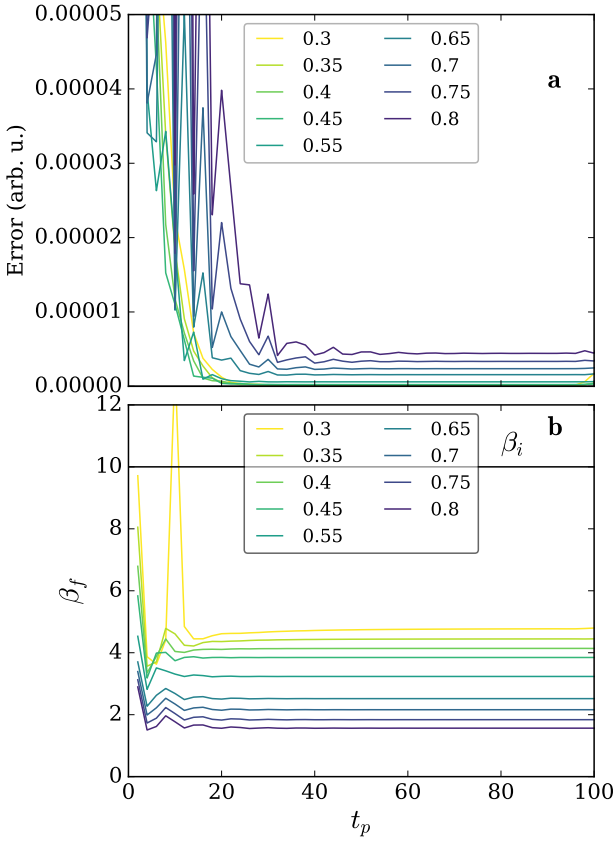

Figure 3.14: **a)** Quadratic fit error of the fluctuation-dissipation relation between different components of the phononic Green's function $D(t, t')$ after an interaction quench from $g_i = 0$ to various g_f. **b)** Best-fit phononic inverse temperature β_f obtained from the fit of the fluctuation-dissipation relations.

To gain more insight on the underlying dynamics, we have to study in more detail what the energy scales are at which the flucutuation-dissipation relation for the electronic system fails. Figure 3.16a shows two examples of the quantities that should be equal when the fluctuation-dissipation relation holds, i.e. $\chi(t_p, \omega)$ (solid lines) and $\tanh\left(\frac{\beta_f \omega}{2}\right) K(t_p, \omega)$ (dashed lines). The blue curves are for $t_p = 40$, i.e. at the minimum lattice distortion (as indi-

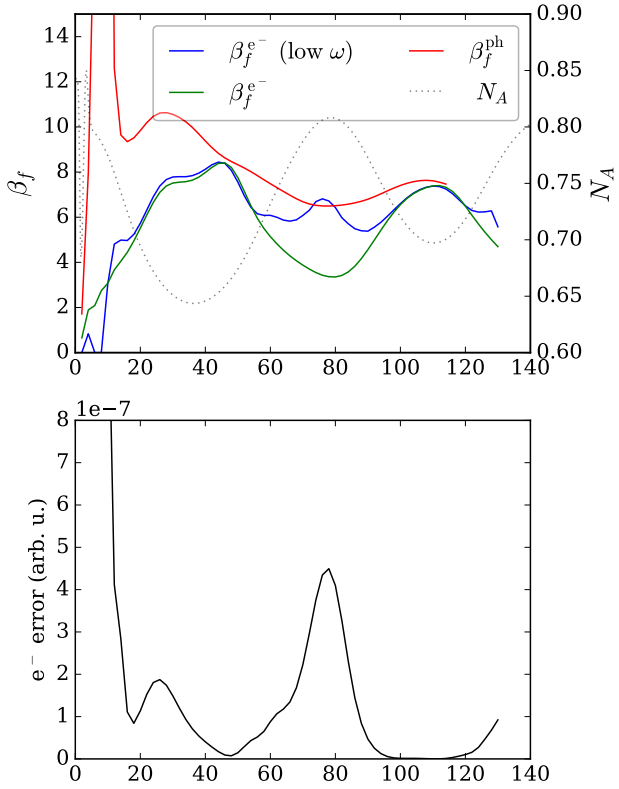

Figure 3.15: **a)** Quadratic fit error (solid lines, left y-axis) of the fluctuation-dissipation relation between $\chi(t_p, \omega)$ and $K(t_p, \omega)$ after an impulsive excitation of the system in the symmetry-broken state for various δh. $\langle N_A(t) \rangle$ (dashed line, right y-axis) for $\delta h = 1.5$. **b)** Best-fit inverse temperature β_f obtained from the fit of the fluctuation-dissipation relations (with the same legend as panel **a**).

cated in the inset of panel b), while the red curves are for $t_p = 75$, i.e. at the maximum of the lattice distortion. Figure 3.16b shows the difference between the dashed and the solid lines of panel a. As expected, $\chi^{pm}(t_p, \omega)$ and $\tanh\left(\frac{\beta_f \omega}{2}\right) K(t_p, \omega)$ perfectly match at high frequencies, since $\tanh\left(\frac{\beta_f \omega}{2}\right)$ tends to unity for large ω and becomes insensitive to changes in temperature. The fact that the fluctuation dissipation relation is not perfectly obeyed becomes

evident on the low-energy side of the spectrum. Figure 3.16b shows that the difference between $\chi^{\rm pm}(t_p,\omega)$ and the best-fit $\tanh\left(\frac{\beta_f\omega}{2}\right)K(t_p,\omega)$ is relevant up to the energy of the gap of the system, whose width oscillates as $\langle X(t)\rangle$ oscillates.

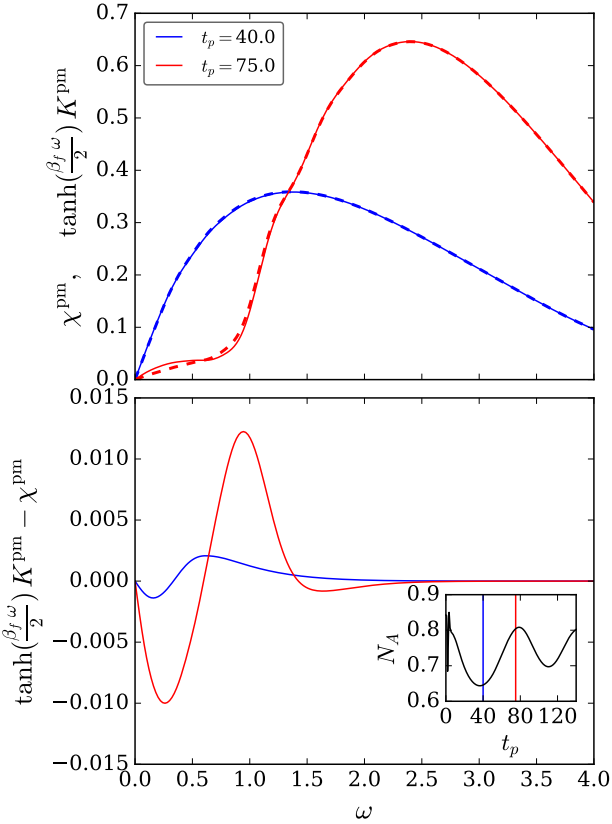

Figure 3.16: **a)** $\mathrm{Im}\chi^{\rm pm}(t_p,\omega)$ (solid) and best-fit $\tanh\left(\frac{\beta_f\omega}{2}\right)K^{\rm pm}$ (dashed) for $t_p = 40$ (blue) and $t_p = 75$ (red). **b)** Difference between the corresponding dashed and solid lines of panel **a**.

The occupied density of states plotted in figure 3.7b allows to draw the following picture. The existence of an out-of-equilibrium population in the upper band, created by the excitation, does not allow the system to be de-

scribed as in a thermal state. Electrons cannot scatter efficiently enough via the phonons, for a thermal distribution to be globally restored after the excitation. Interband transitions with energies of the order of the gap will, therefore, be markedly affected by the presence of a non-thermal population.

On the other hand, within each separate band, the electrons can thermalize more easily via the phonons. Low-energy transitions, which are primarily intraband transitions, will carry the signatures of a state which is more thermalized, with respect to the high-energy transitions.

This can be tested limiting the fit of the fluctuation-dissipation relation to the low-energy part of the spectrum, i.e. from $\omega = 0$ to $\omega = 0.2$. The inverse temperature obtained in this way is plotted as the blue curve in figure 3.15a. As can be seen, the result changes less as a function of time with respect to the inverse temperature obtained fitting the fluctuation-dissipation relation over the whole energy range. This means that, on the low-energy scale, the scattering via the phonons is indeed able to make the electrons thermalize more easily at all times than on the high energy scale.

As seen in figures 3.15 and 3.16, however, at some times of the dynamics the state of the system becomes approximately thermal at all energy scales. This happens in correspondence to the minimum lattice distortion, and hence of the minimum gap width. As the gap is reduced, in fact, the population of the upper band is not as highly non-thermal as when the gap is large, because it is concentrated closer to the Fermi energy.

3.3 Fluctuations of the optical properties

The fluctuation-dissipation analysis allows to study the thermalization dynamics of an out-of-equilibrium system from the theoretical point of view. How can this kind of information be accessed in a pump-probe experiment? Recent experiments have measured, besides the average value of the intensity of the probe pulses reflected from the sample, also its fluctuations, i.e. its variance [3, 4]. In section 2.3.4 we have shown that this quantity is closely related to the fluctuations of the currents in the sample. In fact, the variance of the probe pulse intensity can be written as (equation (2.96))

$$\mathrm{var}[I] \sim \int dt_1 dt_2 \langle E(t_1)\rangle \langle E(t_2)\rangle \langle j(t_1) j(t_2)\rangle_0 .$$

While at equilibrium the fluctuation of the currents at optical frequencies are negligible, when the system is out of equilibrium and its state is non-

thermal, fluctuations can be relevant also at frequencies involved in pump-probe experiments in the near-infrared and visible spectral range.

Fluctuations of the current Before discussing the fluctuations of the intensities of probe pulses in pump-probe experiments, I will therefore describe the evolution of the fluctuations $\langle j(t)j(t')\rangle$ of the current. Figure 3.17 shows the spectrum $\mathrm{Im}\, jj(t_p,\omega)$, where

$$jj(t_p,\omega) = \frac{1}{2\pi}\int ds\; e^{i\omega s}\langle j(t_p+s/2)j(t_p-s/2)\rangle \tag{3.3}$$

is the Fourier transform of the fluctuations of the current as a function of ω for various times t_p and at equilibrium. At equilibrium (black bold line) the fluctuations of the current are significant only at small frequencies. When the system is out of equilibrium, instead, there are finite fluctuations of the current up to frequencies of about 1.5. Moreover, the shape of $\mathrm{Im}\, jj(\omega)$ changes with time, as can be seen in figures 3.17 and 3.18, where $\mathrm{Im}\, jj(t_p,\omega)$ is plotted together with the atomic displacement $\langle X(t)\rangle$ (in the side panels). In fact, the presence of a population in the upper band will allow for the current to fluctuate at frequencies corresponding to the gap energy. At times t_p for which the lattice distortion and the gap are maximum, in addition to a component centred at $\omega = 0$, the spectrum of the current displays a band centred at $\omega \simeq 1$ with finite weight up to $\omega \simeq 1.5$ (yellow curve in figure 3.17). When the lattice distortion is minimum and the gap is reduced, instead, the fluctuations of the current display just a feature centred at $\omega = 0$ with increased weight with respect to the case of maximum distortion.

Fluctuations of the intensity of the probe pulse The temporal evolution of $jj(t_p,\omega)$ can be studied in a pump-probe experiment where the variance of the intensity I of the probe pulses is measured after their interaction with the sample. Equation (2.96) shows, in fact, that $\mathrm{var}[I]$ corresponds to the spectral component of $jj(t_p,\omega)$ at the frequency of the probe pulse.

Figure 3.19 shows $\mathrm{var}[I]$ as a function of time for different excitation intensities δh, with a probe pulse of duration $\Delta t = 4$ and frequency 1.3, i.e. slightly higher than the maximum gap energy. As can be seen, $\mathrm{var}[I]$ is maximum for the maximum lattice distortion, when the population in the upper band is the furthest from the Fermi energy. It should be underlined that the temporal dependence of $\mathrm{var}[I]$ resembles the one of the error in the fit of the flucutuation-dissipation for the current-current correlators (figure 3.15b). In fact, the presence of fluctuations of the current at such high frequencies itself

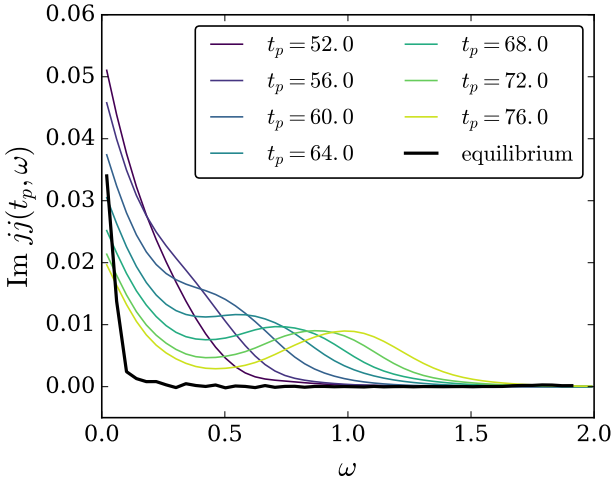

Figure 3.17: Spectrum of the current fluctuations for the system at equilibrium (black line) and at various times with $\delta h = 1.5$.

stems from the non-thermal nature of the state of the system. Its measurement can therefore give information on how much thermal the system is.

3.4 Comparison with experiments on bismuth single crystals

Up to now, however, we have neglected a contribution to the total variance of the intensity of the probe pulses. In fact, equation (2.96) is derived in the assumption that the noise in the light pulses is due just to the noise in the currents which is present without the probe's perturbation. Another, shot-noise-like contribution to the noise is instead present, due to the statistics of the incomig probe pulses. To compare our results with experimental results we can re-add this term to var$[I]$, as a term proportional to the probe pulse intensity.

Figures 3.20a and b show experimental results obtained in pump-probe experiments on bismuth single crystals, with 1.5 eV pump and probe pulses, lasting 80 fs each [4]. Figure 3.20a shows the results for a fluence low enough for the oscillation to be only slightly damped, while the results in figure 3.20b are

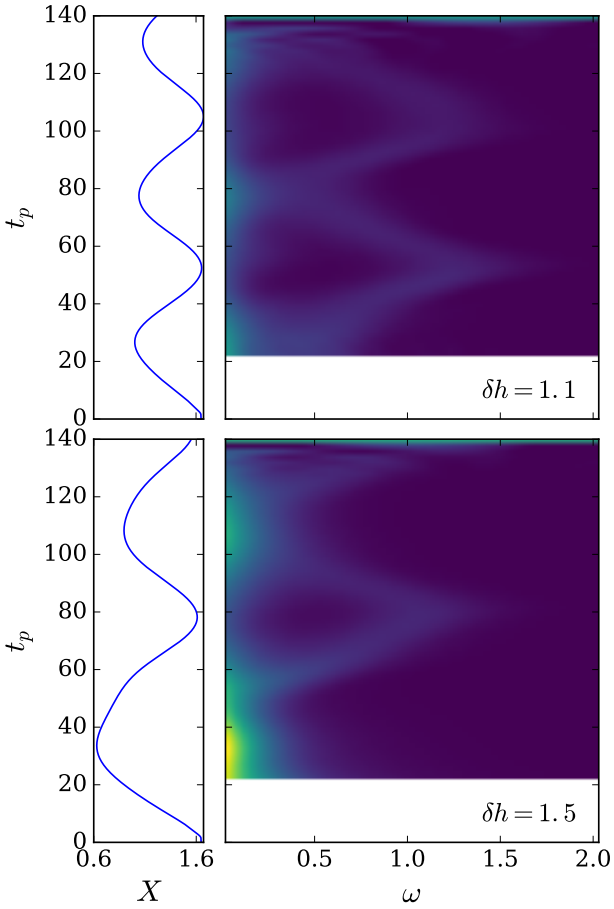

Figure 3.18: Time-dependent spectrum of the current fluctuations for excitation intensity $\delta h = 1.1$ (**a**) and $\delta h = 1.5$ (**b**). Side panels: corresponding $\langle X(t_p) \rangle$

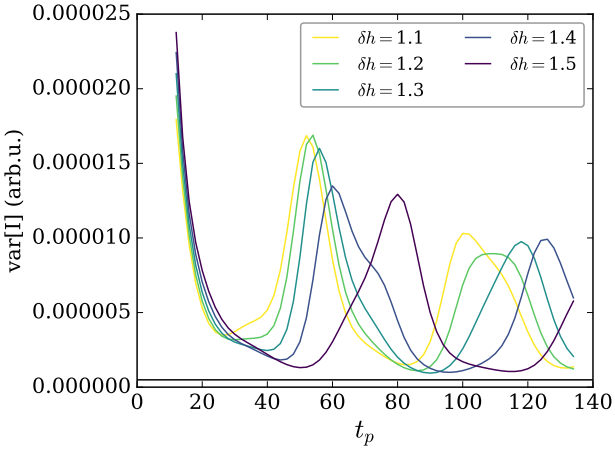

Figure 3.19: Variance of the intensity of the probe pulses as a function of the pump-probe delay t_p.

for a high fluence, which produces a markedly damped oscillating dynamics [1]. Bismuth is the prototypical Peierls' system and, in pump-probe experiments with such pulses, a coherent vibration of its A_{1g} vibrational mode is excited, which can be detected in $\frac{\Delta R}{R}(t_p)$. The measurements have been performed with a single-pulse acquisition scheme [3, 4], which allows to measure, apart from the average of the intensity of the probe pulses, also its variance. The red and blue curves are the relative variation of the reflectivity of the sample after the excitation, while the green and magenta lines display the variance of the intensity of the probe pulses.

As can be seen, the measured variance of the intensity of the probe pulses oscillates too at the frequency of the vibrational mode. However, in its evolution it displays characteristic difference from $\frac{\Delta R}{R}(t_p)$. At low fluence, the variance displays nonlinearities in its oscillation. In particular, for some cycles, the maxima and minima are alternatively shifted from the ones in $\frac{\Delta R}{R}(t_p)$. At high fluence, the major feature in the first oscillation cycle is a shoulder close to the first minimum of the oscillation of the variance.

To try to simulate these results with our calculation, we have to consider the fact that, in bismuth, an expansion of the dimers, i.e. a *decrease* of $\langle X(t) \rangle$ as defined here, corresponds to an *increase* of the reflectivity. Therefore

[1] The plots reported here focus just on a few cycles.

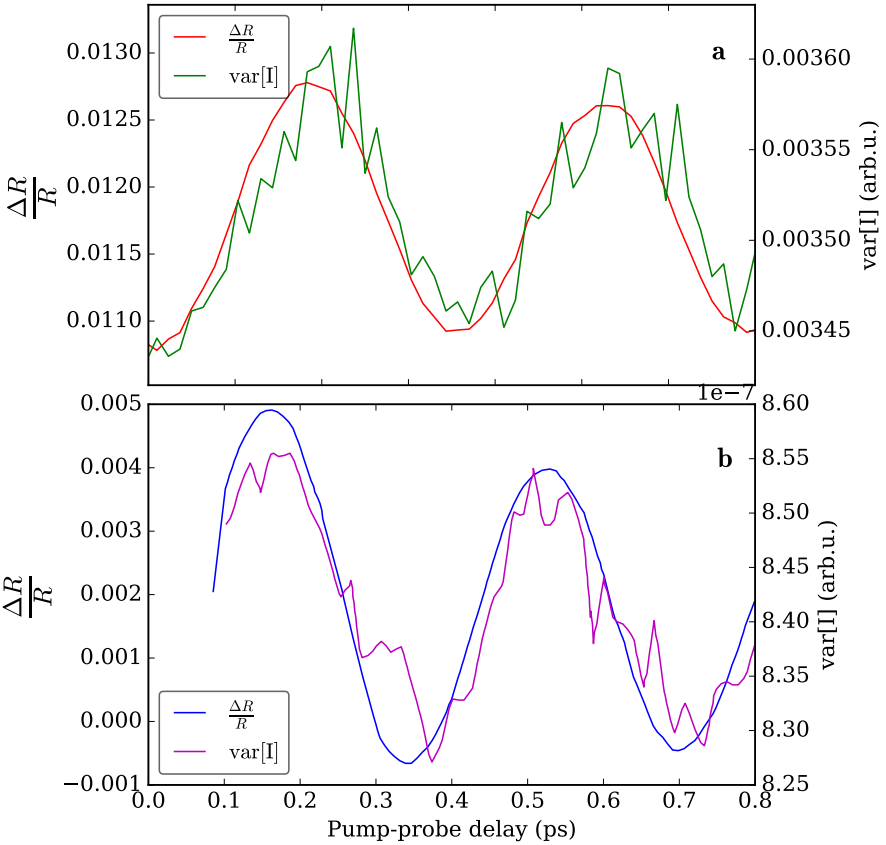

Figure 3.20: Relative variation of the reflectivity $\frac{\Delta R}{R}(t_p)$ and variance of the probe pulses obtained in pump-probe experiments on bismuth single crystals, for a low (**a**) and a high (**b**) fluence.

$\frac{\Delta R}{R}(t)$ can be written as proportional to $\propto -(\langle X(t)\rangle - \langle X\rangle_{eq})$. The evolution with pump-probe delay of a shot-noise-like contribution to the noise, which is proportional to the intensity of the probe pulses, will be proportional to $-(\langle X(t)\rangle - \langle X\rangle_{eq})$. The calculated total noise $\mathrm{var}^{tot}[I]$, i.e. including $\mathrm{var}[I]$ and the shot noise contribution, is shown, together with the calculated $\frac{\Delta R}{R}$, in figures 3.21a and b for $\delta h = 0.5$ and 1.4, respectively. As can be seen, the calculation reproduces variances displaying both the nonlinearity of the oscillation at "low fluence" and the shoulder close to the first minimum at "high fluence". [2]

3.5 Conclusions

The goal of the work described in this part of my thesis has been to theoretically explore the possibilities given by measuring the fluctuations of the optical properties in out-of-equilibrium pump-probe experiments. To do this, we performed nonequilibrium dynamical mean-field theory calculations on the Holstein model describing the Peierls' systems. We showed that nonequilibrium DMFT is able to capture the main features of the dynamics of photoexcited Peierls' systems, i.e. the displacive excitation of coherent vibrations in solids, the softening of the oscillation frequency, the damping of the dynamics and the melting of the symmetry-broken phase.

Via the test of the fluctuation-dissipation relations out of the equilibrium state, we were able to study the thermalization dynamics of the system, which is nontrivial when coherent oscillations are present in the system. This result shows that the assumption that systems in pump-probe experiments can be considered in effectively thermal states must be handled with some care, especially when the dynamics is nontrivial, as it is in the case discussed here.

The measurement of the fluctuations of the probe pulse intensity in pump-probe experiments allows to measure the fluctuations of the currents in the sample, which give informations about how much the system can be considered thermal. Remarkably, our results reproduce experimental measurements of the fluctuations of the probe intensity in experiment on a bismuth single crystal, a prototypical Peierls' system.

[2] In considering such results, one should keep in mind that the probe frequency, with respect to the electronic band, used in the calculation does not necessarily match exactly the one in the experiment, and the coefficient with which the shot-noise-like term is summed to the calculated $\mathrm{var}[I]$ is arbitrary. Nevertheless, it is remarkable that the characteristic features of the experimental results can be reproduced.

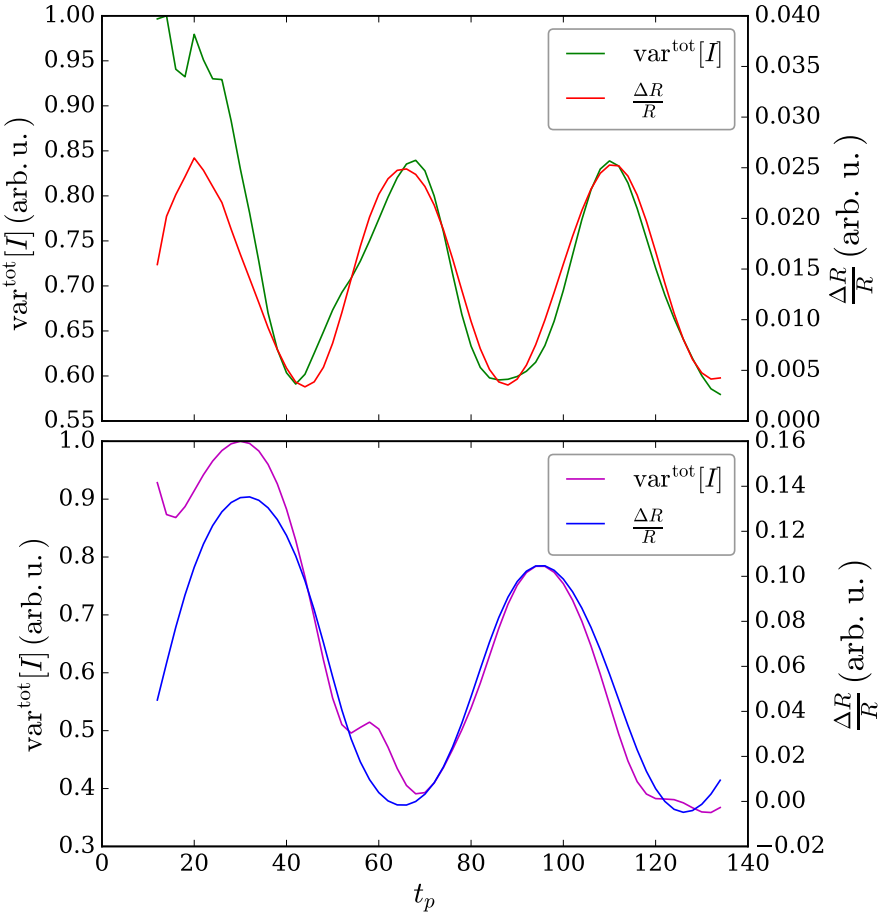

Figure 3.21: Relative variation of the reflectivity $\frac{\Delta R}{R}(t_p)$ and total variance (with the addition of a shot-noise-like contribution) of the intensity of the probe pulses obtained in the simulation of the pump-probe experiment on a bismuth single crystal. for a low (**a**) and a high (**b**) excitation intensity.

Acknowledgements

This work has been performed during my stay at the Max Planck Institute for the Structure and Dynamics of Matter in Hamburg, Germany, in collaboration with Martin Eckstein. We thank Sharareh Sayyad for the critical reading of this work.

Bibliography

[1] O.V. Misochko "Coherent Phonons and Their Properties" Journal of Experimental and Theoretical Physics, **92**(2):246259 (2001).

[2] A. Hussain and S.R. Andrews "Absence of phase-dependent noise in time-domain reflectivity studies of impulsively excited phonons" Phys. Rev. B, **81**, 224304 (2010).

[3] M. Esposito, K. Titimbo, K. Zimmermann, F. Giusti, F. Randi, D. Boschetto, F. Parmigiani, R. Floreanini, F. Benatti, and D. Fausti "Photon number statistics uncover the fluctuations in non-equilibrium lattice dynamics" Nat. comm. **6**, 10249 (2015)

[4] F. Randi, "Pulsed homodyne detection for quantum state reconstruction applied to ultrafast non-equilibrium spectroscopy", Master thesis, Università degli studi di Trieste (2013).

[5] R.E. Peierls "More surprises in theoretical physics" Princeton University Press (1991).

[6] T. Rohwer, S. Hellmann, M. Wiesenmayer, C. Sohrt, A. Stange, B. Slomski, A. Carr, Y. Liu, L.M. Avilla, M. Kalläne, S. Mathias, L. Kipp, K. Rossnagel, and M. Bauer "Collapse of long-range charge order tracked by time-resolved photoemission at high momenta" Nature **471**, 490 (2011)

[7] A. Georges, G. Kotliar, W. Krauth, and M.J. Rozenberg "Dynamical mean-field theory of strongly correlated fermion systems and the limit of infinite dimensions" Rev. Mod. Phyis. **68**, 13 (1996).

[8] H. Aoki, N. Tsuji, M. Eckstein, M. Kollar, T. Oka, and P. Werner "Nonequilibrium dynamical mean-field theory and its applications" Rev. Mod. Phys. **86**, 779 (2014).

[9] L.P. Kadanoff and G. Baym, "Quantum statistical mechanics", (W.A. Benjamin, New York) 1962.

[10] A.A. Abrikosov, L.P. Gorkov, and I.E. Dzyaloshinski "Methods of quantum field theory in statistical physics" (Dover, New York) 1975.

[11] S.W. Teitelbaum, T. Shin, J. Wolfson, Y.H. Cheng, I.J. Porter, M. Kandyla, and K.A. Nelson "A Photoinduced Symmetric Crystalline Phase in Bismuth" arXiv:1609.04048

[12] J. Kogoj, L. Vidmar, M. Mierzejewski, S.A. Trugman, and J. Bonča "Thermalization after photoexcitation from the perspective of optical spectroscopy" Phys. Rev. B **94**, 014304 (2016).

[13] Y. Murakami, P. Werner, N. Tsuji, and H. Aoki "Interaction quench in the Holstein model: Thermalization crossover from electron- to phonon-dominated relaxation" Phys. Rev. B **91**, 045128 (2015).

[14] M. Eckstein, and M. Kollar "Theory of time-resolved optical spectroscopy on correlated electron systems" Phys. Rev. B **78**, 205119 (2008).

[15] D.J. Griffiths, "Introduction to electrodynamics (3rd ed.)", Prentice Hall (1999).

Part IV

Time-resolved photoemission: room for enhancements

Chapter 1

Time-resolved photoemission beyond the energy-time uncertainty

1.1 Introduction

The study of the electronic response function at low energies is one of the standard ways to uncover the mechanisms producing the exotic macroscopic properties of complex materials. [1] Superconductivity, charge density waves, giant magnetoresistance and other phenomena, arising from both electron-electron interactions and interactions between electrons and other degrees of freedom, often become manifest in low-energy features in the electronic single-particle response function [1, 2]. In the systems which display such properties, the dynamics of excited populations and of the electronic structure often cannot be separated, in that the population of the excited state dynamically renormalized the electronic structure. This aspect makes time-resolved photoemission spectroscopy particularly appealing among nonequilibium techniques, since it allows to simultaneously measure the time-dependent band structure and the nonequilibrium distribution of electrons. In this context, time- and angle-resolved photoemission experiments have revealed, for example, the collapse of charge density waves and of Mott gaps [4–6], or the reconstruction of the

[1] The content of this part of the thesis has been submitted as an article to Physical Review B. Here, it has been partly restructured.

gap after photo-induced phase transitions [7, 8].

Time-resolved pump-probe photoemission spectroscopy is affected by the limitation derived from the energy-time uncertainty relation. In fact, even though the current technology allows to produce pulses with durations of the order of 100 as [9], the shorter the pulses are, the larger is their energy bandwidth. In standard time-resolved photoemission, the energy spread of the probe pulse, which photoemits the electrons, is reflected in a corresponding spread in the kinetic energy of the outcoming electrons. This results, with respect to the equilibrium case, in a worsened energy resolution of the photoelectron spectrum, in which the relevant low-energy features may therefore be averaged out.

For this reason, time-resolved photoemission studies have, up to now, been limited to study the dynamics of spectral features occuring on timescales lower than the inverse of their energy width. In general, one could say that the time-evolution takes place *beyond the spectral uncertainty limit* if relevant degrees of freedom evolve faster than the inverse width of their spectroscopic fingerprint.

A paradigmatic example of the latter situation concerns the Kondo effect, i.e. the screening of the magnetic moment on an impurity, which becomes manifest only in a narrow spectral feature close to the Fermi energy. Since a pulse of duration Δt has a minimum bandwidth $\Delta\omega = 1/\Delta t$, it is generally believed that the dynamics of the Kondo screening can be measured only on timescales slower than the inverse of the spectral width of the Kondo peak, while it is known that the Kondo screening itself can evolve on a shorter timescale [10]. A similar situation arises in the case of a BCS superconductor, the dynamics of whose condensate is believed to be observable only on timescales larger than the inverse of the gap energy $\hbar/\Delta_{SC}$. On the other hand, it is expected that oscillations of the gap amplitude at the gap frequency should follow a sudden quench of the superconducting gap [11, 12].

The energy-time uncertainty relation is, however, not a Heisenberg-type uncertainty relation [13], and its consequences on time-resolved photoemission are not of fundamental nature. In this chapter it is shown that the usual tradeoff, believed to be necessary, between the temporal resolution and the resolution on the photoelectron energy is due to the usage of probe pulses with Gaussian envelopes in standard time-resolved photoemission, and that it can be avoided using properly shaped light pulses. In this work, we extended the well established concepts of multidimensional optical spectroscopy [14, 15] to time-resolved photoemission. This theoretical proposal is based on the fact that the full information about the single-particle dynamics in the system, contained in the Green's function $G(t, t')$, can be accurately characterized entirely in the time domain, and that the limitations of the usual mixed time-

frequency approach can be bypassed. In particular, the real-time measurement of the Green's function ca be experimentally implemented in a pump-probe scheme with two probe pulses of arbitrarily short duration, obtained via the splitting, delay and recombination of an original pulse.

This double-pulse photoemission scheme is illustrated with simulations of its application to the study of the buildup of the Kondo peak, and it is highlighted how this scheme could have a general relevance in the measurement of the true timescales of the destruction of electronic orders in, e.g., superconductors [11, 12, 17] and Mott insulators such as the $1T-TaS_2$ dichalcogenide [16].

In addition to the experiments exploiting the modulation of the classical intensity, we envision experiments taking advantage of light pulses with statistical or quantum correlations. Exploiting quantum correlations of light both in controlling and measuring the properties of matter has a wide application in other fields [18–22]. Our proposal, described in chapter IV.2, represent the first attempt to exploit non-coherent states of light to address specific spectroscopic features in time-resolved photoemission experiments.

1.2 Generalized time-resolved photoemission

1.2.1 Theoretical formulation

In a time-resolved angle-integrated photoemission experiment, one measures the probability $I(E, t_p)$ that an electron is emitted under the action of a short probe pulse, as a function of the photoelectron energy E and the temporal delay t_p between the probe pulse and a given excitation (e.g. the pump pulse). The signal $I(E, t_p)$ can be obtained using time-dependent perturbation theory in the light-matter coupling [23]. If $s(t)e^{i\Omega t} + s^*(t)e^{-i\Omega t}$ denotes the temporal profile of the probe vector potential with envelope $s(t)$ and centre frequency Ω, one obtains (see reference [23] and section 2.2)

$$I(E, t_p) \propto -i \int dt\, dt'\; e^{iE(t-t')} G^<(t_p+t, t_p+t')\; S(t, t'). \tag{1.1}$$

Here, the kinetic energy E is defined with respect to the energy $\hbar\Omega - W$ given by the frequency Ω and the work function W, and $S(t, t') = s(t)s(t')^*$ is an autocorrelation function of the probe pulse, which acts as a *filter* determining how $e^{iE(t-t')}G^<(t, t')$ is sampled over the (t, t')-plane in the above integration. Furthermore, $G^<(t, t') = i\langle f^\dagger(t')f(t)\rangle$ is the Green's function of the sample alone, where f ($f^\dagger$) is the annihilation (creation) operator for an electron in a given orbital of the system, $\langle \cdots \rangle$ denotes the expectation value in the initial

state (at $t \to -\infty$), and the time evolution includes all nonequilibrium perturbations besides the probe, such as external pump laser fields. Equation (1.1) can easily be extended by adding a sum over orbitals and matrix elements, but the latter are static and do not alter the following general discussion of the relation between the time-dependent electronic properties and the photoemission signal. Similarly, by inserting suitable matrix elements, the results discussed in this work can be reformulated for angle-resolved photoemission [2].

If the probe pulse is modelled by a Gaussian $s(t) = \exp(-t^2/2\Delta t^2)$ with duration Δt, equation (1.1) can be transformed into a mixed time-frequency representation,

$$I(E, t_p) \propto \int d\omega\, dt\; N(E+\omega, t_p+t)\; e^{-\frac{t^2}{\Delta t^2}} e^{-\omega^2 \Delta t^2}, \tag{1.2}$$

where $N(\omega, t) = \int \frac{ds}{2\pi i}\, e^{i\omega s}\, G^<(t + s/2, t - s/2)$ is the Wigner transform of the Green's function, which could be referred to as a time-dependent occupied density of states. (At equilibrium, $N(\omega) = A(\omega) f(\omega)$ is the product of the spectral function $A(\omega)$ and the Fermi distribution function.) Equation (1.2) emphasizes the origin of the uncertainty limit in time-resolved photoemission: The signal I is related to the underlying spectral information $N(\omega, t)$ by a filter which is subject to the uncertainty $\Delta\omega = 1/\Delta t$ in (t, ω) plane. This is illustrated in figure 1.1, for the simple example of an occupied level which is suddenly shifted in binding energy from ϵ_i to ϵ_f. For simplicity, we choose the zero of enegy such that $\epsilon_i = +1$ ($< \epsilon_{\text{vacuum}}$) and $\epsilon_f = -1$. Figure 1.1a and b show the Wigner transform $N(\omega, t)$ and the result of time-resolved photoemission with a Gaussian pulse, respectively. While $N(\omega, t)$ contains the full information about single-particle properties in the time-evolving quantum state, this information can no longer be easily reconstructed from the photoemission intensity. However, one may now ask, whether probe pulses can be appropriately devised to shape $S(t, t')$, in order to access the underlying information in $G^<(t, t')$ or $N(\omega, t)$ in a more flexible way. There is clearly no physical pulse which could yield $N(\omega, t)$ in a single intensity measurement, since $N(\omega, t)$ can take negative values, while $I(E, t)$ is a non-negative probability [3] [25–27]. Nevertheless, in the following sections we will show that there

[2] Note that this formulation adopts a one-step model of photoemission in which the interaction of the outgoing electrons and the electrons within the solid is neglected (sudden approximation), a common approximation beyond which photoemission cannot be expressed in terms of the properties of the solid alone.

[3] There is an analogy of Eq.(1.2) to the case of a Wigner quasi-probability distribution in phase space, which becomes strictly non-negative only when averaged over phase space regions of size $\Delta x \Delta p \gg \hbar$.

are filters which may be more useful than the Gaussian one in equation (1.2) in analyzing ultrafast dynamics, since they allow to extract different kind of information, or can be used to "tomographically" reconstruct $G^<(t,t')$ and, equivalently, $N(\omega,t)$ with a series of measurements.

1.2.2 Double-probe photoemission: Tomography of $G^<(t,t')$

In this section we propose a probing scheme that allows to determine $G^<(t,t')$ in real time, based on a set of measurements with two probe pulses, which are separated in time, but have a fixed phase relation. The procedure is realistically implementable from the experimental point of view with the current technology, using splitted, delayed and recombined pulses, as shown schematically in figure 1.2. It resembles what is usually done in the established field of multidimensional optical spectroscopy, albeit the fact that what is measured is the number of emitted electrons. If $s_0(t)$ denotes the envelope of the single pulse, the total envelope $s(t)$ in equation (1.1) is given by

$$s(t) \propto s_0(t-t_0) + e^{i\varphi} s_0(t+t_0) \equiv s_+(t) + e^{i\varphi} s_-(t) \tag{1.3}$$

where φ is a relative difference of carrier envelope phase, and $2t_0$ is the temporal separation. Using equation (1.1), the photoemission intensity obtained with this double pulse is given by the sum of the photoemission $I_\pm(E,t_p)$ obtained with the individual pulses $s_\pm(t)$ as if they were used separately, and an *interference signal*

$$I_{\mathrm{intf}}(E,t_p) \propto \mathrm{Im}\Big[e^{iE2t_0-i\varphi}\int dtdt' s_0(t)s_0(t')^* \times e^{iE(t-t')} G^<\big((t_p+t_0)+t,(t_p-t_0)+t'\big)\Big]. \tag{1.4}$$

This is determined by the particular shape of the filter $S(t,t')$ (inset of figure 1.2): The first contribution samples $G^<(t,t')$ on the $t=t'$ diagonal in (t,t')-space, while the interference contribution samples it out of the diagonal [4].

This result is understood most easily in the limit of extremely short pulses $s_0(t)=\delta(t)$. A single ultrashort pulse retrieves only the time-dependent den-

[4] It can be noticed that the coherence time of the observed feature should be long enough to allow such measurement. However, the cases in which the double-probe scheme is useful are exactly the ones in which the spectral features are sharp and, therefore, long-lived.

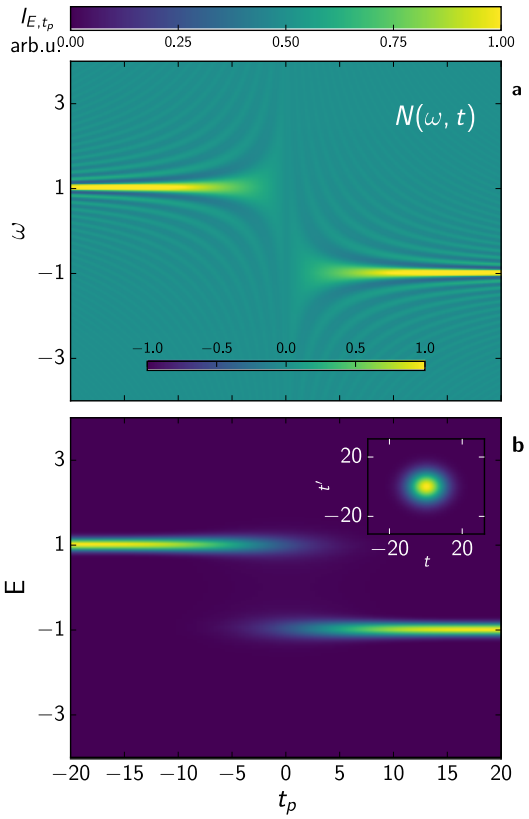

Figure 1.1: Illustration of the effect of the filter $S(t, t')$ (i.e. the probe pulses) in a photoemission experiment: The system of interest is a single level with $H(t) = \text{sign}(t)\epsilon_0 c^\dagger c$, which is initially occupied and then suddenly shifted in energy ($\epsilon_0 = 1$). Panel **a)** shows the Wigner transform $N(\omega, t)$ of the Green's function of the system. **b)** Time-resolved angle-integrated photoemission spectra obtained with a classical Gaussian probe pulse ($S(t, t')$ is shown in the inset), as a function of photoelectron energy and time. The observed switching is resolution limited.

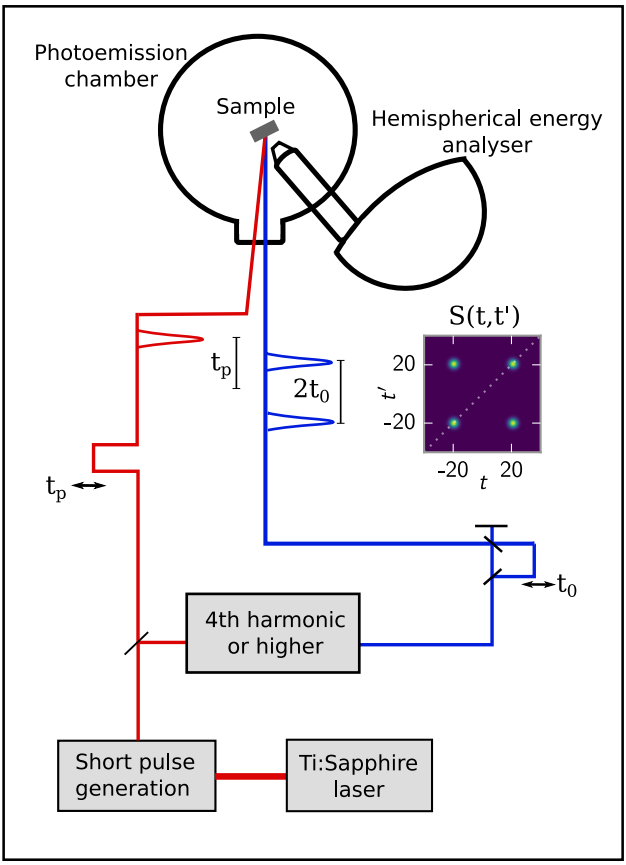

Figure 1.2: Schematic sketch of a Ti:Sapphire laser based experimental set-up that uses the double probe pulses to perform the tomography of the Green's function, by varying t_p and t_0.

sity $n_f = \langle f^\dagger f \rangle$ [c.f. equation (1.1)], so that $I_\pm(t_p, E) \propto n_f(t_p \pm t_0)$, while

$$I_{\mathrm{intf}}(E, t_p) \propto 2\,\mathrm{Im}\Big[\, G^<(t_p + t_0, t_p - t_0) e^{i2Et_0 - i\varphi} \Big]. \tag{1.5}$$

The interference contribution can be extracted in two ways. On the one hand, it can be identified by its oscillating dependence on the photoelectron final-state energy. On the other hand, the diagonal terms $I_\pm$ can be obtained from an independent measurement with a single-probe-pulse experiment. Even without any knowledge of the relative phase φ, one can thus obtain the absolute value $|G^<(t_p + t_0, t_p - t_0)|$ by varying t_p and t_0.

In section 1.3.1 we will demonstrate, for the example of the buildup of the Kondo peak, that this information is valuable to extract key features of the ongoing dynamics of the system, that are otherwise hidden by the uncertainty limit of standard probe pulses. The double-probe measurement scheme may therefore open the path for the application of extremely short pulses to study the dynamics of emergent low-energy degrees of freedom.

In the past, pioneering works [28] explored the possibilities of time-resolved *two*-photon photoemission, which uses two delayed pulses with energies ($\sim$3 eV) *below* the work function of the sample to populate empty states and then photoemit electrons from there. The study of interferometric effects allowed to measure elastic and inelastic scattering rates of excited states at the surface of metals. It is important to underline the differences between this technique and the tomographic measurement proposed here. Because time-resolved two-photon photoemission allows only to study states with energies within 3 eV from the vacuum level, i.e states that are not occupied at equilibrium, it probes a joint density of occupied and unoccupied states rather than the single-particle spectrum, and is therefore unsuited to study how the states below the Fermi energy change after a general kind of excitation, e.g. in an out-of-equilibrium phase transition or in the modification of the low-energy properties of the system. In contrast, in the tomography described in this work the interference comes from different pathways leading to the same *one*-photon photoemission event, which would allow to probe any bound state.

1.3 Illustration and proposals for the double probe experiment

1.3.1 Buildup of the Kondo resonance: standard time-resolved photoemission

In the following we illustrate the real-time measurement of the Green's function with the two-dimensional double-pulse technique (figure 1.2) for the buildup of a Kondo resonance, which is a classical problem of nonequilibrium many-body physics and also a paradigmatic example of dynamics occurring beyond the spectral uncertainty limit. We start by discussing the results in standard photoemission.

The Kondo effect can arise when a localized orbital, such as a quantum dot or an impurity atom on a metallic surface, hybridizes with a continuum of conduction electrons [32]. Depending on the orbital occupancy, a magnetic moment is formed on the impurity when charge fluctuations are suppressed because of the Coulomb repulsion. This moment becomes screened by the conduction electrons below the Kondo temperature T_K, an emergent low-energy scale of the system. The buildup of Kondo screening in real time, e.g., after the impurity is suddenly coupled to the conduction band, has recently been a subject of intensive numerical research [10,33–35]. The spectroscopic signature of the Kondo effect is a narrow resonance of width T_K at the Fermi energy (the so-called Kondo peak), which can be resolved only after times $\hbar/T_K$ [33], while the Kondo screening cloud is formed, to a large extent, on the much shorter timescale set by the hybridization between impurity and conduction band [10]. Thus, the buildup of the Kondo screening turns out to be a process which happens on timescales beyond the spectral uncertainty limit, i.e. too fast to be spectrally resolved.

We now discuss the Kondo effect at equilibrium and the results of time-resolved photoemission during the buildup of the Kondo resonance within the Anderson model,

$$H_K = \sum_\sigma \epsilon_f f_\sigma^\dagger f_\sigma + U f_\uparrow^\dagger f_\uparrow f_\downarrow^\dagger f_\downarrow + \sum_{k\sigma} V_k c_{k\sigma}^\dagger f_\sigma + h.c. + \sum_{k\sigma} \epsilon_k c_{k\sigma}^\dagger c_{k\sigma}. \quad (1.6)$$

Here f_σ and $c_{k\sigma}$ are annihilation operators for electrons with spin σ on the impurity and bath levels, respectively, ϵ_f is the position of the impurity level relatively to the Fermi level, U the on-site Coulomb energy, and V_k the tunneling matrix element between the impurity and the bath. We take the limit $U \to \infty$, so that a double occupancy of the level is suppressed, and assume a hybridization density of states $\Gamma(\epsilon) \equiv 2\pi \sum_k |V_k|^2 \delta(\omega - \epsilon_k) = \Gamma_{\rm dot}/(e^{10(\epsilon/D-1)} +$

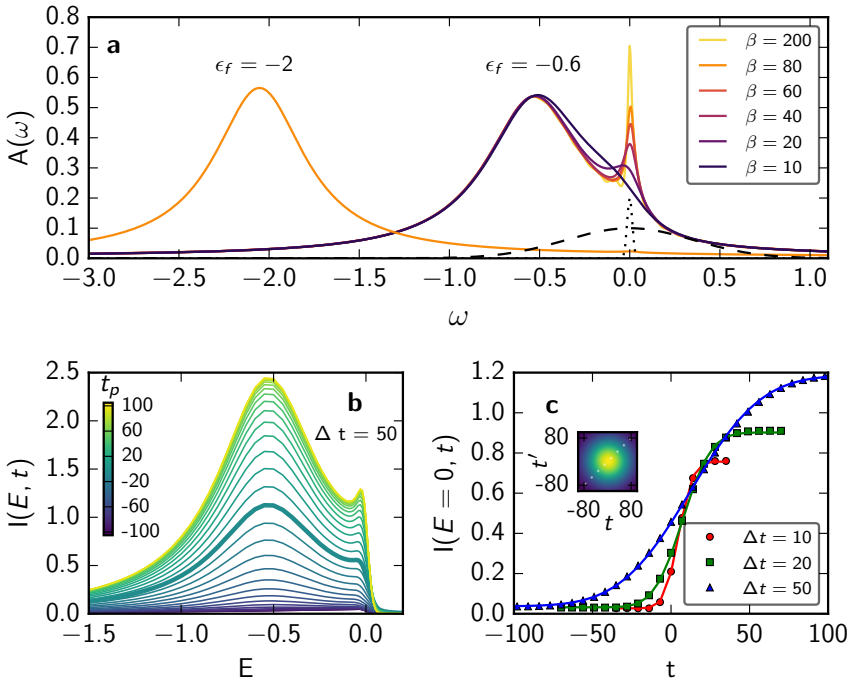

Figure 1.3: **a)** Spectral function of the Kondo model ($\Gamma_{\rm dot} = 0.6$) for various inverse temperatures β at $\epsilon_f = -0.6$ ($T_K \approx 1/200$) and $\epsilon_f = -2$ ($T_K \approx 10^{-9}$). The dotted and dashed lines respectively show the power spectrum $\propto \exp(-\omega^2 \Delta t^2)$ of Gaussian pulses with $\Delta t = 50$ and $\Delta t = 2$ for comparison. **b)** Time-resolved photoemission spectrum $I(E, t_p)$ with a Gaussian probe of $\Delta t = 50$. At $t = 0$, ϵ_f is switched from 2 to -0.6, the temperature is $T = 1/80$. The probe time is varied in steps of $\Delta t_p = 7$. The bold line corresponds to $t_p = 0$. **c)** Photo-emission intensity at $E = 0$, obtained with different probe duration Δt. Lines are fits with an error function profile, $a\,\mathrm{erf}[(t-b)/\Delta t] + c$. Inset: $S(t, t')$ for $\Delta t = 50$.

$1)(e^{-10(\epsilon/D+1)}+1)$ which is constant ($\Gamma_{\rm dot}$) below a smooth high-energy cutoff D. (In the following, $D/4$ and $4\hbar/D$ set the unit of energy and time, respectively.) The Kondo temperature of the model depends exponentially on the position of the level $T_K = De^{-\pi|\epsilon_f|/\Gamma_{\rm dot}}$. The Green's functions $G_f(t,t') = -i\langle T_C f(t) f^\dagger(t')\rangle$ at the impurity site is obtained within the time-dependent non-crossing approximation [33], using the implementation described in reference [36].

Figure 1.3a shows the spectral function $A_f(\omega) = -\frac{1}{\pi}{\rm Im}G_f^{ret}(\omega + i0)$ of the impurity atom at equilibrium. The Lorentz peak of width $1/\Gamma_{\rm dot}$ around $\omega \approx \epsilon_f$ represents the broadened impurity level. For $\epsilon_f = -0.6$ ($T_K \approx 1/200$), a Kondo resonance develops at the Fermi energy, whose width decreases proportionally to T for $T \gtrsim T_K$. Following reference [33], we now compute the buildup of the Kondo effect after the system is suddenly brought into the Kondo regime, by a shift of ϵ_f from a value $\epsilon_0 = 2$, for which the dot is basically empty, to the final value $\epsilon_1 = -0.6$ [5]. This may be thought of as a simplified representation of an experiment in which the orbital energy is suddenly shifted due to a core hole excitation. Figure 1.3b shows the photoemission intensity from the impurity level [equation (1.1)], obtained with a Gaussian probe $s(t) = \exp(-t^2/2\Delta t^2)$ with duration $\Delta t = 50$, which is just long enough to resolve the final Kondo peak in frequency space (the bandwidth of the pulse is represented by the dotted line in figure 1.3a). The buildup of spectral weight at $\omega = 0$ can almost perfectly be fitted by an error function erf with rise time Δt (c.f. figure 1.3c). This means that the buildup of the peak is resolution limited, consistently with reference [33]. With very short pulses $\Delta t < 1/\Gamma_{\rm dot}$ the signal would no longer be temporally resolution limited (because $1/\Gamma_{\rm dot} \approx 3.6$ sets the relaxation time of the impurity occupation, which is proportional to the total spectral weight), but such broadband pulses would completely wash out the Kondo peak.

1.3.2 Buildup of the Kondo resonance: double probe photoemission

In spite of the uncertainty limited buildup of the Kondo peak, as measured via a standard photoemission experiment, an analysis of the Green's function in *real time* can reveal the underlying fast timescale. Figure 1.4 shows $|G_f^<(t,t+s)| = |\langle f^\dagger(t+s) f(t)\rangle|$ for fixed t as a function of difference time s, corresponding to the hypothetical direct measurement of the decay of a hole on the impurity

[5] The precise ramp profile is $\epsilon_f(t) = (\epsilon_1 - \epsilon_0)[1-\cos(2\pi t/t_c)]/2 + \epsilon_0$ within a short ramp time $0 < t < t_c = 1$.

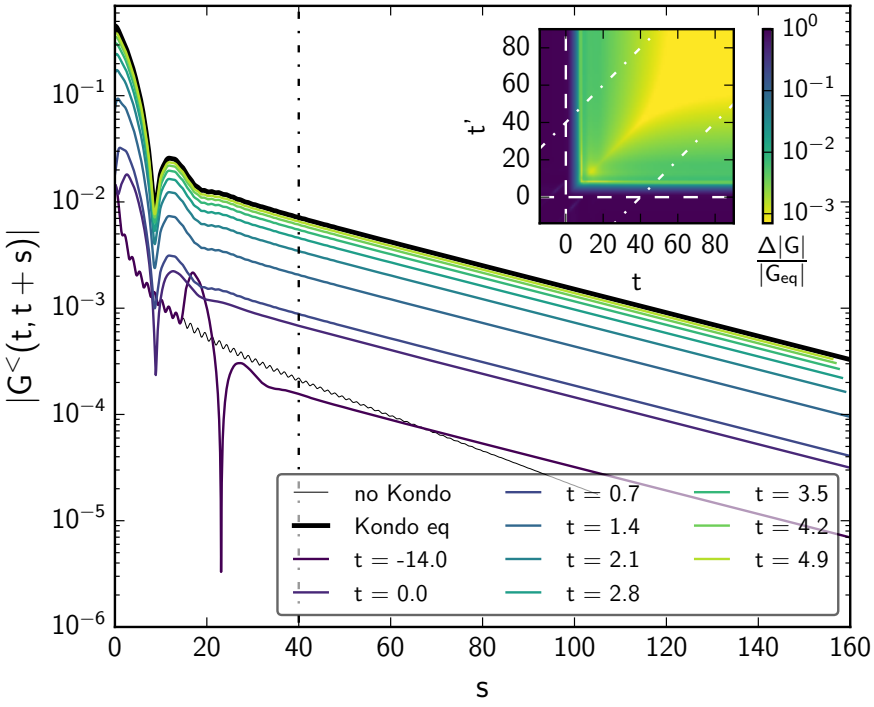

Figure 1.4: Real-time Green's function $|G_f^<(t, t+s)|$ for the same parameters as in figure 1.3b. The bold black line corresponds to the equilibrium result $|G_{eq}^<(t)|$ for $\epsilon_f = -0.6$ and $T = 1/80$. Inset: Relative difference $(|G_f^<(t,t')| - |G_{eq}^<(t-t')|)/|G_{eq}^<(t-t')|$.

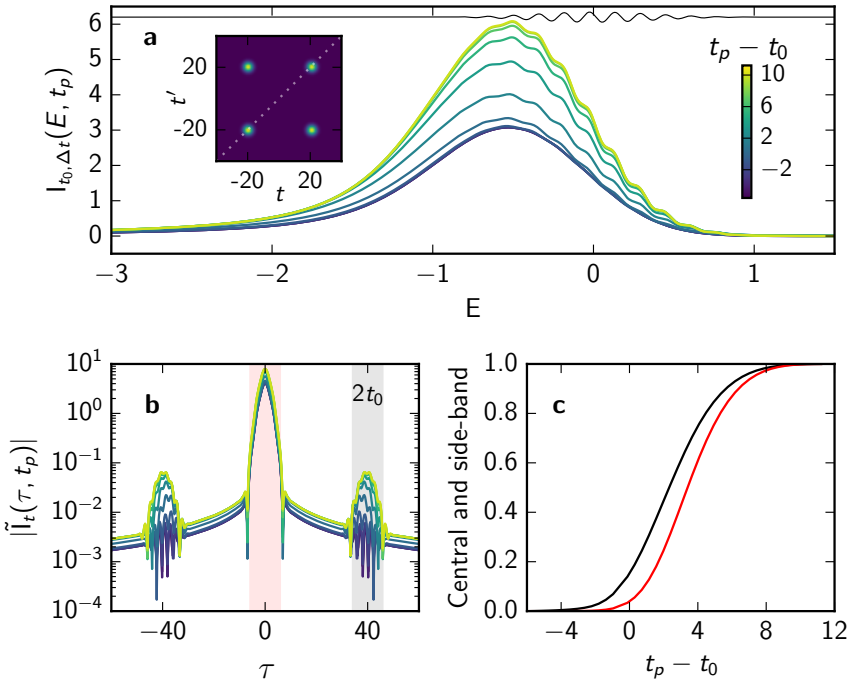

Figure 1.5: **a)** Photoemission signal $I(E, t_p)$ obtained with a double pulse [equation (1.3)] for the same parameters as in figure 1.3b. The individual pulses are separated by $t_0 = 20$ and have a Gaussian envelope with duration $\Delta t = 2$. The black line shows the interference contribution [c.f., equation (1.4)]. Inset: S(t,t') for the double pulse. **b)** Fourier transform of the signal, $\tilde{I}(\tau, t_p) = \int dE e^{iE\tau} I(E, t_p)$. **c)** Fourier component of $\tilde{I}(\tau, t_p) = \int dE e^{iE\tau} I(E, t_p)$ at $\tau = 2t_0$ (black line) and $\tau = 0$ (red line), with normalized intensity.

after it is created at time t. The fast initial drop at $s \lesssim 10$ corresponds to the Fourier transform of the bare energy level, while the slow exponential decay at large s is related to the Kondo resonance. After the quench of the impurity level, we find that the equilibrium Kondo response is almost completely formed on a timescale $1/\Gamma_{\rm dot}$, as soon as the population $n_f(t) = |G_f^<(t,t)|$ on the impurity is equilibrated. The same information is seen quantitatively from the inset in figure 1.4, which shows the relative difference between $|G_f^<(t,t')|$ and the equilibrated value reached for large times, $|G_{eq}^<(t-t')|$.

The particular structure of the inset in figure 1.4 can be seen as the real-time fingerprint that the relevant dynamics in the system occurs on timescales below the spectral uncertainty limit: If $G^<(t,t')$ at given $s = t-t'$ equilibrates on a timescale $\tau_s \ll s$, this process cannot be resolved with a Gaussian probe pulse, because for sufficient time-resolution $\Delta t < \tau_s$ only the Green's function close to the $t = t'$ diagonal ($|t-t'| \lesssim \Delta t$) contributes to the photoemission signal (see the inset of figure 1.1b). In contrast, the double-pulse technique (section 1.2.2 and inset of figure 1.2) is well suited to measure $|G^<(t,t')|$ at $t - t' \gg \Delta t$, i.e. well off from the diagonal.

In order to illustrate the main steps to be performed, we plot in figure 1.5a the result of a photoemission experiment with a double pulse [equation (1.3)] with time resolution $\Delta t = 2$, and $t_0 = 20$, i.e. with pulses separated by $2t_0 = 40$. As in the ideal case [equation (1.5)] of ultrashort pulses, the signal is a superposition of an oscillating component $\propto \sin(2Et_0 + \varphi)$ due to the interference signal produced by the two pulses, and a smooth background from the photoemission due to the individual pulses. For finite Δt the contributions have a finite width $1/\Delta t$ in energy space [6], but they can nevertheless be separated by means of a Fourier transform of the signal with respect to E (figure 1.5b), provided that $\Delta t < t_0$, i.e. that the two probe pulses are separated in time. (Alternatively, the background may also be determined independently by averaging over the phase φ, which can be shifted by changing the relative carrier envelope phase of the two probes.) This choice of t_0 allows to track the slow exponential decay of $|G^<(t,t+s)|$ (see dash-dotted lines in figure 1.4), which is related to the Kondo peak. To study its dynamics in this simple case, it is therefore not necessary to perform the full tomographic measurement, but it is sufficient just to vary t_p at fixed t_0. In this way, the interference signal measures $|G(t_p + t_0, t_p - t_0)|$. The rapid increase of the amplitude of the oscillating signal around $t_p = t_0$ (figure 1.5c) is an evidence of the characteristic fast relaxation dynamics in the Kondo problem (rise time of the black curve in

[6] Note that the two components are centred around the location ϵ_f of the bare energy level and the Kondo peak, respectively.

figure 1.5). This demonstrates how the double-probe scheme allows to analyze the relevant dynamics (the buildup of Kondo screening) with arbitrary temporal resolution (figure 1.5c), not limited by the inverse width of the Kondo peak.

In this specific case, since the Green's function to be reconstructed is characterizable in a simple way, t_0 can be kept fixed and, for each t_p, one single off-diagonal value of $G(t, t')$ has to be extracted (figures 1.5b,c). If, besides scanning t_p, the full tomography has to be performed, i.e. also further scans along t_0 are needed, the values of the Green's function for each t_p and t_0 ($G(t_p + t_0, t_p - t_0)$) would have to be extracted in the same way as above, the difference being that $G(t, t')$ would be sampled over the whole (t, t') plane and not just along the line corresponding to $t_0 = 20$.

1.3.3 Melting of Mott gaps and amplitude mode in a superconductor

The tomographic double-probe scheme (figure 1.2) could also be used to address other questions. How fast can a Mott gap be melted? What is the dynamics of the condensate of a superconductor when the Higgs mode is excited? The true timescales of the destruction of electronic order in systems with charge density waves have not been clearly resolved as, for example, in the Mott-Peierls charge density wave $1T$-TaS_2 dichalcogenide. Recent experiments [6, 16] have determined that, while the lattice charge ordering is destroyed on the timescale of the relevant lattice mode, the electronic order is destroyed quasi-istantaneously on a resolution-limited timescale. Improving the temporal resolution in standard time-resolved photoemission experiments would unavoidably bring a worse sectral resolution, which is however important to resolve the dynamics of splitted bands. The double-probe scheme would, instead, allow to access the true timescale of the process without giving up the spectral resolution.

Attention has also been dedicated to the excitation of the Higgs mode in BCS superconductors, such as $Nb_{1-x}Ti_xN$ thin films. [11, 12, 17] After the excitation with monocycle-like THz pulses, the transmittivity of the sample in the terahertz range oscillates at the frequency $2\Delta_{BCS}$, as predicted for the excitation of the Higgs amplitude mode. Oscillations of the gap of a superconductor at its own frequency fall under the dynamics occurring at the spectral uncertainty limit. The dynamics of the condensate in such a situation could be easily tracked via photoemission with the tomographic double-probe scheme, overcoming the energy-time uncertainty.

1.4 Conclusions

In conclusion, we have analyzed possibilities to use time-resolved photoemission spectroscopy as a tool to probe the evolution of the electronic structure fully in the time domain. Whenever relevant degrees of freedom evolve on timescales comparable to or faster than the inverse width of their spectral signatures, such a pure real-time characterization can provide more insight than a measurement in the usual mixed time-frequency domain, which requires a tradeoff between temporal and spectral resolution. In particular, we proposed a double-probe-pulse technique, which can be used to probe the dynamics of low-energy degrees of freedom with arbitrarily short pulses, possibly in the attosecond range, with a bandwidth that would not be able to resolve the respective linewidths in frequency space if the pulses were taken alone.

The case of dynamics occurring *beyond the spectral uncertainty limit* is actually a quite common feature of correlated systems. As examples, we discussed the buildup of the Kondo resonance, the melting of a Mott gap, and the dynamics of a superconductor when the amplitde mode is excited. Further examples include the melting of other types of electronic order such as spin-density wave gaps [37], and the buildup of screening and plasmon resonances [38].

Acknowledgements

This work has been performed during my stay at the Max Planck Institute for the Structure and Dynamics of Matter in Hamburg, Germany, in collaboration with Martin Eckstein. We thank Fulvio Parmigiani and Sharareh Sayyad for for the insightful discussion and the critical reading of this work.

Chapter 2

Time-resolved photoemission: the non-separable case

2.1 Photoemission with non-coherent states of light

In the previous chapter, I described the theoretical results we obtained about time-resolved photoemission with two probe pulses. Such double pulse is a particular case of a shaped pulse, whose state is a classical wave, and does not encompass all the possible kinds of quantum or statistical states of light. The closest quantum descriptions of classical waves are the coherent states $|\boldsymbol{\alpha}\rangle$, which are therefore also called "quasiclassical". In this chapter, I will present our generalization of the photoemission process, extending it to pulses not in a coherent state $|\boldsymbol{\alpha}\rangle$. While the double probe experiment described in chapter IV.1 allows to reconstruct $G(t,t')$ over the full (t,t') plane through a tomographic process, the manipulation of the state of the probe pulses beyond the coherent-state case can allow to retrieve specific correlations in a single measurement.

Also in this case, the discussion starts from $S(t,t')$. The probe pulse defines a filter $S(t,t')$ in the time domain [equation (1.1) of chapter IV.1] or, correspondingly, in the mixed time-frequency domain [equation (1.2) of chapter IV.1]. Such filter relates the dynamical information contained in $G^<(t,t')$

to the signal $I(E, t_p)$ measured in time-resolved photoemission. In the analysis discussed in chapter IV.1 (and in the literature in the context of standard single-probe photoemission), the pulse autocorrelation function has been generally limited to a form $S(t,t') = s(t)s(t')^*$, which can be *factorized* in the (t,t') time domain. On the other hand, an arbitrary function $S(t,t')$ could be designed to probe specific statistical features and correlations of the dynamics occurring in the system. To see how such a measurement might be implemented, we first note that an arbitrary function of Hermitian symmetry $S(t,t') = S(t',t)^*$ can be expressed, through diagonalization, as the sum of factorizable functions:

$$S(t,t') = \sum_j \eta_j \ \tilde{s}_j(t)\tilde{s}_j(t')^*, \tag{2.1}$$

where j is the label for the eigenvectors. If more than one η_j is different from zero, then $S(t,t')$ is non-factorizable in the (t,t') space. The above expression shows that the result of the hypothetical photoemission experiment with a non-factorizable filter $S(t,t')$ would be a weighted average $I = \sum_j \eta_j I_j$ of signals obtained with different pulses $\tilde{s}_j(t)$. This means that the measurement could be emulated by an equivalent "tomographic" set of experiments with factorizable filters.

The general usage of a factorizable $S(t,t')$ comes from the fact that, in the standard case, coherent states are considered for photoemission. This brings to the question whether the hypothetical tomographic experiment described in the previous chapter can be replaced by a single measurement performed with non-coherent states of light. In order to see what kind of filters $S(t,t')$ can be obtained using general probe pulses, i.e. of quantum or statistical nature, below we show what differences arise if a general state is considered for the light in the photoemission process.

The derivation of the photoemission intensity for a general state of the incoming probe pulse, described by the density matrix ρ, is rather analogous to the semiclassical case discussed in reference [23]. All its details are therefore presented separately in section 2.2, while here only the most important steps are discussed. In the Coulomb gauge ($\boldsymbol{\nabla} \cdot \boldsymbol{A} = 0$), the general vector potential $\boldsymbol{A}$ is given by an operator $A(\boldsymbol{r},t) = A^+(\boldsymbol{r},t) + A^-(\boldsymbol{r},t)$ [30],

$$A^+(\boldsymbol{r},t) = A^-(\boldsymbol{r},t)^\dagger = \sum_{\boldsymbol{q}} \mathcal{A}_{\boldsymbol{q}} \hat{a}_{\boldsymbol{q}} e^{i\boldsymbol{q}\boldsymbol{r} - i\omega_{\boldsymbol{q}} t}, \tag{2.2}$$

where $\mathcal{A}_{\boldsymbol{q}} = \sqrt{\hbar/2V\epsilon_0\omega_{\boldsymbol{q}}}$, and $\hat{a}_{\boldsymbol{q}}$ is the photon annihilation operator. To simplify the notation, we take into account only one propagation direction

$\hat{n}$ ($\boldsymbol{q} = q\hat{n}$) and transverse linear polarization. Choosing the location of the sample to be at $\boldsymbol{r} = 0$, the only change in the expression for the photoemission intensity [equation (1.1) of chapter IV.1]

$$I(E, t_p) \propto -i \int dt\, dt'\ e^{iE(t-t')} G^<(t_p+t, t_p+t')\ S(t, t')$$

is that the autocorrelation function $S(t, t')$ takes its quantum-mechanical form

$$S(t, t') = e^{i\Omega(t'-t)}\ \mathrm{Tr}\left(\rho\, A^-(t) A^+(t')\right). \tag{2.3}$$

As mentioned above, probe pulses which are classical waves can be described as a coherent state $|\Psi\rangle = |\,\boldsymbol{\alpha}\rangle = \prod_q |\alpha_q\rangle$. Using a state $|\,\boldsymbol{\alpha}\rangle$, the standard result is immediately recovered, with $S_{\boldsymbol{\alpha}}(t, t') = s_{\boldsymbol{\alpha}}(t) s_{\boldsymbol{\alpha}}(t')^*$ and probe envelope $s_{\boldsymbol{\alpha}}(t) = \sum_q e^{i(\omega_q - \Omega)t} \alpha_q^* \mathcal{A}_q$. On the other hand, if the state of the probe pulses is different from a product $|\,\boldsymbol{\alpha}\rangle$ of coherent states, i.e. it is not a quasiclassical coherent wave, $S(t, t')$ is not constrained to have the usual factorizable form. In fact, since the probe pulse only enters through the two-time correlation function, it can be shown that every function of the form (2.1) can be obtained from equation (2.3) with a multimode state whose Wigner function is Gaussian, provided that the function is positive definite, i.e. $\eta_j \geq 0$ (for more details see section 2.3). In this way, a tomographic set of measurements aimed at reconstructing the effect of a Hermitian and positive-definite filter $S(t, t')$ can, indeed, be replaced by a single experiment with probe pulses not in a coherent state. Vice versa, every measurement with non-coherent states can be replaced by a tomographic set of measurements with classical pulses, because any state of light ρ can be expressed as an integral over coherent states via the Glauber-Sudarshan P representation [29, 31] $\rho = \int d\,\boldsymbol{\beta}\ \mathcal{P}_\rho(\boldsymbol{\beta})|\,\boldsymbol{\beta}\rangle\langle\boldsymbol{\beta}\,|$.

The potential use of different filters $S(t, t')$ to obtain specific informations, such as the Wigner transform, is illustrated in figure 2.1c for the level quench already discussed in section 1.2.1, where we plot the result of equation (1.1) with a particular choice of an exotic but physical, i.e. hermitian and positive definite, cross-shaped $S(t, t')$. As can be seen, the result shown in figure 2.1c bares some of the characteristic features of the Wigner transform, plotted in panel a. In fact, an infinitely extending cross-shaped filter of the type used in figure 2.1c would yield the sum of a constant background (the contribution from the $t = t'$ diagonal) and the Wigner transform (coming from the $t = -t' + t_p$ antidiagonal), from which the full Green's function can be reconstructed.

From the experimental point of view, even though the generation and manipulation of quantum light pulses in the relevant spectral range for photoemission are not yet established, it should be noted that corrections, with respect

to the standard coherent-state case, to the results of time-resolved photoemission, can arise also if, instead of light with enhanced correlations, incoherent pulses are considered. This situation is also accounted for by the generalized expression with the quantum-mechanical $S(t,t')$. In particular, as compared to coherent light, an incoherent light pulse has a reduced correlation between the various temporal positions in the pulse. In the (t,t') plane, $S(t,t')$ must therefore quickly go to zero moving away from the $t=t'$ diagonal, as shown in the inset of figure 2.1d. This produces a reduced frequency resolution [figure 2.1d], compared to the result obtained with a coherent pulse with the same intensity profile in time.

2.2 Theory of time-resolved photoemission spectroscopy with non-classical light pulses

In the previous section, we postponed the detailed derivation of the expression for the photoemission intensity with a general probe pulse, both for the sake of clarity and because it is rather analogous to the semiclassical derivation discussed in reference [23]. In the following, the complete derivation is presented.

To describe the photoemission process, we start from a general Hamiltonian

$$H = H_{\text{matter}} + H_{\text{em}} + H_{\text{int}}, \tag{2.4}$$

where H_{matter} describes both the solid and the outgoing electron states, H_{em} is the free Hamiltonian for the electromagnetic field, and H_{int} the interaction between matter and the radiation field. The interaction Hamiltonian for light and electrons with charge $-e$ is given by [30]

$$H_{\text{int}} = H_{\text{int}}^{(1)} + H_{\text{int}}^{(2)} \tag{2.5}$$

$$H_{\text{int}}^{(1)} = \frac{e\hbar}{mc} \int d^3x\, \hat{\psi}(\boldsymbol{r})^\dagger \big[\hat{\boldsymbol{A}}(\boldsymbol{r}) \cdot \frac{1}{i}\boldsymbol{\nabla}\big] \hat{\psi}(\boldsymbol{r}) \tag{2.6}$$

$$H_{\text{int}}^{(2)} = \frac{e^2}{2mc^2} \int d^3x\, \hat{\psi}(\boldsymbol{r})^\dagger \hat{\boldsymbol{A}}(\boldsymbol{r})^2\, \hat{\psi}(\boldsymbol{r}), \tag{2.7}$$

where $\hat{\boldsymbol{A}}(\boldsymbol{r})$ is the operator for the vector potential, and $\hat{\psi}(\boldsymbol{r})$ is the fermion field operator. Here and in the following we suppress the spin index. We expand the light-field in modes with wave vector $\boldsymbol{q}$ and polarization λ,

$$H_{\text{em}} = \sum_{\boldsymbol{q},\lambda} \hbar\omega_{\boldsymbol{q}}\, \hat{a}^\dagger_{\boldsymbol{q},\lambda} \hat{a}_{\boldsymbol{q},\lambda}, \tag{2.8}$$

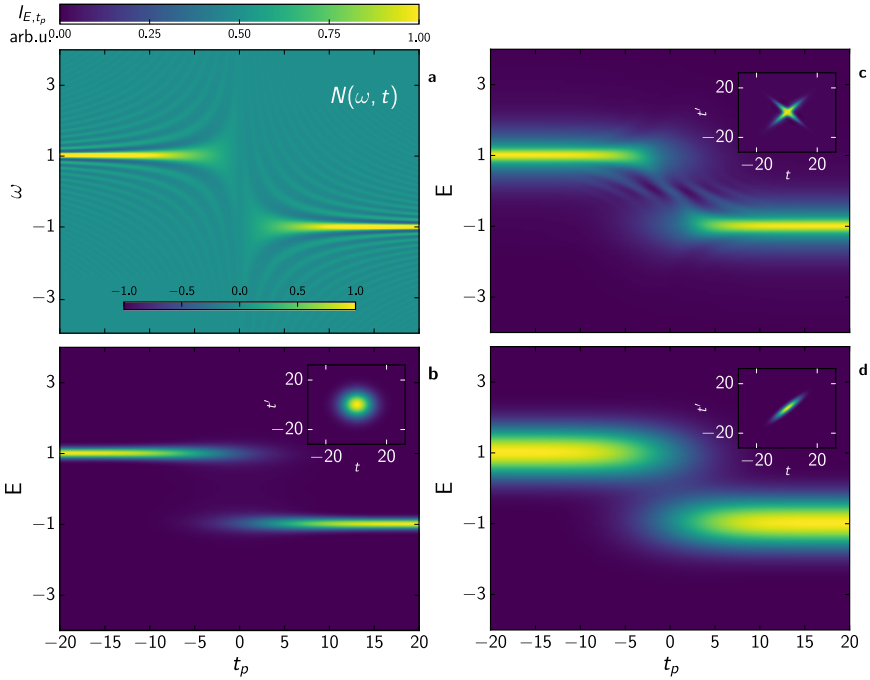

Figure 2.1: Illustration of the use of different filters $S(t, t')$ (pulses) in a photoemission experiment: The system of interest is a single level with $H(t) = \text{sign}(t)\epsilon_0 c^\dagger c$, which is initially occupied and then suddenly shifted in energy ($\epsilon_0 = 1$). Panel **a)** shows the Wigner transform $N(\omega, t)$ of the Green's function of the system. The remaining panels show time-resolved angle-integrated photoemission spectra obtained with different pulses ($S(t, t')$ is shown in the inset), as a function of photoelectron energy and time. **b)** Classical Gaussian probe pulse. The observed switching is resolution limited. **c)** Non-separable positive-definite filter S(t,t'), which, thanks to its off diagonal structure, produces some of the features of the $N(\omega, t)$ in the photoemission spectrum. **d)** Incoherent pulse with the same intensity profile in time as the coherent pulse in **b)**, which yields a lower energy resolution.

so that the vector potential in Coulomb gauge ($\boldsymbol{\nabla}\cdot\boldsymbol{A}=0$) is given by

$$\hat{\boldsymbol{A}}(\boldsymbol{r}) = \hat{\boldsymbol{A}}^{+}(\boldsymbol{r}) + \hat{\boldsymbol{A}}^{-}(\boldsymbol{r}), \tag{2.9}$$

$$\hat{\boldsymbol{A}}^{+}(\boldsymbol{r}) = \hat{\boldsymbol{A}}^{-}(\boldsymbol{r})^{\dagger} = \sum_{\boldsymbol{q},\lambda} \mathcal{A}_{\boldsymbol{q}} \hat{\boldsymbol{\epsilon}}_{\boldsymbol{q},\lambda} \hat{a}_{\boldsymbol{q},\lambda} e^{i\boldsymbol{q}\boldsymbol{r} - i\omega_{\boldsymbol{q}} t}, \tag{2.10}$$

where $\hat{\boldsymbol{\epsilon}}_{\boldsymbol{q},\lambda}$ are unit vectors with $\boldsymbol{q}\cdot\hat{\boldsymbol{\epsilon}}_{\boldsymbol{q},\lambda}=0$, and

$$\mathcal{A}_{\boldsymbol{q}} = \sqrt{\frac{\hbar}{2V\epsilon_0\omega_{\boldsymbol{q}}}}. \tag{2.11}$$

Furthermore, we expand the matter field in a suitable basis

$$\hat{\psi}(\boldsymbol{r}) = \sum_{\boldsymbol{k}} \phi_{\boldsymbol{k}}(\boldsymbol{r}) \hat{f}_{\boldsymbol{k}} + \sum_{\alpha} \chi_{\alpha}(\boldsymbol{r}) \hat{c}_{\alpha}, \tag{2.12}$$

where the index α refers to bound states (e.g., localized atomic wave functions or delocalized states in the solid), and $\boldsymbol{k}$ labels unbound states (outgoing waves) with asymptotic behavior $\phi_{\boldsymbol{k}}(\boldsymbol{r}) \sim e^{i\boldsymbol{k}\boldsymbol{r}}/\sqrt{V}$ and energy $E_{\boldsymbol{k}} = \hbar^2\boldsymbol{k}^2/2m + W$ (energies are considered with respect to the Fermi energy, and W is the work function). The photoemission experiment measures the number of electrons that, under the effect of the light-matter interaction, are emitted into an initially unoccupied outgoing mode $\boldsymbol{k}$, i.e. the occupation probability $\langle \hat{n}_{\boldsymbol{k}} \rangle = \langle \hat{f}^{\dagger}_{\boldsymbol{k}} \hat{f}_{\boldsymbol{k}} \rangle$,

$$I_{\boldsymbol{k}} = \langle n_{\boldsymbol{k}}(t) \rangle_{t\to\infty} = \big\langle \mathcal{U}(t,t_0)^{\dagger}\, n_{\boldsymbol{k}}\, \mathcal{U}(t,t_0) \big\rangle_0. \tag{2.13}$$

Here $\mathcal{U}(t,t') = T_t \exp[-i\int_{t'}^{t} d\bar{t} H(\bar{t})]$ is the time-evolution operator, and $\langle \cdots \rangle_0 = \mathrm{Tr}[\rho_0 \cdots]$ denotes the expectation value in the initial state ρ_0 for $t_0 \to -\infty$, in which light and matter are uncorrelated and $\langle \hat{n}_{\boldsymbol{k}} \rangle_0 = 0$ for all $\boldsymbol{k}$.

The probability (2.13) is computed in standard second-order time-dependent perturbation theory. We include all the non-perturbative processes that drive the system out-of-equilibrium (i.e. the pump pulse) in the time dependence of $H_{\mathrm{matter}}(t)$, and switch to the interaction representation with respect to $H_{\mathrm{matter}}(t)$, so that the time dependence of the operators is understood with respect to the uncoupled evolution $\mathcal{U}_0(t,t_0) = T_t \exp[-i\int_{t_0}^{t} d\bar{t} H_{\mathrm{matter}}(\bar{t})]$. The full time-evolution operator is expanded as

$$\begin{aligned} \mathcal{U}(t,t_0) = \mathcal{U}_0(t,t_0) \Bigg(1 - i\int_{t_0}^{t} dt_1 H_{\mathrm{int}}(t_1) \\ - \int_{t_0}^{t} dt_1 \int_{t_0}^{t_1} dt_2 H_{\mathrm{int}}(t_1) H_{\mathrm{int}}(t_2) + \cdots \Bigg). \end{aligned} \tag{2.14}$$

Because $f_{\boldsymbol{k}}$ gives zero when acting on $\rho_0 = 0$, the only non-vanishing contributions to equation (2.13) up to second order in the probe field are

$$I_{\boldsymbol{k}} = \lim_{t\to\infty} \int_{t_0}^{t} dt_1 dt_2 \left\langle H_{\rm int}^{(1)}(t_1)\, \hat{n}_{\boldsymbol{k}}(t)\, H_{\rm int}^{(1)}(t_2) \right\rangle_0. \tag{2.15}$$

To further simplify this expression, we rewrite $H_{\rm int}^{(1)}$ using the expansion (2.12),

$$H_{\rm int}^{(1)} = \frac{e\hbar i}{mc} \sum_{\boldsymbol{k},\alpha,j} f_{\boldsymbol{k}}^\dagger c_\alpha \int d^3\boldsymbol{r} A_j(\boldsymbol{r}) \phi_{\boldsymbol{k}}(\boldsymbol{r})^* \nabla_{\boldsymbol{r}}^j \chi_\alpha(\boldsymbol{r}) + h.c., \tag{2.16}$$

where the sum over cartesian components j is made explicit. In this expression, we have kept only terms containing mixed products $f_{\boldsymbol{k}}^\dagger c_\alpha$ and $c_\alpha^\dagger f_{\boldsymbol{k}}$, which induce transitions between bound states and outgoing states. Terms proportional to $c_{\alpha'}^\dagger c_\alpha$ or $f_{\boldsymbol{k}'}^\dagger f_{\boldsymbol{k}}$ give no contribution in the expectation value (2.15), as in this case an annihilation operator $f_{\boldsymbol{k}}$ would act on the initial state, which does not have any outgoing electron. To simplify the notation, we will assume linearly polarized light in the following, so that $A(\boldsymbol{r},t)$ and ∇ are understood as the components in the direction of the polarization. It is straightforward to reinsert the sums over cartesian components below. Inserting equation (2.16) in equation (2.15), we thus have

$$I_{\boldsymbol{k}} = \int d1 d2 \left(\frac{e\hbar}{mc}\right)^2 \chi(1)^*\, \nabla_1 \phi(1)\, \chi(2)\, \nabla_2 \phi(2)^* \times \\ \times\ \langle \hat{A}(1)\, \hat{c}(1)^\dagger\, \hat{f}(1)\, \hat{n}_{\boldsymbol{k}}(t)\, \hat{f}(2)^\dagger\, \hat{c}(2)\, \hat{A}(2) \rangle_0, \tag{2.17}$$

with a combined notation for indices $1 \equiv (t_1, \boldsymbol{r}_1, \alpha_1, \boldsymbol{k}_1)$,
$\int d1 = \int_{t_0}^{t} dt_1 \int d^3\boldsymbol{r}_1 \sum_{\boldsymbol{k}_1,\alpha_1}$, $\chi(1) = \chi_{\alpha_1}(\boldsymbol{r}_1)$, $\phi(1) = \phi_{\boldsymbol{k}_1}(\boldsymbol{r}_1)$, $\hat{A}(1) = \hat{A}(\boldsymbol{r}_1, t_1)$,
$\hat{f}(1) = \hat{f}_{\boldsymbol{k}_1}(t_1)$, $\hat{c}(1) = \hat{c}_{\alpha_1}(t_1)$, $\nabla_1 = \nabla_{\boldsymbol{r}_1}$ (acting on $\boldsymbol{r}_1$).

The expectation value in the above integral can be factorized in a two-time correlation function of the field and a three-time correlation function of the electrons. To reduce the expression to the single-particle properties of the solid alone, one commonly neglects the interaction of the outgoing electrons with the electrons within the solid. This so-called sudden approximation implies that the electronic correlation function factorizes in outgoing and bound state, so that the expectation value in (2.17) is given by the product of

$$\langle \hat{f}(1) \hat{n}_{\boldsymbol{k}}(t) \hat{f}(2)^\dagger \rangle_0 = e^{i(t_2-t_1)E_{\boldsymbol{k}}} \delta_{\boldsymbol{k}_2,\boldsymbol{k}} \delta_{\boldsymbol{k}_1,\boldsymbol{k}}\ , \tag{2.18}$$

the lesser Green's function

$$\langle \hat{c}(1)^\dagger \hat{c}(2) \rangle_0 = -iG^<(2,1) = -iG^<_{\alpha_2\alpha_1}(t_2,t_1), \tag{2.19}$$

and the light field correlation function

$$\Psi(1,2) = \langle : \hat{A}(1)\hat{A}(2) : \rangle_0. \tag{2.20}$$

Here $: \hat{B} :$ is the normal ordering, whose effect is to bring all annihilation operators to the right. The difference $\langle \hat{A}(1)\hat{A}(2)\rangle_0 - \langle : \hat{A}(1)\hat{A}(2) : \rangle_0$ is the vacuum expectation value of $\langle \hat{A}(1)\hat{A}(2)\rangle_0$ (a pure number). Since we do not expect spontaneous photoemission from vacuum fluctuations, we can omit these terms.

As a further simplification, we assume that the propagation time $\delta t = L/c$ of light through the probed volume is small compared to the pulse duration Δt. Technically, the mode frequencies in the pulse are distributed around some large carrier frequency Ω and wave vector $\boldsymbol{q}_0$, with widths $\Delta\omega$ and $\Delta q = \Delta\omega/c$, respectively. We can then factor out this main carrier wave vector and set

$$\hat{\boldsymbol{A}}^{\pm}(\boldsymbol{r}) \approx e^{\pm i\boldsymbol{q}_0\boldsymbol{r}}\hat{\boldsymbol{A}}^{\pm}(\boldsymbol{r}=0), \tag{2.21}$$

(with the probe volume centered at $\boldsymbol{r} = 0$), provided that $L\Delta q \ll 1$, which is indeed equivalent to $\delta t \ll \Delta t$ because $\Delta t \approx 1/\Delta\omega$. The approximation can be systematically improved, but, like any precise treatment of matrix elements, it would not alter the general discussion of the properties of time-resolved photoemission. Furthermore, the approximation is exact for a point-like object, like an atom on a surface, or a thin layer. With these considerations and equation (2.9), we can write the light correlation function as

$$\Psi(1,2) \approx \sum_{\sigma_1,\sigma_2=\pm} e^{i\sigma_1\boldsymbol{q}_0\boldsymbol{r}_1} e^{i\sigma_2\boldsymbol{q}_0\boldsymbol{r}_2} \Psi_{\sigma_1,\sigma_2}(t_1,t_2), \tag{2.22}$$

with $\Psi_{\sigma_1,\sigma_2}(t_1,t_2) = \langle : \hat{A}^{\sigma_1}(t_1,0)\hat{A}^{\sigma_2}(t_2,0) : \rangle_0$. Furthermore, it is useful to factor out the carrier frequency Ω

$$\Psi_{\sigma_1,\sigma_2}(t_1,t_2) \equiv e^{-i\Omega(\sigma_1 t_1 + \sigma_2 t_2)} S_{\sigma_1,\sigma_2}(t_1,t_2). \tag{2.23}$$

The time-dependent part of the integral (2.17) is then written by

$$\sum_{\sigma_1,\sigma_2=\pm} (-i) \int_{t_0}^{t} dt_1 dt_2\, G^{<}_{\alpha_2\alpha_1}(t_2,t_1) S_{\sigma_1\sigma_2}(t_1,t_2) \times \\ \times\ e^{i(t_2-t_1)E_{\boldsymbol{k}}} e^{i\Omega(\sigma_1 t_2 + \sigma_2 t_1)}.$$

For large carrier frequency, only the term $(\sigma_1,\sigma_2) = (-,+)$ with exponential factor $e^{i(\Omega - E_{\boldsymbol{k}})(t_1-t_2)}$ will survive the integration. For all the other combinations of σ_1 and σ_2, the exponent contains counter-rotating terms which

oscillate quickly compared to the time-dependence of G and S, thus vanishing upon integration. The final result is

$$I_{\boldsymbol{k}} = \sum_{\alpha\alpha'} p^*_{\boldsymbol{q}_0,\boldsymbol{k},\alpha} p_{\boldsymbol{q}_0,\boldsymbol{k},\alpha'} \times \\ \times \int dt dt' e^{i(t-t')(E_{\boldsymbol{k}}-\Omega)} (-i) G^<_{\alpha\alpha'}(t,t') S(t,t'), \quad (2.24)$$

where $p_{\boldsymbol{q}_0,\boldsymbol{k},\alpha}$ are matrix elements between the bound and outgoing states

$$p_{\boldsymbol{q}_0,\boldsymbol{k},\alpha} = \int d^3\boldsymbol{r}\, e^{i\boldsymbol{q}_0\boldsymbol{r}} \chi_\alpha(\boldsymbol{r}) \nabla \phi_{\boldsymbol{k}}(\boldsymbol{r})^*, \quad (2.25)$$

and

$$S(t,t') = e^{i\Omega(t'-t)} \sum_{q_1,q_2} \mathcal{A}_{q_1} \mathcal{A}_{q_2} e^{i\omega_{q_1} t - i\omega_{q_2} t'} \langle a^\dagger_{q_1} a_{q_2} \rangle_0 \\ = e^{i\Omega(t'-t)} \operatorname{Tr}\left(\rho\, A^-(t) A^+(t')\right) \quad (2.26)$$

as in equation (2.3) of section 2.1.

For a coherent state the expectation value factorizes, so that $S(t,t') = e^{-i\Omega t}\langle\Psi|A^-(t)|\Psi\rangle\langle\Psi|A^+(t')|\Psi\rangle e^{i\Omega t'} \equiv s(t)s(t')^*$ and $A(t) = \langle\Psi|A^-(t)|\Psi\rangle + \langle\Psi|A^+(t)|\Psi\rangle = s(t)e^{i\Omega t} + s(t)^* e^{-i\Omega t}$.

2.3 Pulse correlation for a multimode squeezed state

As an illustration of $S(t,t')$ for more general states with Gaussian Wigner function, we now evaluate equation (2.26) for a multimode squeezed vacuum $|\Psi\rangle = Q^\dagger|0\rangle$, with the squeezing operator

$$Q = \exp\Big[\frac{1}{2}\sum_{\omega\omega'} R_{\omega,\omega'} a^\dagger_\omega a^\dagger_{\omega'} - h.c.\Big]. \quad (2.27)$$

The squeezing matrix R is symmetric in frequency space, but not necessarily Hermitian. (We switched between frequency and momentum labels $\omega = cq$ because light is propagating on one axis only.). We evaluate equation (2.26) in the frequency domain, i.e., we compute

$$S_{\omega,\omega'} = \int dt dt' e^{-i\omega t} S(t,t') e^{i\omega' t'}. \quad (2.28)$$

For simplicity, we set the energy shift $\Omega = 0$ in the following. Inserting equation (2.26) in (2.28) we obtain

$$\frac{1}{(L/c)^2}\mathcal{A}_\omega^{-1} S_{\omega,\omega'} \mathcal{A}_{\omega'}^{-1} = \langle \Psi | a_\omega^\dagger a_{\omega'} | \Psi \rangle. \tag{2.29}$$

The prefactor is the normalization volume, with $\int dt e^{i(\omega-\omega')t} = (L/c)\delta_{\omega,\omega'}$. To evaluate the expectation value $\langle \Psi | a_\omega^\dagger a_{\omega'} | \Psi \rangle$, we use the commutator relation $e^A B e^{-A} = B + [A,B] + \frac{1}{2!}[A,[A,B]] + ...$ to obtain the general identity [30],

$$Q a_\omega Q^\dagger = \sum_{\omega'} \mathcal{C}_{\omega,\omega'} a_{\omega'} - \sum_{\omega'} \mathcal{S}_{\omega,\omega'} a_{\omega'}^\dagger, \tag{2.30}$$

with the functions

$$\mathcal{C} = \sum_{n=0}^{\infty} \frac{(RR^\dagger)^n}{(2n)!}, \;\; \mathcal{S} = \sum_{n=0}^{\infty} \frac{R(R^\dagger R)^n}{(2n+1)!}. \tag{2.31}$$

(For a single mode and $R = |r|e^{i\theta} \in \mathbb{C}$, the two functions correspond to the the hyperbolic functions $\mathcal{C} = \cosh|r|$ and $\mathcal{S} = e^{i\theta}\sinh|r|$.) In the expectation value $\langle 0 | Q a_\omega^\dagger a_{\omega'} Q^\dagger | 0 \rangle$ we thus get, dropping the terms $a|0\rangle$,

$$\begin{aligned} \langle 0 | Q a_\omega^\dagger a_{\omega'} Q^\dagger | 0 \rangle &= \langle 0 | Q a_\omega^\dagger Q^\dagger Q a_{\omega'} Q^\dagger | 0 \rangle & (2.32) \\ &= \sum_{\omega_1,\omega_2} \mathcal{S}^*_{\omega,\omega_2} \mathcal{S}_{\omega'\omega_1} \langle 0 | a_{\omega_2} a_{\omega_1}^\dagger | 0 \rangle & (2.33) \\ &= (\mathcal{S}\mathcal{S}^\dagger)_{\omega',\omega}, & (2.34) \end{aligned}$$

which, together with equation (2.29), concludes the determination of $S_{\omega,\omega'}$.

More interestingly, we can use equations (2.29) and (2.34) to prove the statement, given in section 2.1, that any desired correlation function $S_{\omega,\omega'}$ (or $S(t,t')$) can be, in principle, obtained from a *single* light pulse, provided that the matrix $S_{\omega,\omega'}$ is (i), *Hermitian*, and (ii), *positve definite*. Conditions (i) and (ii) imply that the matrix $M_{\omega,\omega'} \equiv \frac{1}{(L/c)^2}\mathcal{A}_\omega^{-1} S_{\omega,\omega'} \mathcal{A}_{\omega'}^{-1}$ in equation (2.29) can be diagonalized, $M = V d V^\dagger$, where d is diagonal with $d_{\alpha\alpha} \geq 0$. The latter implies that the choice

$$R = V \mathrm{asinh}(\sqrt{d}) V^*, \tag{2.35}$$

with $(V^*)_{\omega,\omega'} = V^*_{\omega,\omega'}$, is a well-defined symmetric matrix. Using equations (2.31) and (2.34) one can then directly verify that equation (2.29) is satisfied, i.e, the squeezed vacuum equation (2.27) with the squeezing matrix (2.35) gives the desired cross-correlation $S_{\omega,\omega'}$.

2.4 Conclusions

The use of quantum or statistical correlations in the light pulse would enhance the possibilities to characterize the dynamics with a time-resolved photoemission experiment. While this may seem technologically challenging at present, it contributes to the questions whether correlations of light can be exploited to enhance, in a similar way, the capabilities of time-dependent measurements in other spectroscopic techniques, such as two-photon photoemission or optical spectroscopy.

Acknowledgements

This work has been performed during my stay at the Max Planck Institute for the Structure and Dynamics of Matter in Hamburg, Germany, in collaboration with Martin Eckstein.

Bibliography

[1] A. Damascelli, Z. Hussain, and Z. Shen, "Angle-resolved photoemission studies of the cuprate superconductors", Rev. Mod. Phys. **75**, 473 (2003).

[2] "Strongly Correlated Systems: Experimental Techniques", edited by A. Avella and F. Mancini, Springer Series in Solid-State Sciences.

[3] C. Giannetti, M. Capone, D. Fausti, M. Fabrizio, F. Parmigiani, and D. Mihailovic, "Ultrafast optical spectroscopy of strongly correlated materials and high-temperature superconductors: a non-equilibrium approach", arXiv:1601.07204.

[4] F. Schmitt et al. "Transient electronic structure and melting of a charge density wave in $TbTe_3$", Science **321** 1649, (2008).

[5] T. Rohwer et al. "Collapse of long-range charge order tracked by time-resolved photoemission at high momenta", Nature **471**, 490 (2011).

[6] J.C. Petersen, S. Kaiser, N. Dean, A. Simoncig, H.Y. Liu, A.L. Cavalieri, C. Cacho, I.C.E. Turcu, E. Springate, F. Frassetto, L. Poletto, S.S. Dhesi, H. Berger, and A. Cavalleri "Clocking the melting transition of charge and lattice order in $1T$-TaS_2 with ultrafast extreme-ultraviolet angle-resolved photoemission spectroscopy" Phys. Rev. Lett. **107**, 177402 (2011).

[7] L. Perfetti, P. A. Loukakos, M. Lisowski, U. Bovensiepen, H. Berger, S. Biermann, P. S. Cornaglia, A. Georges, and M. Wolf, "Time evolution of the electronic structure of $1T$-TaS_2 through the insulator-metal transition", Phys. Rev. Lett. **97**, 067402 (2006).

[8] D. Wegkamp, M. Herzog, L. Xian, M. Gatti, P. Cudazzo, Ch. L. McGahan, R. E. Marvel, R. F. Haglund, A. Rubio, M. Wolf, and J. Stähler,

"Instantaneous band gap collapse in photoexcited monoclinic VO_2 due to photocarrier doping", Phys. Rev. Lett. **113**, 216401 (2014).

[9] M. Chini, K. Zhao, and Z. Chang. "The generation, characterization and applications of broadband isolated attosecond pulses", Nat. Phot., **8**, 178 (2014).

[10] B. Lechtenberg and F. B. Anders, "Spatial and temporal propagation of Kondo correlations", Phys. Rev. B **90**, 045117 (2014).

[11] R. Matsunaga, Y.I. Hamada, K. Makise, Y. Uzawa, H. Terai, Z. Wang, and R. Shimano "Higgs amplitude mode in the BCS superconductor $Nb_{1-x}Ti_xN$ induced by terahertz pulse excitation" Phys. Rev. Lett. **111**, 057002 (2013).

[12] R. Matsunaga, N. Tsuji, H. Fujita, A. Sugioka, K. Makise, Y. Uzawa, H. Terai, Z. Wang, H. Aoki, and R. Shimano "Light-induced collective pseudospin precession resonating with Higgs mode in a superconductor" Science **345**, 1145 (2014).

[13] L. Landau and E. Lifschitz, "Quantum mechanics - Non-relativistic theory", Course of theoretical physics **3**, 157 (§44: The uncertainty relation for energy), Pergamon Press (1977).

[14] S. Mukamel "Principles of Nonlinear Optics and Spectroscopy" Oxford University Press (1995).

[15] W. M. Zhang, V. Chernyak, and S. Mukamel "Multidimensional femtosecond correlation spectroscopies of electronic and vibrational excitons" J. Chem. Phys. **110**, 5011 (1999).

[16] C. Sohrt, A. Stange, M. Bauer, and K. Rossnagel "How fast can a Peierls-Mott insulator be melted?" Faraday Discuss. **171**, 243 (2014).

[17] A. F. Kemper, M. A. Sentef, B. Moritz, J. K. Freericks, and T. P. Devereaux, "Direct observation of Higgs mode oscillations in the pump-probe photoemission spectra of electron-phonon mediated superconductors", Phys. Rev. B **92**, 224517 (2015).

[18] S Haroche, "Nobel lecture: Controlling photons in a box and exploring the quantum to classical boundary", Rev. Mod. Phys. **85**, 1083 (2013).

[19] D. Wineland, "Nobel lecture: Superposition, entanglement, and raising Schrödinger's cat", Rev. Mod. Phys., **85**, 1103 (2013).

[20] R. Schnabel, N. Mavalvala, D. E. McClelland, and P. K. Lam, "Quantum metrology for gravitational wave astronomy", Nat. Comm. **1**, 121 (2010).

[21] N. Treps, U. Andersen, B. Buchler, P. K. Lam, A. Maître, H.-A. Bachor, and C. Fabre, "Surpassing the standard quantum limit for optical imaging using nonclassical multimode light", Phys. Rev. Lett., **88**, 203601 (2002).

[22] M. Esposito, K. Titimbo, K. Zimmermann, F. Giusti, F. Randi, D. Boschetto, F. Parmigiani, R. Floreanini, F. Benatti, and D. Fausti, "Photon number statistics uncover the flucutuations in non-equilibrium lattice dynamics", Nat. Comm. **6**, 10249 (2015).

[23] J. K. Freericks, H. R. Krishnamurthy, and Th. Pruschke. "Theoretical description of time-resolved photoemission spectroscopy: Application to pump-probe experiments", Phys. Rev. Lett., **102**, 136401 (2009).

[24] M. Eckstein and M. Kollar, "Measuring correlated electron dynamics with time-resolved photoemission spectroscopy", Phys. Rev. B, **78**, 245113 (2008).

[25] J. Eberly and K. Wdkiewicz "The time-dependent physical spectrum of ligh" J. Opt. Soc. Am. 67 **9**, 1252 (1997)

[26] S. Mukamel, C. Ciordas-Ciurdariu and V. Khidekel "Wigner Spectrograms for Femtosecond Pulse-Shaped Heterodyne and Autocorrelation Measurements" IEEE J. Quantum Electron. 32 **8**, 1278 (1996)

[27] K. Dorfman and S. Mukamel "Nonlinear spectroscopy with time- and frequency-gated photon counting: A superoperator diagrammatic approach" Phys. Rev. A **86**, 013810 (2012)

[28] H. Petek and S. Ogawa, "Femtosecond time-resolved two photon photoemission studies of electron dynamics in metals", Progress in Surface Science, **56**, 293 (1997).

[29] R. J. Glauber. "Coherent and incoherent states of the radiation field", Phys. Rev. **131**, 2766 (1963).

[30] O. M. Scully and M. S. Zubairy, "Quantum Optics", Cambridge University Press (1997).

[31] E. C. G. Sudarshan. "Equivalence of semiclassical and quantum mechanical descriptions of statistical light beams", Phys. Rev. Lett., **10**, 277 (1963).

[32] A. C. Hewson, "The Kondo problem to heavy fermions", Cambridge University Press (1993).

[33] P. Nordlander, M. Pustilnik, Y. Meir, N. S. Wingreen, and D. C. Langreth, "How long does it take for the Kondo effect to develop?", Phys. Rev. Lett. **83**, 808 (1999).

[34] F. B. Anders and A. Schiller. "Real-time dynamics in quantum-impurity systems: A time-dependent numerical renormalization-group approach", Phys. Rev. Lett. **95**, 196801 (2005).

[35] A. Antipov, Q. Dong, and E. Gull. "Voltage quench dynamics of a Kondo system", arXiv:1508.06633.

[36] M. Eckstein and Ph. Werner. "Nonequilibrium dynamical mean-field calculations based on the noncrossing approximation and its generalizations", Phys. Rev. B, **82**, 115115 (2010).

[37] N. Tsuji, M. Eckstein, and Ph. Werner, "Nonthermal antiferromagnetic order and nonequilibrium criticality in the Hubbard model", Phys. Rev. Lett. **110**, 136404 (2013).

[38] R. Huber, F. Tauser, A. Brodschelm, M. Bichler, G. Abstreiter, and A. Leitenstorfer, "How many-particle interactions develop after ultrafast excitation of an electron-hole plasma", Nature **414**, 286 (2011).

[39] S. Sayyad and M. Eckstein. "Slow down of the electronic relaxation close to the Mott transition" arXiv:1601.02994.

Conclusions

Strongly correlated materials display a variety of macroscopic properties both of fundamental and technological interest, the mechanisms at whose origin are not fully understood. Studying them out of their equilibrium state allows to separately observe the different degrees of freedom which, together, give rise to such properties. In this thesis I have presented four different works that deal with issues related to out-of-equilibrium strongly correlated materials. While the first two parts report experimental results, the third and the fourth parts present two theoretical works.

From the point of view of their technological applications, part of the interest lies in the fact that, in strongly correlated materials, phase transitions can be triggered on timescales of the femto- and picosecond, thus providing, e.g., electronics for ultrafast switching. In part I, I have presented our results on the out-of-equilibrium insulator-to-metal Verwey phase transition in magnetite, studied via pump-probe spectroscopy. Besides the technological aspect, this case study provides insights on the general dynamics of the nonequilibrium analogs of first-order phase transitions. To provide a solid basis for the analysis of the out-of-equilibrium results, we also performed equilibrium ellipsometry to measure how the optical properties of magnetite change across the phase transition.

The out-of-equilibrium phase transition can be triggered, in a sample at a temperature below the critical temperature, by light pulses with a sufficiently high fluence [1]. Our data reveal that, close to the threshold for the triggering of the transition, there is a regime which is closely related to the delivery of latent heat at equilibrium. In this regime, the phase transition occurs through the nucleation of local excitations into volumes of the sample in the high-temperature phase. Out-of-equilibrium phase separation therefore occurs in the sample. For pump fluences well above the threshold, the sample is instead immediately and homogeneously brought in the high-temperature phase. One of the most interesting results I reported is that, in the close-to-

threshold regime, i.e. when out-of-equilibrium phase separation occurs, the relative variation of the reflectivity $\frac{\Delta R}{R}$ of the sample displays a specific mathematical property: it is non-separable in the space of spectra and temporal evolutions. This is a formal way to state that $\frac{\Delta R}{R}$ cannot be written as the product of a single spectral feature with a single temporal evolution for all the probe photon energies, but has to be written as the sum of two or more such terms, or components. Well below and well above threshold, instead, $\frac{\Delta R}{R}$ is separable, i.e. it can be expressed as a single spectro-temporal component. Since this is a model-free, purely mathematical property of the data, one could conjecture that it is a general signature of out-of-equilibrium phase separation beyond the specific case of magnetite. Analysing data present in the literature about similar experiments [2], I have shown that this is indeed the case at least for another material, vanadium dioxide (VO_2).

The experiments on magnetite have been performed with pump pulses at 1.5 eV photon energy. This choice has been determined by the fact that commercial pulsed lasers mostly produce light pulses with such photon energy. In general, this practical constraint forces to adopt the assumption that the excitations these pulses create in the system are "right", in that they are either tuned to the relevant transitions or that the excitations they produce are sufficiently general in character. In the case of the Verwey phase transition, a photon energy of 1.5 eV is indeed tuned to transitions that tend to destroy the charge order of the low-temperature phase, and it is, therefore, a "good" photon energy to study the out-of-equilibrium Verwey phase transition. However, this is not the case for every compound and every process one may want to study.

The degrees of freedom involved in the formation of the superconducting state in the cuprate high-temperature superconductors have typical energies of the order of 10 or 100 meV. To excite them in a controlled way, light pulses in the mid-infrared range are needed. In chapter II.1 of this thesis, I have described the set-up I have built for the production of mid-infrared light pulses with photon energies between 80 and 200 meV.

In chapter II.2 I have then presented pump-probe experiments on the optimally yttrium-doped cuprate Bi2212 ($Bi_2Sr_2Ca_{0.92}Y_{0.08}Cu_2O_8$), with pump pulses in the mid-infrared spectral range. Our data reveal that the dynamics produced by the excitation is strongly k-dependent. At room temperature, we report evidence for the coupling of electrons to fluctuating charge order and to spin excitations. In particular, totally symmetric excitations and excitations along the direction which in the superconducting phase is the antinodal direction are coupled to pairs of spin excitations. Along the direction which at low temperatures becomes the nodal direction, excitations are coupled to a

vibrational mode which is associated to a superstructural modulation of the lattice, which coherently oscillates after the excitation by the pump pulse. As the temperature is lowered, and the sample enters the pseudogap phase, such coherent lattice vibrations disappear. This means either that the coupling of electrons to the superstructural modulation changes, or that the latter disappears as the temperature is lowered. In the superconducting phase, we have been able to separately observe the dynamics of pseudogap excitations and another kind of dynamics via k-selective measurements.

Optical pump-probe experiments are performed measuring the intensity of the probe pulses at different delays between the pump and the probe. To remove the noise, for each pump-probe delay the measurement of the probe intensity is averaged over hundreds or thousands of pulses. How the intensity fluctuates is almost always neglected. Moreover, in many cases, the discussion of the data makes use of the assumption that the state of the system after the excitation can be considered as an effectively thermal state. The work I have presented in part III deals with these two issues. What additional information can be learnt via the measurement of the fluctuations of the out-of-equilibrium optical properties of a system? How does the system thermalize when the ongoing dynamics is nontrivial?

We have shown that, in general, the fluctuations of the optical properties are related to the fluctuations of the current in the system. To contextualize this, we performed nonequilibrium dynamical mean-field theory calculations [3, 4] on the Holstein model, in which an impulsive excitation produces coherent lattice vibrations. We have shown that nonequilibrium DMFT is able to capture the main features of coherent vibrations in Peierls' systems, i.e. the displacive excitation, the softening of the frequency of the vibration, the damping of the oscillation, and the eventual melting of the symmetry-broken phase. This provides a basic nontrivial dynamics to theoretically explore what information can be accessed via the fluctuations of the optical properties. Testing fluctuation-dissipation relations, we have shown that, after the excitation, the system oscillates between thermal and non-thermal states as the gap is modulated. This produces characteristic features in the spectrum of the fluctuations of the current, which can be probed via the measurement of the fluctuations of the probe pulse intensity. With our simulations, we have been able to reproduce experimental results obtained on bismuth single crystals, showing that this kind of measurements can, indeed, give access to new information in out-of-equilibrium all-optical spectroscopies.

Besides all-optical pump-probe experiments, time-resolved photoelectron spectroscopy is one of the prime tools to study out-of-equilibrium condensed

matter, as it allows to simultaneously measure the time-dependent distribution of electrons and the time-dependent band structure. In its standard setting, the energetic and temporal resolutions in time-resolved photoemission are affected by the energy-time uncertainty relation. Such limitation becomes extremely relevant in the study of the nonequilibrium dynamics of the emergent properties of strongly correlated materials. While these become manifest in very sharp spectral features, it is known that some of them can evolve on timescales shorter than the inverse width of their spectroscopic fingerprint [5]. This kind of dynamics beyond the spectral uncertainty limit cannot be resolved in standard time-resolved photoemission. Such limitation is usually taken to be inevitable. The energy-time uncertainty is, however, not of fundamental nature, i.e. it is not a Heisenberg-type relation [6].

In chapter IV.1 I have described our theoretical proposal to bypass the energy-time uncertainty in time-resolved photoemission. This can be achieved using two probe pulses to photoemit the electrons from the system. Such double probe pulse can be obtained by splitting, delaying, and recombining a single pulse of arbitrarily short duration. As a function of the delay between the two pulses, the total probability for an electron to be photoemitted changes. From such dependence, it is possible to tomographically reconstruct the Green's function $G(t, t')$, which contains the full single-particle response of the system. We have illustrated this theoretical proposal with calculations of the buildup of the Kondo resonance, a prototypical dynamics of an emergent phenomenon occurring beyond the spectral uncertainty limit. Moreover, we discussed its relevance and possible applications in other cases, as for example the melting of Mott gaps or the dynamics of superconductors.

Finally, in chapter IV.2 I presented our discussion of the use of quantum or statistical light in photoemission. Specifically shaped quantum or statistical probe pulses would allow to measure specific correlations in the ongoing dynamics in the sample with a single measurement, i.e. without the need to perform the tomographic sequences of measurements discussed in chapter IV.1.

Bibliography

[1] S. de Jong, R. Kukreja, C. Trabant, N. Pontius, C. F. CHang, T. Kachel, M. Beye, F. Sorgenfrei, B. Back, C. H. Bräuer, et al. Speed limit of the insulator-metal transition in magnetite. *Nat. Mater.*, 12:882–886, 2013.

[2] S. Wall, L. Foglia, D. Wegkamp, K. Appavoo, J. Nag, R.F. Haglund, Jr., J. Stähler, and M. Wolf Tracking the evolution of electronic and structural properties of VO_2 during the ultrafast photoinduced insulator-metal transition Phys. Rev. B **87**, 115126 (2013).

[3] A. Georges, G. Kotliar, W. Krauth, and M.J. Rozenberg "Dynamical mean-field theory of strongly correlated fermion systems and the limit of infinite dimensions" Rev. Mod. Phyis. **68**, 13 (1996).

[4] H. Aoki, N. Tsuji, M. Eckstein, M. Kollar, T. Oka, and P. Werner "Nonequilibrium dynamical mean field theory and its applications" Rev. Mod. Phys. **86**, 779 (2014).

[5] B. Lechtenberg and F. B. Anders, "Spatial and temporal propagation of Kondo correlations", Phys. Rev. B **90**, 045117 (2014).

[6] L. Landau and E. Lifschitz, "Quantum mechanics - Non-relativistic theory", Course of theoretical physics **3**, 157 (§44: The uncertainty relation for energy), Pergamon Press (1977).

List of publications

- Phase separation in the nonequilibrium Verwey transition in magnetite, Phys. Rev. B **93** 054305 (2016).
- Bypassing the energy-time uncertainty in time-resolved photoemission, Phys. Rev. B **95** 115132 (2017).
- Fluctations of the out-of-equilibrium optical properties: The case of the Holstein model, in preparation.
- Evidence of fluctuating charge order and local spin excitations in the strange metal phase of optimally doped Bi2212, in preparation.
- Out-of-equilibrium B_{1g} and B_{2g} quasiparticles in the superconducting and pseudogap phases of Bi2212, in preparation.

Other contributions

- Esposito et al., Quantum interferences reconstructon with low homodyne detecton efficiency, EPJ Quantum Technology 3 (1), 1
- Esposito et al., Photon number statstcs uncover the fluctuatons in non-equilibrium lattice dynamics, Nat. Comm 6
- Esposito et al., Pulsed homodyne Gaussian quantum tomography with low detecton efficiency, EPJ 16 (4), 043004

Software

- Python library for the analysis of spectroscopic data (https://github.com/francescorandi/optics). In collaboration with I. Vergara.

Acknowledgements

First of all, I would like to thank Daniele Fausti for giving me the opportunity to work on exciting topics during my PhD, and Martin Eckstein for the great time in Hamburg. Fulvio Parmigiani, for the guidance and for always adding something valuable. I thank Martina, Francesca, Ghil, Andrea, Giulia, Barbara, Sharareh and Giorgia for sharing part of the last three years. A big thank to Federico for being always available to help in the lab, to Goran, Marco, and all the others for sharing ideas with me during the numerous discussion in the office and in the lab.

Begriffe, welche sich bei der Ordnung der Dinge als nützlich erwiesen haben, erlangen über uns leicht eine solche Autorität, dass wir ihres irdischen Ursprungs vergessen und sie als unabänderliche Gegebenheiten hinnemen. Sie werden dann zu ,,Denknotwendigkeiten", ,,Gegebenen a priori" usw. gestempelt. Der Weg des wissenschaftlichen Fortschrittes wird durch solche Irrtümer oft für lange Zeit ungangbar gemacht. Es ist deshalb keine müßige Spielerei, wenn wir darin geübt werden, die längst geläufigen Begriffe zu analysieren und zu zeigen, von welchen Umständen ihre Berechtigung und Brauchbarkeit abhängt, wie sie in einzelnem aus den Gegebenheiten der Erfahrung herausgewachsen sind. Dadurch wird ihre allzu große Autorität gebrochen.

A. Einstein, *Ernst Mach*, Physikalische Zeitschrift, 1. April 1916